# Supramolecular Block Copolymers by Seeded Living Supramolecular Polymerization of Perylene Bisimides

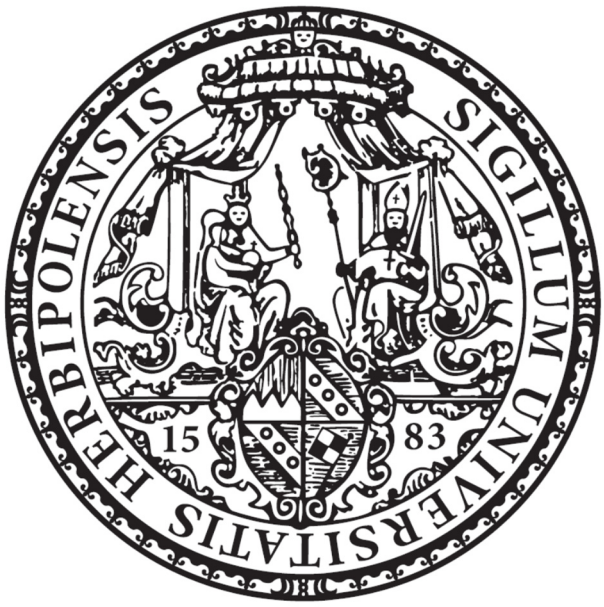


Dissertation zur Erlangung des

naturwissenschaftlichen Doktorgrades

der Julius-Maximilians-Universität Würzburg

vorgelegt von

Wolfgang Wagner

aus Nördlingen

Würzburg 2019

Eingereicht bei der Fakultät für Chemie und Pharmazie am:

_____

Gutachter der schriftlichen Arbeit:

1. Gutachter: Prof. Dr. Frank Würthner

2. Gutachter: _____

Prüfer des öffentlichen Promotionskolloquiums:

1. Prüfer: Prof. Dr. Frank Würthner

2. Prüfer: _____

3. Prüfer: _____

Datum des öffentlichen Promotionskolloquiums:

_____

Doktorurkunde ausgehändigt am:

_____

## List of Abbreviations

| | |
|---|---|
| agg | aggregate |
| AFM | atomic force microscopy |
| $\alpha_{agg}$ | degree of aggregation |
| a.u. | arbitrary unit |
| B3-LYP | Becke-3-parameter-Lee-Yang-Parr (exchange-correlation functional) |
| BCP | block copolymer |
| CD | circular dichroism |
| CDSA | crystallization-driven self-assembly |
| $c_T$ | total molar concentration |
| DCM | dichloromethane |
| $\Delta G^0$ | standard Gibbs free energy |
| $\Delta H^0$ | standard molar enthalpy |
| $\Delta S^0$ | standard molar entropy |
| DFT | density functional theory |
| DMSO | dimethyl sulfoxide |
| $\varepsilon$ | molar extinction coefficient |
| eq. | equivalents |
| ESI | electrospray ionization |
| FT-IR | Fourier-transform infrared |
| h | hour(s) |
| HOPG | highly oriented pyrolytic graphite |
| HRMS | high-resolution mass spectrometry |
| $K$ | binding constant |
| $k_B$ | Boltzmann constant ($k_B = 1.380649 \times 10^{-23}$ J K$^{-1}$) |
| $\lambda$ | wavelength |

| | |
|---|---|
| m.p. | melting point |
| MALDI | matrix-assisted laser desorption/ionization |
| MCH | methylcyclohexane |
| min | minute(s) |
| mon | monomer |
| MS | mass spectrometry |
| NMR | nuclear magnetic resonance |
| PBI | perylene bisimide |
| PDI | polydispersity index |
| $\Phi_{fl}$ | fluorescence quantum yield |
| ppm | parts per million |
| $R$ | universal gas constant ($R$ = 8.314462 J mol$^{-1}$ K$^{-1}$) |
| ref. | reference |
| rpm | revolutions per minute |
| *rt* | room temperature |
| s | second(s) |
| $T$ | temperature |
| $t$ | time |
| TCE | 1,1,2,2-tetrachloroethane |
| THF | tetrahydrofuran |
| TLC | thin-layer chromatography |
| TOF | time of flight |
| Tol | toluene |
| UV | ultraviolet |
| vis | visible |
| v/v | volumetric ratio |

## Table of Contents

# Chapter 1

–

# Introduction and Aim of Thesis

The discovery of living covalent polymerization by Szwarc in the late 1950s initialized a tremendous development in the field of conventional polymer chemistry.[1-3] The exceptional approach of living polymerization as a type of chain-growth polymerization is the most powerful tool for the construction of complex covalent block copolymers (BCPs) with defined length and narrow polydispersity.[2-3] The extraordinary structural versatility of block copolymers has rapidly expanded the scope of applications of covalent polymers as advanced materials and for biological science.[2,4-9]

In the last two decades, the research on supramolecular polymers, which consist of monomeric building blocks self-assembled into polymeric nanostructures by directional non-covalent interactions, has undergone a comprehensive development as supramolecular counterparts of conventional polymers.[10-17] Thus, supramolecular polymers are among the most investigated classes of supramolecular systems because they exhibit a broad variety of novel functionalities, such as stimuli responsiveness and self-healing properties. Therefore such supramolecular systems found a wide range of application in biological science, organic electronics or as functional materials.[13-21] Despite the fact that former studies were focused mainly on analyzing the thermodynamics of supramolecular polymerization by mathematical models,[13,22-27] recent developments in the research field have shown that a precise understanding of kinetics and pathway complexity of self-assembly processes is pivotal to generate a myriad of novel out-of-equilibrium supramolecular architectures.[20,28-44]

Inspired by the pioneering work of Winnik, Manners and coworkers on crystallization-driven self-assembly,[45-52] the concept of living supramolecular polymerization was first introduced by Sugiyasu, Takeuchi and coworkers in 2014 for a supramolecular system based on a zinc porphyrin monomer.[53] With the approach of living supramolecular polymerization the formation of supramolecular polymers with defined size distribution

and narrow polydispersity can be achieved under precise kinetic control.[54-56] The perceptive studies in recent years [53,57-68] revealed the following two prerequisites for living supramolecular polymerization: First, the supramolecular polymerization has to follow the nucleation-elongation mechanism so that the self-assembly proceeds analogous to chain-growth polymerization. Second, a kinetically controlled pre-equilibrium[59,69] has to be involved to suppress the spontaneous nucleation and hence the spontaneous polymerization process. This highly required retardation of spontaneous self-assembly can generally be achieved either by the formation of competing metastable off-pathway aggregated states[53,60-63,65-67] or by properly designed *intra*molecular hydrogen-bonding of the monomeric species leading to a kinetically trapped monomeric state.[57-58,64] The chain-growth-type supramolecular polymerization in such systems, is initiated either through molecular initiators,[58] by a photoisomerization process[59] or most commonly by the addition of pre-prepared polymeric seeds acting as the nuclei for the supramolecular polymerization process.[53,57,60-67]

Although the understanding of living supramolecular polymerization has been significantly increased in the recent years, the non-covalent synthesis of highly desirable supramolecular block copolymers and the rational design of monomeric building blocks for living supramolecular polymerization is still very challenging.[70-72] Up to date, supramolecular block architectures were only generated in exceptional examples by the approach of crystallization-driven self-assembly,[48-50,73-74] multistep synthesis of nanotubular segments,[75] dynamic covalent chemistry,[76] thermodynamically controlled coassembly[77] or seed-induced copolymerization.[70] Therefore, the aim of the thesis is the non-covalent synthesis of the highly desirable supramolecular block copolymers by seeded living supramolecular polymerization in a precisely kinetically controlled process. These interesting supramolecular block architectures might have novel properties based on their multicomponent structures. For that purpose, two monomeric building blocks (A and B) are needed, where the first one forms a kinetically trapped state – either kinetically trapped monomer or aggregate – and from the second one a matching polymeric seed has to be generated (Figure 1). Additionally, both the kinetically trapped state and the seed have to be stable under the same conditions, like for example solvent composition, temperature and concentration. By concept, the addition of an appropriate seed of B to the metastable state of A leads to the formation of unprecedented supramolecular block architectures with A-B-A block pattern by two-component seed-induced living copolymerization (Figure 1).

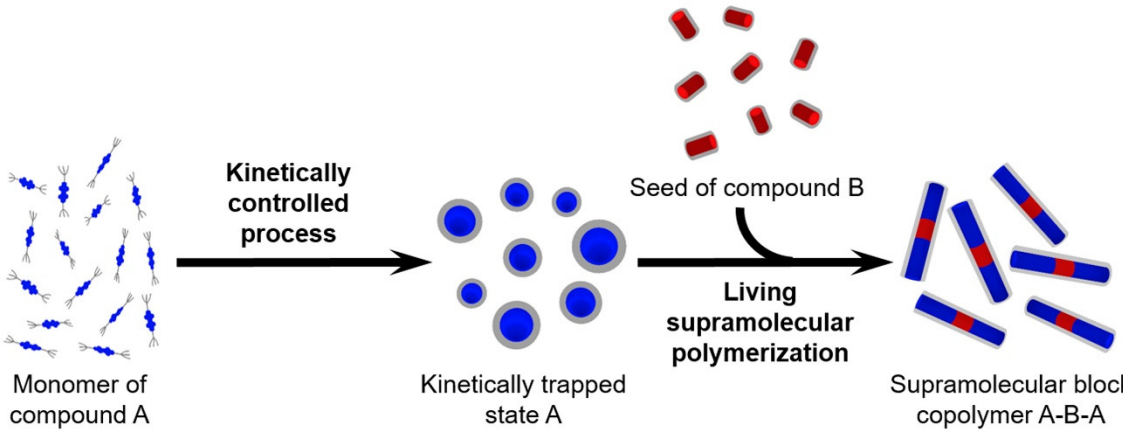


**Figure 1.** Schematic illustration of the two-component seeded copolymerization of the kinetically trapped state of A with the seed of B leading to A-B-A triblock supramolecular block copolymers.

In recent studies of the Würthner group, the approach of seeded polymerization was successfully applied on the highly versatile class of perylene bisimide (PBI) dyes.[57,60] These chromophores have evolved as one of the most investigated classes of dyes in the last decades due to their ideal molecular features,[78-79] such as excellent photostability, easily tunable absorption and emission properties along with high fluorescence quantum yields.[80-82] Those outstanding features lead to numerous applications for example in the field of organic electronics[81,83-84] and photovoltaics.[85-86] Their insightful investigations revealed that the core-unsubstituted PBI organogelator **H-PBI** (Chart 1) bearing amide functionalized side groups at the imide positions is kinetically trapped as a monomer by *intra*molecular hydrogen bonding between the amide protons and the imide oxygens.[57,60] The addition of preformed polymeric seeds of **H-PBI** induces a living supramolecular polymerization of those trapped species at the termini of the seeds under kinetic control.[57,60]

Based on the structure of **H-PBI**, a sophisticated series of novel perylene bisimides bearing identical solubilizing imide side-groups but varying nature or number of bay-substituents at the PBI core was synthesized and investigated within this thesis (Chart 1). The introduction of different bay substituents leads not only to a modification in the molecular features of the PBIs, such as the core twist angles of the perylene cores as well as electronic, absorption and fluorescence properties, but also affects strongly the thermodynamically and kinetically controlled supramolecular polymerization which was studied in detail by Fourier-transform infrared (FT-IR), UV/vis and fluorescence spectroscopy as well as atomic force microscopy (AFM). Furthermore, the variation of bay-substituents of the present PBI series also drastically changes the stability of the kinetically trapped states

leading either to completely thermodynamically controlled polymerization or enabling seeded or even multicycle living supramolecular polymerization. Moreover, the synthesis of unprecedented supramolecular block copolymers of appropriate combinations of PBIs by two-component seeded copolymerization was achieved and it was systematically studied how the ability to form these supramolecular block architectures is governed by the molecular design of the monomeric units.

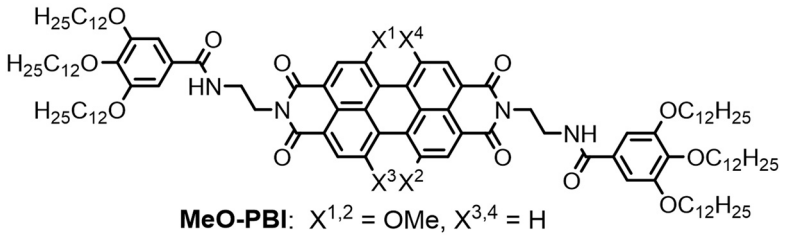

**MeO-PBI**: $X^{1,2}$ = OMe, $X^{3,4}$ = H
**EtO-PBI**: $X^{1,2}$ = OEt, $X^{3,4}$ = H
***i*PrO-PBI**: $X^{1,2}$ = O*i*Pr, $X^{3,4}$ = H
**Cl-PBI**: $X^{1,2}$ = Cl, $X^{3,4}$ = H
**MeS-PBI**: $X^{1,2}$ = SMe, $X^{3,4}$ = H
**1-MeO-PBI**: $X^{1}$ = OMe, $X^{2-4}$ = H
**1,6,7-MeO-PBI**: $X^{1-3}$ = OMe, $X^{4}$ = H
**1,6,7,12-MeO-PBI**: $X^{1-4}$ = OMe
**H-PBI**: $X^{1-4}$ = H

**Chart 1.** Chemical structures of the 1,7-dimethoxy (**MeO-PBI**), 1,7-diethoxy (**EtO-PBI**), 1,7-diisopropyloxy (**1,7-*i*PrO-PBI**), 1,7-dichloro (**Cl-PBI**), 1,7-dimethylthio (**MeS-PBI**), 1-monomethoxy (**1-MeO-PBI**), 1,6,7-trimethoxy (**1,6,7-MeO-PBI**) and 1,6,7,12-tetramethoxy (**1,6,7,12-MeO-PBI**) bay-substituted PBIs studied in this thesis and structure of the core-unsubstituted reference compound **H-PBI**.

*Chapter 2* gives a brief overview about supramolecular polymers and the thermodynamic models to analyze the self-assembly of monomers into polymeric nanostructures. Furthermore, the kinetically controlled self-assembly along with the approaches of seed-induced and living supramolecular polymerization are introduced. At the end of this Chapter a survey about various up to date investigated supramolecular copolymers as well as the corresponding strategies to construct such supramolecular architectures are presented and illustrated by significant literature examples.

In *Chapter 3* the self-assembly of a 1,7-dimethoxy substituted PBI (**MeO-PBI**) is described. Upon cooling of a monomeric solution of **MeO-PBI** an off-pathway kinetically metastable H-aggregate is formed, which can be transformed into the thermodynamically favored fluorescent J-aggregates by seed addition. The living nature of this chain-growth-type process was investigated in detail by FT-IR, UV/vis and fluorescence spectroscopy as well as atomic force microscopy.

*Chapter 4* is focused on the in-depth studies of the supramolecular polymerization of PBI derivatives containing chlorine (**Cl-PBI**) or methylthio substituents (**MeS-PBI**) in 1,7-bayposition. The two-component seeded copolymerization of these two PBIs with the aforementioned **MeO-PBI** leads to the formation of unprecedented supramolecular block architectures, which could be demonstrated by detailed UV/vis spectroscopic and AFM studies. Moreover, by the novel approach of seeded living copolymerization the synthesis of triblock copolymers with either A-B-A or B-A-B block pattern was achieved.

In *Chapter 5*, a series of PBIs with variable number (**1-MeO-PBI**, **MeO-PBI**, **1,6,7-MeO-PBI**, **1,6,7,12-MeO-PBI**) or size (**EtO-PBI**, ***i*PrO-PBI**) of alkoxy substituents in bay-position is analyzed. Detailed optical spectroscopic and AFM studies have shown that the thermodynamic as well as the kinetically controlled aggregation properties of these PBIs are drastically changed even by subtle modifications of the molecular structure of the monomeric units. Moreover, the investigations on two-component seeded copolymerization revealed that the formation of supramolecular block copolymers is only possible for appropriate combinations of PBIs and that the efficiency of seeding is strongly dependent on the shape complementarity of the applied molecular building blocks.

In *Chapter 6* and *Chapter 7* the result of this work are summarized and discussed in English and German.

# Chapter 2

–

# State of Knowledge

## 2.1 Supramolecular Polymers

Since the discovery of the first main-chain supramolecular polymer based on the self-assembly of ditopic monomers connected by complementary three-fold hydrogen-bonding interactions by Lehn *et al.* in 1990,[87] supramolecular polymers have been a subject of intense research in the last decades. Hence, already in 2001 Meijer *et al.* emphasized the technological relevance of supramolecular polymers and predicted a "bright future" for this research field.[11] Supramolecular polymers are defined as arrays of monomeric units that are held together by highly directional and reversible non-covalent interactions, like hydrogen-bonding, $\pi$-$\pi$-stacking, hydrophobic interactions or metal coordination.[11,13] During the last decades, novel strategies were developed to generate a plethora of functional supramolecular architectures, e.g., random coil polymers, cylindrical nanofibers, twisted nanoribbons and nanotubular structures from various kinds of monomeric building blocks (Figure 2).[14]

The properties and nanostructures of these complex supramolecular systems can be controlled by a proper molecular design of the monomeric units and their supramolecular interactions.[13,88] Thus, the variety of monomeric building blocks, different self-assembly mechanisms and stability of these nanostructures provide a powerful tool to construct functional supramolecular polymers, which can be distinguished in general into three major classes, that are illustrated in Figure 3:[88] (1) Functions due to unique mechanical properties defined by the monomer units and the dynamic nature of the non-covalent bonds, (2) electronic and optoelectronic functions based on $\pi$-conjugated monomeric building blocks and (3) biomedical functions of biologically active supramolecular polymers.[14]

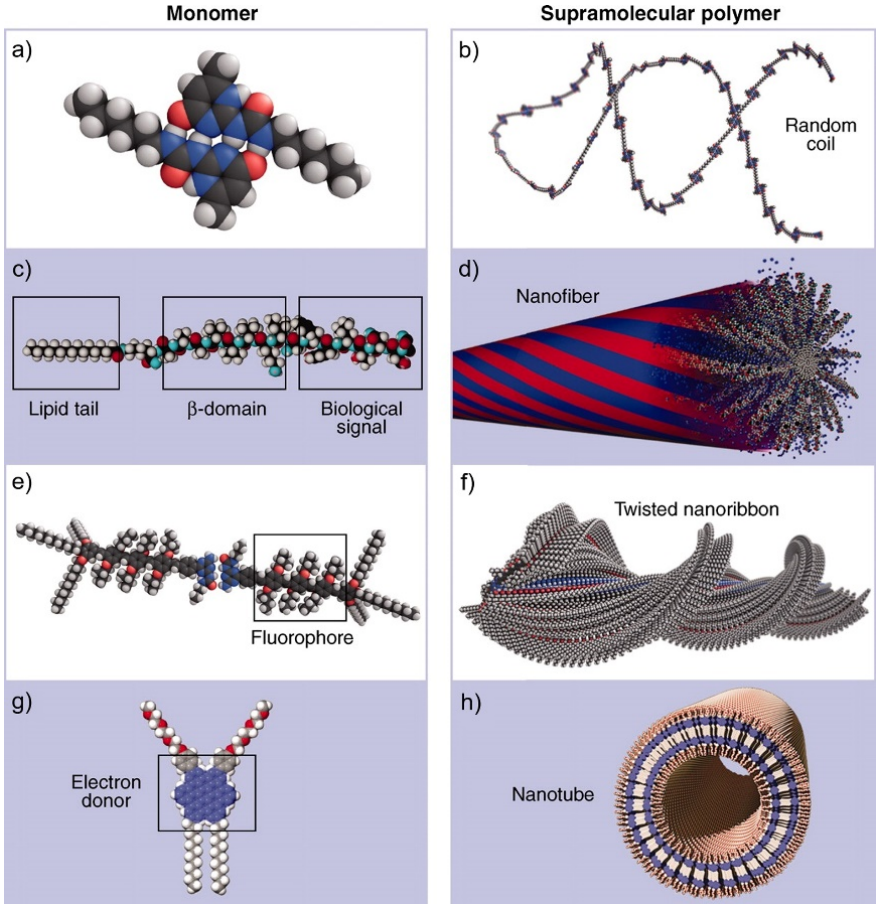


**Figure 2.** Representation of four different monomers and the corresponding supramolecular polymers formed by aggregation through their specific interactions.[14] (a) and (b): Ureidopyrimidinone monomers forming a random coil supramolecular polymer by self-complementary quadruple hydrogen bonds. (c) and (d): Peptide amphiphile monomer capable of forming cylindrical aggregated nanofibers. (e) and (f): Monomers based on the fluorophore oligo(phenylene vinylene) capable of forming twisted nanoribbons. (g) and (h): Nanotubes obtained by self-assembly of hexabenzocoronene based building blocks. Reprinted with permission from ref.[14] Copyright 2012 American Association for the Advancement of Science.

In consequence of this broad variety of novel functionalities, supramolecular polymers exhibit a wide range of applications in material science, organic electronics and biology.[13-17,20,89] For example, supramolecular polymers can be used as stimuli-responsive supramolecular materials with good processability or self-healing properties based on the concept that the monomers generate reversible and dynamic networks by non-covalent bonds.[13,89-90] Furthermore, by self-assembly of $\pi$-conjugated building blocks semiconducting nanofibers, nanotubes and photoconductive nanowires can be generated, which are envisioned to be utilized in organic electronics and photovoltaics.[13-14] In biological applications, supramolecular polymers can be used as thermoplastic elastomers for temporary biomaterials in regenerative medicine or for applications in tissue engineering, e.g., as biomaterials for artificial extracellular matrices.[16-17,89]

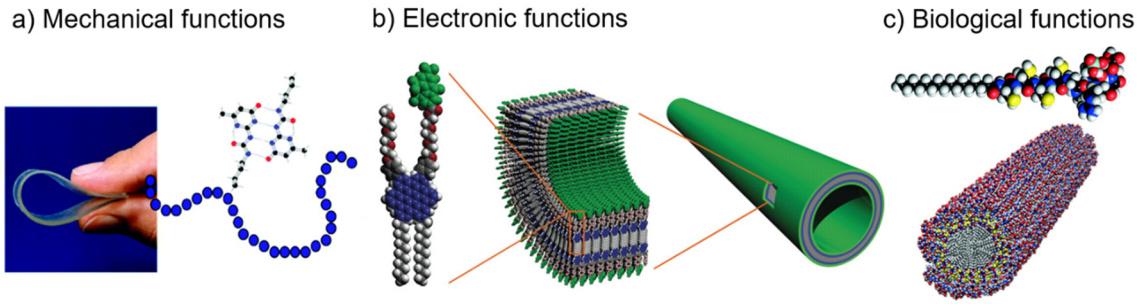


**Figure 3.** Classification of functional supramolecular polymers[88] based on their (a) mechanical function illustrated by a ureidopyrimidinone supramolecular polymer,[89] (b) electronic function exemplified by a nanotube consisting of an amphiphilic hexabenzocoronene building block[91] and (c) biological function as illustrated by a peptide containing nanotubular supramolecular architecture.[92] Adapted with permissions from ref.[89,91-92] Copyright 2001/2006 American Association for the Advancement of Science and Copyright 2017 Royal Society of Chemistry.

## 2.2 Thermodynamics of Supramolecular Polymerization

Since a precise understanding of the self-assembly processes of monomeric building blocks is crucial to predict the structure and function of a formed supramolecular polymer, tremendous focus has been given to elucidate the thermodynamics of the polymerization process in the last decades. The simplest way to describe self-assembly of molecules is the monomer-dimer model, which describes the equilibrium only between monomer and dimer with a dimerization constant $K_D$.[13,93] With the total concentration $c_T$, the degree of aggregation $\alpha_{agg}$ can then be calculated according to equation (1).[93] Although this model can exclusively be used if the dimer is the only aggregated species, the monomer-dimer model was successfully applied for example to describe the aggregation of cyanine,[94] phthalocyanine,[95] and merocyanine dyes.[96]

$$\alpha_{agg} = \frac{4K_D c_T + 1 - \sqrt{8K_D c_T + 1}}{4K_D c_T} \quad (1)$$

The supramolecular polymerization of more extended one-dimensional aggregates can be described by the commonly used isodesmic (also called equal-*K*) model, in which the self-assembly of the monomeric units is defined by a single equilibrium constant *K* (Figure 4). This binding constant is independent on the size of the aggregate and the reactivity of the termini of the supramolecular polymers remains constant during the step-growth like process.[93,97] In general, supramolecular nanostructures formed by an isodesmic polymerization show small sizes and broad length distributions.[27]

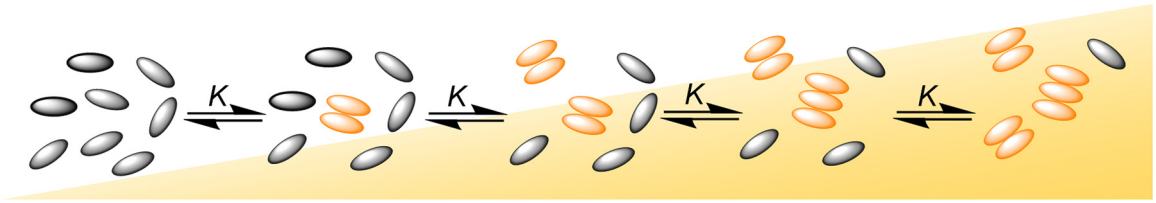


**Figure 4.** Schematic illustration of an isodesmic supramolecular polymerization process.

For an isodesmic polymerization the concentration-dependent degree of aggregation $\alpha_{agg}$ can be calculated with the binding constant $K$ and the total concentration $c_T$ according to the following equation (2).

$$\alpha_{agg} = 1 - \frac{2Kc_T + 1 - \sqrt{4Kc_T + 1}}{2K^2{c_T}^2} \tag{2}$$

For a constant total concentration, the degree of aggregation at variable temperatures $T$ can be calculated by equation (3), where $\Delta H$ is the molar enthalpy release upon formation of the non-covalent bond, $T_m$ is the melting temperature, which is defined as the temperature with $\alpha_{agg} = 0.5$, and $R$ is the molar gas constant.[27,98]

$$\alpha_{agg} \cong \frac{1}{1 + \exp\left[-0.908\Delta H \cdot \frac{T - T_m}{RT_m^2}\right]} \tag{3}$$

For monomers which are capable of establishing multiple (various kind of) non-covalent interactions, e.g., a combination of $\pi$-$\pi$-interaction and hydrogen-bonding, the self-assembly often follows a cooperative supramolecular mechanism and can then be described by the nucleation-elongation model.[13,22] In this model, the polymerization process is divided into two parts: The formation of a nucleus of a certain size described by the binding constant $K_N$ and the elongation process with the equilibrium constant $K_E$ (Figure 5).[13,22]

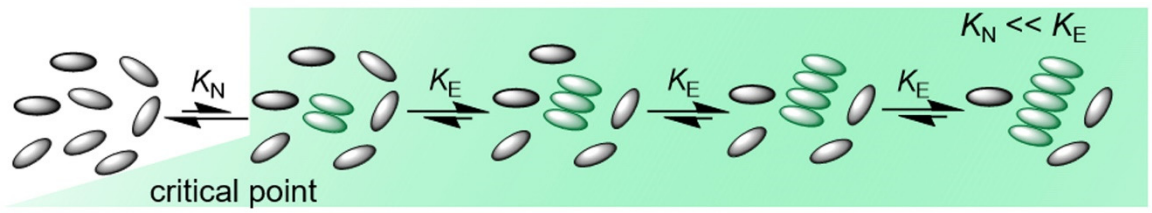


**Figure 5.** Schematic representation of a cooperative supramolecular polymerization following the nucleation-elongation model.

For such systems the cooperativity of the polymerization is described by the cooperativity factor $\sigma = K_N / K_E$. For $\sigma < 1$ the elongation is favored compared to nucleus formation (cooperative polymerization, Figure 5), while for $\sigma > 1$ the formation of larger aggregated

species is less favored (anti-cooperative polymerization). For the above described isodesmic polymerization the cooperativity factor $\sigma$ equals 1.

In general, the concentration-dependent degree of aggregation of a cooperative polymerization process can be described by the Goldstein-Stryer model (4) for polymers with the length $n$ and the concentration of the monomers $c_1$.[99]

$$K_E c_T = \sum_{n=1}^{s} n\sigma^{n-1}(K_E c_1)^n + \sum_{n=s+1}^{\infty} n\sigma^{s-1}(K_E c_1)^n =$$

$$= \frac{s(K_E c_1)^s \sigma^{s-1}}{1 - K_E c_1} + \frac{(K_E c_1)^{s+1}\sigma^{s-1}}{(1 - K_E c_1)^2} + \frac{K_E c_1(s(\sigma K_E c_1)^{s-1} - 1)}{\sigma K_E c_1 - 1} - \frac{\sigma(K_E c_1)^2((\sigma K_E c_1)^{s-1} - 1)}{(\sigma K_E c_1 - 1)^2} \quad (4)$$

This model can be simplified to the $K_2$-$K$ model (5) under the assumption that exclusively a dimer nucleus is formed.[93,100]

$$K_E c_T = (1 - \sigma)Kc_1 + \frac{\sigma K_E c_1}{(1 - K_E c_1)^2} \quad (5)$$

The monomer concentration in the two above described cases is determined numerically and the degree of aggregation $\alpha_{agg}$ can then be calculated according to equation (6).

$$\alpha_{agg} = 1 - \frac{Kc_1}{Kc_T} \quad (6)$$

The temperature-dependence of a cooperative supramolecular polymerization at a constant concentration is described by the nucleation-elongation model of Smulders, Meijer and coworkers.[27,101-102] For the elongation process, the degree of aggregation at variable temperatures $T$ can be calculated by equation (7), in which $T_E$ is the elongation temperature, $\Delta H_E$ the enthalpy corresponding to the elongation process and $\alpha_{sat}$ a parameter to ensure that $\alpha_{agg}$ does not exceed unity.[27,98]

$$\alpha_{agg} = \alpha_{sat}\left(1 - \exp\left[\frac{-\Delta H_E}{RT_E^2}(T - T_E)\right]\right) \quad (7)$$

In this model the degree of aggregation for the nucleation process, i.e., at temperatures above the critical temperature $T_E$, is described by equation (8) with $K_A$ as the dimensionless equilibrium constant of the activation step.[27,102]

$$\alpha_{agg} = K_A^{1/3}\exp\left[\left(\frac{2}{3}K_A^{-1/3} - 1\right)\frac{\Delta H_E}{RT_E^2}(T - T_E)\right] \quad (8)$$

The average size of the nucleus $\langle N_N(T_E)\rangle$ at the elongation temperature can be calculated by equation (9).[102]

$$\langle N_N(T_E)\rangle = \frac{1}{K_A^{1/3}} \tag{9}$$

For an anti-cooperative polymerization a modified $K_2$-$K$ model was introduced by the Würthner group.[100] In this model the formation of even-sized aggregates is more favorable than the formation of odd-numbered aggregates due to the preferential dimerization process. The total concentration $c_T$ can then be calculated by equation (10).

$$c_T = c_1 + \frac{2K_2c_1^2}{(1-KK_2c_1^2)^2} + \frac{KK_2c_1^3(3-KK_2c_1^2)}{(1-KK_2c_1^2)^2} \tag{10}$$

An anti-cooperative polymerization behavior was observed for supramolecular systems, e.g., for PBI dyes with increasing repulsion through steric hindrance upon increasing size of the aggregate[100,103] or for systems in which particular strong electrostatic interactions are drastically reduced after dimer formation, like in the case of dipolar merocyanine dyes.[104]

On the basis of the above described mechanisms, several new mathematical models have been developed to described more complex aggregation phenomena, e.g., self-assembly by two competing cooperative polymerizations[105] or the cooperative polymerization with a favored off-pathway dimer and a disfavored dimer nucleus.[106] In this regard, UV/vis spectroscopy has become a powerful tool to analyze self-assembly processes and to experimentally determine the degree of aggregation $\alpha_{agg}$ for a subsequent analysis with the above described mathematical models. The concentration- or temperature-dependent degree of aggregation can be determined from the apparent molar extinction coefficients $\varepsilon$ at a specific wavelength and the molar extinction coefficients of the monomer $\varepsilon_{mon}$ and aggregate $\varepsilon_{agg}$ by equation (11).

$$\alpha_{agg} = \frac{\varepsilon - \varepsilon_{mon}}{\varepsilon_{agg} - \varepsilon_{mon}} \tag{11}$$

## 2.3 Kinetically Controlled Supramolecular Polymerization

Although a lot of knowledge has been accumulated on supramolecular polymerization under thermodynamic control, the studies in the recent years focus mainly on the kinetically controlled self-assembly which enables the formation of novel out-of-equilibrium

supramolecular nanostructures with high levels of complexity.[20,69,107] Such kinetically controlled states can only be achieved for supramolecular systems with strong or multiple non-covalent interactions leading to self-assembly pathways which are often governed by kinetic effects. In general, these different states of supramolecular polymerization can be categorized into three classes: the thermodynamic equilibrium, dissipative non-equilibrium and non-dissipative non-equilibrium states (Figure 6).[20] In thermodynamic equilibrium, the supramolecular system stays in the global minimum of the free energy landscape and no input of energy is needed to prevail this state.[20] Notably, a supramolecular system in thermodynamic equilibrium is still dynamic with a continuous exchange of monomers between the monomeric and the aggregated species, but its overall composition stays temporally constant. Although the global energy minimum can be changed by different parameters, like for example concentration, temperature or solvent composition, the self-assembly pathway in which it is reached has no influence on the final structure.[69]

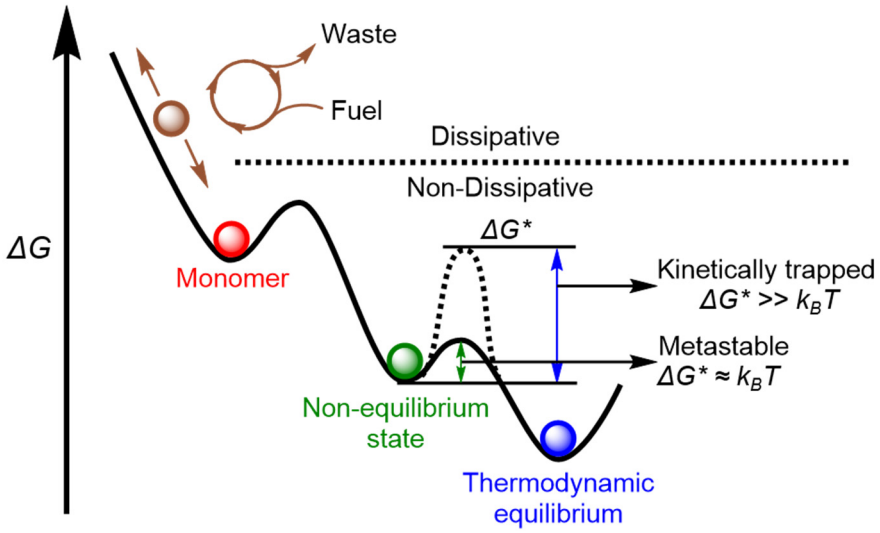


**Figure 6.** Schematic energy landscape illustrating the different states of self-assembly, i.e., thermodynamic equilibrium, non-dissipative non-equilibrium and dissipative non-equilibrium state.[20,69] Adapted with permission from ref.[69] Copyright 2019 WILEY-VCH Verlag GmbH.

For dissipative, also called transient, states, the energy barrier for relaxation into a thermodynamically more favored state is negligibly low.[108-109] Therefore, a dissipative state needs a constant input of energy or matter (e.g., chemical fuel or light) and the removal of waste products to prevent the relaxation into a lower energy minimum.[110] Thus, such far-from-equilibrium supramolecular structures degrade, when no more energy supply is provided.[109] The utilization of dissipative non-equilibrium states was studied in recent literature, e.g., for chemical fuel-induced gelation processes,[111] chemical fuel-mediated

supramolecular pathway selection and self-assembly[37,68] as well as self-oscillating supramolecular polymers of PBI dyes.[112]

A non-dissipative non-equilibrium state is obtained for a supramolecular system that is confined in a local minimum of the respective potential energy curve (Figure 6).[20] In such a case the transformation into an energetically more stable state is, in contrast to the dissipative state, hindered by a non-negligible energy barrier $\Delta G^*$. If this activation barrier is high, i.e., the value of $\Delta G^*$ is much higher than $k_B T$ (where $k_B$ is the Boltzmann constant and $T$ the temperature), the systems remains in this local minimum for much longer than the experimental time.[69] Such a case is called a kinetically trapped state, which can only be transformed into a thermodynamically more favored state by applying an external stimulus. On the other hand, when the activation barrier of the pathway to an energetically more stable state is in the same order of magnitude as $k_B T$, a kinetically metastable structure is formed. These metastable supramolecular species transforms into more stable assemblies in an experimentally observable time scale ranging from minutes to several months.[20]

Besides that, from a mechanistic point of view supramolecular polymers can be subdivided into off-pathway (Figure 7a) and on-pathway (Figure 7b) aggregated states.[43-44,69] In an off-pathway or competitive aggregation process, two supramolecular species can only be transformed into each other by disassembly into monomer units prior to the supramolecular polymerization (Figure 7a).[69]

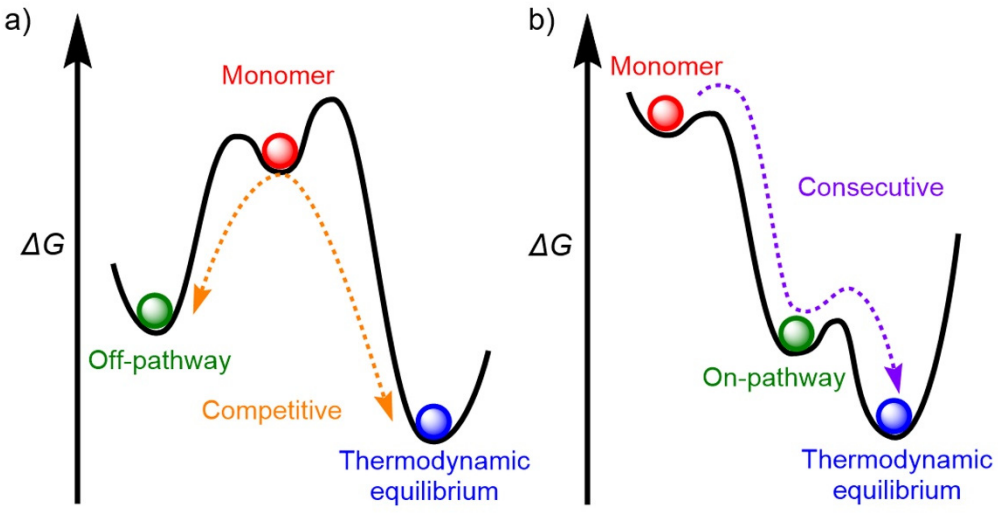


**Figure 7.** Schematic energy landscape illustrating competitive (a) and consecutive (b) self-assembly pathways.[20,69] Adapted with permission from ref.[69] Copyright 2019 WILEY-VCH Verlag GmbH.

In contrast, for on-pathway self-assembly, the thermodynamically stable state is formed directly from the monomers *via* a consecutive aggregation pathway, e.g., by structural

rearrangement of the so called on-pathway intermediates and without disassembly into the monomeric building blocks (Figure 7b). Mainly, these two cases can be distinguished by time-dependent transformation experiments between the respective supramolecular species at different concentrations. For consecutive aggregation the conversion time of the intermediate into the thermodynamically stable supramolecular polymer is decreased for higher concentrations due to an increasing amount of the on-pathway intermediate. If however, the time of conversion into the thermodynamically more stable species is increased for higher total concentrations, a competitive pathway exists and the self-assembly of the kinetically metastable into the thermodynamically stable state can only occur *via* formation of an "active" monomeric species.[69]

A precise understanding of the various self-assembly pathways, which might be created by a complex combination of multiple thermodynamic states[44] of a supramolecular system, unraveled by detailed kinetic analysis, is crucial to control the polymerization process and generate a variety of kinetic structures with distinct properties and functions.[43] Although kinetic models to analyze nucleation-elongation processes have been reported for protein polymerization decades ago,[22,99,113-114] the relevance of these models for supramolecular polymerization has been recognized only recently.[107] The research on kinetically controlled supramolecular polymerization is more challenging compared to the studies of equilibrated systems because the self-assembly pathways are strongly dependent on the preparation method.[43,107] Thus, a variation of the applied experimental protocol, e.g., temperature modulation,[30,40,115-116] utilization of external stimuli,[117-118] or different procedures of solvent addition[29,119-120] can drastically change the outcome of kinetically controlled supramolecular polymerization processes.[17,20]

One of the first studies of a supramolecular polymerization process which is strongly influenced by kinetic effects was reported in 2005 by Würthner and coworkers for the cooperative self-assembly of the bis(merocyanine) dye **1** (Figure 8a).[28,121] The monomers of **1** can form two different types of nanorod-like supramolecular polymers in solvent mixtures of THF (good solvent) and MCH (poor solvent). UV/vis and CD spectroscopy as well as AFM studies revealed that in MCH/THF (7:3, v/v) first centrosymmetric dimers are formed by dipolar interactions and $\pi$-$\pi$-stacking, which bundle into random-coil supramolecular polymers. In a kinetically controlled process, these polymers form off-pathway helical nanorods, which then transform very slowly into another denser helical nanorod structure that is thermodynamically more favored. For this supramolecular system,

the off-pathway aggregate could be kinetically trapped under specific conditions for several days.

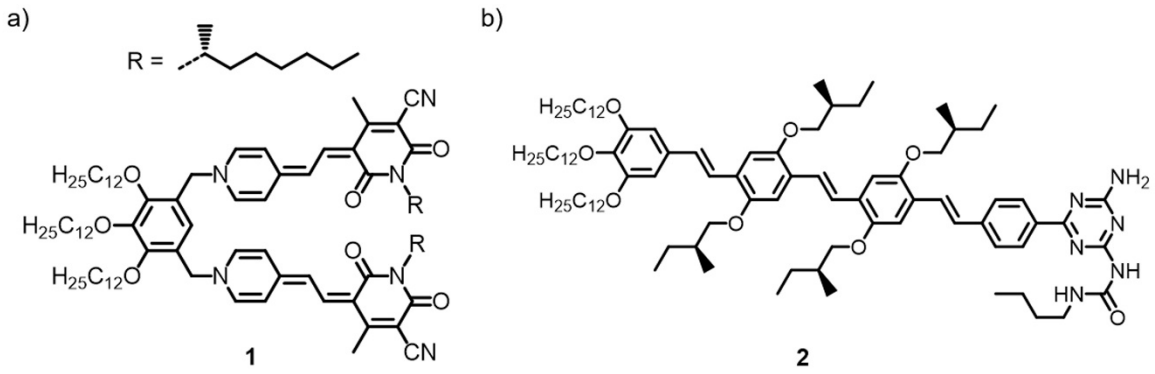


**Figure 8.** a) Chemical structures of the bis(merocyanine) dye **1**.[28] b) Molecular structure of the oligo(*p*-phenylenevinylene) **2** with *S*-chiral alkoxy side chains.[30]

A systematic study of the competition between thermodynamics and kinetics in supramolecular polymerization was performed by Meijer and coworkers for the hierarchical self-assembly of the oligo(*p*-phenylenevinylene) **2** (Figure 8b).[30,101,122] Upon addition of the molecularly dissolved building blocks of **2** in $CHCl_3$ to an excess of MCH, the *S*-chiral monomers first form dimers by quadruple self-complementary hydrogen-bonding, which self-assemble into thermodynamically more favored *M*-type helices. However, at high concentrations the injecting of the monomer solution to the poor solvent leads initially to the formation of off-pathway *P*-type aggregates investigated by stopped-flow CD-experiments. These kinetically metastable self-assemblies transform into the *M*-helical supramolecular polymers over time. The complex self-assembly of **2** could be explained by a mathematical model with two competing nucleation-elongation pathways revealing that the nucleus of the *M*-helical aggregate is slightly less stable than that of the *P*-helical aggregate, while the *M*-helical polymers are thermodynamically more favored than the *P*-helical ones.[30] The authors introduced the term “pathway complexity”, describing the different aggregation pathways competing for one monomeric species.[69]

An example in which the supramolecular polymerization is directed by the solvent composition and order of solvent addition was reported by the Rybtchinski group.[20,29] Their spectroscopic and transmission electron microscopy studies showed that the PBI terpyridine platinum complex **3** (Figure 9a) self-assembles into three different aggregates depending on the applied mixing ratios of the solvents THF and water. For low contents of THF (5%), highly curved fiber-like aggregates were obtained which can be transformed into helical

sinuous nanofibers by increasing the content of THF to 20%. For a THF/water mixture with a ratio of 7:3 (v/v), tightly packed, tubular nanofibers were obtained as thermodynamically most favored structure. Moreover, the authors showed that, depending on the solvent mixing protocol, all these three aggregates can be generated in the same final solvent mixture (THF/water 95:5, v/v), demonstrating the pathway-dependent aggregation behavior.[29] More recently, the Aida group reported a very special example with a thermally bisignate supramolecular polymerization, i.e., the supramolecular polymerization occurs upon the heating and the cooling process.[39] At around 50 °C the investigated metalloporphyrin-based monomers **4a-c** (Figure 9b) form a monomeric state in a mixture of *n*-dodecane (poor solvent) and *n*-hexanol (with small amounts of $CHCl_3$). Upon cooling, these monomers self-assemble into one-dimensional supramolecular polymers through $\pi$-$\pi$-stacking and *inter*molecular multiple hydrogen-bonding with the typical signature of enthalpy-driven supramolecular polymerization. However, heating of the solution above 50 °C leads to a weakening of the non-covalent interactions between the monomers and the solvent molecules (*n*-hexanol) resulting also in the formation of supramolecular polymers.

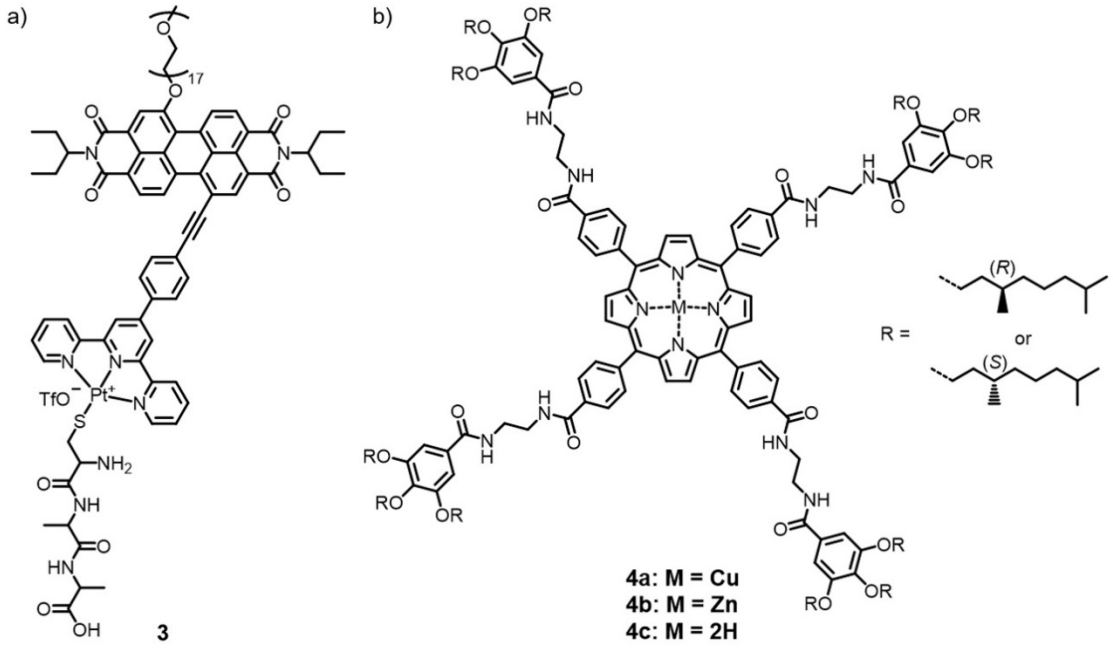


**Figure 9.** Chemical structures of the perylene bisimide terpyridine platinum complex **3** (a)[29] and the metalloporphyrin derivatives **4a-c** (b).[39]

The De Cola group studied the kinetically affected self-assembly of a luminescent platinum complex **5** (Figure 10a), which can form three different supramolecular polymorphs.[35,69,107] In a mixture of water and 1,4-dioxane, the monomers of **5** initially form kinetically metastable nanoparticles converting into the thermodynamically more favored nanorod-like structures

within three weeks. For specific water contents, another kinetically trapped supramolecular species was observed, which can also be generated by light irradiation of the thermodynamically stable nanorods. Since all three aggregates showed very different fluorescence properties because of the varied Pt−Pt interactions and distances, the overall transition from the nanoparticles into the thermodynamically stable nanorods could be monitored *in situ* by confocal fluorescence microscopy.

Interestingly, Meijer and coworkers demonstrated that even very tiny amounts of water in strongly nonpolar organic solvents can have drastic effects on the supramolecular polymerization pathways.[123] The authors investigated the self-assembly of the chiral tetra amide-substituted biphenyl derivative **6** (Figure 10b) in MCH. For water contents below 8 ppm only one chiral supramolecular polymer was formed upon cooling of the monomeric solution. Unexpectedly, for higher water contents up to 47 ppm, the initially formed helical polymers transform into two different aggregates, which can be distinguished by their CD spectral features. Furthermore, the studies revealed that either 0.5 or 2 equivalents of water are incorporated in the respective structures of these two different supramolecular architectures, which was confirmed by analysis with a comprehensive mathematical model.

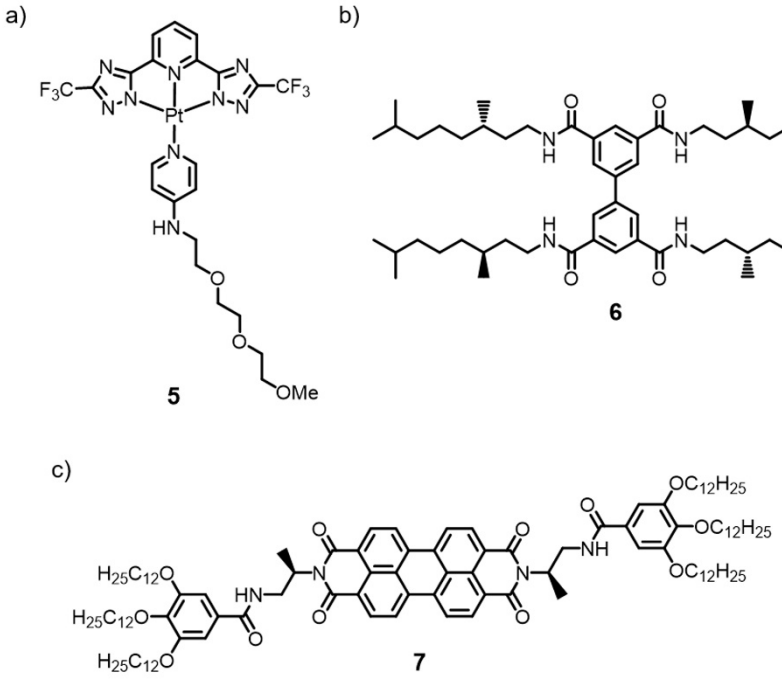


**Figure 10.** Molecular structures of the platinum complex **5** (a),[35] the tetra amide-substituted biphenyl derivative **6** (b)[123] and perylene bisimide organogelator **7** (c).[124]

Recently, Würthner and coworkers demonstrated the first example of "true supramolecular polymorphism" by investigating the effect of ultrasonication on the supramolecular

polymerization of PBI derivative **7** (Figure 10c).[107,124] The PBI organogelator can form three different one-dimensional aggregates in the same solvent mixture and at the same concentration by $\pi$-$\pi$-interactions and hydrogen-bonding, which was studied in detail by UV/vis, CD- and FT-IR spectroscopy. First the monomers of **7** form metastable dimers, that self-assemble into small-sized oligomeric nanoparticles by an anti-cooperative process. The transformation into the other thermodynamically more favored nanofibers can be initiated by mechanical forces like ultrasonication, leading to rearrangement processes within the dimers (nucleation) and subsequent elongation of the supramolecular polymers. Moreover, the self-assembly of the different polymorphs can be regulated also chemically by addition of preformed polymeric seed (*vide infra*). This precise control of self-assembly could only be achieved by in-depth understanding of the different competing supramolecular polymerization pathways.

## 2.4 Seeded and Living Supramolecular Polymerization

One groundbreaking development in the field of kinetically controlled self-assembly is the living supramolecular polymerization, because it enables the fabrication of highly ordered supramolecular polymers with controlled length and narrow polydispersity. [54-56,107] As mentioned in the introduction, the detailed studies on seed-induced and living supramolecular polymerization revealed that two main prerequisites for a living supramolecular chain-growth-type process exist.[53,57-68] First, the polymerization has to follow a nucleation-elongation mechanism, so that supramolecular polymerization can only occur at the active ends of the polymers in the ideal case without the ability of chain termination and recombination. Second, a metastable (dormant) state, e.g., a kinetically trapped monomeric species[57-59,64] or off-pathway aggregate,[53,60-63,65-67] has to be formed in a kinetically controlled pre-equilibrium acting as a kinetically trapped state to prevent the spontaneous polymerization (Figure 11a). This kinetic trapping has to be effective enough to prevent the spontaneous nucleation and to enable control over the supramolecular polymerization, whereby for a system with a too deeply kinetically trapped state the formation of the supramolecular polymer cannot occur at all.[59] In general, a retardation time of the thermodynamically polymerization of several hours is needed for a living polymerization process.[59] In such a system the living supramolecular polymerization can be induced by the addition of an externally prepared polymeric seed, which acts as the nuclei for the chain-growth-type polymerization process (Figure 11b).[53,57,60-67] The degree of polymerization can

be precisely controlled by the ratio of added seed, leading to supramolecular polymers with narrow polydispersity (PDI ≤ 1.1) and controlled length (Figure 11c).[53] Moreover, for well-designed supramolecular systems, in which the active termini of the resulting supramolecular polymer are not terminated through recombination of the aggregates, multicycle living supramolecular polymerization can be achieved.[53,62]

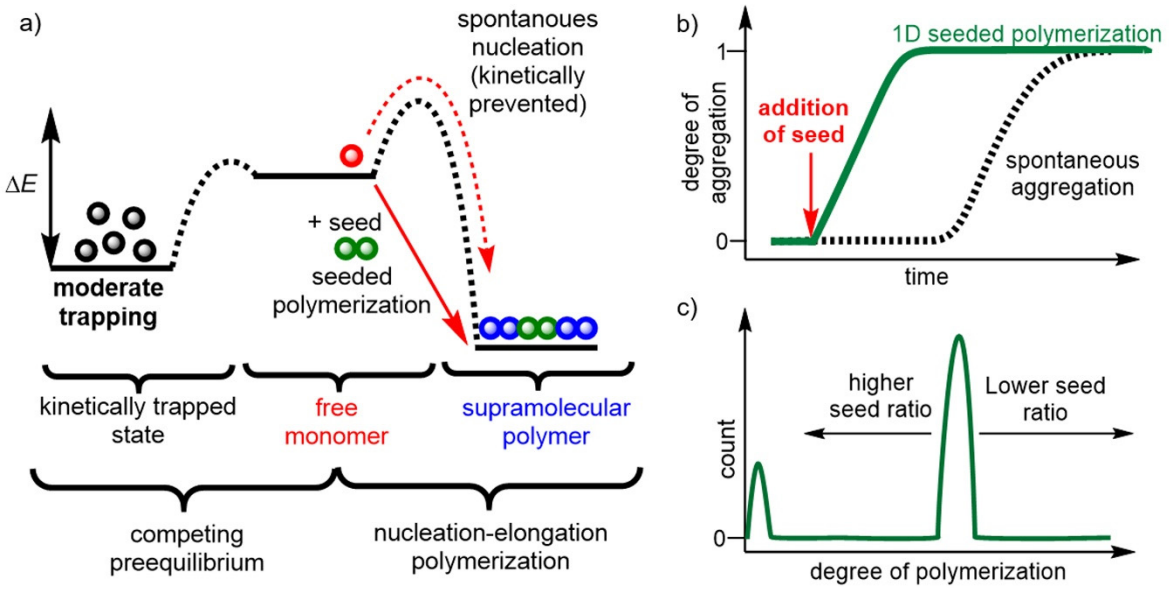


**Figure 11.** a) Qualitative energy diagram of a supramolecular polymerization coupled with a kinetic pre-equilibrium needed for seed-induced supramolecular polymerization. b) Schematic illustration of the degree of aggregation of a seeded polymerization experiment (green line) and of the spontaneous aggregation (black dashed line). c) Schematic illustration of the degree of polymerization dependent on the seed ratio.

Inspired by the work of Winnik, Manners and coworkers[45-49] an living crystallization-driven self-assembly (*cf.* Chapter 2.5.4), the first example of living supramolecular polymerization was demonstrated 2014 by Sugiyasu, Takeuchi and coworkers for a zinc porphyrin derivative **8** (Figure 12a).[53] The monomers of **8** form a kinetically metastable off-pathway J-aggregate by an isodesmic mechanism upon cooling. These kinetically trapped nanoparticles transform into the thermodynamically stable H-aggregated nanofibers over several days. The thermodynamically favored aggregates are formed by self-assembly of the porphyrin monomers by *inter*molecular hydrogen-bonding of the amide groups and $\pi$-$\pi$-stacking of the porphyrin cores in a process following the nucleation-elongation mechanism (Figure 12b). It was shown that the addition of small polymeric seeds of the H-aggregates, obtained by ultrasonication, can initiate instantaneously the polymerization of the trapped state at the termini of the seeds. Moreover, this seeded polymerization can be repeated for several cycles demonstrating the living manner of the seeded polymerization process. This approach

enables to control the length and polydispersity of the polymeric nanofibers (PDI ≤ 1.1) by the added amount of seed and the number of polymerization cycles.

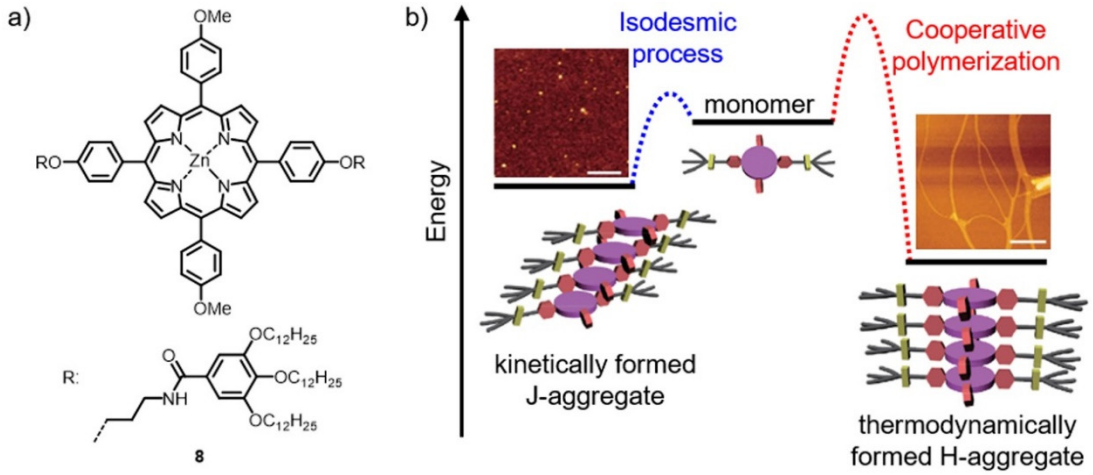


**Figure 12.** a) Chemical structure of the zinc porphyrin derivative **8** and (b) schematic energy diagram representing the different polymerization pathways. The AFM height images of the respective aggregates are shown as insets.[53] Adapted with permission from ref.[53] Copyright 2014 Nature Publishing Group.

In contrast to the above described supramolecular system with a kinetically trapped off-pathway aggregate, the first examples in which kinetically trapped monomeric species, are used for the retardation of the spontaneous polymerization, were reported in 2015 by Aida and coworkers for corannulenes and by Würthner and coworkers for PBIs. In the former supramolecular system, the bowl-shaped corannulene monomers bearing five different amide-containing thioalkyl side chains **9a-f** (Figure 13a) are kinetically trapped through five-fold *intra*molecular hydrogen-bonding in the monomeric state which prevents the supramolecular polymerization. The addition of initiator molecules (**9a-c**), in which the amide groups are *N*-methylated to prevent the aforementioned formation of the kinetically trapped monomers, leads to the opening of the *intra*molecular hydrogen-bonded species concomitant with the formation of *inter*molecularly hydrogen-bonded aggregates (Figure 13b). The "active" ends of these supramolecular species undergo one-dimensional chain-growth supramolecular polymerization (Figure 13c). Moreover, the authors could show that the living polymerization of an achiral monomer (**9d**) with chiral initiators (**9b** or **9c**) leads to the formation of left or right-handed helical aggregates, respectively, with an enantiomeric excess close to unity following the sergeants-and-soldiers principle.[125-127] Furthermore, the living polymerization of chiral monomers (**9e** or **9f**) could only be induced by initiators with matching configurations (**9b** or **9c**) enabling the optical resolution of a racemic mixture of **9e** and **9f**. Nevertheless, this seed-induced supramolecular polymerization is up to date the only

example known in literature of a living polymerization process induced by a monomeric initiator, that is chain-growth living supramolecular polymerization.

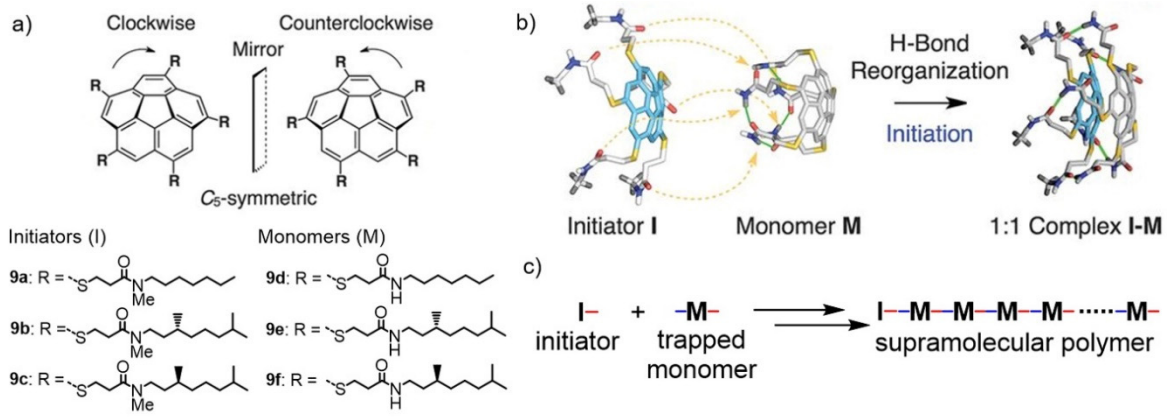


**Figure 13.** a) Chemical structures of the $C_5$-symmetrical corannulenes **9a-f** with different thioalkylside chains. b) Schematic illustration of an initiator molecule (I) opening the kinetically trapped monomer (M). c) Schematic representation of the chain-growth supramolecular polymerization. Adapted with permission from ref.[58] Copyright 2015 American Association for the Advancement of Science.

In the inspiring example of the Würthner group a core-unsubstituted PBI (**H-PBI**) bearing amide groups in imide position was investigated. The PBI, which was originally designed as an supramolecular organogelator,[128-129] forms long helical nanofibers through $\pi$-$\pi$-stacking of the perylene cores and *inter*molecular hydrogen-bonding of the amide groups as the thermodynamically stable equilibrium state in toluene. This spontaneous polymerization is retarded with a lag time of about 1h at 30 °C due to the formation of a kinetically trapped monomeric species by *intra*molecular hydrogen-bonding of the amide proton (N−H) to one of the imide carbonyl groups of the perylene cores (Figure 14a), so that the side chain is located close to the PBI core which blocks the $\pi$-surface for a further polymerization process.

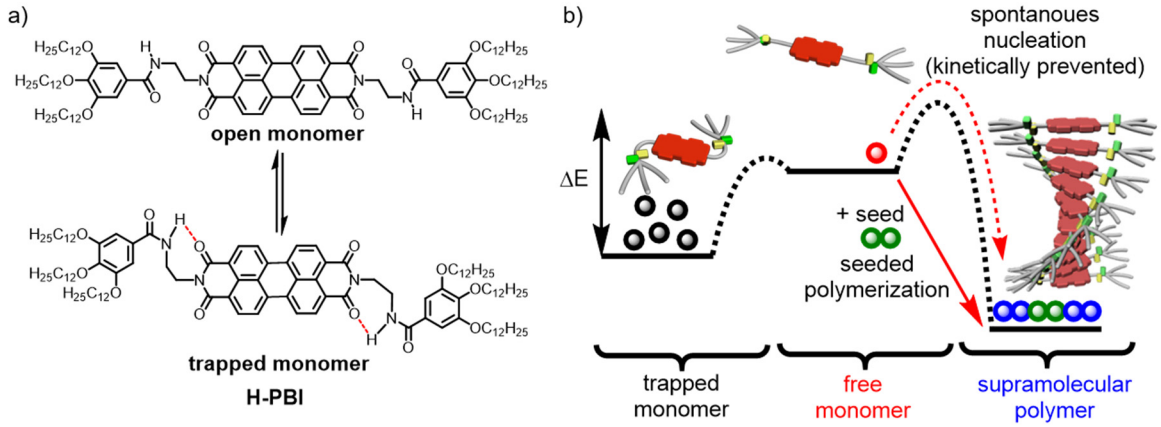


**Figure 14.** a) Equilibrium between the non-hydrogen-bonded open and the *intra*molecularly hydrogen-bonded monomeric species of **H-PBI**. The *intra*molecular hydrogen bonds are indicated by the red-dashed lines. b) Qualitative energy landscape of the self-assembly and the seeded polymerization of **H-PBI**.[57]

The detailed studies have shown that the supramolecular polymerization can be induced by the addition of a small amount of preformed polymeric seeds acting as nuclei for the supramolecular polymerization process (Figure 14b). The small seeds were produced by ultrasonic treatment of the thermodynamically stable H-aggregate solution leading to a fragmentation of the long polymeric nanofibers and producing a high number of active ends of the seeds. The overall time for the seeded polymerization and the length of the formed polymers in such a supramolecular system is controlled by the amount and the polydispersity of the added seed.

In the subsequent work of the Würthner group, the self-assembly of core-unsubstituted PBI derivatives with increasing length of the alkyl spacer from two (**H-PBI**) to three (**H-PBI-C3**), four (**H-PBI-C4**) and five methylene-units (**H-PBI-C5**) was investigated (Figure 15). These studies revealed interesting effects of the variation of the alkyl spacer length on the thermodynamically and kinetically controlled polymerization pathways.[60] Thus, FT-IR spectroscopy showed that the stability of the *intra*molecularly hydrogen-bonded monomers is decreased by increasing spacer length due to formation of energetically more unfavorable ring sizes.

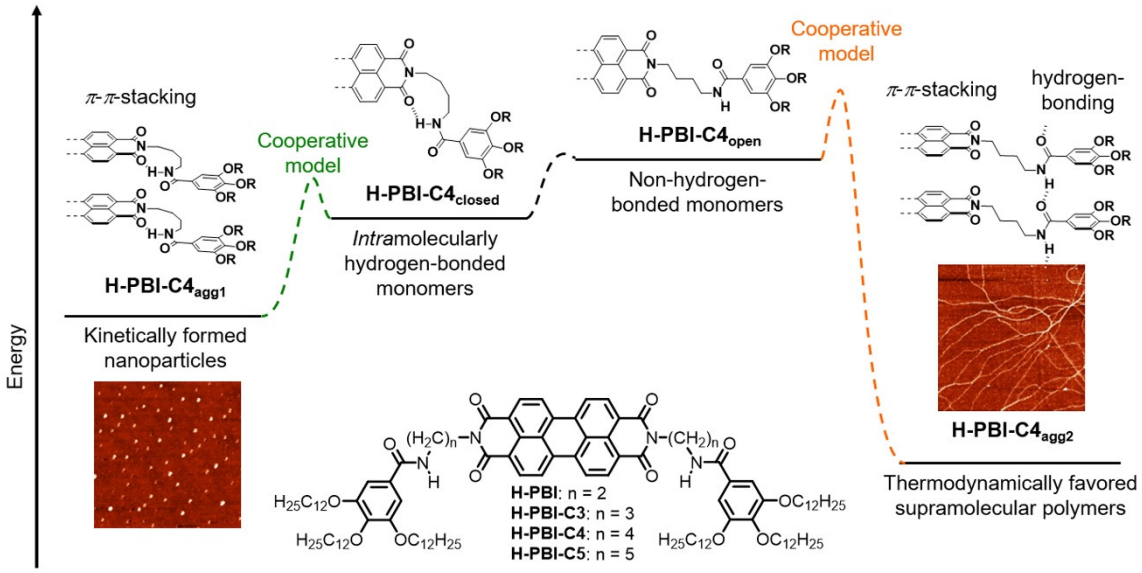


**Figure 15.** Chemical structures of the PBI derivatives with different lengths of the alkyl spacers (**H-PBI**, **H-PBI-C3**, **H-PBI-C4** and **H-PBI-C5**) and qualitative energy landscape of the competing aggregation pathways of **H-PBI-C4**. For simplicity, in the energy landscape only one-half of each molecular structure is shown and dodecyl groups are replaced by R. The AFM height images (5 µM × 5 µM) of the nanoparticles and the helical fibers of **H-PBI-C4** spin-coated onto silicon substrates are shown under the respective aggregate structure. Adapted with permission from ref.[60] Copyright 2016 American Chemical Society.

Although all PBIs of this series form one-dimensional nanofibers as thermodynamically favored states, the kinetic effects on their polymerization behavior drastically differ. While **H-PBI-C3** and **H-PBI-C5** form in a similar polymerization process as the previously described **H-PBI** a kinetically trapped monomeric species, the butylene-tethered **H-PBI-C4** spontaneously self-assembles into nanoparticles (**H-PBI-C4$_{agg1}$**) by a cooperative mechanism (Figure 15). These metastable aggregates are formed by $\pi$-$\pi$-interaction between the *intra*moelcularly hydrogen-bonded monomers (**H-PBI-C4$_{closed}$**). Time- and concentration-dependent UV/vis studies revealed that the transformation of **H-PBI-C4$_{agg1}$** into the thermodynamically stable polymeric nanofibers (**H-PBI-C4$_{agg2}$**) is slower for higher concentrations, demonstrating that **H-PBI-C4$_{agg1}$** is indeed an off-pathway aggregated state. Since in such a supramolecular system this transformation requires monomers in the energetically less favored open form (**H-PBI-C4$_{open}$**), the spontaneous polymerization into the thermodynamically favored supramolecular polymer is efficiently retarded. Thus, by the approach of seed-induced living polymerization the conversion of **H-PBI-C4$_{agg1}$** into the nanofibers **H-PBI-C4$_{agg2}$** can be achieved in a kinetically controlled polymerization process.

The fact that subtle modifications of the monomer units can have a huge influence on the thermodynamically and kinetically controlled aggregation pathways was studied by Sugiyasu, Takeuchi and coworkers.[63] They investigated the self-assembly of a broad series of zinc porphyrins **10a-g** bearing identical amide side groups, but altered size of the alkyloxy-substituents at the porphyrin cores (Figure 16a). This variation of the alkyl chain leads to unprecedented changes in the self-assembly pathways of the porphyrin derivatives. While the zinc porphyrin **10a** forms exclusively H-aggregated nanofibers, the monomers with sterically demanding substituents (**10b** and **10g**) form only J-aggregated nanoparticles under thermodynamic control. In contrast, for the porphyrins **10c** and **10d** the formation of kinetically metastable nanoparticles, which can be transformed into the thermodynamically favored nanofibers by seeded supramolecular polymerization is possible, like in the previously described example of the similar monomeric building block **8** (*vide supra*).[32,53] Surprisingly, the increase of length of the alkyl spacer for **10e** and **10f** enables additional aggregation pathways resulting in a completely new energy landscape of self-assembly (Figure 16b). In this supramolecular system the monomers can assemble into the thermodynamically favored two-dimensional nanosheet-like architectures through van-der-Waals interactions between the side-chains *via* the formation of kinetically metastable on-pathway nanoparticles. In a kinetically controlled polymerization pathway the formation

of out-of-equilibrium nanofibers by $\pi$-$\pi$-interactions and hydrogen-bonding is still possible by increasing the mechanical agitation, e.g., by applying ultrasonication to the solution of the nanoparticles. Moreover, the self-assembly pathways can be controlled by using the approach of seeded polymerization. The addition of the polymeric one-dimensional fibrous seeds to the kinetically trapped nanoparticles induces the transformation into nanofibers, while the addition of two-dimensional seeds leads to the formation of the nanosheet-like supramolecular structures.

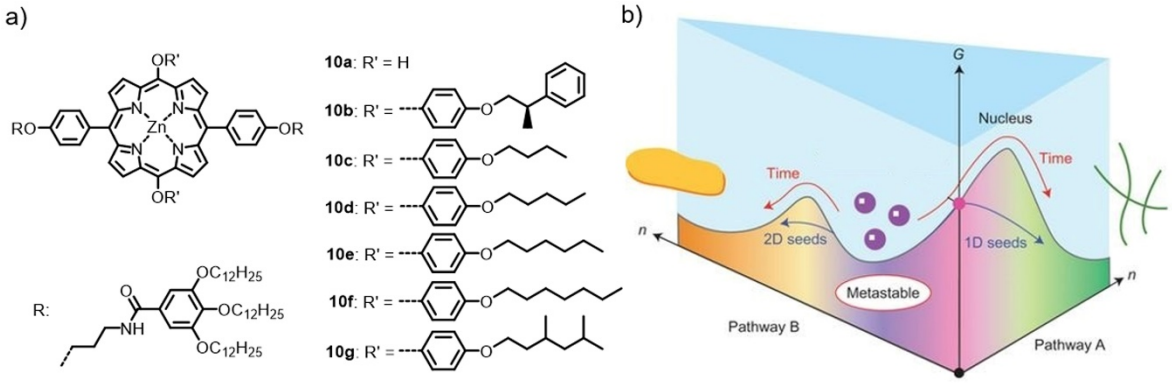


**Figure 16.** a) Chemical structures of the investigated zinc porphyrins **10a-g** bearing various substituents. b) Qualitative energy landscape for different self-assembly pathways of **10e** and **10f** leading either to the formation of one-dimensional nanofibers or two-dimensional nanosheets. Adapted with permission from ref.[63] Copyright 2017 Nature Publishing Group.

Based on the above described concepts of seeded and living polymerization several novel supramolecular systems were investigated in the recent years,[59,64-67,130] either applying the approach on monomeric building blocks with different core units or on supramolecular systems which are mainly differing in the nature of the dormant species.[59,64,76,130] While in an example of Ogi, Yamaguchi et al. the kinetically trapped species is produced by a hydrogen-bonding driven *intra*molecular folding process of a properly designed pyrene-substituted amino-acid based diimide,[64] a dormant monomer can also be generated by a photoisomerization of an azobenzene derivative as demonstrated by Sugiyasu, Takeuchi and coworkers.[59] In a recent example of Sugiyasu, Takeuchi et al. the monomer is kinetically trapped in the presence of a "dummy" monomer, which is similar in structure to the reactive monomeric building block, but incapable of forming the extended supramolecular polymer.[130] This coassembly process of the monomeric units with the "dummy" monomer leads to a retardation of the spontaneous polymerization and enables the seeded polymerization under kinetic control. In an unusual example reported by van der Gucht, Otto and coworkers the approach of dynamic combinatorial chemistry is used to generate kinetically trapped trimeric or tetrameric disulfide-bridged macrocycles of thiol-

functionalized peptide monomers by air oxidation.[76] These out-of-equilibrium species can be transformed into thermodynamically favored fibrous nanostructures of hexameric macrocycles by a nucleation-elongation supramolecular polymerization in a living manner. In their studies, also initial attempts were realized to produce supramolecular block copolymers of two very similar building blocks applying a seeded approach.

## 2.5 Supramolecular Copolymers

Linear supramolecular copolymers consisting of two monomeric units A and B can be categorized analogous to covalent copolymers by the pattern of monomer enchainment into random, alternating, periodic, block and blocky coassemblies.[72] While in random costructures the monomers are statistically distributed along the supramolecular polymer chain, in alternating copolymers monomeric units are enchained in a regular alternating pattern. The periodic copolymer contains monomeric units in a sequenced regular pattern, e.g., two monomers of A are connected to one monomer of B. In the highly desirable supramolecular block copolymers the monomer units are self-assembled into long sequences of each individual monomer. These polymeric blocks can be arranged for example in an A-B or A-B-A type leading to the formation of di- or triblock copolymers, respectively. In multiblock (blocky) copolymers multiple short blocks of each monomer are present in the polymeric nanostructure.[72]

### 2.5.1 Random Supramolecular Copolymers

Some of the earliest examples of supramolecular copolymers are obtained under thermodynamic control by statistical copolymerization experiments, which were designed to demonstrate the chiral amplification in one-dimensional supramolecular polymers.[72,131] These random copolymers were achieved mainly following three principles of chiral amplification, namely the sergeant-and-soldiers,[102,125-127,132-133] the majority-rules[134-137] and the diluted-majority-rules principle.[138-139] In a sergeant-and-soldiers experiment achiral monomers (the soldiers) are mixed with a small amount of their chiral counterparts (the sergeants) leading to a control of the overall helicity of the supramolecular copolymer.[131] The majority-rules principle describes the mixing of two chiral enantiopure monomer units with a slight excess of one enantiomer which induces a strong bias for the helicity of the excess enantiomer.[131] In a dilution-majority-rules experiment mixing of two enantiomers in

the same supramolecular copolymer was achieved by diluting the enantiomeric mixtures of these chiral sergeants with achiral soldiers.[139] In such a supramolecular system the mixing of the enantiopure monomers in a majority-rules experiment leads only to narcissistic self-sorting of the individual components into homopolymers.[139] The utilized monomers in the above described examples exhibit, in general, an identical core-structure and differ only slightly in their achiral or chiral side-chains. Therefore, the copolymerization was mainly studied only by CD spectroscopy. Although in most cases a statistical incorporation of the monomers into the copolymer is assumed, the experimental and structural prove for the random incorporation is hard to achieve.[72] Nevertheless, in recent examples random copolymerization was employed to control the thermodynamic stability of self-assembled nanofibers[140] or to create functional copolymers in aqueous media for biological applications.[141-142]

### 2.5.2 Alternating Supramolecular Copolymers

The first example of an alternating supramolecular copolymer was already reported by Lehn and coworkers in 1990 who investigated the copolymerization of complementary monomeric units based on multiple hydrogen-bonding.[87,143] Since then, several examples of alternating copolymers were reported for example based on isodesmic copolymerization of complementary units,[10,144] hierarchical self-assembly by complementary hydrogen-bonding[145] and copolymerization by charge transfer interaction of donor-acceptor monomers.[146-147] In a more recent example, Besenius and coworkers showed the formation of alternating copolymers based on benzene tricarboximide monomers **11a** and **b** bearing $\beta$-sheet encoding oligopeptides (Figure 17).[148-149]

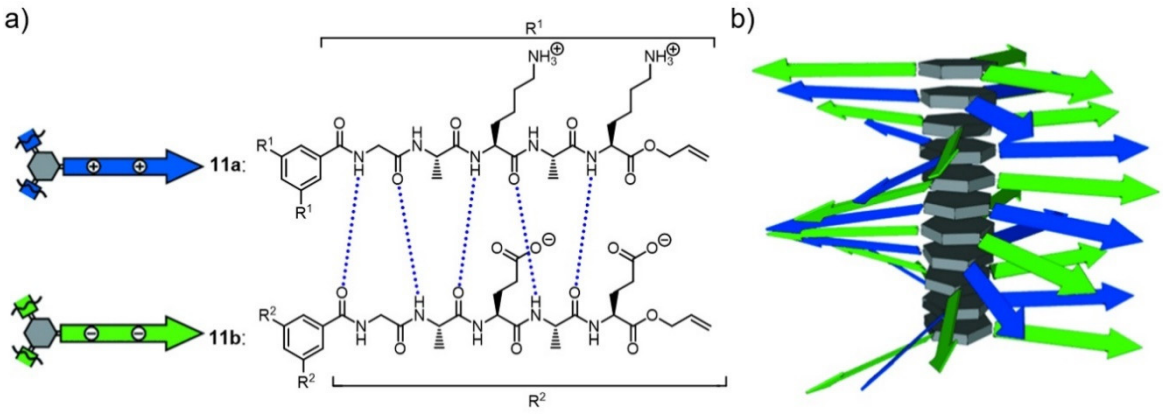


**Figure 17.** a) Chemical structures of the cationic and anionic benzene tricarboximide derivatives **11a** and **b**. b) Schematic illustration of the alternating supramolecular copolymer. Adapted with permission from ref.[148] Copyright 2013 WILEY-VCH Verlag GmbH.

These positively (**11a**) and negatively (**11b**) charged monomeric units self-assemble by electrostatic and hydrogen-bonding interactions, which enables the pH-dependent switching between co- and homopolymerization.[150] Moreover, they were able to demonstrate the kinetically controlled sequential growth of an alternating supramolecular copolymer on a functionalized Au-surface.[34]

Another interesting example of an alternating copolymer was reported by Haino and coworkers in 2017.[151] They investigated the coassembly of three different heteroditopic monomers possessing complementary biscalix[5]arene-$C_{60}$, bisporphyrin-trinitrofluorene and Hamilton's bis(acetamidopyridinyl)isophthalamide-barbiturate host-guest complex forming units. With these monomeric building blocks an alternating supramolecular terpolymer with an $(ABC)_n$ sequence was generated in solution and solid state, which was confirmed by NMR spectroscopy and mass spectrometry as well as atomic force microscopy.[151]

### 2.5.3 Periodic Supramolecular Copolymers

Since the design of periodic supramolecular copolymers is very challenging, only very few examples exist in literature, which are likely discovered by serendipity.[72] In 2009, Yagai, Würthner and coworkers reported the coassembly of the azobenzene-functionalized melamine **12a** and the tetrabay-substituted perylene bisimide **12b** (Figure 18a).[152] Upon mixing the monomers of **12a** (A) and **12b** (B) in a ratio of 2:1 in methylcyclohexane a helical periodic copolymer with an alternating $A_2B$-pattern is formed by complementary multiple hydrogen-bonding. From the UV/vis, dynamic light scattering and AFM studies the authors proposed the unconventional hydrogen-bonding between the monomeric units in the copolymer, illustrated in Figure 18a, where the neighboring melamine units have a *syn* orientation. The hierarchical coassembly into J-type aggregates directed by hydrogen-bonding can only be realized by a defined experimental protocol, i.e., exactly defined molar ratios of the monomers, equilibration times and temperatures, to overcome kinetic barriers and to reach the thermodynamic equilibrated alternating copolymer.[152]

A more recent example of a periodic copolymer was reported by the Würthner group in 2015.[153] They investigated the coassembly of a planar (**13a**: A) and a core-twisted PBI derivative (**13b**: B) leading to supramolecular copolymers with the alternating sequence of $(A_mBB)_n$ as revealed by transmission electron microscopy, 2D-NMR and optical

spectroscopy studies (Figure 18b). The copolymerization was achieved by a specially designed experimental protocol by injection of water into a THF solution of the monomeric PBIs in a molecular ratio of 2:1 (**13a**:**13b**) and subsequent evaporation of THF. In contrast to the stiff nanorods and irregular nanoworms formed by homopolymerization of **13a** and **13b**, respectively, by copolymerization of both PBIs highly defined ultralong nanowires were obtained in a kinetically controlled process. Further investigations revealed that upon heating the kinetically metastable polymers transform into the thermodynamically more favored self-sorted homopolymers.[153]

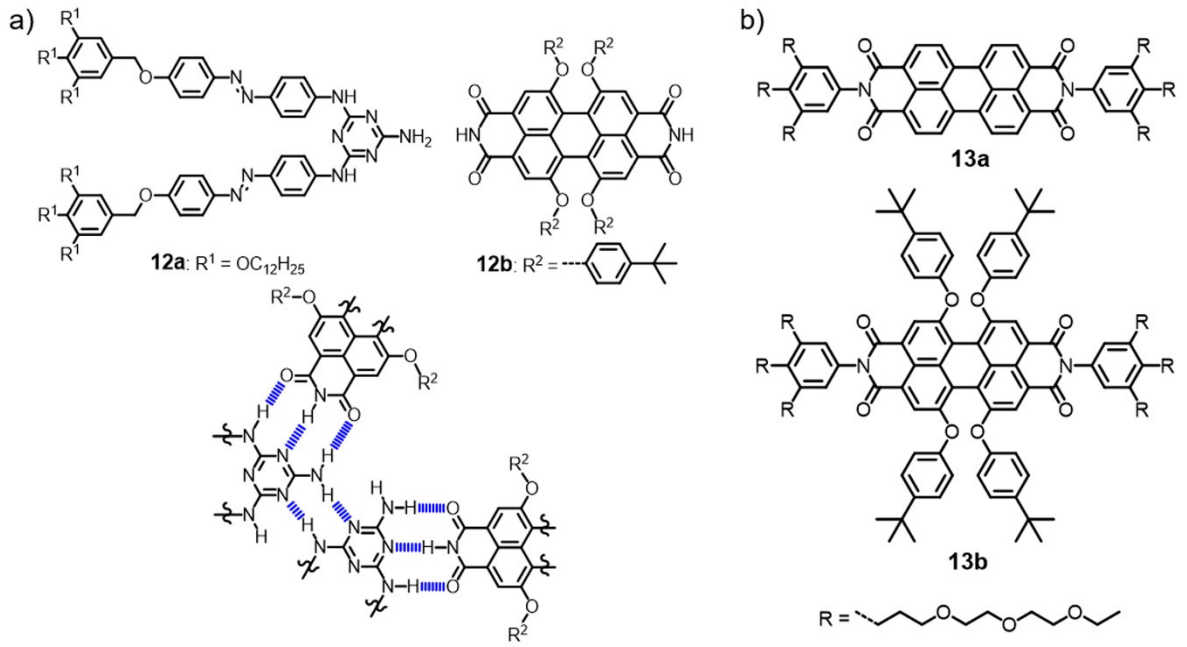


**Figure 18.** a) Molecular structures of the melamine linked azobenzene **12a**, the perylene bisimide **12b** and the possible hydrogen-bonding pattern in the alternating $A_2B$ helical copolymer of **12a** and **12b**. b) Chemical structures of the planar (**13a**) and core-twisted (**13b**) PBI derivatives with identical solubilizing ethylene glycol functionalized imide substituents.

### 2.5.4 Supramolecular Block Copolymers

Since covalent block copolymers are an outstanding class of polymers with interesting properties and numerous applications, the challenging synthesis of their supramolecular counterpart, i.e., supramolecular block copolymers, is highly desirable. One powerful method to construct supramolecular block architectures is the crystallization-driven self-assembly (CDSA), which was introduced 2007 by Winnik, Manners and coworkers. They reported the synthesis of cylindrical block copolymer micelles consisting of poly(ferrocenyldimethyl-silane) block copolymers as monomeric units for the supramolecular polymerization in a

kinetically controlled process.[45] These comicelles showed high stability and low polydispersity because of the living behavior of the polymerization process. With the approach of living crystallization-driven self-assembly, a plethora of block architectures based on poly(ferrocenyldimethylsilane) block copolymers monomer units was achieved, like di- and triblock comicelles,[48-49] fluorescent multiblock micelles,[154-155] comicelles between linear and brushed units[156] and multidimensional supermicelles obtained by hierarchical self-assembly of comicelles.[52,73,157-158] Furthermore, other types of monomeric building blocks were used for living crystallization-driven self-assembly, like for example poly(*p*-phenylvinylene)s.[159] Recently, the seeded CDSA approach was utilized for the copolymerization of electron poor and electron rich poly(di-*n*-hexylfluorene) block copolymers (**14a** and **b**) into conjugated semiconducting polymeric nanofibers, exhibiting a long-range exciton transport (Figure 19a).[74]

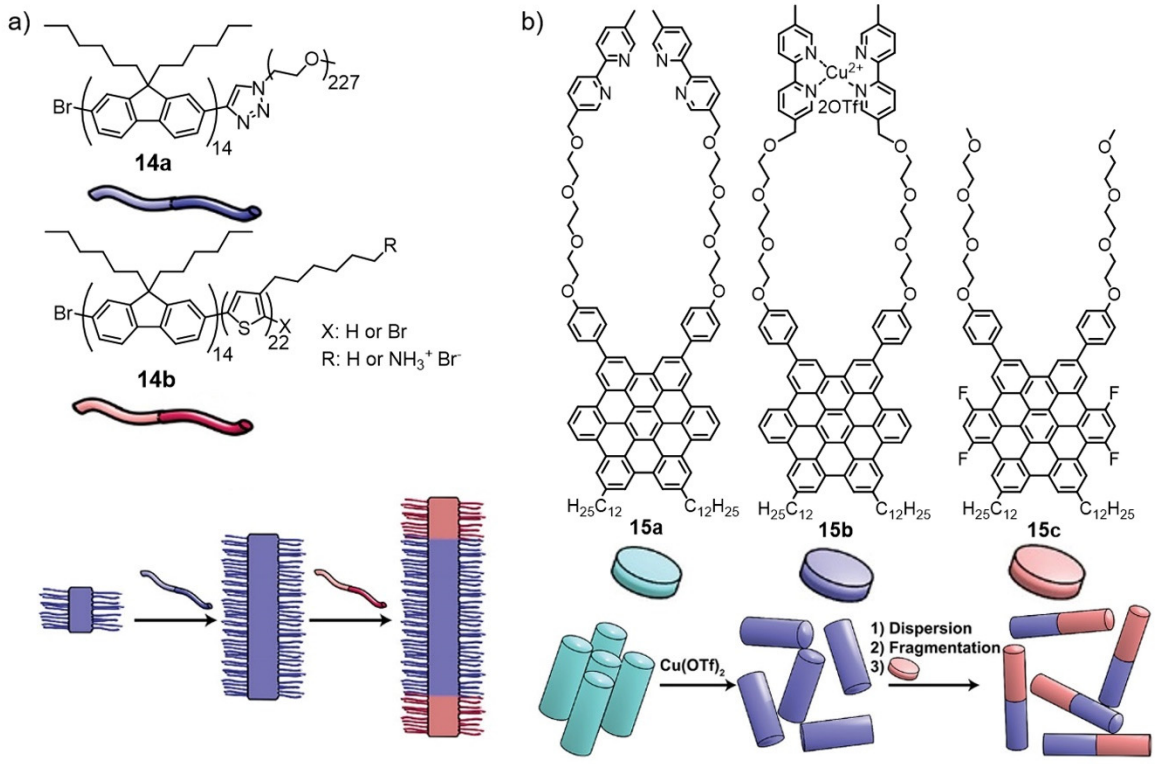


**Figure 19.** a) Illustration of triblock comicelles obtained by crystallization-driven self-assembly of the covalent block copolymer building blocks **14a** and **14b** featuring a crystalline midblock of poly(di-*n*-hexylfluorenes). b) Schematic illustration of multistep synthesis of supramolecular block copolymers of electron rich and electron poor hexabenzocoronene-based monomer units (**15a-c**). Adapted with permission from ref.[72] Copyright 2019 American Chemical Society.

An exceptional example of block copolymers was reported by Aida and coworkers by demonstrating the multistep non-covalent synthesis of nanotubular block copolymers based on hexabenzocoronene monomers functionalized with bipyridine groups (Figure 19b).[75]

The monomers of **15a** assemble into bundled nanotubes, in which the bipyridyl unit can undergo a metalation with copper to form the polymeric blocks consisting of **15b**. Upon ultrasonication and fragmentation of this charged nanotubes, small seeds can be obtained. The addition of monomers of **15c** to the aforementioned seed solution results in the formation of a mixture of di- and triblock copolymers. In further seminal work they showed that the use of one-handed helical nanotubular seeds, which were produced by multistep non-covalent synthesis of chiral hexabenzocoronene monomeric units, leads to the formation of one-handed helical block copolymers following the sergeants-and-soldiers principle.[160]

While the above described examples of block costructures are produced by kinetically controlled processes, the up to date only example of a supramolecular block copolymer formed under thermodynamic control was reported by Palmans, Meijer and coworkers (Figure 20a).[77]

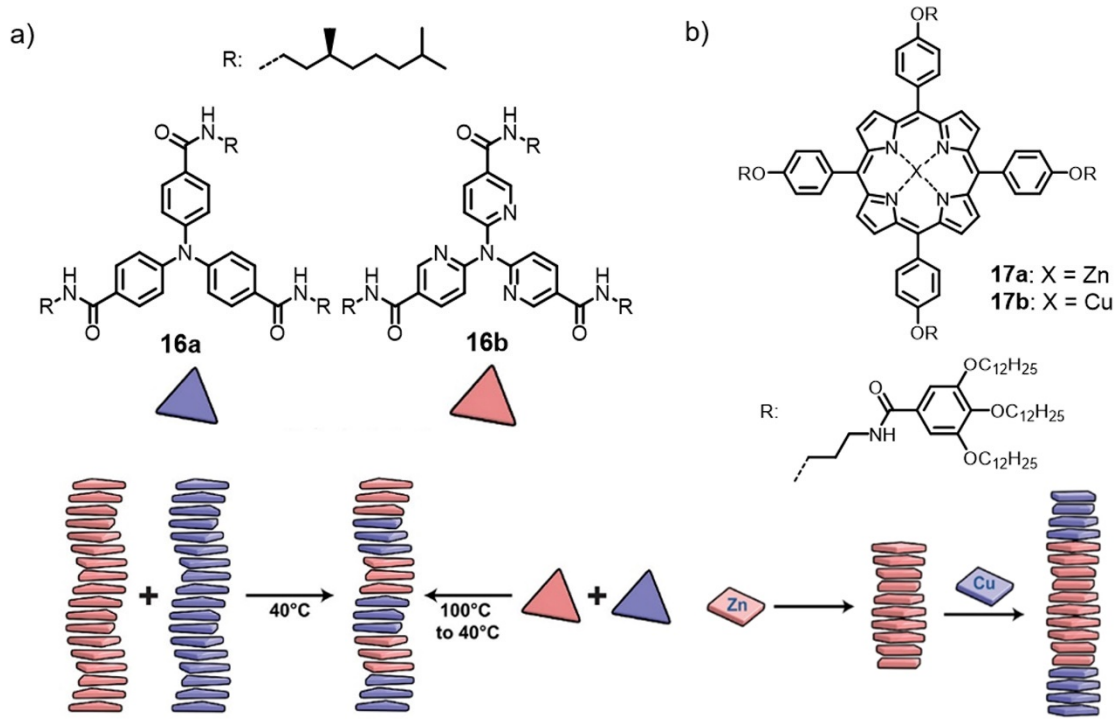


**Figure 20.** a) Illustration of the supramolecular multiblock copolymer formed by polymerization of the triphenylamine tricarboximide **16a** and tripyridylamine tricarboxamide **16b** under thermodynamic control. b) Formation of an A-B-A triblock copolymer by seeded two-component polymerization of a zinc porphyrin **17a** and a copper porphyrin **17b**. Adapted with permission from ref.[72] Copyright 2019 American Chemical Society.

They investigated the coassembly of a triphenylamine tricarboximide **16a** and tripyridylamine tricarboximide **16b** and showed, that supramolecular multiblock copolymers are produced both, by copolymerization of the monomeric units and by directly mixing the

homopolymers consisting of the individual building blocks. The very high thermodynamic stability of the supramolecular block copolymers allowed their characterization with optical spectroscopy and super resolution fluorescence microscopy techniques.

The novel strategy of seeded copolymerization to generate block copolymers was very recently investigated by Pavan, Takeuchi, Sugiyasu and coworkers (Figure 20b).[70] They were able to generate seeds of homopolymers of a zinc porphyrin **17a** by ultrasonication. Following a special designed solvent mixing protocol, similarly to the aforementioned CDSA approach, the addition of the copper porphyrin derivative **17b** to the seed solution of a zinc porphyrin **17a** leads to the formation of supramolecular block copolymers with controlled length and narrow polydispersity through seeded supramolecular polymerization. Interestingly, the A-B-A block structure prevented the disassembly of the inner block in the presence of a depolymerization agent because the monomer exchange occurs only from the termini of the supramolecular polymer, which was also corroborated by sophisticated molecular simulations. However, the individual blocks of the copolymer formed by the respective monomer units could not be identified by spectroscopic or microscopic techniques because of the very similar structure and properties of both monomeric building blocks.

# Chapter 3

–

# Living Supramolecular Polymerization of a Perylene Bisimide Dye into Fluorescent J-aggregates

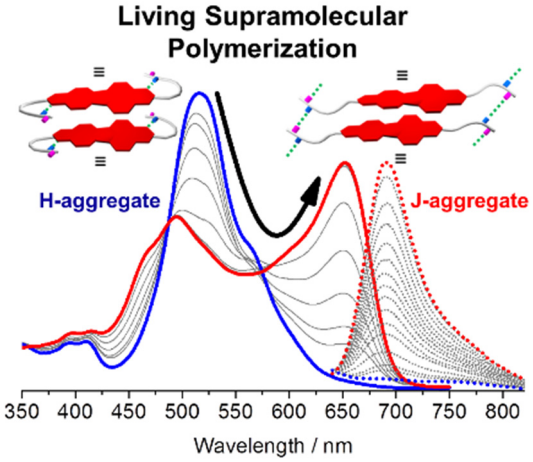


This Chapter was published in: W. Wagner, M. Wehner, V. Stepanenko, S. Ogi, F. Würthner, *Angew. Chem. Int. Ed.* **2017**, *56*, 16008-16012.



**Abstract**: The self-assembly of a new perylene bisimide organogelator with 1,7-dimethoxy substituents in bay position affords non-fluorescent H-aggregates at high cooling rates and fluorescent J-aggregates at low cooling rates. Under properly adjusted conditions, the kinetically trapped off-pathway H-aggregates are transformed into the thermodynamically favored J-aggregates, a process that can be accelerated by the addition of J-aggregate seeds. Spectroscopic studies revealed a subtle interplay of $\pi$-$\pi$-interactions as well as *intra*- and

*inter*molecular hydrogen bonding for monomeric, H-, and J-aggregated species. Multiple polymerization cycles initiated from the seed termini demonstrate the living character of this chain-growth supramolecular polymerization process.

## 3.1 Introduction

Although living covalent polymerization was introduced as early as in the late 1950s[1] and has since undergone comprehensive development,[2,161-162] its supramolecular counterpart has emerged only recently. Spearheaded by research on seeded "living" block copolymer self-assembly from crystal facets by Manners,[45,48] Sugiyasu, Takeuchi and coworkers described for the first time in 2014 the seed-initiated living supramolecular polymerization of a single aggregate chain with a porphyrin dye.[53] This step marks the logical advancement of a research field that was initially established based on thermodynamic considerations, that is, the formation of equilibrium structures,[11,13-14] and only later on developed towards kinetic control[15,17,121] leading to off-pathway products,[30-31,43,153] that is, out-of-equilibrium species.[54-56] The final step towards living supramolecular polymerization has been achieved recently by both the seed-induced[53,57,63,160,163] as well as the initiator-molecule induced approach,[58] where either added seeds or properly designed molecules function as initiators for the chain-growth of monomers into one-dimensional non-covalently bound molecular aggregates.

A crucial requirement for chain-growth supramolecular polymerization is the retardation of the competing spontaneous self-assembly of monomers, which can be accomplished with kinetically trapped "inactive" species.[53-58,63,160,163] We have recently shown that such kinetically trapped species can be programed by molecular design.[57,60] Thus simple perylene bisimide (PBI) organogelator molecules bearing terminal amide groups are kinetically trapped by *intra*molecular hydrogen bonding under appropriate conditions either in unimolecular[57] or off-pathway aggregate[60] states, and hence inactivated for spontaneous supramolecular polymerization but active upon addition of seeds. With a similar design, Miyajima, Aida, and coworkers demonstrated that the spontaneous polymerization of a bowl-shaped corannulene bearing multiple amide groups can be retarded by *intra*molecular hydrogen bonding, and its chain-growth polymerization can be initiated by the addition of a non-hydrogen bonded derivative.[58]

A unique feature of living polymers is their active termini, which enable initiation of repeated growth cycles of monomers until the living ends are terminated.[2,161-162] Thus far, such repeated cycles have been shown only for very few living supramolecular polymerization systems,[53,58] which are, however, not yet exciting from a functional point of view. Herein, we report the first multicycle living supramolecular polymerization of a PBI dye leading to a fluorescent J-aggregate.[164] Our present studies revealed that the newly designed core twisted PBI organogelator **MeO-PBI** (Chart 2) self-assembles into kinetically trapped non-fluorescent H-type aggregates, which can be transformed into thermodynamically favored fluorescent J-aggregates by seed-induced living polymerization. More significantly, the polymerization cycle can be repeated several times by using the living polymer of the preceding cycle.

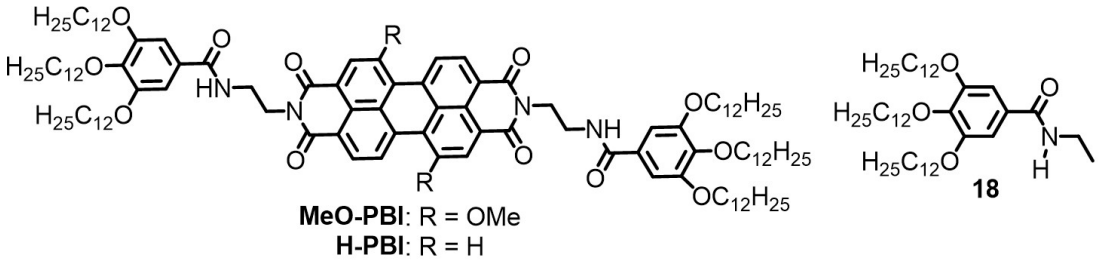


**Chart 2.** Chemical structures of the dimethoxy-substituted **MeO-PBI**, the reference PBI organogelator **H-PBI**,[57,129,165] and benzamide **18**.

## 3.2 Results and Discussion

The PBI organogelator **MeO-PBI** was synthesized by imidization of 1,7-dimethoxyperylene-3,4:9,10-tetracarboxylic acid bisanhydride with *N*-(2-aminoethyl)-3,4,5-tris(dodecyloxy) benzamide[129,165] in imidazole using $Zn(OAc)_2$ as the catalyst (Scheme 3). The bisanhydride precursor was synthesized by a recently developed copper-mediated cross-coupling reaction[166] from 1,7-dibromoperylene-3,4:9,10-tetracarboxylic acid tetrabutylester (see *Chapter 8.1* for details).

The optical properties of monomeric **MeO-PBI** were investigated by UV/vis absorption and steady-state fluorescence spectroscopy in 1,1,2,2-tetrachloroethane (TCE). In this solvent, the absorption spectrum of **MeO-PBI** shows the characteristic vibronic structure of bay-substituted PBIs with an absorption maximum at $\lambda_{max}$ = 577 nm (Figure 56), which is bathochromically shifted compared to that of the previously reported core-unsubstituted **H-PBI** ($\lambda_{max}$ = 533 nm).[129,165] The methoxy substituents at the 1,7-bay positions lead to a

twist of the perylene core of 11.4° according to DFT calculations (Figure 55). This distortion of the perylene core evokes a decrease in the extinction coefficient of **MeO-PBI** ($\varepsilon = 6.0 \times 10^4$ M$^{-1}$ cm$^{-1}$ in TCE) compared with that of the core-planar reference compound **H-PBI** ($\varepsilon = 8.1 \times 10^4$ M$^{-1}$ cm$^{-1}$ in TCE).[129,165] The fluorescence spectrum of **MeO-PBI** shows a maximum at $\lambda = 598$ nm and resembles a mirror image of the absorption spectrum (Figure 56). Interestingly, **MeO-PBI** exhibits a remarkably higher fluorescence quantum yield ($\Phi_{fl} = 0.68$) than **H-PBI** ($\Phi_{fl} = 0.10$) in TCE. The appreciable intense fluorescence of the former might be explained by the less electron-deficient character of the dimethoxy-substituted PBI core, which renders the photoinduced electron transfer from the electron-rich tridodecyloxyphenyl side groups to the core unfavorable.

The supramolecular polymerization of **MeO-PBI** was studied by temperature-dependent UV/vis spectroscopy in a 2:1 (v/v) solvent mixture of methylcyclohexane and toluene at varying cooling/heating rates (Figure 21). Upon cooling the monomer solution of **MeO-PBI** from 90 to 10 °C at a cooling rate of 5 °C min$^{-1}$, the absorption maximum was hypsochromically shifted with a loss of vibronic fine structure and the concomitant appearance of a weak transition at higher wavelength ($\lambda = 620$ nm). These spectral features are typical for the formation of PBI H-aggregates (denoted here as **MeO-PBI$_{agg\ I}$**).[129,165] A plot of the apparent extinction coefficients ($\varepsilon$) at the absorption maximum of the monomer (560 nm) against temperature reveals a sigmoidal transition, which is indicative of an isodesmic aggregation mechanism[13] (Figure 21a, inset). Surprisingly, upon cooling the same solution from 90 to 10 °C at a slower cooling rate of 1 °C min$^{-1}$, the formation of a J-type aggregate (denoted as **MeO-PBI$_{agg\ II}$**) with a strongly bathochromically shifted absorption maximum at 655 nm was observed (Figure 21b). A plot of the $\varepsilon$ values at 560 nm against temperature for the aggregation of **MeO-PBI$_{agg\ II}$** shows, in contrast to that of **MeO-PBI$_{agg\ I}$**, a pronounced hysteresis of about 25 °C between the thermodynamically controlled heating and the kinetically controlled cooling process (Figure 21a,b, insets). The non-sigmoidal (Figure 21b, inset) transition observed upon heating could be fitted by using the cooperative nucleation-elongation model introduced by Smulders and coworkers,[27] giving a critical temperature of $T_e = 359$ K and an elongation enthalpy of $\Delta H_e = -88.6$ kJ mol$^{-1}$ at $c_T = 15 \times 10^{-6}$ M (Figure 57 and Table 1). Upon diluting the total concentration, the elongation temperature $T_e$ decreased in a linear fashion as the van't Hoff plot illustrates (Figure 58). From this plot, the standard enthalpy ($\Delta H^0$) and entropy ($\Delta S^0$) were determined to be −97.6 kJ mol$^{-1}$ and −179.7 J mol$^{-1}$ K$^{-1}$, respectively; the former value is in good

agreement with the $\Delta H_e$ value determined by fitting the temperature-dependent data to the cooperative model (Figure 57).

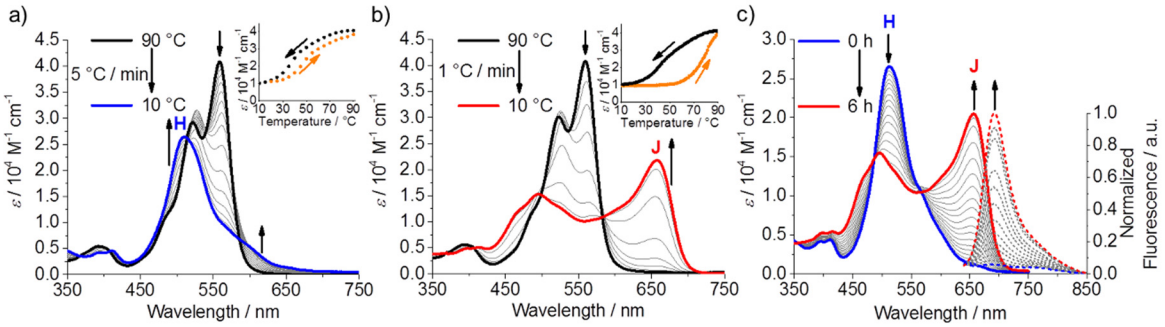


**Figure 21.** Temperature-dependent absorption spectra of **MeO-PBI** ($c_T = 15 \times 10^{-6}$ M) in MCH/Tol (2:1, v/v) upon cooling from 90 to 10 °C at a cooling rate of 5 °C min$^{-1}$ (a) and a lower cooling rate of 1 °C min$^{-1}$ (b). Plots of the extinction coefficients ($\varepsilon$) at 560 nm against temperature for the respective cooling (black dots) and heating (orange dots) processes are shown in the insets (cooling and heating rates: 5 °C min$^{-1}$ for (a) and 1 °C min$^{-1}$ for (b)). c) Time-dependent UV/vis absorption (solid lines) and emission spectra (dashed lines, $\lambda_{ex} = 487$ nm) of the spontaneous transformation of the H-aggregate **MeO-PBI$_{agg\ I}$** ($c_T = 15 \times 10^{-6}$ M) into the J-aggregate **MeO-PBI$_{agg\ II}$** at 20 °C.

Monitoring a solution ($c_T = 15 \times 10^{-6}$ M) of the kinetically formed H-aggregate **MeO-PBI$_{agg\ I}$** in MCH/Tol (2:1, v/v) by time-dependent UV/vis spectroscopy at 20 °C revealed an interesting transformation of the H-aggregate **MeO-PBI$_{agg\ I}$** into the J-aggregate **MeO-PBI$_{agg\ II}$** (Figure 21c, solid lines). The time-dependent absorption data clearly confirm that **MeO-PBI$_{agg\ I}$** is a kinetically metastable aggregate that is completely transformed into the thermodynamically favored **MeO-PBI$_{agg\ II}$** within a period of about 6 h. Repeating the measurements at different concentrations revealed that the transformation of **MeO-PBI$_{agg\ I}$** into **MeO-PBI$_{agg\ II}$** is faster when the total concentration is decreased from $20 \times 10^{-6}$ M to $10 \times 10^{-6}$ M (Figure 59). This concentration dependence indicates that **MeO-PBI$_{agg\ I}$** is an off-pathway (kinetically trapped) aggregate.[30,53] The transformation of the H- into the J-aggregates caused a drastic change in fluorescence. Whereas the H-aggregate **MeO-PBI$_{agg\ I}$** is nearly non-fluorescent, **MeO-PBI$_{agg\ II}$** is appreciably fluorescent with a quantum yield of $\Phi_{fl} = 0.14$ (Figure 21c and Figure 62). Time-dependent fluorescence spectra (Figure 21c, dashed lines) with excitation at the isosbestic point of **MeO-PBI$_{agg\ I}$** and **MeO-PBI$_{agg\ II}$** ($\lambda_{ex} = 487$ nm) highlighted the transformation of the non-fluorescent H-aggregate **MeO-PBI$_{agg\ I}$** into the emissive J-aggregate **MeO-PBI$_{agg\ II}$** with a strong increase in fluorescence. Such unique changes in the fluorescence properties upon transformation of a kinetically trapped H-aggregate into the thermodynamically stable J-aggregate have rarely been reported.[40]

The influence of hydrogen bonding on the stabilization of the different aggregated species was investigated by Fourier-transform infrared (FT-IR) spectroscopy (for details, see *Chapter 8.1* and Figure 63, 64). These FT-IR studies revealed that the aggregates of **MeO-PBI$_{agg\ II}$** formed from monomers adopt extended conformations (denoted as **MeO-PBI$_{open}$**) by *inter*molecular hydrogen bonding between the amide groups while **MeO-PBI$_{agg\ I}$** consists of *intra*molecularly hydrogen-bonded monomers **MeO-PBI$_{closed}$** that self-assemble *via* $\pi$-$\pi$-interactions between the PBI molecules (Figure 22).

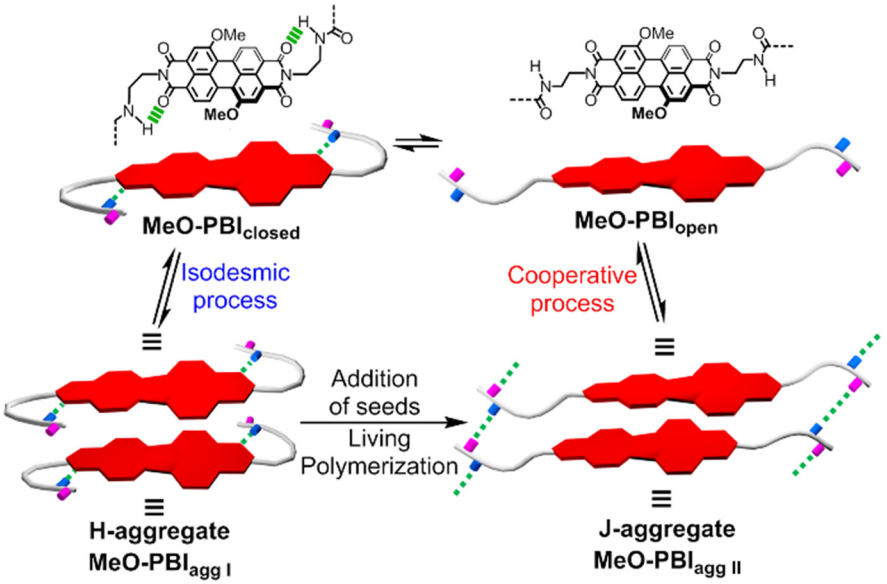


**Figure 22.** The equilibrium between the open (**MeO-PBI$_{open}$**) and the closed conformation (**MeO-PBI$_{closed}$**) and formation of the metastable H-aggregate **MeO-PBI$_{agg\ I}$** and the thermodynamically favored J-aggregate **MeO-PBI$_{agg\ II}$**.

As discussed before, **MeO-PBI** shows an interesting interplay between the kinetically trapped and the thermodynamically stable aggregate states. Therefore, we explored the seed-induced living supramolecular polymerization of this PBI. For this purpose, seeds of **MeO-PBI$_{agg\ II}$** with different lengths were produced by treating solutions of **MeO-PBI$_{agg\ II}$** in an ultrasonic bath for various time intervals. Increasing the sonication time from 2 to 10 min led to a decrease in the length of the seeds of **MeO-PBI$_{agg\ II}$** from 55 – 200 nm (2 min) to 45 – 170 nm (5 min) and 20 – 80 nm (10 min) as revealed by atomic force microscopy (Figure 66). However, the morphology, that is, the helical structure of the individual strands of the seeds, is similar to that of the polymer (**MeO-PBI$_{agg\ II}$**), and the UV/vis spectrum of **MeO-PBI$_{agg\ II\text{-}seed}$** also resembles that of freshly prepared **MeO-PBI$_{agg\ II}$**. The addition of **MeO-PBI$_{agg\ II\text{-}seed}$** (ratio 1:100, sonication time: 10 min) instantaneously induced the transformation of **MeO-PBI$_{agg\ I}$** into **MeO-PBI$_{agg\ II}$** (Figure 23), which indicates that polymers with controlled length and size dispersions can be

obtained. Thus, the seeded polymerization occurs without a lag time, and the transformation rate is remarkably higher than that of the spontaneous aggregation process. Stirring (400 rpm) the **MeO-PBI$_{\text{agg I}}$** solution is another option to accelerate the transformation of **MeO-PBI$_{\text{agg I}}$** into **MeO-PBI$_{\text{agg II}}$**, which, however, only occurs after an induction period of about 30 min, which is obviously needed for nucleation (Figure 23b).

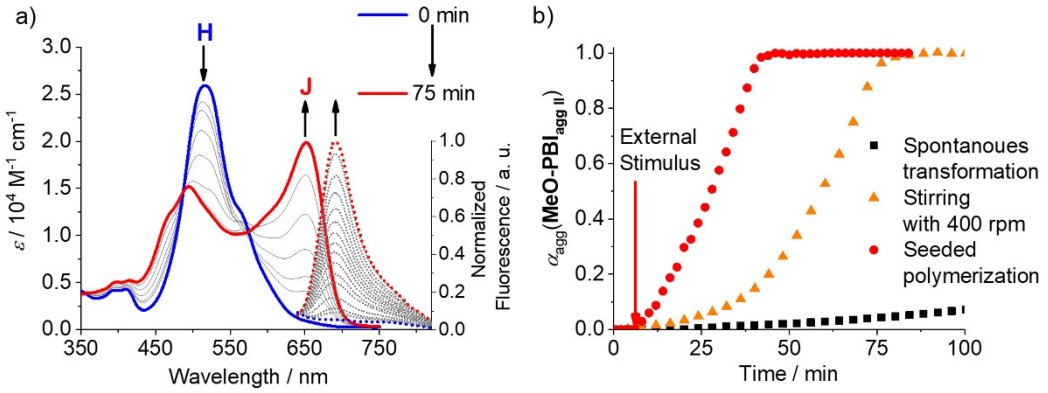


**Figure 23.** a) Time-dependent UV/vis absorption (solid lines) and emission spectra (dotted lines, $\lambda_{ex}$ = 487 nm) of the transformation from the H-aggregate **MeO-PBI$_{\text{agg I}}$** ($c_T = 15 \times 10^{-6}$ M) into J-aggregate **MeO-PBI$_{\text{agg II}}$** at 20 °C after addition of seeds **MeO-PBI$_{\text{agg II-seed}}$**. b) Plot of $\alpha_{agg}$(**MeO-PBI$_{\text{agg II}}$**) calculated from the apparent extinction coefficients at 655 nm against the time for the spontaneous transformation of **MeO-PBI$_{\text{agg I}}$** into **MeO-PBI$_{\text{agg II}}$** (black squares), after addition of seeds **MeO-PBI$_{\text{agg II-seed}}$** (red dots) and stirring during the measurement with 400 rpm (orange triangles).

Final proof for the living growth of the supramolecular polymer chain of **MeO-PBI** from the seed termini was obtained by UV/vis absorption spectroscopy in MCH/Tol (2:1, v/v), applying the experimental protocol illustrated in Figure 24a and Figure 52. For this purpose, 1 eq. of a freshly prepared solution of kinetically trapped **MeO-PBI$_{\text{agg I}}$** in this solvent mixture was added to 1 eq. of a solution of **MeO-PBI$_{\text{agg II-seed}}$** (sonication time: 10 min) at 20 °C. Upon mixing of these two stock solutions, supramolecular polymerization occurred instantaneously and was completed after a few minutes because of the high fraction of "active" seeds that function as initiators. Subsequently, 1 eq. of the supramolecular polymer solution obtained after the first cycle was removed to keep the overall volume of the sample constant. For a second cycle, another 1 eq. of **MeO-PBI$_{\text{agg I}}$** was added to the remaining polymer solution (1 eq.), which now acted as the seed for the subsequent polymerization cycle. This procedure was repeated for another three cycles. With this experiment, the living supramolecular polymerization process could be followed very easily by monitoring the apparent absorbance at 655 nm (absorption maximum of **MeO-PBI$_{\text{agg II}}$**) during the whole experiment and plotting the absorbance data against time (Figure 24b).

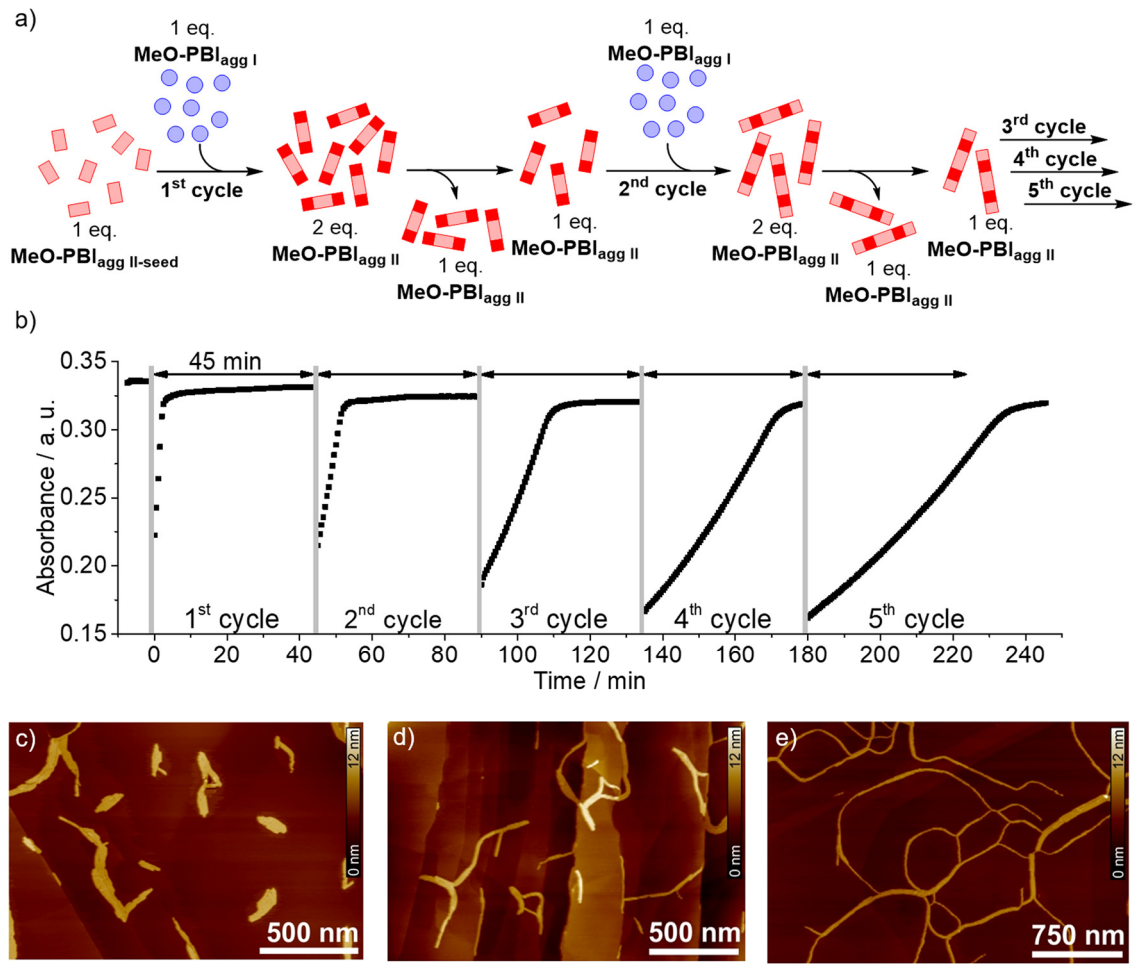


**Figure 24.** a) Stepwise living supramolecular polymerization process of **MeO-PBI**. b) Time-dependent changes in the apparent absorbance at 655 nm ($\lambda_{max}$ of **MeO-PBI$_{agg\ II}$**) during the living polymerization of **MeO-PBI**. The gray areas indicate the time taken for opening the sample compartment to add the respective equivalent of **MeO-PBI$_{agg\ I}$**. c-e) AFM height images of the supramolecular polymers (**MeO-PBI$_{agg\ II}$**) obtained after the first (c), second (d), and fourth cycle (e) prepared by spin-coating of the respective solutions on HOPG. The Z scale is 12 nm (c, d, e).

After the first addition of **MeO-PBI$_{agg\ I}$**, the apparent absorbance at 655 nm drops to 0.22, and subsequently a very fast seeded supramolecular polymerization process occurs, accompanied by an increase in the absorption, which nearly reaches the initial value of 0.33. This observation confirms the transformation of the kinetically trapped aggregates **MeO-PBI$_{agg\ I}$** into a "first-generation" thermodynamically stable polymer **MeO-PBI$_{agg\ II}$**. The polymers obtained after the first cycle can now act as the nuclei for the second cycle and so on. Interestingly, the rate of the polymerization into **MeO-PBI$_{agg\ II}$** becomes lower with increasing cycle number because the number of "active termini" of the seed is reduced by half after each cycle. The initial slopes of the graphs determined by fitting the respective first data points with a linear relationship are supportive of this conclusion. The values of the initial slopes can be fitted according to the exponential equation

$y = 0.0303\ \text{min}^{-1} \times (1/2)^{n-1}$ with cycle number $n$ (Figure 61), clearly showing that the values of the initial slopes are reduced by half for each cycle. Concomitantly, the fiber length should increase, which was confirmed by AFM. Indeed, AFM images of the samples prepared by spin-coating of the polymer solutions obtained after each cycle (Figure 24c-e and Figure 67) showed a successive increase in polymer length from 35 – 130 nm (1st cycle) to 50 – 300 nm (2nd cycle), 150 – 600 nm (3rd cycle), and extended micrometer-long polymer networks (4th and 5th cycles). These remarkable results clearly corroborate that the polymers **MeO-PBI$_{\text{agg II}}$** can indeed act as seeds for kinetically trapped **MeO-PBI$_{\text{agg I}}$** and that the formed polymers remain unchanged during the time course of our experiments. The results discussed above clearly reveal the living character of this supramolecular polymerization of **MeO-PBI**, which proceeds *via* a chain-growth mechanism from the fiber termini, through precise kinetic control of the aggregation process.

## 3.3 Conclusion

In conclusion, we have presented the first example of a living supramolecular polymerization leading to a fluorescent J-aggregate. This progress was enabled by the molecular design of a slightly core-twisted PBI that self-assembles preferentially into metastable off-pathway H-aggregates (**MeO-PBI$_{\text{agg I}}$**), which could be transformed into thermodynamically more stable fluorescent J-aggregates (**MeO-PBI$_{\text{agg II}}$**) by seed-induced living supramolecular polymerization. The experimental procedure developed for the living polymerization has potential for the construction of interesting functional supramolecular polymers and even supramolecular block copolymers, which may serve as highly promising architectures for the investigation of exciton and charge carrier transport phenomena on the nanoscale.

# Chapter 4

–

# Supramolecular Block Copolymers by Seeded Living Polymerization of Perylene Bisimides

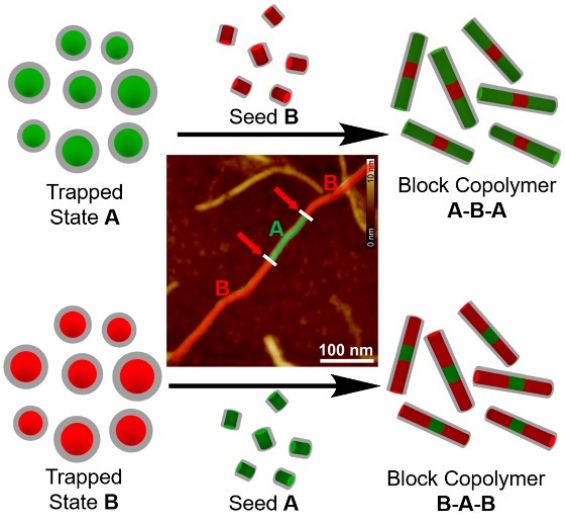


This Chapter was published in: W. Wagner, M. Wehner, V. Stepanenko, F. Würthner, *J. Am. Chem. Soc.* **2019**, *141*, 12044-12054.



**Abstract**: Living covalent polymerization has been a subject of intense research for many decades and has culminated in the synthesis of a large variety of block copolymers with structural and functional diversity. In contrast, the research on supramolecular BCPs is still in its infancy and their generation by living processes remains a challenge. Here we report the formation of supramolecular block copolymers by two-component seeded living polymerization of properly designed perylene bisimides under precise kinetic control. Our

detailed studies on thermodynamically and kinetically controlled supramolecular polymerization of three investigated PBIs, which contain hydrogen-bonding amide side groups in imide position and chlorine, methoxy, or methylthio substituents in 1,7 bay-positions, revealed that these PBIs form kinetically metastable H-aggregates, which can be transformed into the thermodynamically favored J-aggregates by seed-induced living polymerization. We show here that copolymerization of kinetically trapped states of one PBI with seeds of another PBI leads to the formation of supramolecular block copolymers by chain-growth process from the seed termini as confirmed by UV/vis spectroscopy and atomic force microscopy. This work demonstrates for the first time the formation of triblock supramolecular polymer architectures with A-B-A and B-A-B block pattern by alternate two-component seeded polymerization in a living manner.

## 4.1 Introduction

The discovery of living polymerization more than half a century ago launched a groundbreaking development in the field of conventional polymer chemistry.[1,3] This unique approach, which implies a controlled chain-growth polymerization of monomeric units into polymers of defined length and narrow polydispersity, enabled the synthesis of a myriad of block copolymers with unattainable levels of architectural complexity and functional versatility that find applications in different fields such as advanced materials and biological science.[2,4-9] The supramolecular counterpart of covalent polymers, i.e., supramolecular polymers, where monomeric building blocks are self-assembled into polymeric nanostructures by directional noncovalent interactions, constitute a younger class of materials albeit they experienced a tremendous development in the last two decades.[10,12-20,168-169] Supramolecular polymers are intrinsically of dynamic nature due to the reversible and weak interactions between the constituent subunits which imparts unique properties like self-healing and stimuli responsiveness.[13-20,169] Initially, supramolecular polymers were created under thermodynamic control, leading to concentration-dependent equilibrium structures with broad length distribution.[13,22,24-26] During the past decade, considerable focus has been given on the kinetically controlled self-assembly pathways that provide access to novel out-of-equilibrium supramolecular polymers.[20,28-41,105,112,170-171] Along this path, living supramolecular polymerization under kinetic control has recently been developed to achieve supramolecular architectures with controlled size and narrow polydispersity.[53,57-59,61-66,172] The insightful studies on living supramolecular

polymerization in recent years revealed that as prerequisite for this process a supramolecular system is needed, which follows the nucleation-elongation mechanism combined with a kinetically controlled pre-equilibrium to attain the highly required retardation of spontaneous polymerization that can be achieved either by properly designed *intra*molecular hydrogen-bonding of the monomeric states,[57-58,64] or by formation of competing metastable off-pathway aggregated states.[53,61-63,65-67] In such systems, the chain-growth supramolecular polymerization can be initiated either by addition of pre-prepared polymeric seeds, [53,57,61-67,172] molecular initiators,[58] or by a photoisomerization process.[59]

Despite significant knowledge has been accumulated on living supramolecular polymerization during the past few years, the noncovalent synthesis of supramolecular BCPs by a living process, analogous to covalent chain-growth polymerization, is still very challenging.[63,70-71] Manners, Winnik, and coworkers have pioneered the living self-assembly of covalent block polymers using fragmented crystalline cores as seeds for epitaxial growth process leading to one-dimensional cylindrical nanostructures with controlled lengths and low polydispersity.[45] Undoubtedly, this seminal work has nourished the development of living supramolecular polymerization of small molecules in recent years. More intriguingly, the authors have shown that living crystallization-driven self-assembly of large macromolecules with extended contact surface is a powerful tool to obtain a plethora of one,[45-46,48-49] two[52,73] and three-dimensional[50,158] supramolecular architectures. Moreover, the CDSA approach enables even the formation of unique multidimensional supermicellar nanostructures through hierarchical self-assembly of polymeric building blocks.[49-50,157-158] Block architectures of small molecules were also obtained by seeded coassembly of nanotubular segments,[75,160] or by the approach of dynamic combinatorial chemistry.[76] In the sparse examples of supramolecular BCPs of unimeric building blocks reported recently, the formation of block copolymers with A-B-A pattern has been achieved by kinetically controlled seeded polymerization employing specially designed solvent mixing protocols where different solvents were used for the seed preparation and the seeded polymerization mimicking the CDSA process.[70-71] Recently, Meijer, Palmans, and coworkers have reported the formation of supramolecular BCPs by copolymerization of triarylamin-based monomers under thermodynamic control.[77]

We have previously reported that copolymerization of a core-unsubstituted and a core-tetrasubstituted PBI leads to the formation of kinetically controlled supramolecular block

copolymers with alternating $A_mB_n$ patterns.[153] Recently, we have demonstrated seeded supramolecular polymerization of a core-unsubstituted PBI[57] and multicycle living polymerization of the core-disubstituted PBI derivative **MeO-PBI** (for structure see Figure 25a).[62] These results encouraged us to explore the synthesis of supramolecular BCPs by kinetically controlled seeded living polymerization of PBI building blocks bearing various bay-substituents at 1,7-postitions (Figure 25a). Here we report for the first time the formation of supramolecular BCPs with A-B-A and B-A-B block patterns by seed-induced living supramolecular polymerization of properly designed core-disubstituted PBI derivatives under precise kinetic control with seed preparation and chain-growth polymerization in the same solvent system. Although supramolecular BCPs of A-B-A pattern have been reported previously,[63,70-71] noncovalent synthesis of BCPs with A-B-A and B-A-B block patterns using the same pair of unimeric building blocks by inverted seeded living polymerization is to date unprecedented. Here we present the first examples of supramolecular BCPs with this alternate block pattern accomplished by seeded living polymerization of perylene bisimides.

## 4.2 Results and Discussion

### 4.2.1 Synthesis and Optical Properties of the Monomeric PBIs

We have previously reported seeded living supramolecular polymerization under kinetic control of PBI derivative **MeO-PBI** bearing two methoxy substituents at 1,7 bay-positions.[62] To explore the possibility for the formation of supramolecular block copolymers by two-component seeded polymerization, we have designed two new PBI derivatives that contain chloro (**Cl-PBI**) or methylthio substituents (**MeS-PBI**) at 1,7 bay-positions but contain identical imide substituents as **MeO-PBI** (Figure 25a). The new PBIs were synthesized according to the routes displayed in Scheme 4 (*cf. Chapter 8.2*). The detailed synthetic procedures and the characterization data of the new compounds are reported in the Appendix (*Chapter 8.2*). The UV/vis absorption spectra (Figure 25b) of the monomeric **Cl-PBI** and **MeS-PBI** were measured in $CHCl_3$ for comparison with **MeO-PBI**, and the optical properties of all three PBIs are summarized in the Appendix (*Chapter 8.2*, Table 3).

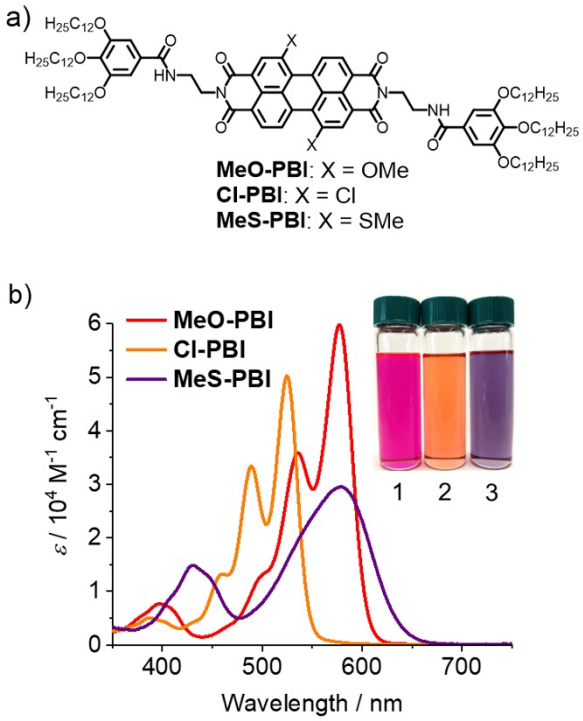


**Figure 25.** a) Structures of the core-disubstituted perylene bisimide dyes **MeO-PBI**, **Cl-PBI** and **MeS-PBI**. b) UV/vis absorption spectra of the monomeric PBIs in $CHCl_3$ ($c_T$ = 10 × $10^{-6}$ M) at 23 °C. Inset: Photograph of the solutions of **MeO-PBI** (1), **Cl-PBI** (2), and **MeS-PBI** (3) in $CHCl_3$.

### 4.2.2 Supramolecular Polymerization of the Unimolecular Building Blocks

First, we have studied the supramolecular polymerization properties of the new PBI derivatives **Cl-PBI** and **MeS-PBI** by temperature-dependent UV/vis spectroscopy. Similar to the previously reported **MeO-PBI**,[62] these PBIs form upon fast cooling (15 °C/min) of a monomeric solution from 90 to 20 °C kinetically trapped H-aggregates (Figure 26). Likewise, upon slow cooling (1 °C/min) the self-assembly of these PBIs affords the thermodynamically favored supramolecular polymers. Accordingly, in a 2:1 (v/v) solvent mixture of methylcyclohexane and toluene at a molar concentration of $c_T$ = 15 × $10^{-6}$ M, both new PBIs form the thermodynamically equilibrated J-type aggregates (denoted as **Cl-PBI$_{agg}$** and **MeS-PBI$_{agg}$**) similarly to **MeO-PBI**[62] as indicated by the bathochromic shift of the absorption maxima compared to that of the monomers (Figure 26).

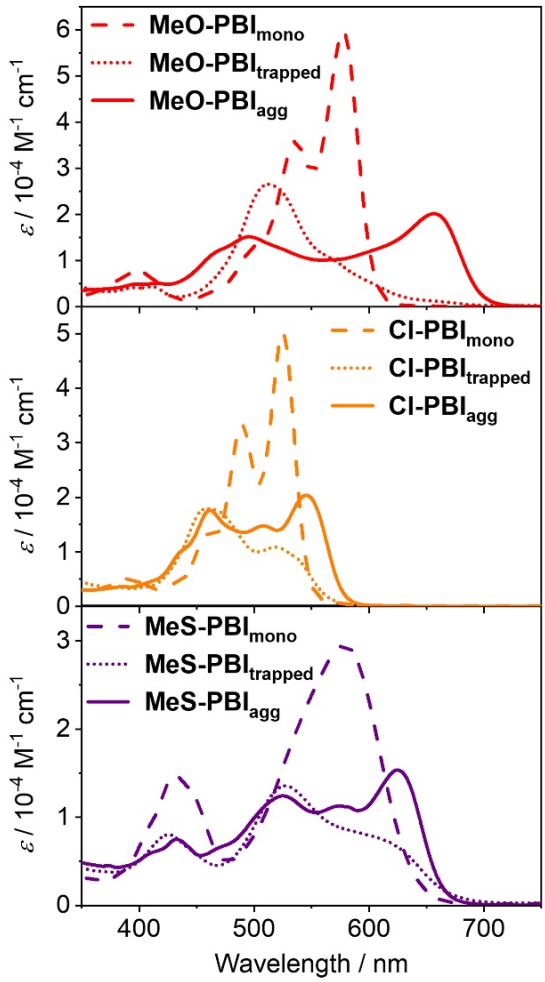


**Figure 26.** UV/vis absorption spectra of the monomeric PBIs in $CHCl_3$ ($c_T$ = 10 × $10^{-6}$ M, dashed lines), the kinetically trapped H-aggregates (dotted lines), and the thermodynamically equilibrated J-aggregates (solid lines) in MCH/Tol 2:1 (v/v, $c_T$ = 15 × $10^{-6}$ M) of **MeO-PBI** (top), **Cl-PBI** (middle) and **MeS-PBI** (bottom) at 23 °C.

Upon heating of a solution of these thermodynamically favored J-aggregates **Cl-PBI$_{agg}$** (Figure 27a) or **MeS-PBI$_{agg}$** (Figure 68) in MCH/Tol (2:1, v/v) from 10 to 90 °C with 1 °C/min, the disassembly into the monomeric species takes place. These heating processes occur under thermodynamic control, whereas the assembly of the monomeric species is by molecular design strongly influenced by kinetic effects. This is illustrated, e.g., by a shift of the critical temperature $T_e$ upon cooling a monomeric solution of **Cl-PBI** with varied cooling rates, while change of the heating rates has no effect on the disassembly of the aggregates (Figure 69). Therefore, reliable thermodynamic parameters could be obtained by analyzing the heating curves[53,57,63,124] rather than the cooling processes as previously applied for nucleation-growth self-assembly.[101-102] For both PBIs, the nonsigmoidal plots of the degree of aggregation against the temperature for varying total concentrations ($c_T$) in the range from 5 × $10^{-6}$ M to 25 × $10^{-6}$ M can be fitted very well by the cooperative

nucleation-elongation model (Figure 27b, Figure 68)[27,98,101-102] to obtain the elongation enthalpy $\Delta H_e$, the critical temperatures $T_e$, and the equilibrium constant of the activation step $K_a$ (Table 4, 5). From the decrease of the elongation temperatures upon dilution, the Gibbs free energy $\Delta G^0$ of the polymerization process can be obtained by van't Hoff analysis (Table 6). For **Cl-PBI** ($\Delta H_e$ = −83.3 kJ mol$^{-1}$, $\Delta G^0$ = −43.4 kJ mol$^{-1}$) and **MeS-PBI** ($\Delta H_e$ = −83.3 kJ mol$^{-1}$, $\Delta G^0$ = −43.7 kJ mol$^{-1}$) the elongation enthalpy as well as the Gibbs free energy are very similar to those of **MeO-PBI** ($\Delta H_e$ = −86.4 kJ mol$^{-1}$, $\Delta G^0$ = −44.0 kJ mol$^{-1}$).[62] Accordingly, the aggregates of these three core-disubstituted PBIs exhibit similar thermodynamic stability, which is a prerequisite for the self-assembly of supramolecular copolymers in the same solvent system.

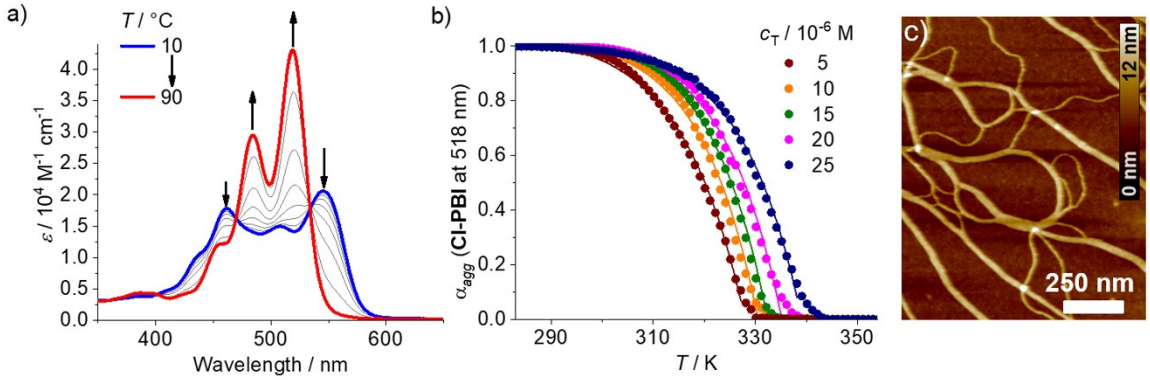


**Figure 27.** a) Temperature-dependent UV/vis spectra of **Cl-PBI** in MCH/Tol (2:1, v/v) upon heating from 10 to 90 °C with a rate of 1 °C/min ($c_T$ = 15 × 10$^{-6}$ M). b) Plots of the degree of aggregation, calculated from the apparent extinction coefficients at 518 nm, against the temperature and the respective fits of the elongation processes with the nucleation-elongation model for different total concentrations ($c_T$) from 5 × 10$^{-6}$ M to 25 × 10$^{-6}$ M. c) AFM height image of a sample prepared by spin-coating of the **Cl-PBI** aggregate solution ($c_T$ = 15 × 10$^{-6}$ M) in MCH/Tol (2:1, v/v) onto a silicon wafer. *Z* scale is 12 nm.

The morphologies of the aggregates formed by supramolecular polymerization of **Cl-PBI** and **MeS-PBI** in MCH/Tol (2:1, v/v) under thermodynamic control were characterized by atomic force microscopy. The AFM images of these samples prepared by spin-coating of the solutions onto silicon wafers showed the formation of helical fibers of both left- and right-handed helices that bundle into fibrous networks on the substrates (Figure 27c, Figure 70, 71). Since the diameter of the present PBI derivatives are identical as they possess the same imide substituents, the average height or width of the polymers of these PBIs is in the narrow range from 3.6 nm for **Cl-PBI** to 4.0 nm for **MeS-PBI** and **MeO-PBI**[62] (Table 7). Interestingly, the helical pitch of **Cl-PBI** nanofibers with a value of 10 nm differs strongly from that of **MeS-PBI** (5.0 nm) and **MeO-PBI** (5.0 nm). This would provide the

opportunity to characterize the respective blocks within BCPs consisting of **Cl-PBI** and **MeO-PBI** by AFM (*vide infra*).

### 4.2.3 Living Supramolecular Polymerization

For the precise kinetic control of a supramolecular polymerization process, detailed insight into the self-assembly pathways is crucial. Therefore, we have explored the effect of the varied bay-substituents on the kinetically controlled self-assembly of the individual PBIs by UV/vis spectroscopy. For the supramolecular polymerization of **Cl-PBI** and **MeS-PBI**, a comparable hysteresis between the cooling cycle (5 °C/min) and the heating cycle (1 °C/min) was observed with elongation temperatures of 30 and 45 °C for the cooling ($T_e$') and 59 and 80 °C for the heating ($T_e$) processes of **Cl-PBI** and **MeS-PBI**, respectively (Figure 72). For the previously investigated polymerization of **MeO-PBI**, a similar hysteresis between the cooling ($T_e$ = 40 °C) and the heating cycle ($T_e$ = 85 °C) was observed.[62] These results indicate the kinetically controlled formation of supramolecular species of the PBIs upon cooling with a distinct thermal stability. This kinetic effect has been elucidated by time-dependent UV/vis spectroscopic studies. Upon rapid cooling (ca. 15 °C/min) from 90 to 20 °C, both **Cl-PBI** and **MeS-PBI** ($c_T = 15 \times 10^{-6}$ M) form a kinetically metastable off-pathway H-aggregate (denoted as **Cl-PBI$_{trapped}$** and **MeS-PBI$_{trapped}$**) as indicated by strong hypsochromic shifts of the absorption maxima compared to those of the corresponding monomeric PBI dyes (Figure 26). These kinetically trapped states transform into the thermodynamically favored J-type aggregates within a time course of 30 min (for **Cl-PBI**) and 50 min (for **MeS-PBI**) at 20 °C (Figure 73). As reported previously,[62] **MeO-PBI** also forms kinetically trapped aggregates by *intra*molecular hydrogen bonding; however, the conversion time into the thermodynamically favored aggregates is drastically higher (7 h at 20 °C). The significant decrease of the kinetic stability of the trapped states of **Cl-PBI** and **MeS-PBI** compared to **MeO-PBI** might be explained based on the increasing sterical demand of the bay-substituents of the former PBIs which leads to a weakening of the $\pi$-$\pi$-interactions due to more distorted PBI cores (*vide infra*). The stability of **Cl-PBI$_{trapped}$** and **MeS-PBI$_{trapped}$** can be increased at lower temperature as the conversion of these trapped states into the thermodynamically favored aggregate can be slowed down from 30 to 220 min (**Cl-PBI**) and from 50 min to more than 200 min (**MeS-PBI**) by rapid cooling of the monomeric solution from 90 to 10 °C (15 °C/min), instead of 20 °C, revealing that this process is

indeed under kinetic control (Figure 73). Thus, for these two new PBIs, the spontaneous polymerization is, at least at 10 °C, sufficiently retarded and the stability of the kinetically trapped aggregate is strong enough to perform seed-induced living supramolecular polymerization experiments. For this purpose, seeds of **Cl-PBI** and **MeS-PBI** were produced by treating the solutions (MCH/Tol 2:1, v/v) of **Cl-PBI$_{agg}$** and **MeS-PBI$_{agg}$** ($c_T$ = 15 × 10$^{-6}$ M) in an ultrasonic bath for 30 min at 10 °C. The ultrasonication leads to a fragmentation of the aggregates into shorter seeds without changing the optical properties and the morphology compared to that of the freshly prepared supramolecular polymers. The addition of **Cl-PBI$_{seed}$** [molar ratio $c_T$(**Cl-PBI$_{seed}$**) : $c_T$(**Cl-PBI$_{trapped}$**) = 1:25] to the freshly prepared solution of **Cl-PBI$_{trapped}$** at 10 °C induced the transformation of **Cl-PBI$_{trapped}$** into **Cl-PBI$_{agg}$** instantaneously (Figure 28a), and the time for full conversion into the thermodynamically favored aggregate (ca. 20 min after seed addition) is drastically reduced compared to the spontaneous transformation (220 min). For a higher seed ratio (e.g., 1:10) the transformation into **Cl-PBI$_{agg}$** can be further accelerated (ca. 10 min), confirming that the seeds indeed act as nuclei for the polymerization process in a living manner (Figure 74).

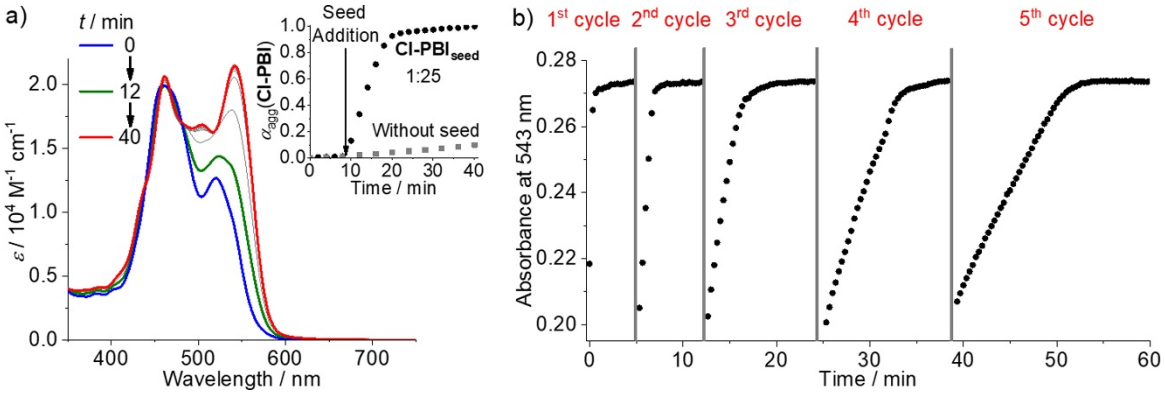


**Figure 28.** a) Time-dependent UV/vis spectra of the seed-induced supramolecular polymerization of **Cl-PBI** with **Cl-PBI$_{seed}$** in a molar seed ratio of 1:25 ($c_T$ = 15 × 10$^{-6}$ M, MCH/Tol 2:1, v/v). Inset: Plot of the degree of aggregation $\alpha_{agg}$ calculated from the apparent extinction coefficients at 543 nm of this seeded polymerization experiment (black dots) and of the spontaneous polymerization (gray squares) against the time. b) Time course of the apparent absorbance at 543 nm ($\lambda_{max}$ of **Cl-PBI$_{agg}$**) during multicycle living polymerization of **Cl-PBI** at 10 °C. The gray areas indicate the time for opening the sample compartment to add the respective equivalent of **Cl-PBI$_{trapped}$**.

To further substantiate the living growth of the supramolecular polymer of **Cl-PBI**, we performed a multicycle polymerization process by employing a recently developed experimental protocol.[62] In this experiment, 1 eq. of the kinetically trapped state **Cl-PBI$_{trapped}$** ($c_T$ = 15 × 10$^{-6}$ M) in MCH/Tol (2:1, v/v) was added to 1 eq. of **Cl-PBI$_{seed}$** at

10 °C. Upon addition of the seed solution, the polymerization proceeds instantaneously until full conversion into **Cl-PBI$_{agg}$** which takes only a few minutes due to the high molar fraction of seeds. After this first polymerization cycle, 1 eq. of the supramolecular polymers was removed to keep the sample volume constant. Subsequently, another 1 eq. of the kinetically trapped state **Cl-PBI$_{trapped}$** was added to the residual solution of supramolecular polymers acting now as the new seeds for the second cycle. This experimental protocol was repeated for several cycles, and the living supramolecular polymerization was studied by time-dependent UV/vis spectroscopy by measuring the apparent absorbance at 543 nm ($\lambda_{max}$ of **Cl-PBI$_{agg}$**). The seed-induced transformation of **Cl-PBI$_{trapped}$** into **Cl-PBI$_{agg}$** is clearly indicated by the increase of absorbance to about 0.27, and the polymers obtained in the respective previous cycle act as seeds for the following cycle (Figure 28b). This is in good agreement with a living chain-growth polymerization process. The transformation rate, which can be determined by fitting the respective first data points of the UV/vis measurements with a linear relationship, is reduced by each cycle (Figure 75). Since the number of "active" termini is by concept reduced by half, the initial slope of the transformation process is bisected for each cycle. Thus, the values of the initial slopes against the cycle number can be fitted very well with an exponential equation clearly proving that the transformation rate is bisected by increasing cycle number (Figure 75).

The model of Zhao and Moore[22] was previously applied to determine the rate constants of seeded polymerization of a PBI derivative that forms an equilibrium between two species, i.e., unimolecular monomeric trapped state and polymer.[57] However, this model cannot be applied for the present supramolecular systems as three states, i.e., kinetically trapped aggregate, monomer, and thermodynamically stable polymer, are involved in the equilibrium. Nevertheless, the seeded process follows a linear time dependency indicating that this process is indeed a one-dimensional supramolecular polymerization.[63]

For **MeS-PBI**, a similar living polymerization behavior as for **Cl-PBI** was observed in same solvent mixture (MCH/Tol, 2:1, v/v) at identical temperature (10 °C) and concentration ($c_T$ = 15 × 10$^{-6}$ M) by analogous UV/vis studies as described above (Figure 74, 75). The only difference being that the kinetic stability of the trapped state of **MeS-PBI** is notably higher than that of **Cl-PBI**. Importantly, the living polymerization behavior of these two new PBIs matches very well with that of the previously reported **MeO-PBI** what makes them excellent candidates for copolymerization with the latter to approach supramolecular block copolymers. Moreover, since all these PBIs show kinetically

controlled polymerization, they can be used either as seed or as the kinetically trapped state in two-component seeded polymerizations to achieve supramolecular BCPs.

### 4.2.4 Two-Component Seeded Living Polymerization

The basic concept for the noncovalent synthesis of supramolecular triblock copolymers under kinetic control is schematically illustrated in Figure 29. In this two-component seeded polymerization, the addition of polymeric seeds of B to the kinetically trapped state of A, which is produced by rapid cooling of the monomeric solution under kinetic control, would lead to the formation of block copolymers of A-B-A pattern with defined length and polydispersity. For a system, in which both compounds follow strictly the living polymerization behavior, the pattern of the BCP can be alternated to B-A-B type by adding seeds of A to kinetically trapped B. This approach should enable the control of the length of each individual polymer blocks by the amount of seeds.

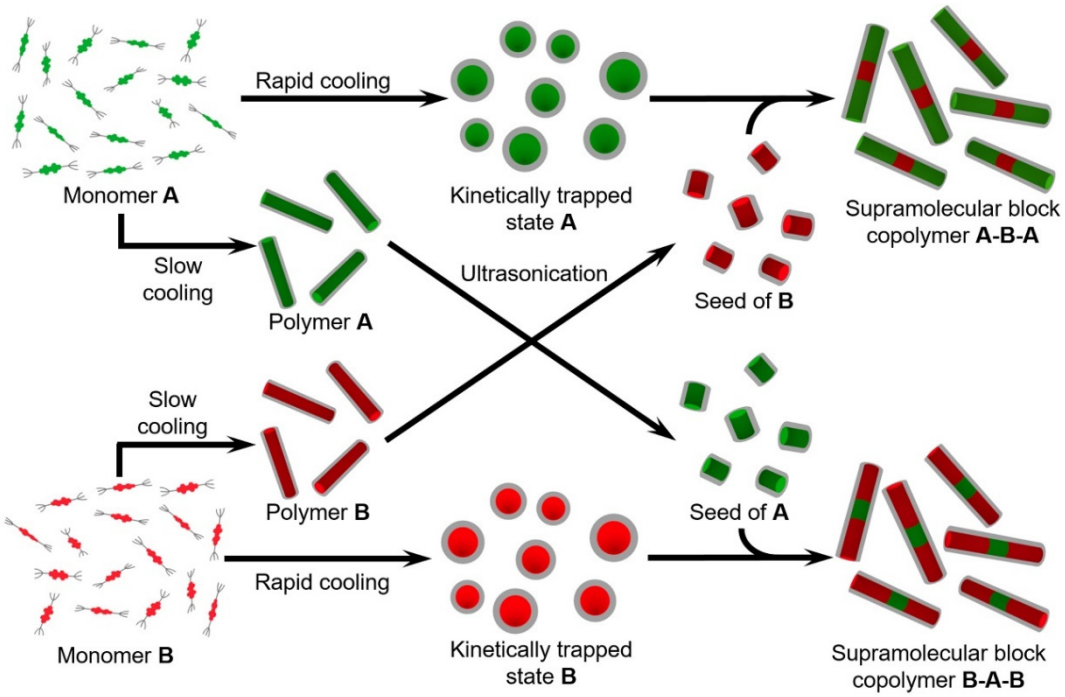


**Figure 29.** Schematic illustration of the two-component seeded living polymerization to obtain supramolecular triblock copolymers with A-B-A or B-A-B pattern under kinetic control.

### 4.2.5 Supramolecular Block Copolymers of A-B-A Type

First, we have studied the two-component seeded polymerization of the kinetically trapped **MeO-PBI$_{trapped}$** (species "A") and **Cl-PBI$_{seed}$** (species "B") under similar conditions used

for unimolecular living polymerization to achieve A-B-A type supramolecular BCPs applying the experimental protocol depicted in Figure 30.

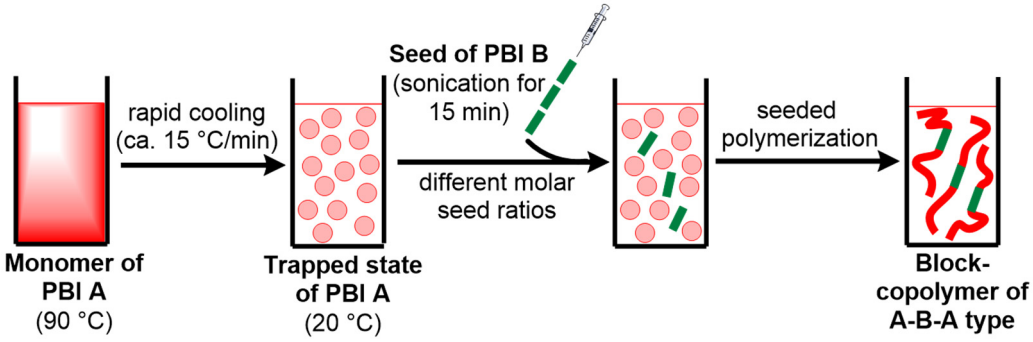


**Figure 30.** Schematic illustration of the experimental protocol of the two-component seeded copolymerization using the kinetically trapped state of **PBI A** and polymeric seeds of **PBI B**.

Thus, a solution of **MeO-PBI** ($c_T$ = 15 × $10^{-6}$ M) in MCH/Tol (2:1, v/v) was rapidly cooled to 20 °C with a cooling rate of ca. 15 °C/min to freshly produce the kinetically trapped state **MeO-PBI$_{trapped}$**. Subsequently, the seed solution of **Cl-PBI** in MCH/Tol (2:1, v/v) prepared by ultrasonication (*vide supra*) was added in a molar ratio of $c_T$(**Cl-PBI$_{seed}$**) : $c_T$(**MeO-PBI**) = 1:10 to initiate the copolymerization, and the process was monitored by time-dependent UV/vis spectroscopy (Figure 31a). The UV/vis measurement was started immediately after preparation of **MeO-PBI$_{trapped}$** ($t$ = 0 min), and the seed was directly added before measuring the spectrum at $t$ = 12 min to cross-check the kinetic trapping of **MeO-PBI$_{trapped}$**. Upon addition of **Cl-PBI$_{seed}$** to **MeO-PBI$_{trapped}$** with a seed ratio of 1:10, the transformation of the kinetically trapped **MeO-PBI** into the thermodynamically favored **MeO-PBI$_{agg}$** was induced instantaneously without a lag time as clearly indicated by the increase of the absorption at 650 nm ($\lambda_{max}$ of **MeO-PBI$_{agg}$**). In this seeded polymerization, the time for the full conversion into **MeO-PBI$_{agg}$** was drastically reduced (ca. 36 min) compared to the spontaneous transformation (7 h),[62] because the kinetic barrier caused by the nucleation event is circumvented by seed addition. Repeating the two-component seeded polymerization with a higher amount of seed, i.e., a molar ratio of **Cl-PBI$_{seed}$** and **MeO-PBI$_{trapped}$** of 1:5, leads to an acceleration of the supramolecular polymerization process (transformation time: 24 min), while decreasing of the seed ratio to 1:25 (96 min) or 1:50 (140 min) has the opposite effect as illustrated by the plot of the dilution corrected degree of aggregation against the time (Figure 31b). Most importantly, the transformation starts for all seed ratios immediately after seed addition and follows a linear relationship, indicating that the polymerization occurs at the active ends of the seed and there is almost no fusion of the polymers until a very high degree of

aggregation. To confirm that the minimal dilution of **MeO-PBI$_{trapped}$** with the seed solution and the presence of monomeric species of **Cl-PBI** have no effect on the seeded two-component polymerization, we have performed a control experiment according to the scheme illustrated in Figure 76. For this purpose, a mixture of **MeO-PBI** and **Cl-PBI$_{seed}$** in MCH/Tol (2:1, v/v) in a molar ratio of $c_T$(**Cl-PBI$_{seed}$**) : $c_T$(**MeO-PBI**) = 1:10 was first heated for 15 min at 90 °C to produce the monomeric state of both PBIs. Subsequently, the solution was rapidly cooled down to 20 °C at a cooling rate of 15 °C/min, and the time-dependent UV/vis studies were performed (Figure 77). In this experiment, the time course of the conversion of **MeO-PBI$_{trapped}$** into **MeO-PBI$_{agg}$** (Figure 31b, brown triangles) resembles exactly the spontaneous transformation process of the unimolecular **MeO-PBI** (Figure 31b, black squares).

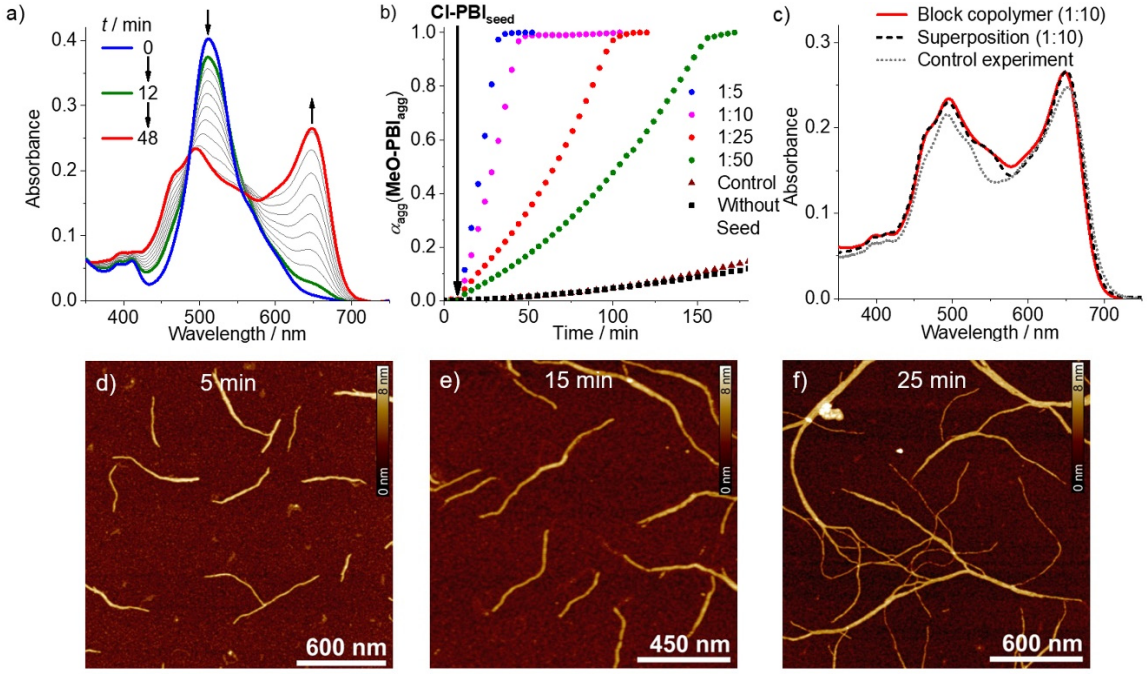


**Figure 31.** a) Time-dependent UV/vis spectra of the two-component seeded polymerization of **MeO-PBI$_{trapped}$** with **Cl-PBI$_{seed}$** seed ratio [$c_T$(**Cl-PBI$_{seed}$**) : $c_T$(**MeO-PBI$_{trapped}$**) = 1:10]. b) Plots of the degree of aggregation ($\alpha_{agg}$) of **MeO-PBI$_{agg}$**, calculated from the deconvoluted apparent extinction coefficient at 650 nm, against time upon addition of seed solution of **Cl-PBI** in ratios of $c_T$(**Cl-PBI$_{seed}$**) : $c_T$(**MeO-PBI$_{trapped}$**) = 1:5 (blue dots), 1:10 (purple dots), 1:25 (red dots) and 1:50 (green dots). The control experiment of a 1:10 mixture of **Cl-PBI** and **MeO-PBI** (brown triangles) and spontaneous polymerization of unimolecular **MeO-PBI** (black squares) are shown for comparison. c) UV/vis spectrum of the block copolymer [seed ratio $c_T$(**Cl-PBI$_{seed}$**) : $c_T$(**MeO-PBI**) = 1:10; red line] and superposition with the calculated spectrum in a ratio of **Cl-PBI** : **MeO-PBI** = 1:10 (black dashed line) and spectrum of the random copolymer in the control experiment (gray dotted line). AFM height images of samples prepared by spin-coating of the respective solutions onto silicon wafers taken at (d) 5 min, (e) 15 min and (f) 25 min after addition of **Cl-PBI$_{seed}$** to **MeO-PBI$_{trapped}$** in a seed ratio of 1:10.

This control experiment confirms that the minimal dilution with the solvent of the seed and even the kinetically trapped state of the seed has no influence on the supramolecular polymerization and that the copolymerization process is initiated only by the added aggregate seeds under kinetic control. Although the BCPs are formed in a kinetically controlled process, time-dependent UV/vis studies showed that the block structures are stable in solution for about 10 h (Figure 78). For further equilibration time, the BCPs precipitate out of solution and thus no transformation into a thermodynamically favored state can be observed.

For further confirmation of the block structure, we have analyzed the UV/vis spectra of the resulting block copolymers in more detail. Assuming that the heterojunction contact points between **MeO-PBI** and **Cl-PBI** in a supramolecular block structure are negligibly low compared to the extended $\pi$-stacks formed between the individual components, the spectrum of the BCP should be approximately the superposition of the individual J-aggregate spectra of the components in the respective ratios. Indeed, for the two-component seeded polymerization of **Cl-PBI** with **MeO-PBI** with a seed ratio of 1:10 the spectrum of the created BCP (Figure 31c, red line) nicely resembles the calculated superposition of **Cl-PBI$_{seed}$** and **MeO-PBI$_{agg}$** in a ratio of 1:10 (Figure 31c, black dashed line). The same holds true for a comparison of the respective spectra for varied seed ratios (Figure 79). Accordingly, the very characteristic bathochromic shift upon formation of **Cl-PBI** and **MeO-PBI** J-aggregates (Figure 26) due to excitonic coupling of the chromophores corroborates the presence of extended blocks in these supramolecular block copolymers. The very small deviation of the experimental spectra from the calculated superposition might be attributed to the neglected hetero $\pi$-$\pi$-stacking interaction between the two components at the boundaries of the polymeric blocks. Importantly, the spectrum of the polymer obtained from the monomeric mixture of **MeO-PBI** and **Cl-PBI** by spontaneous copolymerization deviates from that of the respective BCP and the calculated superposition (Figure 31c). Under these experimental conditions monomers of the individual PBI components are probably more randomly distributed or assembled in smaller blocks in statistical polymeric structures leading to a change of the excitonic coupling of the chromophores compared to BCPs.

The living nature of the seeded copolymerization of **Cl-PBI** and **MeO-PBI** was further confirmed by time-dependent AFM. The AFM images (Figure 31) of samples taken at (d) 5 min, (e) 15 min, and (f) 25 min after addition of **Cl-PBI$_{seed}$** to **MeO-PBI$_{trapped}$**

($c_T$ = 15 × $10^{-6}$ M, MCH/Tol, 2:1) in a seed ratio of 1:10 showed a successive increase of the length of the helical polymers from 300-600 nm (5 min) to 0.8-1.0 µm (15 min) and 1.5-3.0 µM (25 min). This length increase is caused by the living chain-growth polymerization of **MeO-PBI**, which can only occur at the "active" ends of the nanofibers. Furthermore, upon decreasing the seed ratio, the length of the block copolymers is increased confirming the living behavior of the supramolecular polymerization from the seed termini (Figure 80). Since the helical pitches of the polymers formed from **Cl-PBI** (10 nm) and **MeO-PBI** (5 nm) differ markedly (Table 7), we have analyzed the obtained BCPs in more detail by AFM. In AFM images taken after 5 min, the block structure of the polymers with connecting point of **Cl-PBI$_{seed}$** and **MeO-PBI$_{trapped}$** could be clearly observed (Figure 32, Figure 81) by a change in the helical pitch of the BCP. Particularly, in the phase image, the interconnection of helical aggregates with 10 nm (**Cl-PBI$_{seed}$**) and 5 nm helical pitch (**MeO-PBI$_{seed}$**) is distinctly visible (Figure 32b, red arrow).

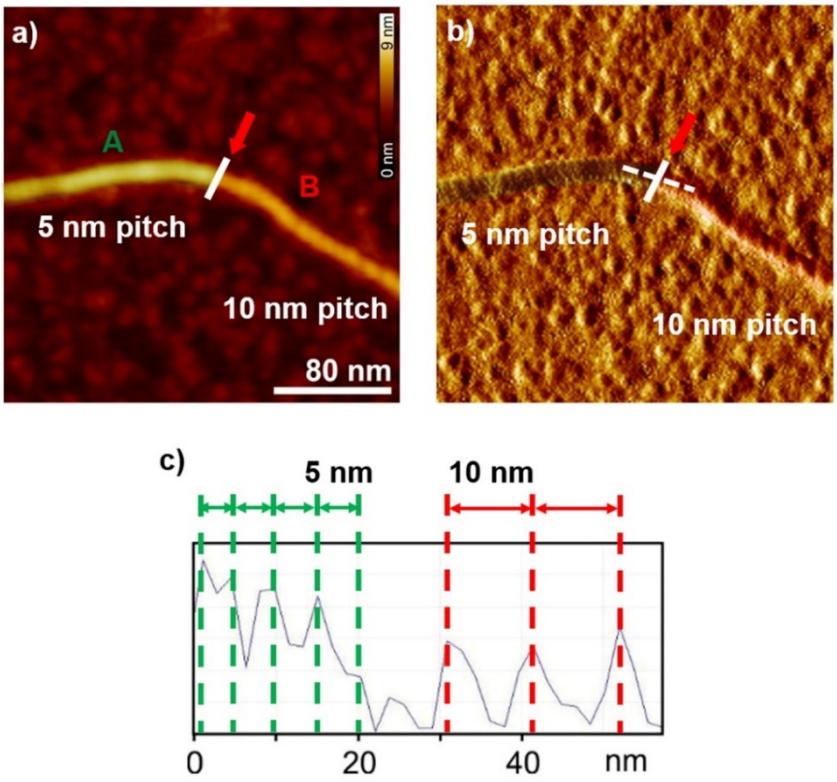


**Figure 32.** AFM height (a, Z-scale: 9 nm) and phase image (b) prepared by spin-coating of a solution in MCH/Tol (2:1, v/v) taken 5 min after addition of **Cl-PBI$_{seed}$** to **MeO-PBI$_{trapped}$** (seed ratio 1:10) onto silicon wafers. The red arrows indicate the position at which the helical pitch changes from 5 to 10 nm. Please note that for better visualization, the structures assigned to **MeO-PBI** and **Cl-PBI** are slightly colored with light-green and red, respectively. For the original AFM images, see Figure 81. c) Cross-section analysis along the dashed white line in phase image (b) demonstrating the change of the helical pitch from 5 to 10 nm.

Likewise, the AFM images of a sample taken at 10 min after seed addition showed the formation of a copolymer consisting of a block with 10 nm helical pitch, which corresponds to **Cl-PBI$_{seed}$**, and two blocks at both termini of the seed with a helical pitch of 5 nm each for **MeO-PBI$_{agg}$** (Figure 82). The heterojunction points of **MeO-PBI** and **Cl-PBI** at which the helical pitch changes from 5 to 10 nm can be clearly observed, especially in the cross-section analysis of the AFM phase image (Figure 82). This morphology corroborates the formation of A-B-A block copolymers through two-component seeded polymerization. However, for samples taken at longer times after seed addition (e.g., 25 min), the formation of larger polymeric strands and networks was observed probably caused by bundling and partial fusion of the block copolymers. Although a detailed analysis of the block structure for these polymeric networks is not possible by AFM, the heteroconnections of the seeds of **Cl-PBI** and **MeO-PBI$_{agg}$** in some part of the resulting nanofibers are still observable.

Further, we have studied the two-component seeded polymerization of **MeO-PBI$_{trapped}$** with **MeS-PBI$_{seed}$** by UV/vis spectroscopy under identical conditions as applied for the combination of **MeO-PBI$_{trapped}$** with **Cl-PBI$_{seed}$** and very similar results were obtained (Figure 83). Thus, we conclude that also for **MeS-PBI$_{seed}$**, respectively, supramolecular A-B-A block copolymers are formed. However, the block segments of BCPs formed with **MeS-PBI$_{seed}$** cannot be identified by AFM because the polymers of **MeO-PBI** and **MeS-PBI** exhibit the same helical pitch (5 nm). Nevertheless, the cross-seeding of **MeO-PBI$_{trapped}$** with seeds of **Cl-PBI** or **MeS-PBI** with a seed ratio of 1:10 exhibits a similar polymerization efficiency with a full conversion time of 36 and 40 min, respectively (Figure 84). These conversion times are notably higher compared to the self-seeding of **MeO-PBI$_{trapped}$** with **MeO-PBI$_{seed}$** (20 min). We hypothesize that a shape complementarity of the respective seeds with **MeO-PBI$_{trapped}$** is a prerequisite for the initiation of the supramolecular polymerization and that the twist angle of the PBI cores plays a major role. Thus, we calculated by geometry optimization of the monomeric building blocks with DFT calculations (Figure 85, Table 8) the dihedral angles for **Cl-PBI** (20.5°) and **MeS-PBI** (20°) in comparison to that of **MeO-PBI** (11.4°). The stronger core twist of **Cl-PBI** and **MeS-PBI**, apparently due to higher steric demand of the Cl and MeS substituents, may hamper the $\pi$-$\pi$-stacking and hydrogen-bonding supramolecular interactions between the "active" ends of the seeds and the kinetically trapped state **MeO-PBI$_{trapped}$**. Thus, the seed termini show a lower activity as nucleation catalysts, and

larger conversion time was required for the heteroseeding with **Cl-PBI** and **MeS-PBI** compared to self-seeding.

### 4.2.6 Supramolecular Block Copolymers of B-A-B Type

After successful preparation of supramolecular BCPs with **MeO-PBI** as kinetically trapped state and **Cl-PBI** or **MeS-PBI** as seeds, we have addressed the question whether seeding with **MeO-PBI$_{seed}$** (A) would also be possible. By concept, such a dual function as seed and trapped state in two-component seeded polymerization should lead to a switching from A-B-A to B-A-B type supramolecular BCPs (Figure 29). However, such double function of a building block in seeded supramolecular polymerization has never been reported. As mentioned before, **Cl-PBI** forms a kinetically trapped state in the same solvent mixture as **MeO-PBI**. Accordingly, **Cl-PBI** is a potential candidate (B) for an inverted two-component seeded polymerization. Indeed, our UV/vis studies showed that the addition of **MeO-PBI$_{seed}$,** which was prepared by ultrasonication for 30 min, to kinetically trapped **Cl-PBI**, created by rapid cooling from 90 to 10 °C in MCH/Tol (2:1, v/v), in a molar ratio of $c_T$(**MeO-PBI$_{seed}$**) : $c_T$(**Cl-PBI$_{trapped}$**) = 1:10 leads to a very fast transformation (ca. 12 min) of **Cl-PBI$_{trapped}$** into **Cl-PBI$_{agg}$** without a lag time (Figure 33a,b). Surprisingly, the transformation into **Cl-PBI$_{agg}$** upon addition of **MeO-PBI$_{seed}$** is almost as efficient as the self-seeding of **Cl-PBI$_{trapped}$** with **Cl-PBI$_{seed}$** with a seed ratio of 1:10 but much faster than the two-component seeded polymerization of **MeO-PBI$_{trapped}$** with **Cl-PBI$_{seed}$** (Figure 86). This is due to higher kinetic stability of **MeO-PBI$_{trapped}$** than that of **Cl-PBI$_{trapped}$** as shown before by the time-dependent UV/vis experiments of these PBIs (Figure 73). Similarly to the two-component seeded polymerization of **MeO-PBI$_{trapped}$** with **Cl-PBI$_{seed}$,** the inverse polymerization starts instantaneously after addition of **MeO-PBI$_{seed}$** to **Cl-PBI$_{trapped}$** and is strongly dependent on the molar ratio of **MeO-PBI$_{seed}$** (Figure 33b). Compared to the two-component seeded polymerization with a seed ratio of 1:10, the time for full conversion into the block copolymer is decreased to 8 min for a higher seed ratio (1:5) and increased to 26 and 40 min for lower seed ratios (1:25, 1:50, respectively), but in all these cases, the polymerization is strongly accelerated compared to the control experiment and the spontaneous process (216 min). The UV/vis spectrum of the resulting polymer with a 1:10 seed ratio (Figure 33c, red line) resembles very well with the calculated superposition of individual spectra of **MeO-PBI$_{seed}$** and **Cl-PBI$_{agg}$** in a ratio of 1:10 (Figure 33c, black dashed line). The same holds true for a comparison of the respective spectra for

varied seed ratios (Figure 87). Moreover, the spectrum of the polymer obtained from a heated mixture of **MeO-PBI** and **Cl-PBI** (1:10) monomers by the control experiment (Figure 33c, gray dotted line, Figure 88) showed a strong deviation from that of the polymer formed by two-component seeded polymerization and the calculated superposition. In the spectrum of the control polymer, particularly the band at 650 nm ($\lambda_{max}$ of **MeO-PBI** J-aggregate) is almost completely vanished, indicating that in this case **MeO-PBI** is not surrounded by its own and is randomly distributed in undefined statistical polymeric nanostructures with **Cl-PBI**.

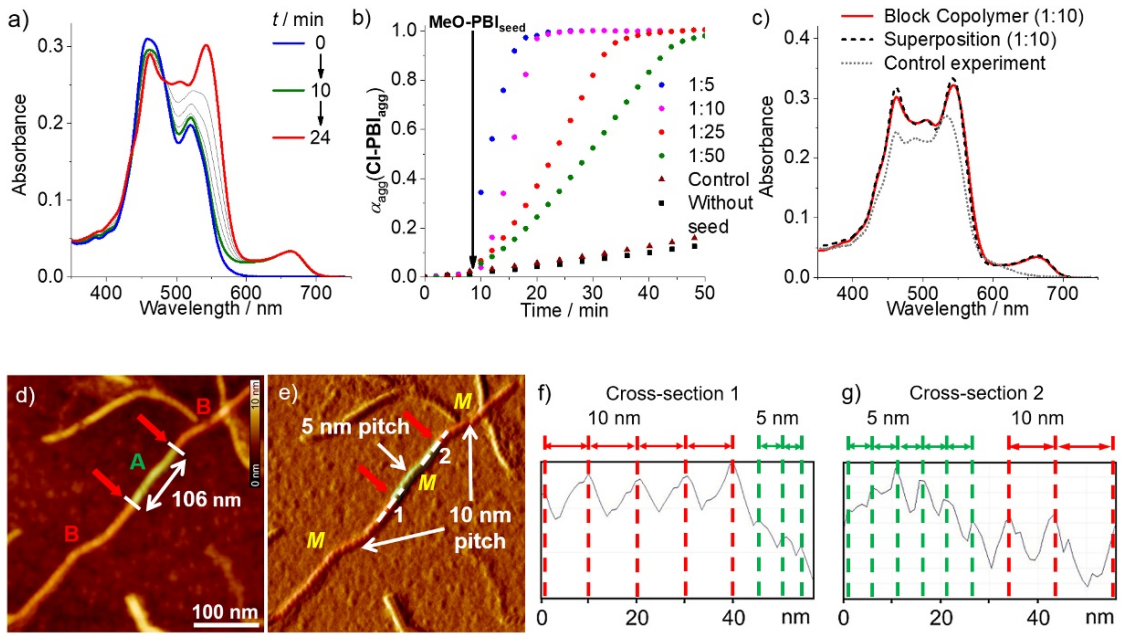


**Figure 33.** a) Time-dependent UV/vis spectra of the two-component seeded polymerization of **Cl-PBI$_{trapped}$** with **MeO-PBI$_{seed}$** (seed ratio: 1:10) in MCH/Tol (2:1, v/v) at 10 °C. b) Plots of the degree of aggregation ($\alpha_{agg}$) of **Cl-PBI$_{agg}$**, calculated from the deconvoluted apparent extinction coefficient at 543 nm, against the time upon addition of **MeO-PBI$_{seed}$** solutions in ratios of $c_T$(**MeO-PBI$_{seed}$**) : $c_T$(**Cl-PBI$_{trapped}$**) = 1:5 (blue dots), 1:10 (purple dots), 1:25 (red dots) and 1:50 (green dots). The control experiment with 1:10 mixture of **MeO-PBI** and **Cl-PBI** (brown triangles) and the spontaneous polymerization of unimolecular **Cl-PBI** (black squares) are shown for comparison. c) UV/vis spectrum of the block copolymer (seed ratio $c_T$(**MeO-PBI$_{seed}$**) : $c_T$(**Cl-PBI**) = 1:10; red line), superposition of the calculated spectrum in a ratio of **MeO-PBI** : **Cl-PBI** = 1:10 (black dashed line) and spectrum of the mixed polymer in the control experiment (gray dotted line). AFM height (d) and phase images (e) of a sample prepared by spin-coating the solutions taken 4 min after addition of **MeO-PBI$_{seed}$** to **Cl-PBI$_{trapped}$** onto silicon wafers. The red arrows indicate the position in the aggregate, where the helical pitch changes from 5 nm to 10 nm. In the images (d) and (e), the blocks assigned to **MeO-PBI$_{seed}$** (light-green) and **Cl-PBI$_{agg}$** (red) are marked in color for visualization. In the phase image (e) the helicity (*M*) of an individual block copolymer is indicated. For original AFM images, see Figure 91. Cross-section analysis along the dashed white lines in the (e) image demonstrating the change of the helical pitch from (f) 10 to 5 nm (cross-section 1) and from (g) 5 to 10 nm (cross-section 2).

The random copolymerization of the monomeric mixture of **MeO-PBI** and **Cl-PBI** (ratio 1:10) upon cooling from 90 to 10 °C is also indicated by AFM analysis as only the formation of aggregates with the helical pitch of **Cl-PBI** (10 nm), which was used in excess, was observed (Figure 89). All the above-described results show that block polymers are also formed in the inverse two-component seeded polymerization of **Cl-PBI$_{trapped}$** with **MeO-PBI$_{seed}$**. The formed B-A-B block copolymers are stable in solution about 20 h as indicated by time-dependent UV/vis spectroscopy (Figure 90). After that time period, the BCPs start to precipitate probably caused by bundling and fusion of the polymeric strands.

Further evidence for the formation of B-A-B block copolymers was obtained by AFM studies. The AFM image of a sample of two-component seeded polymerization (seed ratio 1:10) taken 4 min after addition of **MeO-PBI$_{seed}$** to **Cl-PBI$_{trapped}$** showed the presence of block copolymers comprising of a segment with a helical pitch of 5 nm and a length of 106 nm, which corresponds to the seed of **MeO-PBI**, and two segments (length: 160 and 260 nm) at both ends of the seed each having a helical pitch of 10 nm for **Cl-PBI$_{agg}$** (Figure 33d, Figure 91). The points at which the helical pitch changes from 10 to 5 nm (red arrows) can be clearly observed, especially, in the phase image of the block copolymer (Figure 33e) and by cross-section analysis of the image (Figure 33f,g).

This morphology confirms the B-A-B pattern of the supramolecular block copolymer formed by seeded polymerization of **Cl-PBI$_{trapped}$** with **MeO-PBI$_{seed}$**. In the AFM images of a sample taken 8 min after seed addition not only an increase of the length of the formed BCPs but also the same B-A-B block pattern was observed (Figure 92). In that sample, one block consisting of **MeO-PBI$_{seed}$** (helical pitch of 5 nm) with a length of 140 nm and two blocks of **Cl-PBI** (helical pitch of 10 nm) at the termini with a length of 250 and 300 nm, respectively, were observed. The helicity of the blocks formed by a chain-growth process at the termini of the seed is obviously determined by the handedness of the seeds, which were used as a racemic mixture of left- and right-handed helices that are formed from achiral monomers. Thus, both seed (block A) and the two terminal helical blocks (block B) of one BCP show identical helicity in the AFM images (Figure 33e and Figure 91, 92). These observations corroborate again the living nature of the polymerization of **Cl-PBI$_{trapped}$** with **MeO-PBI$_{seed}$** and the formation of B-A-B triblock copolymers. Notably, after a longer time (e.g., 60 min) of polymerization, the BCPs start to form more extended networks through fusion and bundling of the individual polymeric strands. Nevertheless, AFM studies confirm the stability of the individual blocks incorporated into the polymeric

network as already indicated by time-dependent UV/vis spectroscopy of the copolymerization (*vide supra*). Thus, in AFM images of a sample taken 60 min after seed addition blocks comprising of the respective PBIs can be identified by the helical pitch (Figure 34).

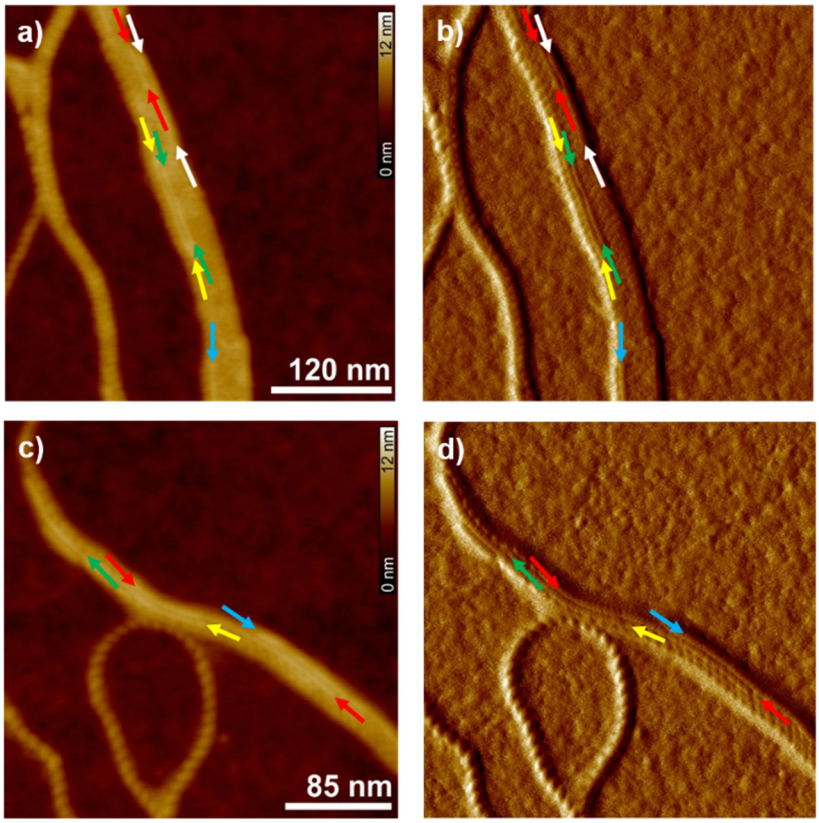


**Figure 34.** AFM height (a,c) and phase (b,d) images of a sample prepared by spin-coating a solution in MCH/Tol (2:1, v/v) taken at 60 min after addition of **MeO-PBI$_{seed}$** to **Cl-PBI$_{trapped}$** (seed ratio 1:10) onto silicon wafers. The Z scale is 12 nm (a,c). The arrows indicate the position in the supramolecular polymer where the helical pitch changes to 5 nm. The blocks comprising of **MeO-PBI$_{seed}$** (helical pitch: 5 nm) that belong to the same polymeric strand are marked with arrows of identical color.

Since the formation of A-B-A block copolymers from **MeO-PBI$_{trapped}$** and **MeS-PBI$_{seed}$** could be shown (*vide supra*), we have finally explored the two-component seeded polymerization with **MeS-PBI$_{trapped}$** and **MeO-PBI$_{seed}$** to assess the possibility for the formation of respective B-A-B block copolymers. UV/vis spectroscopic studies of the system **MeS-PBI$_{trapped}$** and **MeO-PBI$_{seed}$** under identical conditions as applied for the seed-induced polymerization of **Cl-PBI$_{trapped}$** with **MeO-PBI$_{seed}$** revealed very similar behavior as observed for the latter system (Figure 93), which suggest the formation of B-A-B block copolymers by two-component seeded polymerization of **MeS-PBI$_{trapped}$** and **MeO-PBI$_{seed}$**.

Our detailed investigation on seeded supramolecular polymerization of a set of PBI building blocks with twisted PBI $\pi$-scaffold have convincingly shown that the synthesis of supramolecular block copolymers is achievable by two-component seeded living polymerization of small molecules under kinetic control. In contrast to the crystallization-driven self-assembly approach of Manners and Winnik, in which macromolecular block copolymer building blocks were used as unimers, the here reported supramolecular block copolymers consist of unimolecular monomers. Thus, the obtained supramolecular polymeric nanofibers have much smaller dimensions than the micellar architectures obtained by the CDSA approach. Furthermore, in contrast to CDSA where in general different solvents (good and poor) were used for the seed preparation and copolymerization, in our approach both processes were conducted in the same solvent system which enables the switching of the block pattern from A-B-A to B-A-B that is unprecedented to date.

## 4.3 Conclusion

We have explored the supramolecular copolymerization of three PBI derivatives bearing identical hydrogen-bonding imide groups but different substituents at the 1,7 bay-positions. Our studies revealed that these PBIs form kinetically metastable *intra*molecular hydrogen-bonded H-aggregates, which can be transformed into the thermodynamically favored *inter*molecular hydrogen-bonded J-type aggregates by kinetically controlled seed-induced polymerization of the individual PBIs. The living nature of supramolecular polymerization of the three perylene bisimides **Cl-PBI**, **MeO-PBI**, and **MeS-PBI** has been demonstrated by multicycle seed-initiated polymerization. By utilizing this feature of living chain-growth supramolecular polymerization, we have achieved for the first time the formation of A-B-A supramolecular triblock copolymers of PBI dyes by a newly designed two-component seeded polymerization approach. Thus, we have shown that supramolecular block copolymers of both A-B-A and B-A-B sequence can be obtained from the same set of two building blocks by two-component seeded polymerization in the same solvent system for the seed preparation and chain-growth polymerization. The formation of such out-of-equilibrium supramolecular block copolymers can only be achieved by a precise kinetic control of the polymerization process. Our detailed analysis by UV/vis spectroscopy and atomic force microscopy suggests that this process is strongly dependent on the shape complementarity of the applied building blocks and that for the copolymerization a precise control of the kinetically trapped states is required. As we have shown that the approach of

living copolymerization is not limited to a special pair of PBI dyes, we envision that by multicomponent living supramolecular polymerization more complex supramolecular architectures with novel properties may become accessible.

# Chapter 5

–

# Impact of Molecular Shape on Supramolecular Copolymer Synthesis in Seeded Living Polymerization of Perylene Bisimides

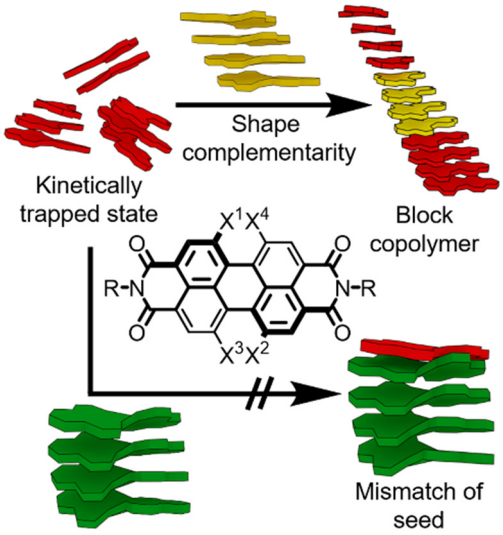


This Chapter was published in: W. Wagner, M. Wehner, V. Stepanenko, F. Würthner, *CCS Chem.* **2019**, *1*, *accepted article (September 2019)*.



**Abstract**: Supramolecular polymerization properties have been studied for a series of perylene bisimide dyes which contain identical hydrogen-bonding amide groups in imide positions but variable number or size of alkoxy substituents in bay-positions. Temperature- and time-dependent UV/vis and AFM studies revealed that the number and steric demand

of the alkoxy substituents in bay-positions has a strong impact on thermodynamically and more importantly on kinetically controlled supramolecular polymerization of these PBIs in solvent mixtures of methylcyclohexane and toluene. Our studies revealed that, in the case of core tri- and tetramethoxy substituted PBIs the kinetically controlled aggregation pathway is completely suppressed, whereas monomethoxy and 1,7-dialkoxy PBI derivatives form kinetically trapped species. The monomethoxy-substituted PBI can be successfully used in self-seeded chain-growth polymerization of monomeric building blocks under precise kinetic control to obtain supramolecular polymers with controlled length and low polydispersity. Two-component seed-induced living copolymerization of the present series of PBIs revealed that the formation of supramolecular block copolymers is only feasible for appropriate combinations of PBIs and that the seeding efficiency is strongly dependent on the shape complementarity of the applied individual components. Thus, seeded supramolecular polymerization and copolymerization of PBIs can be modulated by subtle changes of the molecular shape through a rational design of the monomers.

## 5.1 Introduction

Supramolecular polymerization has been a rapidly growing research field since two decades.[11,18-19,169,174] This development is fueled by the prospects to produce supramolecular materials for potential application in different fields such as material and biological sciences as they possess inherent functionalities like good processability, self-healing and stimuli responsiveness.[14-17,20-21,175] While initial studies of supramolecular polymerization mainly focused on the thermodynamic understanding,[13,22-26] recent studies have shown that in-depth insights into the kinetics and pathway complexity of self-assembly are essential to achieve precisely controlled formation of highly complex out-of-equilibrium supramolecular architectures.[17,20,32-42,105,176-177]

One intriguing recent development of kinetically controlled self-assembly is the living supramolecular polymerization, which leads to the formation of supramolecular polymers with controlled length and narrow size distribution.[54-56] The living supramolecular polymerization is a type of chain-growth process, in which the spontaneous polymerization of the monomeric building blocks is kinetically retarded either by formation of a dormant monomeric species through *intra*molecular hydrogen-bonding[57-59,64] or by a

pre-equilibrium with a competing off-pathway aggregated state.[53,60-63,65-67,172] The polymerization process of such supramolecular systems can be initiated either by addition of preformed small polymeric seeds acting as nuclei,[53,57,60-67,172] or molecular initiators for the chain-growth process.[58] An intriguing recent development of kinetically controlled seeded supramolecular polymerization is the noncovalent synthesis of highly desirable supramolecular block copolymers.[70,72,167] Inspired by the pioneering work of Manners, Winnik and coworkers on living crystallization-driven self-assembly of covalent block copolymers,[45,48,50,73] such supramolecular architectures of unimeric building blocks were achieved by multistep synthesis of nanotubular segments,[75] by the approach of dynamic covalent chemistry,[76] thermodynamically controlled coassembly,[77] or seed-induced copolymerization.[70-71,167] Despite all these highly appreciable developments, the rational design of monomeric building blocks for supramolecular polymerization and particularly for living polymerization and copolymerization is still very challenging because even slight changes in the molecular structure, e.g., an increase of the size of peripheral alkyl substituents, can strongly change the supramolecular polymerization behavior.[60,63,66]

In our recent studies, we could widen the scope of living supramolecular polymerization on the highly versatile and functional class of PBIs[78-79,178] by demonstrating seeded polymerization of core-unsubstituted PBI (**H-PBI**)[57] and living polymerization of core 1,7-dimethoxy-substituted PBI (**1,7-MeO-PBI**) into fluorescent J-aggregates.[62] Furthermore, supramolecular block copolymers of 1,7-disubstituted PBIs with A-B-A or B-A-B block pattern have been achieved very recently by two-component seeded copolymerization under kinetic control.[167] It is well known that the introduction of substituents in bay-area of PBIs leads to a distortion of the PBI core due to steric constraints[78,178-179] and thus by variation of bay-substituents the optical and the electronic properties of PBI dyes can be modulated.[180-182] Although several studies have previously shown that the variation of the core-twist angles of PBIs by introducing different bay-substituents has also a pronounced influence on the thermodynamically controlled aggregation processes,[78,183-185] i.e., lowering of the aggregation constants upon increasing twist angles[183] or changes in the molecular arrangements of the self-assemblies,[183-185] the effect of bay-substituents on kinetically controlled supramolecular polymerization has not been studied to date. Therefore, to explore the impact of bay-substituents on the kinetically controlled supramolecular polymerization and copolymerization, we have investigated a

series of PBI dyes bearing identical hydrogen-bonding amide side groups but variable number or size of alkoxy substituents in bay-positions (Chart 3).

Here we report that both number and size of bay-substituents decisively effect the kinetically controlled supramolecular polymerization pathways of the PBI dyes in solvent mixtures of methylcyclohexane and toluene. Our studies revealed that variation of the bay-substituents drastically changes the stability of the kinetically metastable states due to twisting of perylene core imparted by the substituents, which can, on the one hand, lead to a completely thermodynamically controlled polymerization or, on the other hand, can be utilized for seeded polymerization of kinetically trapped monomers under precise kinetic control. Moreover, we demonstrate here how the molecular design of the monomeric units influences the ability to form supramolecular block copolymers by two-component seeded copolymerization of perylene bisimides. Our detailed studies showed that the shape complementarity of the seeds with the kinetically trapped state plays a decisive role in seeded living copolymerization process.

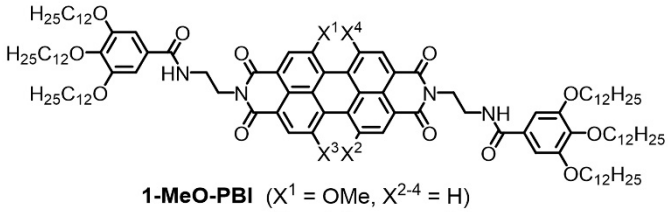


**1-MeO-PBI** ($X^1$ = OMe, $X^{2-4}$ = H)
**1,7-MeO-PBI**[a] ($X^{1,2}$ = OMe, $X^{3,4}$ = H)
**1,6,7-MeO-PBI** ($X^{1-3}$ = OMe, $X^4$ = H)
**1,6,7,12-MeO-PBI** ($X^{1-4}$ = OMe)
**1,7-EtO-PBI**[a] ($X^{1,2}$ = OEt, $X^{3,4}$ = H)
**1,7-*i*PrO-PBI**[a] ($X^{1,2}$ = O*i*Pr, $X^{3,4}$ = H)
**H-PBI** ($X^{1-4}$ = H): reference compound

**Chart 3.** Chemical structures of the investigated 1-monomethoxy (**1-MeO-PBI**), 1,7-dimethoxy (**1,7-MeO-PBI**),[62] 1,6,7-trimethoxy (**1,6,7-MeO-PBI**), 1,6,7,12-tetramethoxy (**1,6,7,12-MeO-PBI**), 1,7-diethoxy (**1,7-EtO-PBI**) and 1,7-diisopropyloxy (**1,7-*i*PrO-PBI**) bay-substituted PBIs and the structure of core-unsubstituted reference compound **H-PBI**.[57]
[a] In the following *Chapter 5* and the corresponding Appendix (*Chapter 8.3*), all the 1,7-disubstituted PBIs (**MeO-PBI**, **EtO-PBI**, ***i*PrO-PBI**) are denoted by indicating the positions of the substituents as **1,7-MeO-PBI**, **1,7-EtO-PBI** and **1,7-*i*PrO-PBI**, respectively, for a better clarity of this Chapter.

## 5.2 Results and Discussion

### 5.2.1 Synthesis and Molecular Properties

To investigate the effect of bay-substituent pattern on supramolecular polymerization and copolymerization of PBI dyes, we have synthesized a broad series of PBI derivatives that

bear identical imide side-groups but variable number or size of alkoxy substituents at bay-positions (Chart 3). The mono- (**1-MeO-PBI**), 1,7-di- (**1,7-MeO-PBI**), 1,6,7-tri- (**1,6,7-MeO-PBI**) and 1,6,7,12-tetramethoxy (**1,6,7,12-MeO-PBI**) substituted PBIs were synthesized in three steps starting from the respective perylene-3,4:9,10-tetracarboxylic acid tetrabutylesters[186-189] according to the route depicted in the Appendix (*Chapter 8.3*, Scheme 5). The 1,7-diethoxy (**1,7-EtO-PBI**) and 1,7-diisopropyloxy (**1,7-*i*PrO-PBI**) PBI derivatives were obtained from *N*,*N*'-dicyclohexyl-1,7-dibromoperylene-3,4:9,10-tetracarboxylic acid bisimide[190] according to the synthetic route shown in Scheme 6. The detailed synthetic procedures and the characterization data of all new PBI derivatives are reported in the Appendix (*Chapter 8.3*).

The optical properties of the monomeric PBIs were characterized by UV/vis and steady-state fluorescence spectroscopy in $CHCl_3$ ($c_T = 10 \times 10^{-6}$ M) at 23 °C. The absorption spectra of the monomers show the characteristic spectral features of alkoxy bay-substituted PBIs,[166,183] i.e., a loss of vibronic fine structure of $S_0$-$S_1$ transition compared to that of the core-unsubstituted **H-PBI** (Figure 35, Figure 104).[57] With increasing number of methoxy substituents in bay-positions, the absorption maximum is gradually red-shifted from 558 nm (**1-MeO-PBI**) to 577 nm (**1,7-MeO-PBI**), 600 nm (**1,6,7-MeO-PBI**) and 616 nm (**1,6,7,12-MeO-PBI**) with concomitant decrease of extinction coefficient (Figure 35, Table 9), while an increase of the alkyl chain length from methyl to ethyl and branched isopropyl group has almost no effect on the absorption maximum and extinction coefficient of the respective 1,7-alkoxy-substituted PBIs (Figure 104). The fluorescence spectra of the present PBIs revealed a similar trend as observed for their absorption spectra. With the increasing number of MeO substituents the emission maxima are increasingly red-shifted, while a small increase of chain length of the 1,7-alkoxy substituents has only minor effect on the fluorescence maxima (Figure 35, Figure 104). Notably, an increase in number of methoxy substituents at core leads to a strong increase of the fluorescence quantum yield ($\Phi_{fl}$) from 21% (**1-MeO-PBI**), 68% (**1,7-MeO-PBI**), 79% (**1,6,7-MeO-PBI**) to a maximum of 85% (**1,6,7,12-MeO-PBI**) concomitant with an increase of the fluorescence lifetimes of the respective PBIs (Table 9). This might be explained in terms of a decreasing electron affinity of the PBI core with increasing number of methoxy substituents, which leads to a suppression of the photoinduced electron transfer from the electron-rich aryloxy side groups in imide positions to the PBI core.[78,191]

The hydrogen-bonding properties of the core alkoxy-substituted PBIs were studied by Fourier-transform infrared (FT-IR) spectroscopy in $CHCl_3$ at room temperature. The FT-IR spectra of all PBIs of the present series display a N−H stretching band at around $\nu$(N−H) = 3400-3409 $cm^{-1}$ (Figure 105). These values are very similar to that of the core-unsubstituted reference **H-PBI** ($\nu$(N−H) = 3409 $cm^{-1}$).[57] However, the N−H stretching frequencies of these alkoxy-substituted PBIs are significantly shifted to lower wavenumbers compared with those of non-hydrogen bonded N−H groups appearing at around 3470-3430 $cm^{-1}$.[60,124] This shift clearly indicates the presence of *intra*molecular hydrogen bonds between the amide N−H and carbonyl group of the PBI core in the monomeric state.[60,62,124]

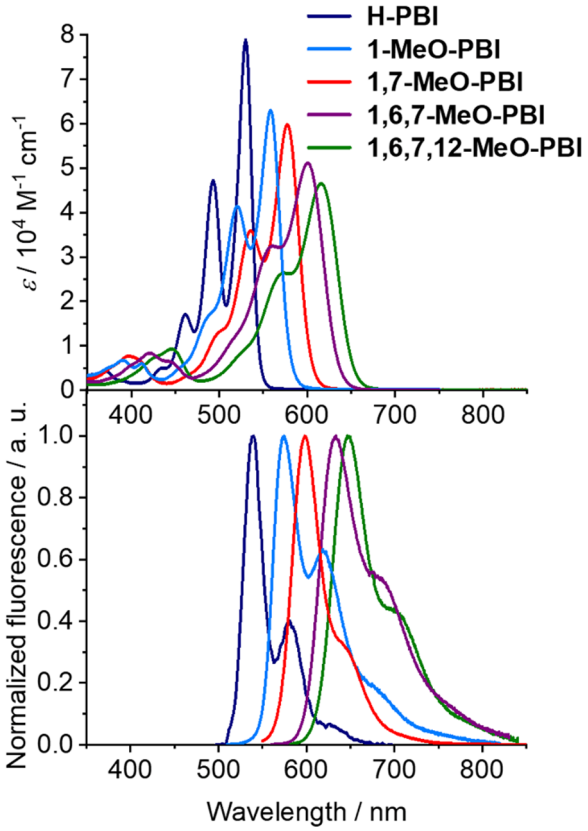


**Figure 35.** UV/vis absorption (top panel, $c_T = 10 \times 10^{-6}$ M) and fluorescence spectra (bottom panel, OD ≤ 0.05) of the monomeric **H-PBI** ($\lambda_{ex}$ = 490 nm),[60] **1-MeO-PBI** ($\lambda_{ex}$ = 500 nm), **1,7-MeO-PBI** ($\lambda_{ex}$ = 540 nm), **1,6,7-MeO-PBI** ($\lambda_{ex}$ = 550 nm) and **1,6,7,12-MeO-PBI** ($\lambda_{ex}$ = 570 nm) in $CHCl_3$ at 23 °C.

Next, we have explored the effect of different bay-substituents on the molecular geometry of the PBIs by DFT calculations. These studies revealed that increasing number of methoxy substituents leads to a strong increase of the twist angles $\alpha$ of the respective perylene core from 0°/0.7° (**1-MeO-PBI**) to 11.4° (**1,7-MeO-PBI**), 15.0°/29.9° (**1,6,7-MeO-PBI**) and

30.5° (**1,6,7,12-MeO-PBI**) due to increasing sterical constraints imposed by increasing number of bay-substituents (Figure 36 and Figure 106, Table 10). Notably, for **1-MeO-PBI** and **1,6,7-MeO-PBI** two different dihedral angles, respectively, are observed because of the unsymmetrical PBI cores. Moreover, the twist angles of **1,7-MeO-PBI**, **1,7-EtO-PBI** and **1,7-*i*PrO-PBI** are quite similar with values of 11.4°, 12.4° and 13.0°, respectively, indicating that small increase in alkyl chain length or branching has comparatively little effect on the core twist angle of the PBIs (Figure 107, Table 10). Furthermore, in the geometry optimized structures of the PBIs a very close distance between the amide hydrogens of the spacer unit and the carbonyl groups of the perylene core ($d$(N−H·····O=C) = 2.1-2.2 Å) is evident (Figure 36a, Figure 106 and 107) which is indicative of a formation of *intra*molecular hydrogen bonds of medium strength in the monomeric PBIs (Table 10). These findings corroborate the results of the FT-IR studies discussed above.

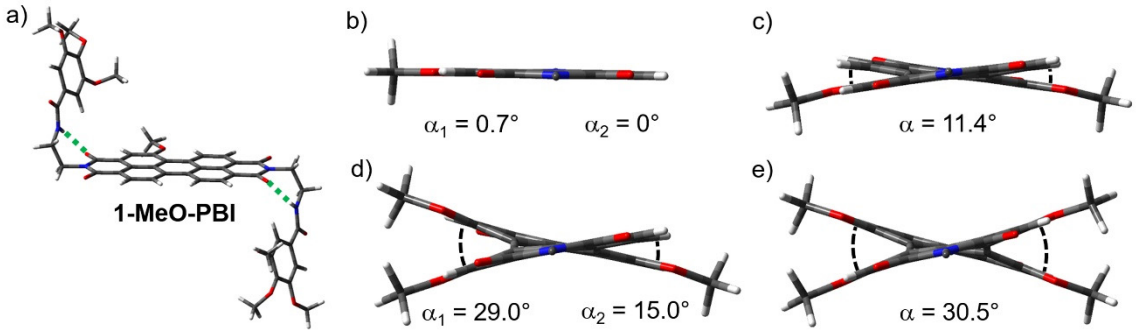


**Figure 36.** a) Side view of the DFT energy minimized structure of a model compound ($OC_{12}H_{25}$ residues are replaced by OMe) of **1-MeO-PBI** as an example. Green dashed lines indicate *intra*molecular hydrogen bonds. Molecular structure (view along the *N*-*N* axis) of the methoxy-substituted PBIs (b) **1-MeO-PBI**, (c) **1,7-MeO-PBI**, (d) **1,6,7-MeO-PBI** and (e) **1,6,7,12-MeO-PBI** obtained by energy minimization *via* DFT calculations. The imide substituents are omitted for better visualization of the twist angles $\alpha$ of the PBI core.

### 5.2.2 Thermodynamics of Supramolecular Polymerization

First, we have characterized the thermodynamically favored supramolecular polymerization of the present series of PBIs in a 2:1 (v/v) mixture of methylcyclohexane and toluene by UV/vis spectroscopy. Interestingly, in contrast to the 1,7-bay-substituted PBIs (**1,7-MeO-PBI, 1,7-EtO-PBI** and **1,7-*i*PrO-PBI)** which form J-type aggregates (denoted as **1,7-MeO-PBI$_{agg}$**, **1,7-EtO-PBI$_{agg}$** and **1,7-*i*PrO-PBI$_{agg}$**), other PBIs of the present series form typical H-type aggregates (denoted as **1-MeO-PBI$_{agg}$**,

**1,6,7-MeO-PBI$_{agg}$** and **1,6,7,12-MeO-PBI$_{agg}$**) (Figure 37). While the respective J-type aggregates show a sharp fluorescence band with an appreciably high fluorescence quantum yields (14-22%), the fluorescence of the H-aggregates is strongly quenched ($\Phi_{Fl} \leq 2\%$) (Figure 108, Table 12).

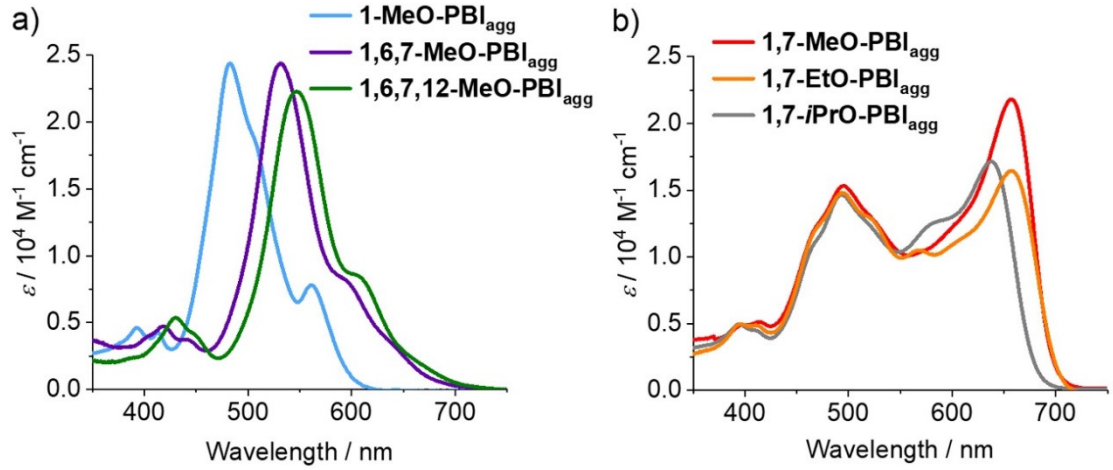


**Figure 37.** UV/vis absorption spectra of the thermodynamically favored aggregates in MCH/Tol (2:1, v/v) of (a) **1-MeO-PBI** ($c_T$ = 20 × 10$^{-6}$ M), **1,6,7-MeO-PBI** ($c_T$ = 20 × 10$^{-6}$ M) and **1,6,7,12-MeO-PBI** ($c_T$ = 200 × 10$^{-6}$ M) and (b) **1,7-MeO-PBI** ($c_T$ = 20 × 10$^{-6}$ M), **1,7-EtO-PBI** ($c_T$ = 20 × 10$^{-6}$ M) and **1,7-*i*PrO-PBI** ($c_T$ = 30 × 10$^{-6}$ M) at 23 °C.

For the determination of thermodynamic parameters, temperature-dependent UV/vis spectra of the respective disassembly processes were measured in the temperature range from 10 to 90 °C with a heating rate of 1 °C/min at varying concentrations (Figure 38a-c, Figure 109) since the respective cooling processes are kinetically influenced, like in the case of the previously reported **1,7-MeO-PBI**.[62] The thermodynamically controlled non-sigmoidal plots of the degree of aggregation $\alpha_{agg}$ of **1-MeO-PBI** (Figure 38d), **1,7-EtO-PBI** (Figure 38e), **1,7-*i*PrO-PBI** (Figure 109a,b) and **1,6,7-MeO-PBI** (Figure 109c,d) against the temperature for different total concentrations can be fitted very well by cooperative nucleation-elongation model[27,101] to obtain the elongation enthalpy $\Delta H_e$, the equilibrium constant of the activation step $K_a$ and the average nucleus size $\langle N_N(T_E)\rangle$ (Table 13-16). This analysis reveals that with increasing number of methoxy substituents the elongation enthalpy changes from −94.4 kJ mol$^{-1}$ (**1-MeO-PBI**) to −86.4 kJ mol$^{-1}$ (**1,7-MeO-PBI**)[62] and −72.3 kJ mol$^{-1}$ (**1,6,7-MeO-PBI**) which indicates a remarkably lower driving force for self-assembly than that of the core-unsubstituted reference **H-PBI** ($\Delta H_e$ = −108.1 kJ mol$^{-1}$).[57] Likewise, the increasing sterical demand of the substituents for twofold bay-substituted PBIs leads also to a decrease of the driving force with elongation enthalpies of −86.4 kJ mol$^{-1}$ (**1,7-MeO-PBI**),[62] −78.2 kJ mol$^{-1}$ (**1,7-EtO-PBI**) and

−64.0 kJ mol$^{-1}$ (**1,7-*i*PrO-PBI**). The Gibbs free energy $\Delta G^0$ of the supramolecular polymerization was determined by van't Hoff analysis of the decreasing elongation temperatures $T_e$ upon increasing total concentration $c_T$ (Figure 110).

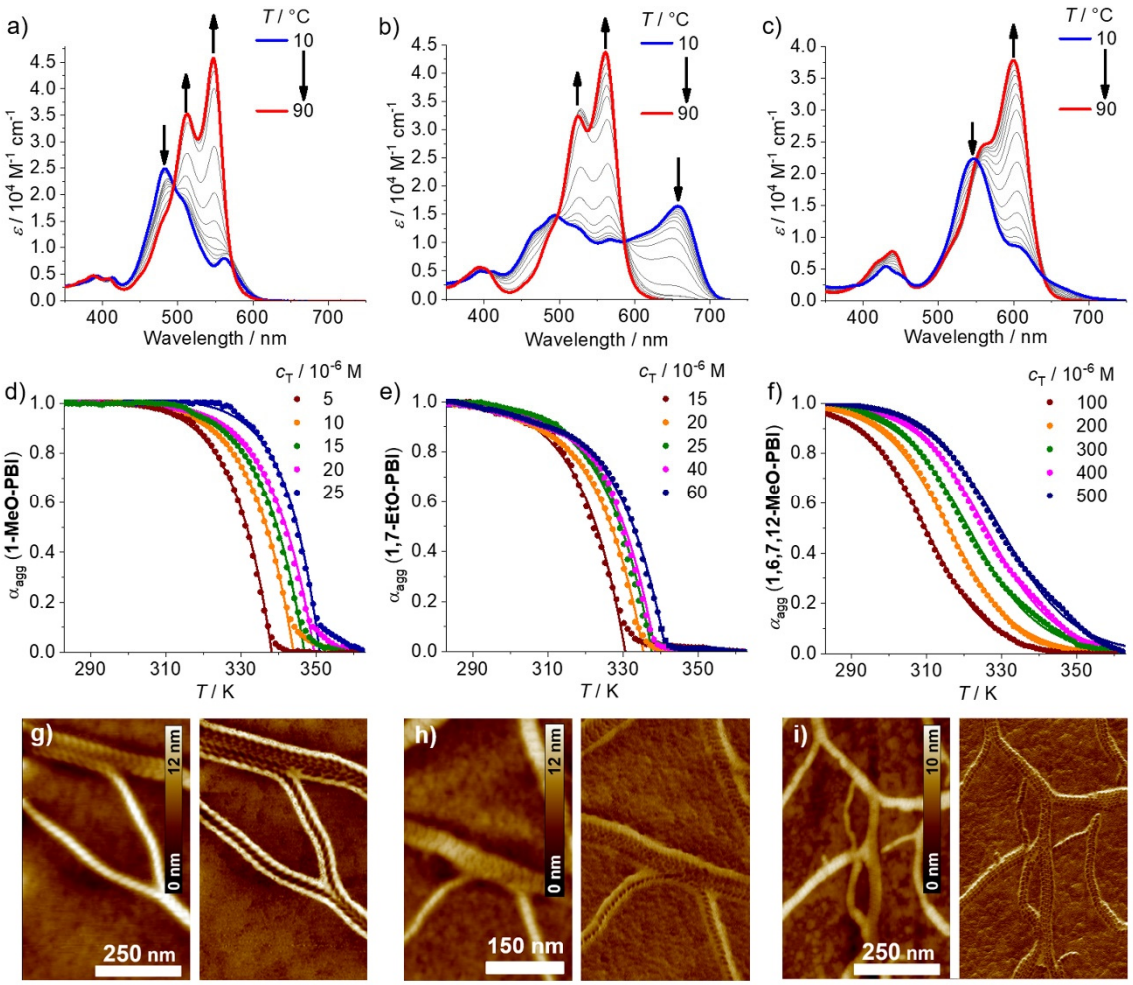


**Figure 38.** Temperature-dependent UV/vis spectra of (a) **1-MeO-PBI** ($c_T$ = 20 × 10$^{-6}$ M), (b) **1,7-EtO-PBI** ($c_T$ = 20 × 10$^{-6}$ M) and (c) **1,6,7,12-MeO-PBI** ($c_T$ = 200 × 10$^{-6}$ M) in MCH/Tol 2:1 (v/v) upon heating from 10 to 90 °C with a rate of 1 °C/min. Plots of the degree of aggregation ($\alpha_{agg}$), calculated from the apparent extinction coefficients at 548 nm (**1-MeO-PBI**), 561 nm (**1,7-EtO-PBI**) and 600 nm (**1,6,7,12-MeO-PBI**), against the temperature for the thermodynamically controlled disassembly processes and the respective fits of the elongation processes with the nucleation-elongation model for (d) **1-MeO-PBI** and (e) **1,7-EtO-PBI** or with the isodesmic model for (f) **1,6,7,12-MeO-PBI** at different total concentrations $c_T$. AFM height (left image, respectively) and phase (right image, respectively) images of samples prepared by spin-coating of aggregate solutions of (g) **1-MeO-PBI$_{agg}$** ($c_T$ = 20 × 10$^{-6}$ M), (h) **1,7-EtO-PBI$_{agg}$** ($c_T$ = 20 × 10$^{-6}$ M) and (i) **1,6,7,12-MeO-PBI$_{agg}$** ($c_T$ = 200 × 10$^{-6}$ M) in MCH/Tol (2:1, v/v) onto silicon wafers. The *Z* scale is 12 nm (g,h) and 10 nm (i).

Since the self-assembly is enthalpy-driven, for the $\Delta G^0$ values a similar trend compared to that of $\Delta H_e$ was observed. Thus, with increasing number of methoxy substituents $\Delta G^0$ values change from −47.2 kJ mol$^{-1}$ (**H-PBI**)[57] to −44.8 kJ mol$^{-1}$ (**1-MeO-PBI**),

−44.0 kJ mol$^{-1}$ (**1,7-MeO-PBI**)[62] and −35.2 kJ mol$^{-1}$ (**1,6,7-MeO-PBI**). Likewise, with increasing steric demand of the 1,7-bay-substituents $\Delta G^0$ values change from −44.0 kJ mol$^{-1}$ (**1,7-MeO-PBI**) to −39.5 kJ mol$^{-1}$ (**1,7-EtO-PBI**) and −33.8 kJ mol$^{-1}$ (**1,7-*i*PrO-PBI**). The observed decrease of the driving forces for the elongation is apparently provoked by the increase of the twist angle of the perylene core of the monomeric building blocks with increasing number or steric demand of alkoxy substituents as revealed by DFT calculations (*vide supra*).

In contrast to the previously discussed PBI derivatives, the self-assembly process of core-tetrasubstituted derivative **1,6,7,12-MeO-PBI** (Figure 38c,f) could not be fitted with the cooperative model as the only exception in the present series. However, this process can be properly described by the isodesmic model[13,27] to obtain the molar enthalpy release $\Delta H$ upon formation of the aggregate, the equilibrium constant $K$ and the Gibbs free energy $\Delta G^0$ (Figure 38f and Table 17). Since cooperativity in supramolecular polymerization is generally facilitated by multiple non-covalent interactions between monomeric building blocks,[24] the absence of cooperativity for the aggregation of **1,6,7,12-MeO-PBI** indicates that only one non-covalent interaction dominates in this case. The very strong core twist (30.5°) of this PBI derivative probably hampers the $\pi$-$\pi$-interactions, [78,183] which results in a non-cooperative isodesmic aggregation governed mainly by hydrogen-bonding. Indeed, poor $\pi$-$\pi$-interaction for the aggregation of **1,6,7,12-MeO-PBI** is corroborated by the drastically lower thermodynamic driving force ($\Delta G^0$ = −26.2 kJ mol$^{-1}$) of the polymerization compared to that of the other PBIs of the series (Table 18).

To confirm the involvement of *inter*molecular hydrogen-bonding in the supramolecular polymerization of these PBIs, FT-IR studies were performed in MCH/Tol (2:1, v/v) at a concentration of $c_T = 0.5 \times 10^{-3}$ M. In the FT-IR spectra of the supramolecular polymers N−H stretching vibrations ranging between 3250-3312 cm$^{-1}$ were observed (Figure 39). These N−H stretching frequencies correspond to the *inter*molecular hydrogen bonds between the N−H and the C=O groups of the amide side chains, [124] like in the case of reference **H-PBI**[57,60] and **1,7-MeO-PBI**.[62] However, upon increasing the number of methoxy substituents at bay-positions, the strength of the hydrogen bonding is clearly decreased as indicated by a shift of the N−H stretching vibrations to larger wavenumbers, i.e., higher energies (Figure 39). Nevertheless, the N−H stretching frequencies for the aggregates of all PBIs of the series are still in the same range indicating *inter*molecular hydrogen bonds of comparable strength. These results imply that the change of aggregation

strength of the present PBIs upon increasing the number of the core substituents is mainly caused by the weaker $\pi$-$\pi$-interactions between the PBI cores due to increased $\pi$-scaffold distortion and sterical congestion caused by the bay-substituents. It is well known for PBIs that the distortion of the perylene core has a significant impact on the *inter*molecular $\pi$-$\pi$-stacking interaction strength for aggregates in solution as well as in the solid state.[78,180,183] Furthermore, the strong effect of the $\pi$-$\pi$-interactions in the supramolecular polymerization is corroborated by the fact that upon increasing the steric demand of the bay-substituents of the 1,7-alkoxy substituted PBIs, the N−H stretching vibrations are hardly affected, while the aggregation strength is strongly reduced.

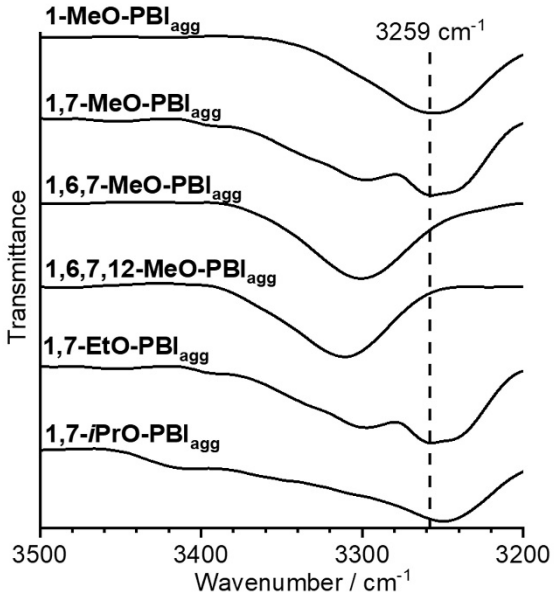


| | $\nu$(N−H) / cm$^{-1}$ |
|---|---|
| **1-MeO-PBI$_{agg}$** | 3255 |
| **1,7-MeO-PBI$_{agg}$**[62] | 3259 |
| **1,6,7-MeO-PBI$_{agg}$** | 3300 |
| **1,6,7,12-MeO-PBI$_{agg}$** | 3312 |
| **1,7-EtO-PBI$_{agg}$** | 3257 |
| **1,7-*i*PrO-PBI$_{agg}$** | 3251 |

**Figure 39.** N−H stretching regions of the FT-IR spectra of thermodynamically favored aggregates of **1-MeO-PBI**, **1,7-MeO-PBI**, **1,6,7-MeO-PBI**, **1,6,7,12-MeO-PBI**, **1,7-EtO-PBI** and **1,7-*i*PrO-PBI** in MCH/Tol (2:1, v/v) at a concentration of $c_T = 0.5 \times 10^{-3}$ M and comparison of the N−H stretching frequencies.

The morphologies of the aggregates formed by thermodynamically controlled supramolecular polymerization of core-alkoxy substituted PBIs were characterized by AFM. For this purpose, samples of the respective PBI aggregates were prepared by spin-coating of their solutions in MCH/Tol (2:1) onto silicon substrates. The AFM images of these samples showed the formation of helical nanofibers that bundle into fibrous networks on the substrates (Figure 38g-i, Figure 111-115). Since the different alkoxy substituents at bay-positions have almost no influence on the diameter of the PBI derivatives studied here, the average height of the polymeric strands of these PBIs is very similar with values between 3.8 and 4.4 nm (Table 19). However, the bay-substituents do have a substantial

effect on the helicity of the individual nanofibers as the helical pitch varies from 14 nm down to 5 nm depending on the bay-substituents (Table 19). The helical pitch of monomethoxy-substituted derivative **1-MeO-PBI** (14 nm) is very close to that of the core-unsubstituted reference **H-PBI** (15 nm)[57] which might be attributed to their structural similarity, i.e., both PBIs possess an (almost) flat perylene core (*cf.* DFT calculations). The dimethoxy- and trimethoxy-substituted derivatives, **1,7-MeO-PBI** and **1,6,7-MeO-PBI**, show significantly smaller helical pitches of 5.0 nm and 5.3 nm, respectively, while those of **1,7-EtO-PBI** (7.1 nm), **1,7-iPrO-PBI** (7.6 nm), **1,6,7,12-MeO-PBI** (8.9 nm) lie in between.

### 5.2.3 Kinetically Controlled and Single-component Seeded Supramolecular Polymerization

Once it has been confirmed that the variation of alkoxy bay-substituents of PBIs strongly effects the thermodynamic aggregation into one-dimensional nanofibers, we have explored the kinetically controlled supramolecular polymerization of the present PBI series by temperature-depended heating (1 °C/min) and cooling (5 °C/min) experiments monitored by UV/vis absorption spectroscopy. For **1-MeO-PBI** in MCH/Tol (2:1, v/v), a thermal hysteresis between the thermodynamically controlled disassembly process upon heating and the kinetically influenced cooling process was observed with an elongation temperature of 77 °C for the heating ($T_e$) and 67 °C for the cooling ($T_e$') cycle (Figure 40a).

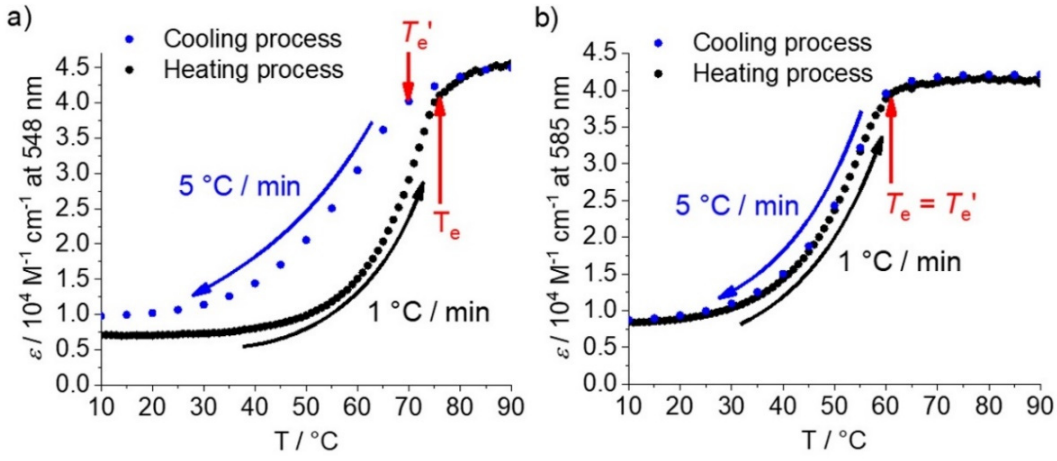


**Figure 40.** Temperature-dependent apparent extinction coefficients of (a) **1-MeO-PBI** at 548 nm and (b) **1,6,7-MeO-PBI** at 585 nm ($c_T$ = 20 × $10^{-6}$ M) in MCH/Tol (2:1, v/v) observed in the respective cooling (rate of 5 °C/min, blue dots) and respective heating (rate of 1 °C/min, black dots) processes.

For **1,7-EtO-PBI** ($T_e$ = 60 °C, $T_e$' = 40 °C) and **1,7-*i*PrO-PBI** ($T_e$ = 45 °C, $T_e$' = 25 °C), a similar hysteresis between the heating and the cooling cycle was revealed by the UV/vis studies, indicating the formation of a kinetically metastable supramolecular species, e.g., kinetically trapped monomer or kinetically trapped aggregate, upon self-assembly of the monomers (Figure 116). However, the hysteresis of above-mentioned PBIs is markedly smaller than that of **1,7-MeO-PBI** ($T_e$ = 85 °C, $T_e$' = 40 °C),[62] indicating a lower thermal stability of the kinetically trapped species of these PBIs compared with that of **1,7-MeO-PBI**. In contrast, for the tri- and tetra-substituted derivatives **1,6,7-MeO-PBI** ($T_e$ = $T_e$' = 60 °C, Figure 40b) and **1,6,7,12-MeO-PBI** (Figure 116c), the latter self-assembles *via* the isodesmic mechanism (*vide supra*), no hysteresis is observed, demonstrating that no kinetically trapped state is involved and that the polymerization of these PBIs is completely thermodynamically controlled under these experimental conditions (MCH/Tol = 2:1, v/v).

These results clearly confirm that the variation of the bay-substituents drastically influences the kinetically controlled aggregation pathways of the PBIs, i.e., the formation of kinetically trapped species is disfavored for the stronger core-twisted tri- and tetramethoxy substituted PBI derivatives with their lower $\pi$-$\pi$-interaction strength, while for the less core-distorted mono- and dimethoxy substituted PBIs as well as for **1,7-EtO-PBI** and **1,7-*i*PrO-PBI** kinetically controlled polymerization pathways are viable.

The kinetically controlled aggregation of **1,7-EtO-PBI** and **1,7-*i*PrO-PBI** was then further studied by time-dependent UV/vis spectroscopy. Upon rapid cooling (ca. 15 °C/min) from 90 to 20 °C, both PBIs form in MCH/Tol (2:1, v/v) kinetically metastable off-pathway H-aggregates which can be transformed into the thermodynamically stable J-type aggregates (Figure 117). Unfortunately, the time for the full conversion of the kinetically into the thermodynamically favored aggregates of **1,7-EtO-PBI$_{agg}$** (32 min) and **1,7-*i*PrO-PBI$_{agg}$** (24 min) is much shorter compared to that of **1,7-MeO-PBI$_{agg}$** (7 h).[62] This can be explained in terms of strongly reduced kinetic stability of the trapped aggregates of **1,7-EtO-PBI** and **1,7-*i*PrO-PBI** due to higher sterical demand of the bay-substituents and concomitantly decreased $\pi$-$\pi$-interaction strength which most likely also applies to the kinetically metastable aggregate. Since the stability of the kinetically metastable aggregates of these PBIs is too low and the transformation into the thermodynamically favored polymer starts without a lag time, they cannot be used – different from **1,7-MeO-PBI**[62] – as kinetically trapped states for seeded supramolecular polymerization.

The very small hysteresis observed for **1-MeO-PBI** in MCH/Tol (2:1, v/v) indicates also a very low stability of the kinetically trapped state and, accordingly, the conversion into the thermodynamically favored aggregate is too fast for a detailed study (Figure 118). Notably, similar as for the parent **H-PBI**,[57] this trapped state of **1-MeO-PBI** originates from a monomeric species with *intra*molecular hydrogen-bonds (Figure 36a) and not from an off-pathway aggregation product as in the case of 1,7-alkoxy-substituted PBIs. We have accordingly adjusted the solvent mixture towards decreased binding strength, i.e., a higher polarity environment where $\pi$-$\pi$-stacking and hydrogen-bonding interactions are weakened, and explored the kinetically controlled aggregation process of **1-MeO-PBI** in the optimized solvent mixture of MCH/Tol (1:2, v/v). By decreasing the content of the poor solvent (MCH) in this solvent system, the kinetic barrier for the supramolecular polymerization is increased because the driving force for the spontaneous nucleation of the kinetically trapped monomers is reduced. Accordingly, **1-MeO-PBI** forms in MCH/Tol (1:2, v/v, $c_T = 15 \times 10^{-6}$ M) upon cooling from 90 to 30 °C a kinetically trapped monomeric species (denoted as **1-MeO-PBI$_{trapped}$**) which is transformed into the thermodynamically stable **1-MeO-PBI$_{agg}$** within a now enhanced time course of 220 min (Figure 41a). An increase of the total concentration ($c_T$ = 20 or 30 × $10^{-6}$ M) accelerates the transformation time of **1-MeO-PBI$_{trapped}$** into **1-MeO-PBI$_{agg}$**, while decreasing the concentration ($c_T = 10 \times 10^{-6}$ M) slows down the supramolecular polymerization of the kinetically trapped state **1-MeO-PBI$_{trapped}$** (Figure 41b).

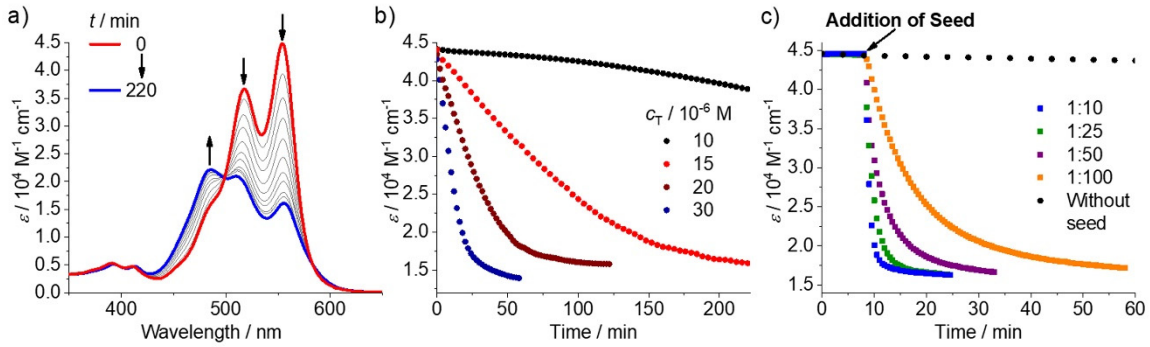


**Figure 41.** a) Time-dependent UV/vis spectra of **1-MeO-PBI** ($c_T = 15 \times 10^{-6}$ M) in MCH/Tol (1:2, v/v) after rapid cooling (ca. 15 °C/min) from 90 to 30 °C. b) Time course of the apparent extinction coefficients of **1-MeO-PBI** at 555 nm after rapid cooling from 90 °C to 30 °C for different total concentrations $c_T$ in MCH/Tol (1:2, v/v). c) Plots of apparent extinction coefficients of **1-MeO-PBI** against the time upon addition of **1-MeO-PBI$_{seed}$** solutions in molar ratios of $c_T$(**1-MeO-PBI$_{seed}$**) : $c_T$(**1-MeO-PBI$_{trapped}$**) = 1:10 (blue squares), 1:25 (green squares), 1:50 (purple squares) and 1:100 (orange squares). The spontaneous polymerization of **1-MeO-PBI** (black dots) is shown for comparison.

These results corroborate that **1-MeO-PBI** forms a kinetically trapped monomer by *intra*molecular hydrogen-bonding, which is in conformity with the FT-IR spectroscopic studies (*vide supra*), and that bimolecular association of **1-MeO-PBI$_{trapped}$** governs the nucleation kinetics and therefore the time for a full conversion into the thermodynamically favored aggregates. Accordingly, this transformation time is also strongly dependent on the temperature. Thus, cooling the monomeric solution from 90 to 25 °C or 20 °C accelerates the spontaneous polymerization resulting in a conversion time of ca. 150 min or 40 min, respectively (Figure 119). This reduction of the stability of the kinetically trapped state, which is illustrated through an acceleration of the spontaneous transformation of the kinetically trapped monomers into the thermodynamically favored aggregates, is due to a faster spontaneous nucleation process at lower temperatures. The formation of such kinetically trapped monomeric species was previously observed for core-unsubstituted **H-PBI**,[57] whereas **1,7-MeO-PBI**[62] and 1,7-alkoxy-substituted PBIs **1,7-EtO-PBI** and **1,7-*i*PrO-PBI** exhibit an alternative self-assembly pathway involving kinetically metastable off-pathway aggregates as kinetically trapped states.

Since the stability of the kinetically trapped state **1-MeO-PBI$_{trapped}$** in MCH/Tol (1:2, v/v) at a concentration of $c_T = 10 \times 10^{-6}$ M is high enough and the spontaneous aggregation is sufficiently retarded, we next explored the possibility of seeded supramolecular polymerization of **1-MeO-PBI**. For this purpose, seeds of **1-MeO-PBI$_{agg}$** (denoted as **1-MeO-PBI$_{seed}$**) were produced by applying ultrasonication to a solution of **1-MeO-PBI$_{agg}$** ($c_T = 15 \times 10^{-6}$ M) in MCH/Tol (1:2, v/v) for 30 min. The obtained seeds of **1-MeO-PBI** are with a length of ca. 50-150 nm much shorter than the polymeric nanofibers obtained by spontaneous polymerization as revealed by AFM (Figure 42).

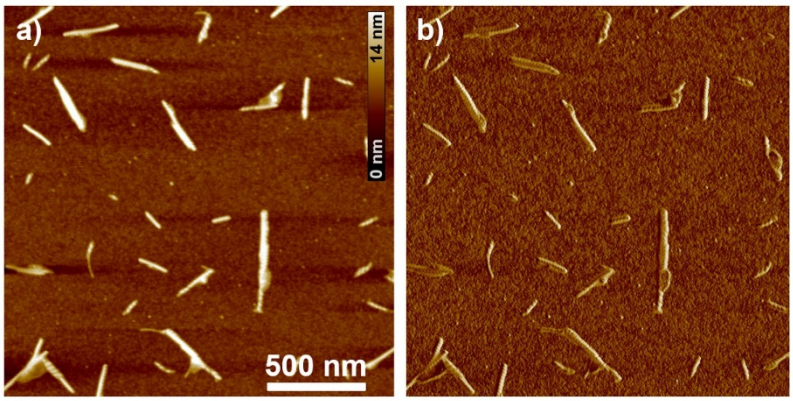


**Figure 42.** AFM height (a) and phase (b) images of **1-MeO-PBI$_{seed}$** prepared by spin-coating a solution of the polymeric seeds in MCH/Tol (1:2, v/v), produced by ultrasonication for 30 min, onto a silicon wafer. The *Z* scale is 14 nm.

However, the UV/vis absorption spectrum and the helical pitch of the seeds are identical with that of the polymeric nanofibers. Upon addition of **1-MeO-PBI$_{seed}$** at 30 °C to a freshly prepared solution of **1-MeO-PBI$_{trapped}$** (molar seed ratio $c_T$ (**1-MeO-PBI$_{seed}$**) : $c_T$(**1-MeO-PBI$_{trapped}$**) = 1:50), the polymerization into the thermodynamically stable **1-MeO-PBI$_{agg}$** is induced without a lag time in a much shorter transformation time of ca. 20 min (after seed addition) compared to the spontaneous process (Figure 41c). Upon increasing the seed ratio to 1:25 or 1:10, the transformation time into the **1-MeO-PBI$_{agg}$** can be further reduced to about 10 or 5 min, respectively, while decreasing of the seed ratio (1:100) leads to slower seeded polymerization process (ca. 50 min). Importantly, for all these experiments the polymerization is induced instantaneously after seed addition, indicating that the polymerization occurs at the "active" ends of the polymeric seeds by chain-growth polymerization in a living manner.[53,63,167] The seed-induced supramolecular polymerization behavior of **1-MeO-PBI** resembles that of **H-PBI**,[57] which can be attributed to the close structural similarity of these PBIs as both of them exhibit almost flat perylene cores according to DFT calculation and similar aggregate structures according their UV/vis absorption spectra (*vide supra*).

### 5.2.4 Two-component Seeded Supramolecular Copolymerization

Our recent studies have shown that the formation of supramolecular block copolymers of A-B-A type can be achieved by two-component seeded copolymerization of **1,7-MeO-PBI$_{trapped}$** with structurally similar 1,7-dichloro or 1,7-dimethylthio-substituted PBI derivatives. [167] Here, we explore in detail the seed-induced copolymerization of **1,7-MeO-PBI** with a large series of PBIs to elucidate the impact of molecular shape complementarity on such supramolecular block copolymer synthesis. To analyze the two-component seeded polymerization, we performed time-dependent UV/vis studies applying the experimental protocol schematically illustrated in Figure 43a.[167] The kinetically trapped state of **1,7-MeO-PBI** was produced by rapid cooling (ca. 15 °C/min) of the monomeric solution ($c_T = 15 \times 10^{-6}$ M) in MCH/Tol 2:1 (v/v) from 90 to 20 °C. Subsequently, the time-dependent UV/vis measurement was started ($t = 0$) to cross-check the stability of **1,7-MeO-PBI$_{trapped}$**. The freshly prepared seeds of the respective PBIs were added in appropriate molar ratios prior to taking the spectrum at $t = 10$ min.

In such a two-component seeded copolymerization experiment, the addition of **1,7-EtO-PBI$_{seed}$** in a molar ratio of 1:10 to the kinetically trapped state of **1,7-MeO-PBI** leads to a very fast transformation of **1,7-MeO-PBI$_{trapped}$** into the thermodynamically favored **1,7-MeO-PBI$_{agg}$** in about 34 min (Figure 43b) after seed addition which is much faster than the spontaneous polymerization of **1,7-MeO-PBI$_{trapped}$** (7 h). The full conversion into **1,7-MeO-PBI$_{agg}$** is accelerated by addition of **1,7-EtO-PBI$_{seed}$** in a higher seed ratio of 1:5 (20 min), while decreasing of the seed ratio to 1:25 (50 min) or 1:50 (80 min) has the opposite effect (Figure 43c). Importantly, in all these two-component seeded experiments the polymerization starts instantaneously after seed addition and follows a linear time-dependency, indicating that this process is indeed a one-dimensional supramolecular polymerization initiated by the seeds.[63,167]

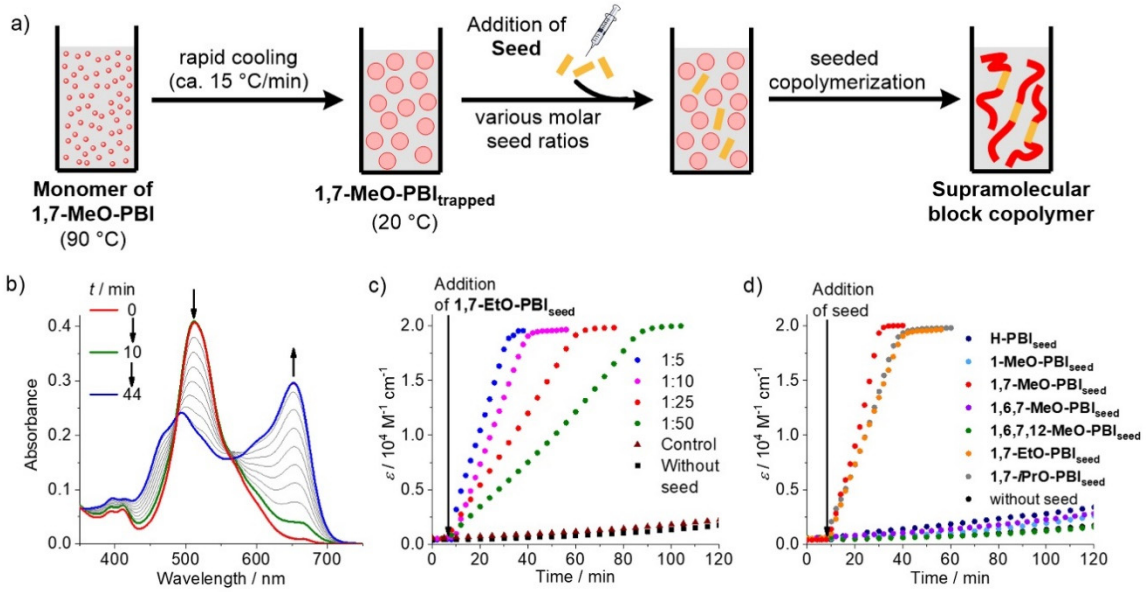


**Figure 43.** a) Schematic illustration of the two-component seeded copolymerization experiment. b) Time-dependent UV/vis spectra of the two-component seeded copolymerization of **1,7-MeO-PBI$_{trapped}$** ($c_T$ = 15 × 10$^{-6}$ M) with **1,7-EtO-PBI$_{seed}$** (seed ratio $c_T$(**1,7-EtO-PBI$_{seed}$**) : $c_T$(**1,7-MeO-PBI$_{trapped}$**) = 1:10 in MCH/Tol 2:1 (v/v) at 20 °C. c) Plots of the apparent extinction coefficients ($\varepsilon$) at 650 nm of **1,7-MeO-PBI$_{agg}$** against time upon addition of seed solutions of **1,7-EtO-PBI** in molar ratios of $c_T$(**1,7-EtO-PBI$_{seed}$**) : $c_T$(**1,7-MeO-PBI$_{trapped}$**) = 1:5 (blue dots), 1:10 (pink dots), 1:25 (red dots) and 1:50 (green dots). The control experiment of a 1:10 mixture of **1,7-EtO-PBI** and **1,7-MeO-PBI** (brown triangles) and spontaneous polymerization of unimolecular **1,7-MeO-PBI** (black squares) are shown for comparison. d) Plots of the apparent extinction coefficients at 650 nm of **1,7-MeO-PBI$_{agg}$** against the time upon addition of different seed solutions of **H-PBI** (dark blue dots), **1-MeO-PBI** (light blue dots), **1,7-MeO-PBI** (self-seeding, red dots), **1,6,7-MeO-PBI** (purple dots), **1,6,7,12-MeO-PBI** (green dots), **1,7-EtO-PBI** (orange dots) and **1,7-*i*PrO-PBI** (grey dots) to the kinetically trapped **1,7-MeO-PBI$_{trapped}$** with a ratio of $c_T$(seed) : $c_T$(**1,7-MeO-PBI$_{trapped}$**) = 1:10.

Furthermore, a control experiment was performed (schematically illustrated in Figure 120) in which the monomeric mixture of **1,7-EtO-PBI** and **1,7-MeO-PBI** in MCH/Tol (2:1, v/v)

with a molar ratio of 1:10 was rapidly cooled from 90 to 20 °C and monitored by time-dependent UV/vis spectroscopy. The time course of conversion of **1,7-MeO-PBI$_{trapped}$** into **1,7-MeO-PBI$_{agg}$** in this control experiment resembles very well the spontaneous polymerization process (Figure 43c). This behavior clearly confirms that the minimal dilution and the presence of monomeric **1,7-EtO-PBI** do not affect the polymerization and that the copolymerization is exclusively initiated through the active termini of the seeds. The living behavior of the two-component seeded copolymerization of **1,7-MeO-PBI$_{trapped}$** with **1,7-EtO-PBI$_{seed}$** was corroborated by time-dependent AFM studies (Figure 121). In the AFM images of samples taken at 5, 10, 20 and 30 min after addition of **1,7-EtO-PBI$_{seed}$** to **1,7-MeO-PBI$_{trapped}$** (seed ratio 1:10) a successive increase of the length of the polymeric nanofibers was observed from 100-400 nm (5 min) to 200-850 nm (10 min), 0.45-2.0 μm (20 min) and extended micrometer long polymer networks (30 min). This length increase is due to the living chain-growth of **1,7-MeO-PBI** which occurs only at the active termini of the polymeric seeds of **1,7-EtO-PBI**. These results confirm, accordingly, the formation of block copolymers of both PBIs. Unfortunately, different from our previous study,[167] the block segments cannot be identified by AFM because of the very similar helical pitches of the individual block segments.

For the two-component seeded copolymerization of **1,7-MeO-PBI$_{trapped}$** with **1,7-*i*PrO-PBI$_{seed}$** very similar results to the seeded copolymerization with **1,7-EtO-PBI$_{seed}$** were obtained (Figure 122). These results are in very good agreement with our previously reported studies,[167] and clearly indicate the formation of supramolecular block copolymers of **1,7-MeO-PBI** with both **1,7-EtO-PBI** and **1,7-*i*PrO-PBI**. The efficiency of the hetero-seeding of **1,7-MeO-PBI$_{trapped}$** with seeds of **1,7-EtO-PBI$_{seed}$** or **1,7-*i*PrO-PBI$_{seed}$** is, with a full conversion time of ca. 30 min for an identical seed ratio of 1:10, very similar but slightly slower compared to the self-seeding with **1,7-MeO-PBI$_{seed}$** with a conversion time of ca. 20 min (Figure 43d). In contrast, the addition of **H-PBI$_{seed}$**, **1-MeO-PBI$_{seed}$**, **1,6,7-MeO-PBI$_{seed}$** or **1,6,7,12-MeO-PBI$_{seed}$** has virtually no effect on the polymerization of **1,7-MeO-PBI$_{trapped}$**, revealing that the seeds of these four PBIs with their reduced shape complementarity to **1,7-MeO-PBI** are no suitable nuclei to initiate the chain-growth polymerization process of **1,7-MeO-PBI$_{trapped}$** (Figure 43d).

To further investigate the effect of PBI core twist on cross-seeding and the formation of supramolecular block copolymers, two-component seeded copolymerization experiments were performed using now the nearly core planar **1-MeO-PBI** as kinetically trapped state

and seeds of other PBIs of the present series. For this purpose, **1-MeO-PBI$_{trapped}$** ($c_T$ = 10 × 10$^{-6}$ M) in MCH/Tol 1:2 (v/v) was produced freshly and the two-component seeded polymerizations were conducted at 30 °C following the above described protocol (Figure 43a). Indeed, UV/vis studies showed that upon addition of seeds of the second PBI with planar core, i.e., bay-unsubstituted **H-PBI** (seed ratio 1:50), to the freshly prepared kinetically trapped state of **1-MeO-PBI** leads to a transformation of **1-MeO-PBI$_{trapped}$** into **1-MeO-PBI$_{agg}$** within a time course of ca. 30 min (Figure 44a).

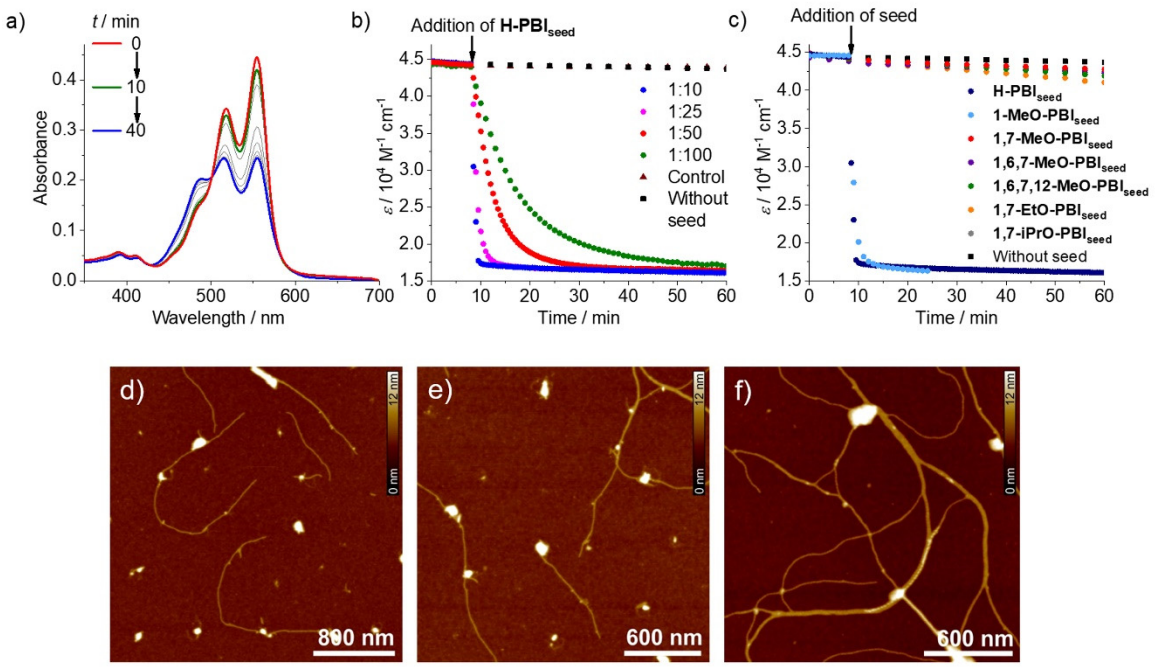


**Figure 44.** a) Time-dependent UV/vis spectra of the two-component seeded copolymerization of **1-MeO-PBI$_{trapped}$** ($c_T$ = 10 × 10$^{-6}$ M) with **H-PBI$_{seed}$** (seed ratio $c_T$(**H-PBI$_{seed}$**) : $c_T$(**1-MeO-PBI$_{trapped}$**) = 1:50 in MCH/Tol 1:2 (v/v) at 30 °C. b) Plots of the apparent extinction coefficients at 555 nm ($\varepsilon$) of **1-MeO-PBI$_{agg}$** against time upon addition of seed solution of H-PBI$_{seed}$ in ratios of $c_T$(**H-PBI$_{seed}$**) : $c_T$(**1-MeO-PBI$_{trapped}$**) = 1:10 (blue dots), 1:25 (pink dots), 1:50 (red dots) and 1:100 (green dots). The control experiment of a 1:10 mixture of **H-PBI** and **1-MeO-PBI** (brown triangles) and spontaneous polymerization of unimolecular 1-MeO-PBI (black squares) are shown for comparison. c) Plots of the apparent extinction coefficients at 555 nm of **1-MeO-PBI$_{agg}$** against the time upon addition of different seed solutions of **H-PBI** (dark blue dots), **1-MeO-PBI** (self-seeding, light blue dots), **1,7-MeO-PBI** (red dots), **1,6,7-MeO-PBI** (purple dots), **1,6,7,12-MeO-PBI** (green dots), **1,7-EtO-PBI** (orange dots) and **1,7-*i*PrO-PBI** (grey dots) to **1-MeO-PBI$_{trapped}$** with a constant ratio of $c_T$(seed) : $c_T$(**1-MeO-PBI$_{trapped}$**) = 1:10. AFM height images of samples prepared by spin-coating of the respective solutions onto silicon wafers taken at (d) 4, (e) 8 and (f) 20 min after addition of **H-PBI$_{seed}$** with a seed ratio of 1:50 to **1-MeO-PBI$_{trapped}$** ($c_T$ = 10 × 10$^{-6}$ M) in MCH/Tol (1:2, v/v) at 30 °C. The Z-scale is 12 nm.

In good accordance with the concept of seeded polymerization, the transformation time is fast for higher seed ratios, e.g., 1:10 and 1:25, and slow for a lower seed ratio 1:100, but in all these cases the two-component seeded polymerization is strongly accelerated compared to the spontaneous process and the control experiment (Figure 44b). Importantly, the

seeded polymerization starts also without a lag time indicating that the polymerization is induced indeed through the termini of the seeds and that block copolymers of **1-MeO-PBI** and **H-PBI$_{seed}$** are formed. The seed-induced chain-growth polymerization was further corroborated by time-dependent AFM. The AFM images (Figure 44d-f) of samples taken at 4, 8 and 20 min after addition of **H-PBI$_{seed}$** (seed ratio 1:50) to **1-MeO-PBI$_{trapped}$** showed a successive length increase of the polymeric nanofibers from 50 nm − 1 μm (4 min) to 400 nm − 3 μm (8 min) and extended several micrometer-long polymeric networks (20 min). Moreover, the transformation of **1-MeO-PBI$_{trapped}$** into **1-MeO-PBI$_{agg}$** upon addition of **H-PBI$_{seed}$** is as efficient as the self-seeding process with a constant seed ratio of 1:10 (Figure 44c). In contrast, the addition of the seeds of the other alkoxy-substituted PBIs to the kinetically trapped state of **1-MeO-PBI** in a seed ratio of 1:10 has no effect on the polymerization of **1-MeO-PBI$_{trapped}$** (Figure 44c), demonstrating again the impact of shape complementarity on seed-induced living supramolecular block copolymer synthesis.

We have recently reported that switching of the kinetically trapped states and seeds of well-designed PBIs dyes is possible.[167] Such dual function as trapped state and seed leads to a switching of the block pattern of the supramolecular copolymer from A-B-A to B-A-B by the experimental protocol. The above described successful formation of block copolymers of **1-MeO-PBI$_{trapped}$** with **H-PBI$_{seed}$** makes these two PBIs potential candidates for the inverted two-component seeded polymerization. **H-PBI** forms kinetically trapped monomers upon cooling of a monomeric solution from 90 to 30 °C in toluene ($c_T$ = 20 × 10$^{-6}$ M) which transforms into the thermodynamically favored H-aggregate over time,[57] like in the case of **1-MeO-PBI**. Indeed, the addition of seeds of **1-MeO-PBI$_{seed}$** in different seed ratios to the kinetically trapped state of **H-PBI$_{trapped}$** directly induces transformation into the thermodynamically favored aggregate in an analogous two-component seeded copolymerization (Figure 123). The transformation is induced instantaneously and the transformation time is only dependent on the seed ratios, similarly to the above described two-component seeded polymerization processes of **1-MeO-PBI$_{trapped}$** and **H-PBI$_{seed}$** demonstrating the formation of supramolecular block copolymers. These UV/vis studies shows that the switching from A-B-A to B-A-B block pattern is possible for **H-PBI** and **1-MeO-PBI** by inverted two-component seeded copolymerization. However, individual blocks cannot be identified by AFM because the helical pitches of the polymeric nanofibers of these two PBIs (15 nm and 14 nm, respectively) are almost identical.

### 5.2.5 Discussion on Two-component Seeded Copolymerization

All our studies on two-component polymerization have shown that the copolymerization of two PBIs can only be achieved for appropriate combinations of kinetically trapped states and polymeric seeds. Thus, a precise shape complementarity of the respective seed molecules and the kinetically trapped molecules is crucial for an efficient supramolecular copolymerization process. This shape complementarity is already encoded in the molecular building blocks and can be rationalized by the molecular geometry of the monomeric PBIs. Indeed, the core twist angles estimated by DFT calculations for **1,7-EtO-PBI** ($\alpha$ = 12.4°) and **1,7-*i*PrO-PBI** ($\alpha$ = 13.0°) are close to that of **1,7-MeO-PBI** ($\alpha$ = 11.4°). Therefore, the seeds of former two PBIs are very efficient for copolymerization with the kinetically trapped state of **1,7-MeO-PBI$_{trapped}$** and accordingly supramolecular block copolymers of these PBIs can be achieved (Figure 45, lower part, left). The matching geometry of these PBIs enables both *inter*molecular hydrogen bonding as well as $\pi$-$\pi$-interactions between the different PBI monomers enabling a copolymerization by seeds of one derivative and kinetically trapped state of the other derivative. In contrast, the twist angles of the very flat **H-PBI** ($\alpha_1$ = 0°) and **1-MeO-PBI** ($\alpha_1$ = 0°, $\alpha_2$ = 0.7°) as well as the very strongly core-twisted **1,6,7-MeO-PBI** ($\alpha_1$ = 15.0°, $\alpha_2$ = 29.9°) and **1,6,7,12-MeO-PBI** ($\alpha$ = 30.5°) are drastically differing from that of **1,7-MeO-PBI**. This mismatch of the PBI cores leads to very inefficient non-covalent interactions between the two different PBI building blocks and, therefore, prevents the seed-induced copolymerization of these PBIs with **1,7-MeO-PBI$_{trapped}$** (Figure 45, lower right and bottom). The pivotal role of shape complementarity of the molecular building blocks in the copolymerization of the PBIs is further corroborated by the very efficient two-component seed-induced polymerization of **1-MeO-PBI$_{trapped}$** and **H-PBI$_{seed}$** as these monomeric building blocks possess very good matching geometry (Figure 45, upper part, right). The cores of both PBIs are nearly planar according to DFT calculations (*vide supra*) which directs in both cases a cofacial stacking[192] with H-type exciton coupling by means of strong $\pi$-$\pi$-interactions between the PBIs. This structural similarity with a perfect matching of these core-planar PBIs enabled a successful copolymerization in both directions, i.e., including the inverted seeded copolymerization of **H-PBI$_{trapped}$** and **1-MeO-PBI$_{seed}$**. For the other alkoxy-substituted PBIs, the sterical bulkiness of the bay-substituents provokes a strong twist of the PBI cores attenuating *inter*molecular interactions between **1-MeO-PBI$_{trapped}$** and the seeds of these PBIs. This mismatch in geometry of the monomeric building blocks prevents the

copolymerization of **1-MeO-PBI** with seeds of the respective core-twisted PBIs (Figure 45, upper part, left), presumably leading to a narcissistic self-sorting process[193] or just to disassembly of the polymeric seeds.

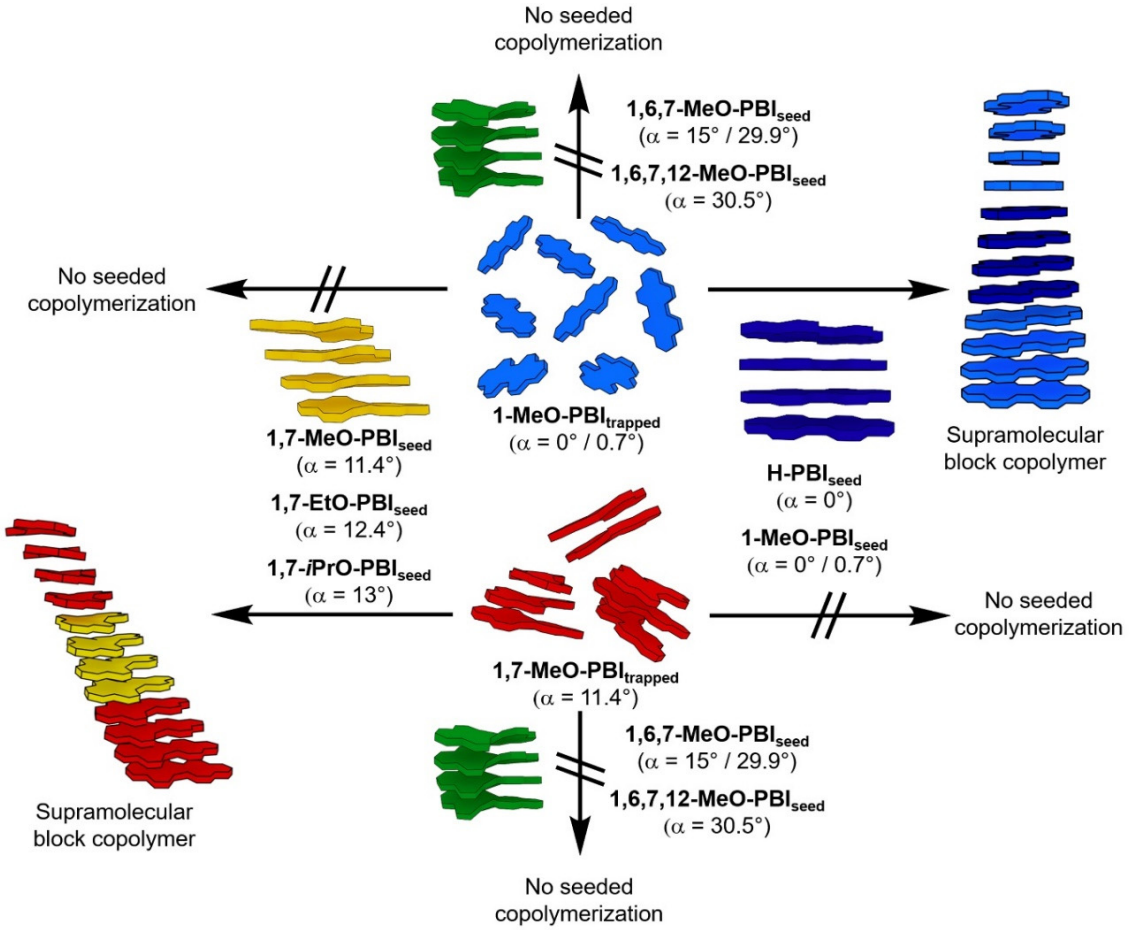


**Figure 45.** Schematic illustration of the effect of various seeds on the kinetically trapped monomers of **1-MeO-PBI** or the kinetically trapped aggregates of **1,7-MeO-PBI**, leading either to a seed-induced supramolecular block copolymerization or to no copolymerization which is explained by the different level of shape complementarity of the respective PBI components.

Our studies have shown that cross-seeding of PBIs is strongly affected by the shape complementarity of the respective monomeric building blocks, which was here adjusted by the core twist imparted by bay-substituents. Thus, our conclusion is that the formation of supramolecular block copolymers by a seed-induced copolymerization process can only be achieved for appropriate combinations of PBIs with a sufficient degree of shape complementarity encoded in the monomeric units.

## 5.3 Conclusion

Supramolecular polymerization properties of a series of PBI dyes bearing identical imide substituents but a different number or size of alkoxy substituents in bay-area have been studied. Our comprehensive studies revealed that subtle variation of the substituent pattern in bay-area has a strong influence on thermodynamically and, more importantly, on kinetically controlled supramolecular polymerization of these PBIs. Increasing number of methoxy bay-substituents at the perylene core leads to a decrease of the $\pi$-$\pi$-interactions in supramolecular polymers due to increasing sterical hindrance caused by a pronounced PBI core twist concomitant with a decrease of thermodynamic driving force. Our studies have shown that, nevertheless, all PBIs of the present series can be self-assembled in suitably chosen solvent mixtures of MCH and toluene to give thermodynamically favored helical nanofibers. However, the kinetics of the aggregation is drastically changed on variations of the substituent pattern and the solvent composition. While the self-assembly of tri- and tetramethoxy-substituted PBIs (**1,6,7-MeO-PBI** and **1,6,7,12-MeO-PBI**) is exclusively thermodynamically controlled in MCH/Tol (2:1, v/v) because of the very low stability of the kinetically metastable state, the polymerization of mono- and dialkoxy-substituted PBI derivatives is influenced by kinetically controlled pathways in the same solvent system. Here, 1,7-disubstituted PBIs (**1,7-MeO-PBI**, **1,7-EtO-PBI**, **1,7-*i*PrO-PBI)** form metastable off-pathway aggregates and mono-substituted **1-MeO-PBI** forms a kinetically trapped *intra*molecularly hydrogen-bonded monomer that can be transformed into the thermodynamically stable *inter*molecularly hydrogen-bonded polymer by addition of preformed polymeric seeds acting as nuclei for the chain-growth polymerization process in a living manner.

Moreover, we could show that the formation of A-B-A supramolecular block copolymers is possible by two-component seeded copolymerization applying the kinetically trapped state of one PBI and seeds of another appropriate PBI. The hetero-seeded copolymerization of PBIs is strongly governed by the shape complementarity of the individual components, which is determined by the twist angle of the respective perylene cores, strongly effecting the $\pi$-$\pi$-stacking geometry and enthalpy between the monomeric building blocks. While for unsuitable combinations of PBIs a copolymerization is totally prevented due to mismatching geometry, for the appropriate combination of the core planar **H-PBI** and **1-MeO-PBI** even the switching from an A-B-A to B-A-B block pattern was demonstrated by changing the experimental protocol. These insightful studies on the two-component

living seeded copolymerization using a broad series of PBIs showed that a precise control of the supramolecular polymerization and the synthesis of block copolymers can only be achieved through monomeric building blocks possessing a high degree of shape complementarity.

# Chapter 6

–

# Summary and Conclusion

The research on supramolecular polymerization has undergone a rapid development in the last two decades, particularly since supramolecular polymers exhibit a broad variety of functionalities and applications in organic electronics, biological science or as functional materials (*Chapter 2.1*). Although former studies have focused on investigation of the thermodynamics of supramolecular polymerization (*Chapter 2.2*), the academic interest in the recent years shifted towards gaining insight into kinetically controlled self-assembly and pathway complexity to generate novel out-of-equilibrium architectures with interesting nanostructures and features (*Chapter 2.3*). Along this path, the concepts of seeded and living supramolecular polymerization were recently developed to enable the formation of supramolecular polymers with controlled length and low polydispersity under precise kinetic control (*Chapter 2.4*). Besides that, novel strategies were developed to achieve supramolecular copolymerization resulting in complex multicomponent nanostructures with different structural motives. The classification of these supramolecular copolymers on the basis of literature examples and an overview of previously reported principles to create such supramolecular architectures are provided in *Chapter 2.5*.

The aim of the thesis was the non-covalent synthesis of highly desirable supramolecular block copolymers by the approach of living seeded supramolecular polymerization and to study the impact of the molecular shape of the monomeric building blocks on the supramolecular copolymerization. Based on the structure of the previously investigated PBI organogelator **H-PBI**,[57,60] a series of novel PBIs, bearing identical hydrogen-bonding amide side-groups in imide-position and various kind or number of substituents in bay-position, was synthesized and analyzed within this thesis. The new PBIs were successfully obtained in three steps starting from the respective bromo-substituted perylene-3,4:9,10-tetracarboxylic acid tetrabutylesters (**19a-c**) or from the *N*,*N'*-dicyclohexyl-1,7-dibromoperylene-3,4:9,10-tetracarboxylic acid bisimide **22** according to the synthesis route

depicted in Scheme 1. All target compounds were obtained in the final step by imidization reactions of the respective perylene tetracarboxylic acid bisanhydride precursors (**21a-d**, **24a-d**) with *N*-(2-aminoethyl)-3,4,5-tris(dodecyloxy)-benzamide **25** and were fully characterized by $^{1}H$ and $^{13}C$ NMR spectroscopy as well as high resolution mass spectrometry.

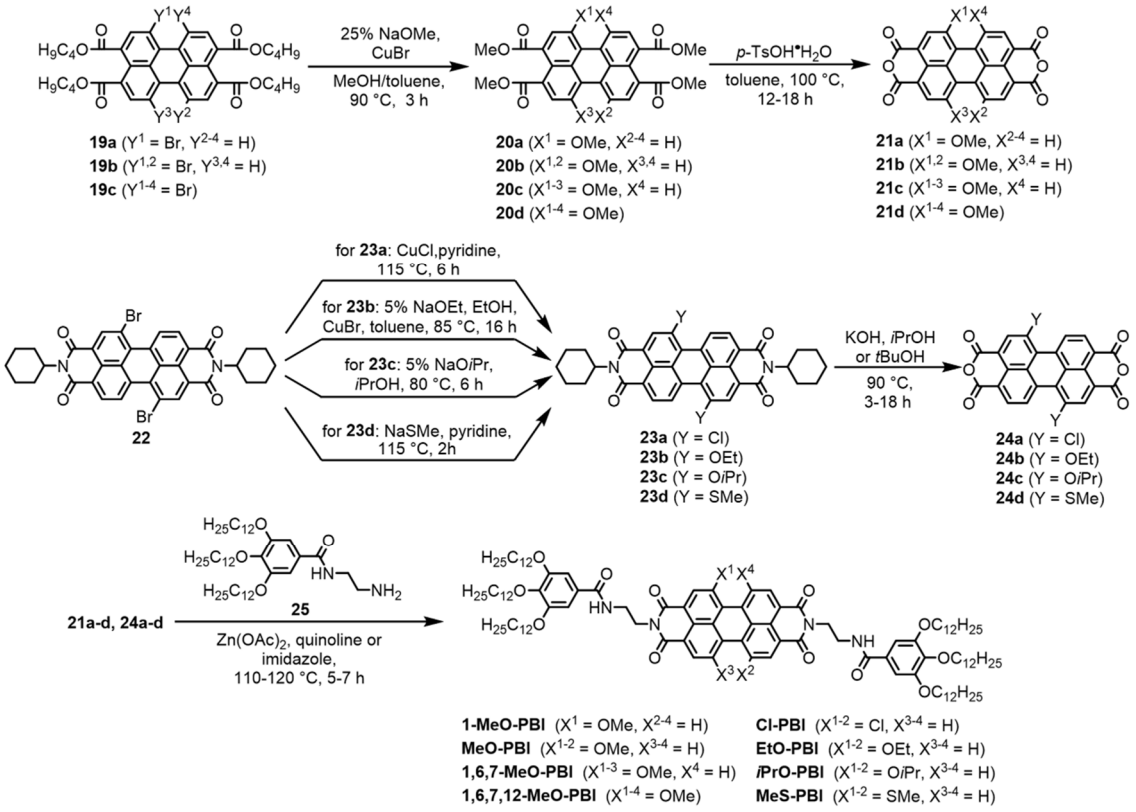


**Scheme 1.** Synthesis of the various bay-substituted target molecules studied within this thesis.

The variation of bay-substituents strongly changes the optical properties of the monomeric PBIs which were investigated by UV/vis and fluorescence spectroscopy. The increase of the number of the methoxy-substituents provokes, for example, a red-shift of the absorption maxima concomitant with a decrease of extinction coefficients and leads to a drastic increase of the fluorescence quantum yields. Furthermore, the molecular geometry of the PBIs is also affected by variations of the bay-substituents. Thus, increasing the steric demand of the bay-substituents leads to an enlargement of the twist angles of the PBI cores as revealed by DFT calculations.

Especially the 1,7-dimethoxy bay-substituted **MeO-PBI** proved to be very well-suited for the studies envisioned within this thesis. The self-assembly of this PBI derivative was analyzed in detail by UV/vis, fluorescence and FT-IR spectroscopy as well as atomic force

microscopy (*Chapter 3*). These studies revealed that **MeO-PBI** forms in a solvent mixture of methylcyclohexane and toluene (2:1, v/v) kinetically trapped off-pathway H-aggregated nanoparticles upon fast cooling of a monomeric solution from 90 to 20 °C. However, upon slow cooling of the monomer solution fluorescent J-type nanofibers are formed by $\pi$-$\pi$-interactions and *inter*molecular hydrogen-bonding.

The kinetically metastable off-pathway H-aggregates can be transformed into the thermodynamically more favored J-type aggregates by addition of seeds, which are produced by ultrasonication of the polymeric nanofibers. Interestingly, the living character of this seed-induced supramolecular polymerization process was proven by a newly designed multicycle polymerization experimental protocol (Figure 46). This living polymerization experiment clearly proves, that the polymerization can only occur at the "active" ends of the polymeric seed and that almost no recombination or chain termination processes are present. Hence, the approach of living supramolecular polymerization enables the formation of supramolecular polymers with controlled length and narrow polydispersity.

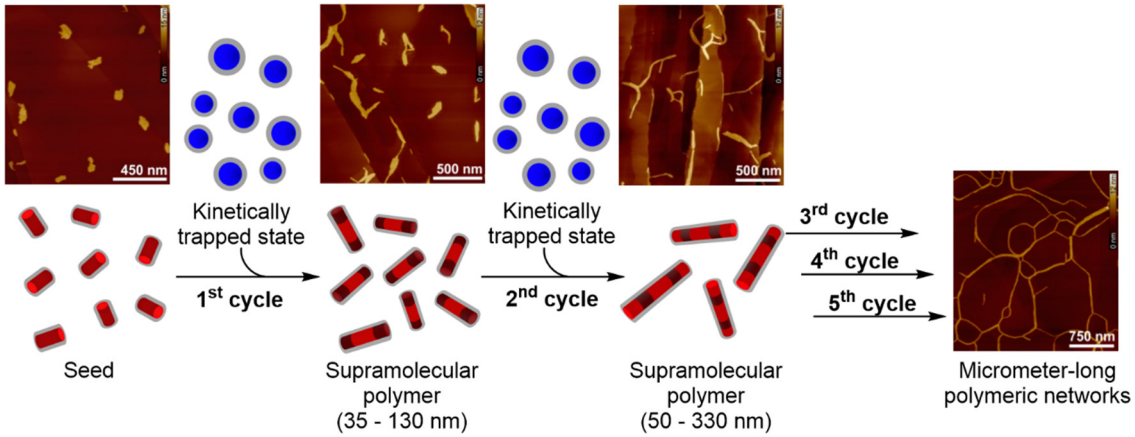


**Figure 46.** Schematic illustration of the multicycle living supramolecular polymerization of **MeO-PBI**. The AFM height images show the increasing polymer length obtained after subsequent polymerization cycles.

In *Chapter 4* the copolymerization of **MeO-PBI** with the structurally similar 1,7-dichloro (**Cl-PBI**) and 1,7-dimethylthio (**MeS-PBI**) bay-substituted PBIs is studied in detail. Both PBIs form analogous to **MeO-PBI** kinetically trapped off-pathway aggregates, which can be converted into the thermodynamically stable supramolecular polymers by seed-induced living supramolecular polymerization under precise kinetic control. However, the stability of the kinetically trapped aggregates of **Cl-PBI** and **MeS-PBI** is distinctly reduced compared to that of **MeO-PBI**, because the $\pi$-$\pi$-interactions of the kinetically metastable

aggregates are hampered through the increased twisting of the PBI-cores of the former PBIs. UV/vis studies revealed that the two-component seeded copolymerization of the kinetically trapped state of **MeO-PBI** with seeds of **Cl-PBI** leads to the formation of unprecedented supramolecular block copolymers with A-B-A pattern by a living supramolecular polymerization process at the termini of the seeds (Figure 47a-c). Remarkably, the resulting A-B-A block pattern of the obtained copolymers was clearly confirmed by atomic force microscopy studies as the respective blocks formed by the individual monomeric units could be distinguished by the pitches of the helical nanofibers (Figure 47).

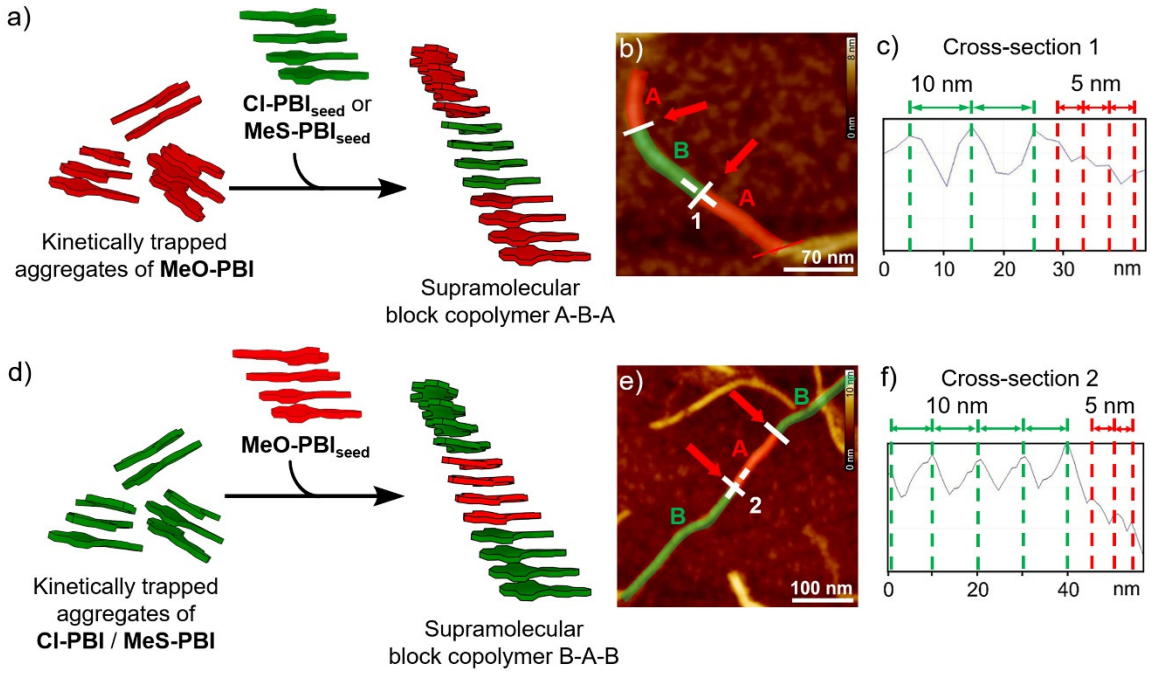


**Figure 47.** Schematic illustration of the two-component seeded copolymerization to generate supramolecular copolymers with A-B-A (a) and B-A-B (d) block pattern. AFM height image of block copolymers obtained after seeded copolymerization of **MeO-PBI$_{trapped}$** with **Cl-PBI$_{seed}$** (b) and of **Cl-PBI$_{trapped}$** with **MeO-PBI$_{seed}$** (e). The blocks assigned to the nanofibers of **MeO-PBI** (red) and **Cl-PBI** (green) are marked in color for visualization. The cross-section analysis along the white dashed lines in image (b) and (e) are shown in section (c) and (f), respectively, illustrating the change of the helical pitches from 10 to 5 nm.

Moreover, detailed UV/vis and AFM studies have shown that by inverted two-component seed-induced polymerization, e.g., upon addition of seeds of **MeO-PBI** to the kinetically trapped aggregates of **Cl-PBI**, triblock supramolecular copolymers with B-A-B pattern can be generated (Figure 47d-f). The switching of the block pattern could only be achieved because of the perfectly matching conditions for the copolymerization process and the tailored molecular geometry of the individual building blocks of both PBIs. These studies

have demonstrated for the first time, that the block pattern of a supramolecular copolymer can be modulated by the experimental protocol through the approach of living supramolecular polymerization. Furthermore, by UV/vis analysis of the living copolymerization of **MeO-PBI** and **MeS-PBI** similar results were obtained showing also the formation of both A-B-A and B-A-B type supramolecular block copolymers. Although for these two PBIs the individual blocks could not be identified by AFM because the helical nanofibers of both PBIs exhibit identical helical pitches, these studies revealed for the first time that the approach of seeded living polymerization is not limited to a special pair of monomeric building blocks.

In the last part of the thesis (*Chapter 5*) a systematic study on the two-component living copolymerization of PBIs with various sterical demanding bay-substituents is provided. Thus, a series of PBIs containing identical hydrogen-bonding amide groups in imide position but variable number (**1-MeO-PBI**, **MeO-PBI**, **1,6,7-MeO-PBI**, **1,6,7,12-MeO-PBI**) or size (**EtO-PBI**, ***i*PrO-PBI**) of alkoxy bay-substituents was investigated. The molecular geometry of the monomeric building blocks has a strong impact on the thermodynamically and even more pronounced on the kinetically controlled aggregation in solvent mixtures of MCH and Tol. While the mono- and dialkoxy-substituted PBIs form kinetically metastable species, the self-assembly of the tri- and tetramethoxy-substituted PBIs (**1,6,7-MeO-PBI** and **1,6,7,12-MeO-PBI**) is completely thermodynamically controlled. The two 1,7-alkoxy substituted PBIs (**EtO-PBI**, ***i*PrO-PBI**) form very similar to **MeO-PBI** kinetically off-pathway H-aggregates and thermodynamically more favored J-type aggregates. However, the stability of the kinetically metastable state is drastically lower and the conversion into the thermodynamically favored state much faster than for **MeO-PBI**. In contrast, the monomethoxy-substituted PBI derivative (**1-MeO-PBI**) forms a kinetically trapped species by *intra*molecular hydrogen-bonding of the monomers, which can be transformed into the thermodynamically favored nanofibers by seeded polymerization.

Importantly, the two-component seeded copolymerization of the kinetically trapped **MeO-PBI** with seeds of other PBIs of the present series was studied by UV/vis and AFM revealing that the formation of supramolecular block copolymers is only possible for appropriate combinations of PBI building blocks. Thus, the seeded polymerization of the trapped state of the moderately core-twisted **MeO-PBI** with the, according to DFT-calculations, structurally similar PBIs (**EtO-PBI** and ***i*PrO-PBI**) leads to the formation of

A-B-A block copolymers, like in the seeded copolymerization of **MeO-PBI$_{trapped}$** with seeds of **Cl-PBI** and **MeS-PBI** already described in *Chapter 4* (Figure 48, right panel). However, by addition of seeds of the almost planar PBIs (**H-PBI** and **1-MeO-PBI**) or seeds of the strongly core-twisted PBIs (**1,6,7-MeO-PBI** and **1,6,7,12-MeO-PBI**) to the kinetically trapped state of **MeO-PBI** no block copolymers can be obtained (Figure 48, left panel). The mismatching geometry of these molecular building blocks strongly hampers both the *inter*molecular hydrogen-bonding and the $\pi$-$\pi$-interactions between the two different PBIs and consequently prevents the copolymerization process.

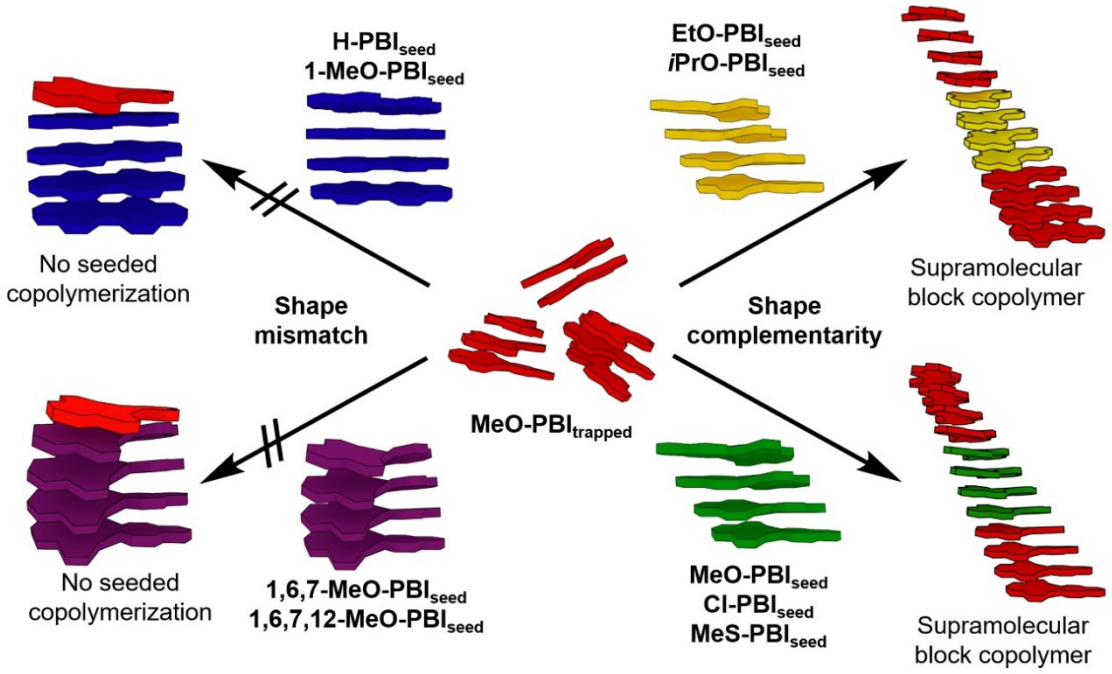


**Figure 48.** Schematic illustration of addition of various seeds to the kinetically trapped state of **MeO-PBI**, leading either to no copolymerization (left panel) or to the formation of supramolecular triblock copolymers (right panel).

Furthermore, the studies of the two-component seeded copolymerization of the kinetically trapped species of **1-MeO-PBI** with seeds of the other PBIs also corroborated that a precise shape complementarity is crucial to generate supramolecular block copolymers. Thus, by addition of seeds of **H-PBI** to the kinetically trapped monomers of **1-MeO-PBI** supramolecular block copolymers were generated. Both PBIs exhibit an almost planar PBI core according to DFT-calculations leading to strong non-covalent interactions between these PBIs. This perfectly matching geometry of both PBIs also enables the inverted seeded copolymerization of the kinetically trapped monomers of **H-PBI** with **1-MeO-PBI$_{seed}$** concomitant with a switching of the block pattern of the supramolecular copolymer from A-B-A to B-A-B type. In contrast, the seeding with the moderately twisted (**MeO-PBI**,

**EtO-PBI** and ***i*PrO-PBI**) and the strongly twisted PBIs (**1,6,7-MeO-PBI** and **1,6,7,12-MeO-PBI**) has no effect on the kinetically trapped state of **1-MeO-PBI**, because the copolymerization of these PBIs is prevented by the mismatching geometry of the molecular building blocks.

In conclusion, the supramolecular polymerization and two-component seeded copolymerization of a series of PBI monomers was investigated within this thesis. The studies revealed that the thermodynamically and kinetically controlled self-assembly can be strongly modified by subtle changes of the monomeric building blocks. Moreover, the results have shown that living supramolecular polymerization is an exceedingly powerful method to generate unprecedented supramolecular polymeric nanostructures with controlled block pattern and length distribution. The formation of supramolecular block copolymers can only be achieved under precise kinetic control of the polymerization process and is strongly governed by the shape complementarity already imparted in the individual components. Thus, these insightful studies might enable a more rational design of monomeric building blocks for the non-covalent synthesis of highly complex supramolecular architectures with interesting properties for possible future applications, e.g., as novel functional materials.

# Chapter 7

–

# Zusammenfassung und Fazit

Das Forschungsgebiet der supramolekularen Polymerisation hat sich in den letzten Jahrzehnten sehr rasch entwickelt, zumal da supramolekulare Polymere eine Fülle an Anwendungsmöglichkeiten in der organischen Elektronik, der Biologie oder als Funktionsmaterialen bieten (*Kapitel 2.1*). Während frühere Studien den Fokus auf die Untersuchung der Thermodynamik der supramolekularen Polymerisation gelegt haben (*Kapitel 2.2*), hat sich das akademische Interesse in jüngster Zeit dahingehend verschoben, Einblicke in kinetisch kontrollierte Selbstassemblierungsprozesse zu erhalten, um neuartige Strukturen mit faszinierenden Eigenschaften zu generieren (*Kapitel 2.3*). Im Zuge dieser Entwicklung wurde das Konzept der Saat-induzierten und der lebenden supramolekularen Polymerisation entwickelt, welche die Bildung von supramolekularen Polymeren mit geringer Polydispersität in kinetisch kontrollierten Prozessen ermöglichen (*Kapitel 2.4*). Des Weiteren wurden neue Strategien zu Erzeugung von Nanostrukturen entwickelt, die aus verschiedenen Komponenten aufgebaut sind und somit neue komplexe Strukturmotive zeigen. Eine Einteilung dieser supramolekularen Copolymere anhand einiger Literaturbeispiele und eine kurze Übersicht über die bisherigen Methoden, solche supramolekularen Strukturen zu erzeugen ist in *Kapitel 2.5* dargestellt.

Das Ziel der Doktorarbeit war die nicht-kovalente Synthese von erstrebenswerten supramolekularen Blockcopolymeren mittels lebender Saat-induzierter Polymerisation und zu erforschen, wie die molekulare Form der Monomerbausteine die supramolekulare Copolymerisation beeinflusst. Basierend auf der Molekülstruktur des zuvor untersuchten Perylenbisimidfarbstoffes **H-PBI** wurden in dieser Arbeit eine Reihe von neuen Perylenbisimiden mit identischen Amid-Seitengruppen in Imidposition und unterschiedlicher Art oder Anzahl von Buchtsubstituenten synthetisiert und charakterisiert. Die neuen Perylenbisimide wurden erfolgreich in drei Stufen nach den in Schema 2 dargestellten Syntheserouten erhalten, wobei von den jeweiligen Brom-substituierten

Perylen-3,4:9,10-tetracarbonsäuretetrabutylestern **19a-c** oder von *N*,*N'*-Dicyclohexyl-1,7-dibromperylen-3,4:9,10-tetracarbonsäurebisimid **22** ausgegangen wurde. Alle Zielverbindungen wurden im letzten Syntheseschritt mittels einer Imidisierungsreaktion der jeweiligen Perylenbisanhydridvorstufen (**21a-d**, **24a-d**) mit *N*-(2-Aminoethyl)-3,4,5-tris(dodecyloxy)benzamid **25** erhalten und mittels $^{1}$H- und $^{13}$C-NMR-Spektroskopie sowie mit hochauflösender Massenspektrometrie charakterisiert.

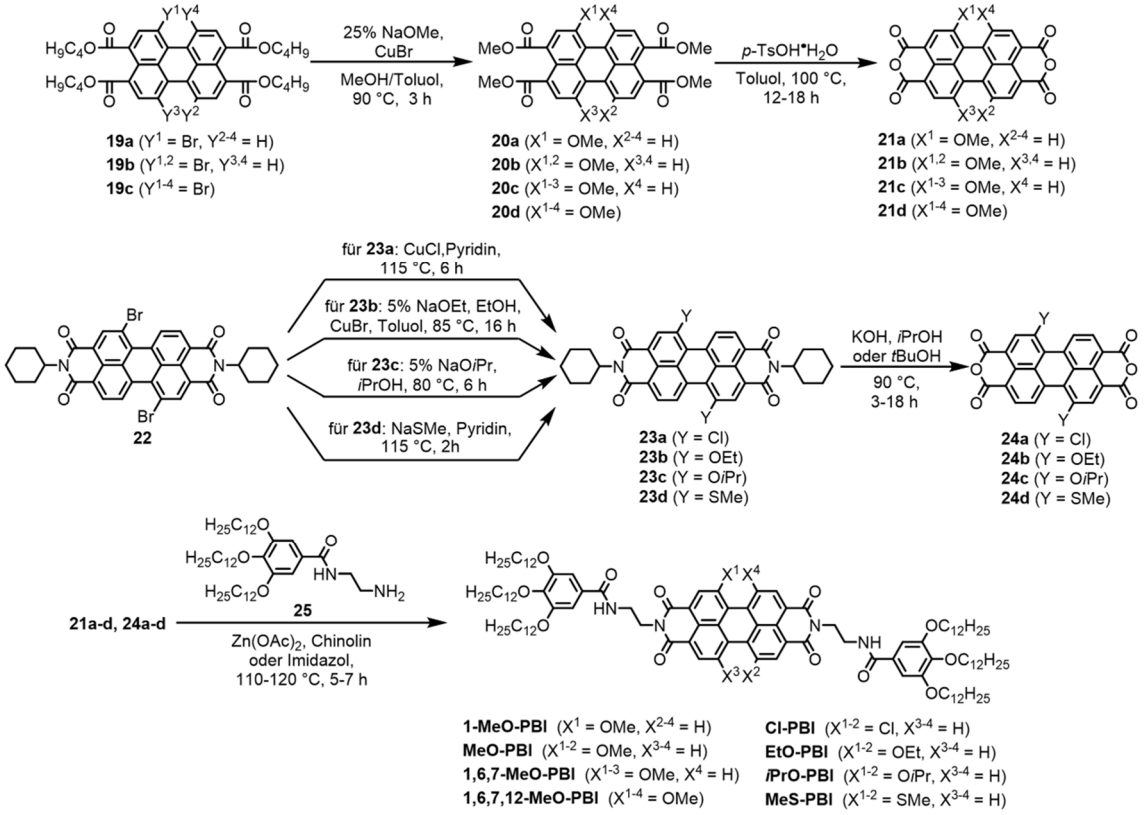


**Schema 2.** Syntheseschema der in dieser Arbeit untersuchten unterschiedlich Bucht-substituierten Perylenbisimidfarbstoffe.

Die Variation der Buchtsubstituenten hat einen starken Einfluss auf die optischen Eigenschaften der Perylenbisimidmonomere, was mittels UV/vis- und Fluoreszenzspektroskopie untersucht wurde. Die ansteigende Zahl der Methoxysubstituenten verursacht zum Beispiel eine Rotverschiebung der Absorptionsmaxima, welche mit einer Abnahme der Extinktionskoeffizienten einhergeht, und führt zu einem starken Anstieg der Fluoreszenzquantenausbeute. Außerdem wird auch die Molekülgeometrie der Perylenbisimide durch die Variation der Buchtsubstituenten beeinflusst. Mittels DFT-Rechnungen konnte gezeigt werden, dass eine Zunahme des sterischen Anspruchs der Buchtsubstituenten eine Vergrößerung des Torsionswinkels der Perylenbisimidkerne zur Folge hat.

Als besonders geeignet für die im Rahmen dieser Arbeit anvisierten Studien erwies sich das mit zwei Methylgruppen in 1,7-Buchtposition substituierte **MeO-PBI**. Die Selbstassemblierung dieses 1,7-Dimethoxy-substituierten Perylenbisimid-Derivates wurde mit Hilfe von UV/vis-, Fluoreszenz- und FT-IR-Spektroskopie sowie mittels Rasterkraftmikroskopie detailliert analysiert (*Kapitel 3*). Diese Studien haben gezeigt, dass **MeO-PBI** in einem Lösungsmittelgemisch aus Methylcyclohexan und Toluol (2:1, v/v) in einem kinetisch kontrollierten Prozess durch schnelles Abkühlen der Monomerlösung von 90 auf 20 °C „off-pathway“ Nanopartikel ausbildet. Durch langsames Abkühlen der Monomerlösung entstehen hingegen fluoreszierende, J-aggregierte Nanofasern aufgrund von $\pi$-$\pi$-Wechselwirkungen und *inter*molekularen Wasserstoffbrückenbindungen. Die kinetisch metastabilen „off-pathway“ H-Aggregate können durch Zugabe einer polymeren J-Aggregat-Saat, welche durch eine Behandlung der polymeren Nanofasern mit Ultraschall gewonnen werden kann, in die thermodynamisch begünstigten J-Aggregate transformiert werden. Außerdem wurde der lebende Charakter dieser supramolekularen Saat-induzierten Polymerisation durch ein neu entworfenes multizyklisches Versuchsprotokoll nachgewiesen (Abbildung 49). Diese Experimente zur lebenden supramolekularen Polymerisation zeigen deutlich, dass der Polymerisationsprozess nur an den „aktiven“ Enden der polymeren Saat stattfinden kann und dass außerdem kaum Rekombinations- oder Kettenterminationsprozesse auftreten. Folglich ermöglicht die Methode der lebenden supramolekularen Polymerisation die Synthese von supramolekularen Polymeren mit kontrollierbarer Polymerlänge und geringer Polydispersität.

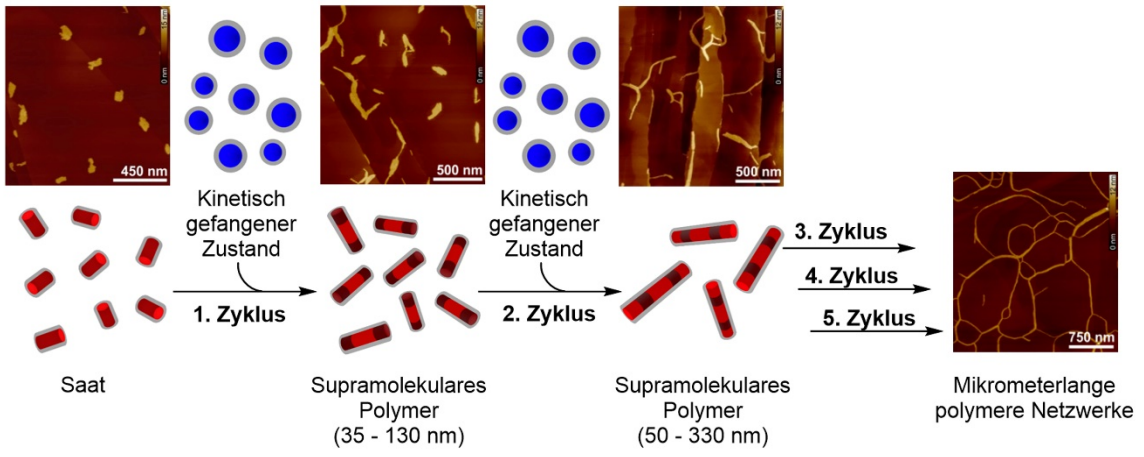


**Abbildung 49.** Schematische Darstellung der multizyklischen lebenden supramolekularen Polymerisation von **MeO-PBI**. Die Rasterkraftmikroskopie-Höhenbilder zeigen den Anstieg der Polymerlänge nach dem jeweiligen Polymerisationszyklus.

In *Kapitel 4* wird die Copolymerisation von **MeO-PBI** mit den strukturell ähnlichen 1,7-Dichlor- (**Cl-PBI**) und 1,7-Dimethylthiosubstituierten (**MeS-PBI**) Perylenbisimiden ausgeführt. Beide neuen Perylenbisimide bilden analog zu **MeO-PBI** „off-pathway" Aggregate, die durch Saatzugabe in einem kinetisch kontrollierten Prozess in die thermodynamisch stabileren supramolekularen Polymere umgewandelt werden können. Die Stabilität der kinetisch gefangenen Aggregate von **Cl-PBI** und **MeS-PBI** ist jedoch verglichen mit den metastabilen Aggregaten von **MeO-PBI** deutlich geringer, da die $\pi$-$\pi$-Wechselwirkungen zwischen den molekularen Bausteinen aufgrund des vergrößerten Torsionswinkels der Peryleneinheiten stark reduziert sind. UV/vis-spektroskopische Studien zeigen, dass die Saat-induzierte Copolymerisation des kinetisch gefangenen Zustandes von **MeO-PBI** mit der Saat von **Cl-PBI** durch einen lebenden Kettenwachstumsprozess an den Polymerenden der Saat zur Ausbildung von neuartigen supramolekularen Blockcopolymeren mit A-B-A-Blockstruktur führt (Abbildung 50).

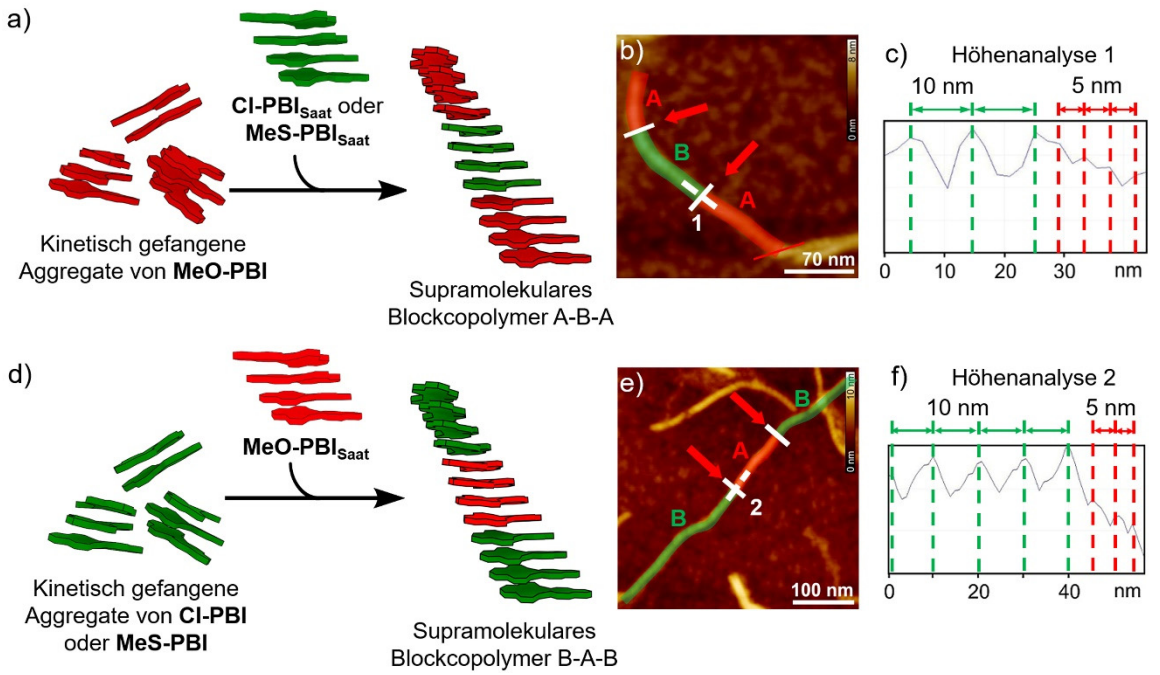


**Abbildung 50.** Schematische Darstellung der Saat-induzierten Zweikomponenten-Copolymerisation, um supramolekulare Copolymere mit A-B-A- (a) und B-A-B- (d) Blockschema zu erzeugen. Rasterkraftmikroskopie-Höhenbilder der Blockcopolymere, welche durch Saat-induzierte Copolymerisation von **MeO-PBI$_{gefangen}$** mit **Cl-PBI$_{Saat}$** (b) oder von **Cl-PBI$_{gefangen}$** mit **MeO-PBI$_{Saat}$** (e) erhalten wurden. Die Blocksegmente, die den Nanofasern von **MeO-PBI** (rot) und **Cl-PBI** (grün) zugeordnet sind, sind für eine bessere Visualisierung in der jeweiligen Farbe markiert. Die Höhenanalysen entlang der weißen gestrichelten Linien in den Bildern (b) und (e) sind jeweils im Abschnitt (c) und (f) gezeigt, um die Veränderung der helikalen Ganghöhen von 10 nach 5 nm zu verdeutlichen.

Die erzeugte A-B-A-Blockstruktur der erhaltenen Copolymere konnte eindeutig mittels Rasterkraftmikroskopie bestätigt werden, da die jeweiligen Polymerblöcke bestehend aus den einzelnen monomeren Einheiten anhand der Ganghöhe der helikalen Nanofasern unterschieden werden können (Abbildung 50). Ausführliche UV/vis- und Rasterkraftmikroskopiestudien haben außerdem demonstriert, dass, zum Beispiel durch Zugabe der Saat von **MeO-PBI** zu den kinetisch gefangenen Aggregaten von **Cl-PBI**, Triblockcopolymere mit B-A-B-Blockstruktur in einer invertierten Saat-induzierten Zweikomponenten-Copolymerisation, erzeugt werden können. Dieser Wechsel der Blockstruktur kann nur durch perfekt abgestimmte Bedingungen für die Copolymerisation und bei übereinstimmender Molekülgeometrie der Monomereinheiten erreicht werden. Diese Studien zeigen erstmals, dass die Blockstruktur der supramolekularen Polymere durch das Versuchsprotokoll der lebenden supramolekularen Polymerisation variiert werden kann. Des Weiteren lieferten UV/vis-spektroskopische Untersuchungen der lebenden Copolymerisation von **MeO-PBI** und **MeS-PBI** ähnliche Ergebnisse, was darauf hindeutet, dass ebenfalls supramolekulare Blockcopolymere mit A-B-A- und B-A-B-Struktur gebildet werden können. Obwohl die einzelnen Polymerblöcke in diesem Fall wegen der identischen Helixganghöhe der Nanofasern nicht zugeordnet werden konnten, so zeigten diese Experimente doch, dass die Methode der Saat-induzierten lebenden Polymerisation nicht auf ein spezielles Paar von Monomerbausteinen limitiert ist.

Im letzten Abschnitt der Doktorarbeit (*Kapitel 5*) wird eine systematische Studie der lebenden Zweikomponenten-Copolymerisation von Perylenbisimiden mit unterschiedlich sterisch anspruchsvollen Buchtsubstituenten dargestellt. Dementsprechend wurde eine Reihe von Perylenbisimiden mit identischen Amidseitenketten, aber unterschiedlicher Anzahl (**1-MeO-PBI**, **MeO-PBI**, **1,6,7-MeO-PBI**, **1,6,7,12-MeO-PBI**) oder Größe (**EtO-PBI**, ***i*PrO-PBI**) der Alkoxybuchtsubstituenten untersucht. Die Molekülgeometrie der Monomereinheiten hat einen starken Einfluss auf das thermodynamisch und mehr noch auf das kinetisch kontrollierte Aggregationsverhalten in Lösungsmittelgemischen aus Methylcyclohexan und Toluol. Während die mono- und dialkoxysubstituierten Perylenbisimide kinetisch metastabile Zustände ausbilden, findet die Selbstassemblierung der tri- und tetramethoxysubstituierten Perylenbisimide (**1,6,7-MeO-PBI**, **1,6,7,12-MeO-PBI**) vollständig unter thermodynamischer Kontrolle statt. Die zwei 1,7-alkoxysubstituierten Perylenbisimide (**EtO-PBI**, ***i*PrO-PBI**) bilden analog zu **MeO-PBI** sowohl kinetische „off-pathway“ H-Aggregate als auch thermodynamisch

begünstigte J-Aggregate. Verglichen mit **MeO-PBI** ist jedoch die Stabilität der kinetisch metastabilen Zustände von **EtO-PBI** und ***i*PrO-PBI** viel geringer und die Umwandlung in die thermodynamisch stabileren Aggregate geschieht daher viel schneller. Das monomethoxysubstituierte Perylenbisimid-Derivat (**1-MeO-PBI**) bildet im Gegensatz dazu kinetisch gefangene Monomere durch *intra*molekulare Wasserstoffbrücken-bindungen, welche sich durch Saat-induzierte Polymerisation in die thermodynamisch begünstigteren Nanofasern transformieren lassen.

Die Saat-induzierte Zweikomponenten-Copolymerisation des kinetisch gefangenen Zustands von **MeO-PBI** durch Saatzugabe der anderen Perylenbisimide der Reihe wurde mittels UV/vis-Spektroskopie und Rasterkraftmikroskopie analysiert. Diese Studien eröffneten, dass die Bildung von supramolekularen Blockcopolymeren nur für geometrisch passende Kombinationen der Perylenbisimide möglich ist. Dementsprechend führt die Saat-induzierte Polymerisation des kinetisch gefangenen Zustands von **MeO-PBI** mit den, laut DFT-Rechnungen, strukturell ähnlichen Perylenbisimiden (**EtO-PBI**, ***i*PrO-PBI**) zur Bildung von A-B-A-Blockcopolymeren, analog zu dem im *Kapitel 4* beschriebenem Fall der Saat-induzierten Copolymerisation mit **Cl-PBI** und **MeS-PBI** (Abbildung 51, rechte Seite).

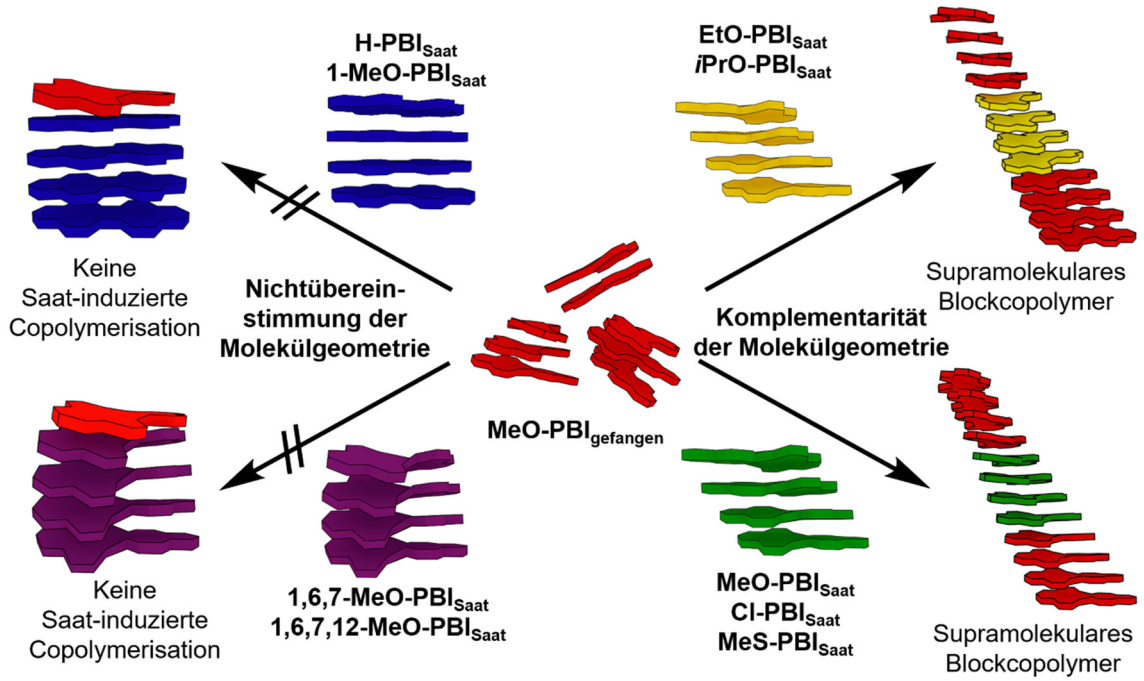


**Abbildung 51.** Schematische Darstellung der Zugabe verschiedener polymerer Saaten zum kinetisch gefangenen Zustand von **MeO-PBI**, welche entweder zu keiner Copolymerisation (linke Seite) oder zur Bildung von supramolekularen Triblockcopolymeren (rechte Seite) führt.

Die Zugabe einer Saat der planaren Perylenbisimide (**H-PBI**, **1-MeO-PBI**) oder der Perylenbisimide mit stark verdrehten Perylenkernen (**1,6,7-MeO-PBI**, **1,6,7,12-MeO-PBI**) zum kinetisch metastabilen Zustand von **MeO-PBI** führt dagegen nicht zur Bildung von Blockcopolymeren (Abbildung 51, linke Seite). Der Unterschied in der Molekülgeometrie dieser Monomerbausteine vermindert erheblich die Stärke der $\pi$-$\pi$-Wechselwirkungen zwischen den unterschiedlichen Perylenbisimiden und verhindert daher deren Copolymerisation.

Die Studien zur Saat-induzierten Zweikomponenten-Copolymerisation des kinetisch gefangenen Zustands von **1-MeO-PBI** mit den anderen Perylenbisimiden der Serie bestätigte weiterhin, dass eine genaue Übereinstimmung der molekularen Geometrie entscheidend für die Erzeugung von supramolekularen Blockcopolymeren ist. Durch Zugabe der Saat von **H-PBI** zum kinetisch metastabilen Zustand von **1-MeO-PBI** konnten folglich supramolekulare Blockcopolymere generiert werden. Mittels DFT-Rechnungen wurde gezeigt, dass beide Perylenbisimide einen relativ planaren Perylenkern aufweisen, was zu sehr starken, nicht-kovalenten Wechselwirkungen zwischen diesen beiden Monomerbausteinen führt. Die übereinstimmende Geometrie beider Perylenbisimide ermöglicht auch die invertierte Saat-induzierte Copolymerisation des kinetisch gefangenen Zustands von **H-PBI** mit **1-MeO-PBI$_{Saat}$**, was mit einem Wechsel der Blockstruktur des supramolekularen Blockcopolymers von A-B-A zu B-A-B einhergeht. Die Zugabe der Saat der mäßig (**EtO-PBI**, ***i*PrO-PBI**) und stark verdrehten Perylenbisimide (**1,6,7-MeO-PBI**, **1,6,7,12-MeO-PBI**) hat im Gegensatz dazu keinen Effekt auf den kinetisch gefangenen Zustand von **1-MeO-PBI**, da die Copolymerisation dieser Perylenbisimide durch die Nichtübereinstimmung der Molekülgeometrie der Monomerbausteine verhindert wird.

Abschließend lässt sich zusammenfassen, dass in dieser Arbeit die supramolekulare Polymerisation und Saat-induzierte Zweikomponenten-Copolymerisation einer Reihe von Perylenbisimidmonomeren untersucht worden ist. Die Studien haben demonstriert, dass die thermodynamisch und kinetisch kontrollierten Selbstassemblierungsprozesse durch subtile Änderungen der Monomerbausteine stark variiert werden können. Außerdem zeigen die Ergebnisse, dass die lebende supramolekulare Polymerisation eine sehr leistungsfähige Methode zur Erzeugung von neuartigen supramolekularen, polymeren Nanostrukturen mit kontrollierter Blockstruktur und Längenverteilung darstellt. Die Bildung dieser supramolekularen Blockcopolymere kann nur unter präziser kinetischer Kontrolle erreicht werden und ist durch die Komplementarität der einzelnen molekularen Komponenten stark

beeinflusst. Diese aufschlussreichen Studien bilden möglicherweise die Grundlage für ein rationaleres Design neuer Monomerbausteine zur nicht-kovalenten Synthese von hochkomplexen, supramolekularen Strukturen mit potentiell einzigartigen Eigenschaften für mögliche Anwendungen, beispielsweise als neuartige Funktionsmaterialien.

# Chapter 8

–

# Appendix

## 8.1 Supporting Information for *Chapter 3*: Living Polymerization of a Perylene Bisimide Dye into Fluorescent J-Aggregates[62]

### Materials and methods

All chemicals and solvents were purchased from commercial suppliers and used without further purification. The spectroscopic measurements were conducted under ambient conditions using dry solvents of spectroscopic grade. The UV/vis spectra of the samples were measured with *Jasco* V-670 and *Jasco* V-770 spectrophotometers equipped with a PAC-743R Auto Peltier 6/8-cell changer for temperature control. The temperature-dependent absorption spectra were density corrected for the different temperatures. The fluorescence spectra were recorded with a PTI QM4-2003 fluorescence spectrometer (R928 photomultiplier-detector, GL302 dye laser) and were corrected against photomultiplier and lamp intensity. The fluorescence quantum yields were determined by the optical dilution method (OD = 0.05) as the average value of 5 different excitation wavelengths with Lumogen Red (*BASF*) as reference (in $CHCl_3$, $\Phi_{fl}$ = 0.96).[194] The FT-IR spectroscopic analyses were performed on a *Jasco* FT/IR-430 spectrometer using a *Beckmann* Quick-mount IR Multicell Kit with KBr windows and path length of 1 mm. The $^1H$ NMR and the $^{13}C$ NMR spectra were recorded with a *Bruker* Avance III HD (400 MHz) spectrometer and calibrated against the residual proton signal or natural abundance carbon resonance of the used deuterated solvent from tetramethylsilane as the internal standard. The chemical shifts $\delta$ are indicated in ppm and the coupling constants $J$ in Hz. The multiplicities are given at center of the respective signal as s (singlet), d (doublet), dd (doublet of doublets), t (triplet), q (quartet) and m (multiplet). The MALDI-TOF mass spectra were measured with a *Bruker* Daltonics autoflex II LRF by using DCTB as a matrix. The high-resolution mass spectra (HRMS) were measured by electrospray ionization (ESI) at the microTOF Focus from *Bruker* Daltonics. AFM measurements were performed under ambient conditions

using a *Bruker* Multimode 8 SPM system operating in tapping mode in air. Silica cantilevers (OMCL-AC200TS, *Olympus*) with a resonance frequency of ~150 kHz and a spring constant of ~10 $Nm^{-1}$ were used. The samples were prepared by spin-coating the respective solutions onto highly oriented pyrolytic graphite (HOPG) with 2000 rpm. The molecular modeling calculation was carried out with MacroModel version 9.3.

## Living supramolecular polymerization protocol

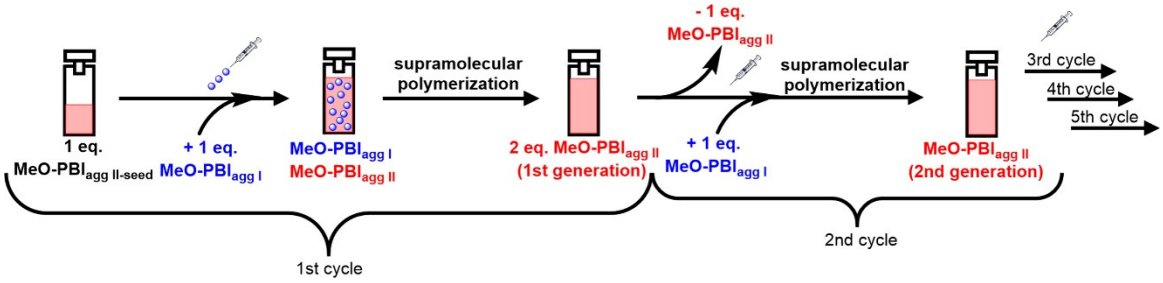


**Figure 52.** Schematic illustration of the experimental design to investigate the living character of the supramolecular polymerization of **MeO-PBI**.

## Synthesis and Characterization of the Compounds

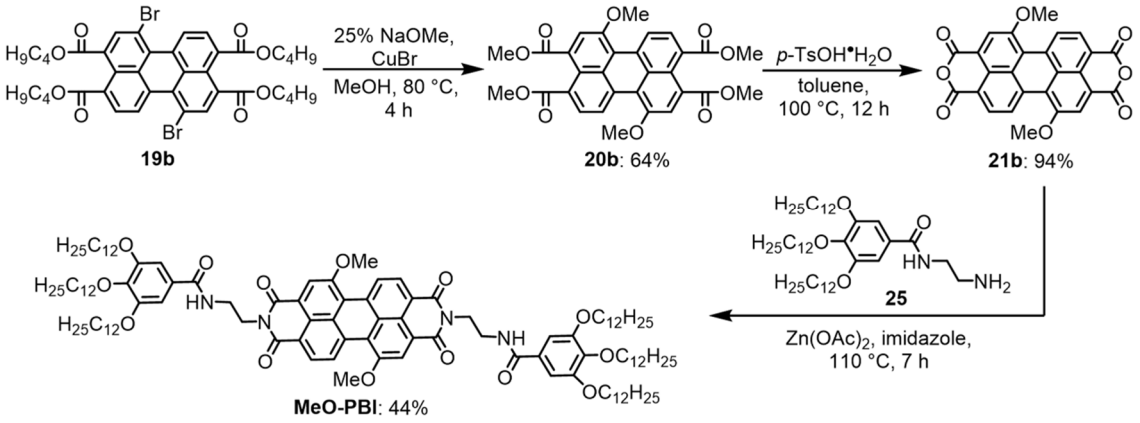


**Scheme 3.** Synthesis of the dimethoxy-substituted perylene bisimide **MeO-PBI** starting with the literature known 1,7-dibromoperylene-3,4:9,10-tetracarboxylic acid tetrabutylester **19b**.[188]

**1,7-Dimethoxyperylene-3,4:9,10-tetracarboxylic acid tetramethylester 20b**

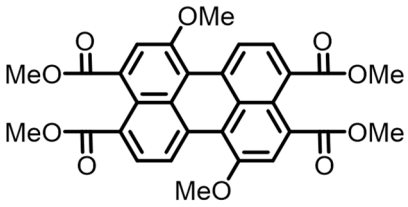


A suspension of CuBr (0.60 g, 4.18 mmol, 2.3 eq.) in anhydrous ethylacetate (5 mL) was added to a freshly prepared 25% NaOMe solution in methanol (30 mL) under nitrogen atmosphere. To the reaction mixture a solution of 1,7-dibromoperylene-3,4:9,10-tetracarboxylic acid tetrabutylester **19b**[188] (1.50 g, 1.85 mmol) in anhydrous toluene (5 mL) was added and the mixture was stirred for 4 h at 80 °C. After being cooled to room temperature, the reaction mixture was quenched with water and the product was extracted with dichloromethane ($2 \times 50$ mL). The crude product was purified by column chromatography (*n*-pentane:acetone 7:3, v/v) on silica gel.

**Yield**: 0.65 g (1.19 mmol, 64%), red orange solid

**M. p.** 174-176 °C

**$^1$H NMR** (400 MHz, $CDCl_3$): $\delta$ [ppm] = 9.03 (d, $J$ = 8.1 Hz, 2H, CH), 7.99 (d, $J$ = 8.1 Hz, 2H, CH), 7.93 (s, 2H, CH), 4.13 (s, 6H, $OCH_3$), 3.94 (s, 12H, $OCH_3$).

**$^{13}$C NMR** (100 MHz, $CDCl_3$): $\delta$ [ppm] = 169.2, 168.8, 155.0, 132.2, 131.8, 130.4, 128.5, 128.3, 127.2, 123.2, 119.9, 117.8, 56.9, 52.4, 52.3.

**MS** (MALDI, positive, DCTB): *m/z* calculated: 544.14 $[M]^+$, found: 544.13.

**1,7-Dimethoxyperylene-3,4:9,10-tetracarboxylic acid bisanhydride 21b**

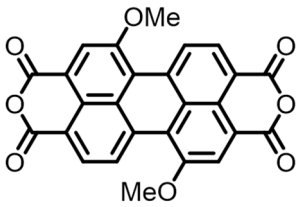


A suspension of 1,7-dimethoxyperylene-3,4:9,10-tetracarboxylic acid tetramethylester **20b** (300 mg, 0.55 mmol) and *p*-toluenesulfonic acid monohydrate (1.15 g, 6.11 mmol, 11 eq.) in toluene (30 mL) was refluxed for 18 h at 100 °C. After being cooled to room temperature, the solvent was evaporated under reduced pressure and water (20 mL) was

added to the residue and sonicated for 5 min. The precipitate was separated by filtration and washed several times with water.

**Yield:** 234 mg (517 µmol, 94%), dark purple solid

**M. p.** > 350 °C

**$^1$H NMR** (400 MHz, $D_2SO_4$): $\delta$ [ppm] = 9.83 (d, $J$ = 8.0 Hz, 2H, CH), 8.79 (d, $J$ = 8.0 Hz, 2H, CH), 8.61 (s, 2H, CH), 4.28 (s, 6H, $OCH_3$).

**MS** (MALDI, negative, DCTB): *m/z* calculated: 452.05 $[M]^-$, found: 452.13.

**$^{13}$C NMR** could not be measured because of the low solubility of the compound.

***N,N′*-(2-(3,4,5-Tris(dodecyloxy)benzamido)ethyl)-1,7-dimethoxy-perylene-3,4:9,10-tetracarboxylic acid bisimide MeO-PBI**

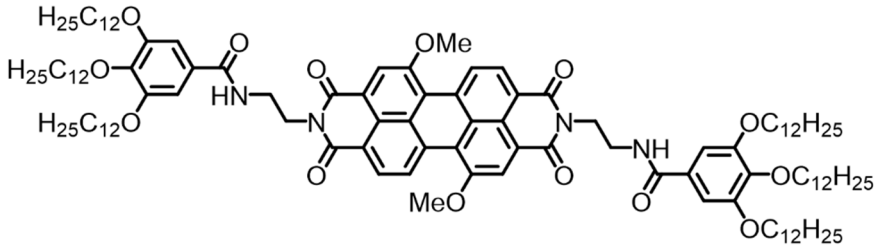


A mixture of 1,7-dimethoxyperylene-3,4:9,10-tetracarboxylic acid bisanhydride **21b** (70.0 mg, 0.155 mmol), $Zn(OAc)_2$ (80 mg, 0.436 mmol, 2.8 eq.) and *N*-(2-aminoethyl)-3,4,5-tris(dodecyloxy)benzamide **25** (250 mg, 0.349 mmol, 2.2 eq.) in imidazole (4.00 g) was stirred for 7 h at 110 °C under nitrogen atmosphere. After being cooled to room temperature, the reaction mixture was diluted with DCM (25 mL) and washed with aqueous 1N HCl (25 mL) solution and water (25 mL). The organic layer was separated and dried over $Na_2SO_4$ and the solvent was removed under reduced pressure. The obtained crude product was purified by column chromatography on silica gel ($CHCl_3$ and EtOAc:*n*-pentane 7:3). The resulting solid was dissolved in ca. 1 mL of chloroform and then precipitated with methanol. The obtained precipitate was concentrated by centrifugation and was dried in high vacuum.

**Yield:** 125 mg (67.5 µmol, 44%), purple solid

**M. p.** 280-282 °C

**$^1$H NMR** (400 MHz, TCE, 360 K): $\delta$ [ppm] = 9.60 (d, $J$ = 8.4 Hz, 2H, CH), 8.65 (d, $J$ = 8.4 Hz, 2H, CH), 8.57 (s, 2H, CH), 7.01 (s, 4H, CH), 6.84 (t, $J$ = 4.7 Hz, 2H, NH), 4.61-4.57 (m, 4H, $NCH_2$), 4.35 (s, 6H, $OCH_3$), 4.09-4.00 (m, 12H, $OCH_2$), 3.92-3.89 (m, 4H, $NCH_2$), 1.87-1.72 (m, 12H, $CH_2$), 1.58-1.23 (m, 108H, $CH_2$), 0.95-0.90 (m, 18H, $CH_3$).

**$^{13}$C NMR** (100 MHz, $CDCl_3$, 295 K): $\delta$ [ppm] = 167.9, 164.1, 164.0, 157.0, 153.2, 140.9, 133.6, 129.7, 128.3, 122.4, 120.7, 105.7, 73.6, 69.3, 39.6, 32.0, 32.0, 30.5, 30.3, 29.9, 29.8, 29.8, 29.7, 29.5, 29.5, 26.2, 22.8, 14.3.

**MS** (MALDI, positive, DCTB): *m/z* calculated: 1850.49 $[M+H]^+$, found: 1850.32

**HRMS** (ESI, positive, chloroform/acetonitrile): *m/z* 1872.3081 calculated for $C_{116}H_{176}N_4NaO_{14}$: $[M+Na]^+$, found 1872.3075.

**UV/vis**: (TCE at $20 \times 10^{-6}$ M): $\lambda_{max}$ / nm ($\varepsilon_{max}$ / L mol$^{-1}$ cm$^{-1}$) = 577 (60000).

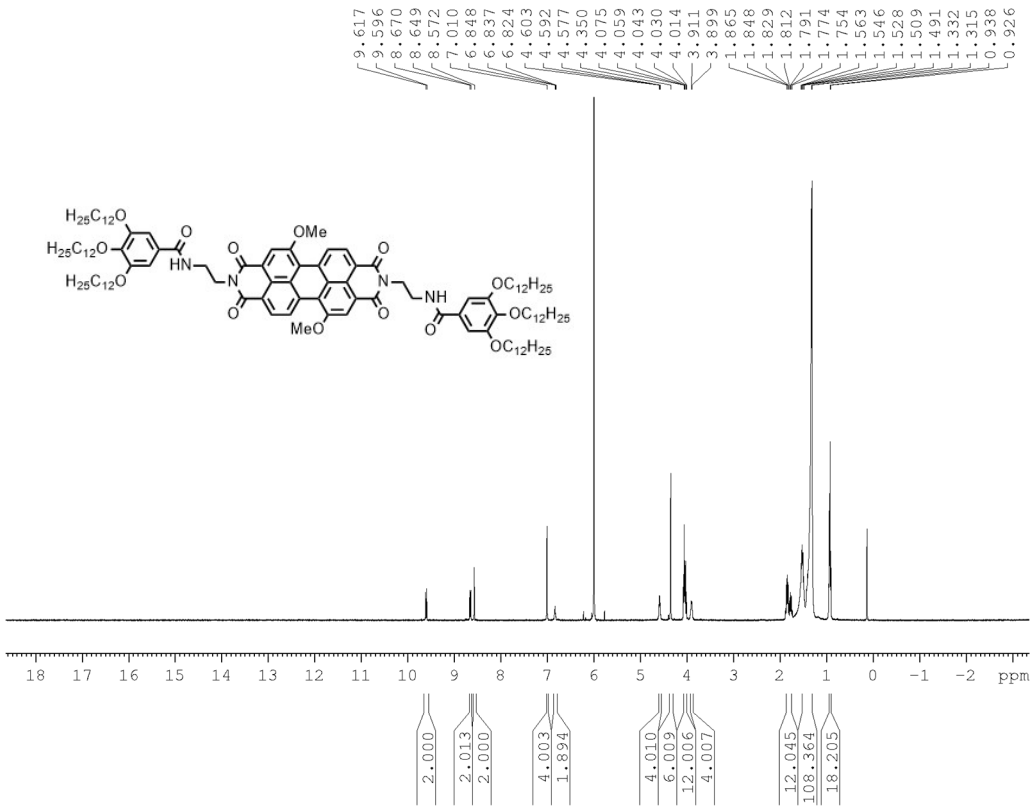


**Figure 53.** $^1$H NMR spectrum (400 MHz) of **MeO-PBI** at 360 K in 1,1,2,2-tetrachloroethane-$d_2$.

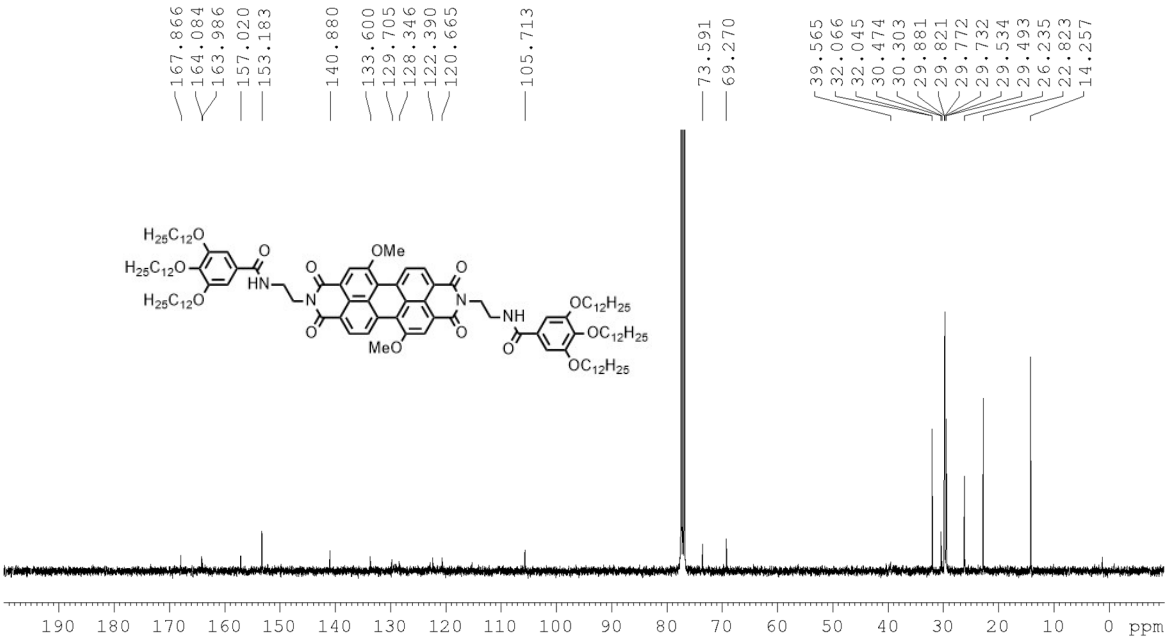


**Figure 54.** $^{13}$C NMR spectrum (100 MHz) of **MeO-PBI** in $CDCl_3$ at 295 K.

## Geometry optimized DFT calculations

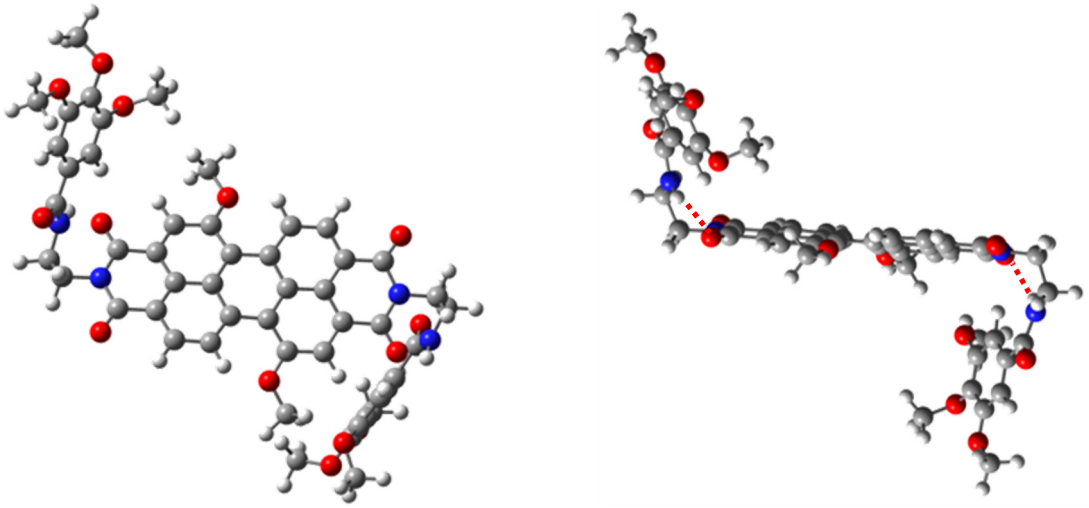

Top view Front view

**Figure 55.** Top and front view of the energy minimized structure a model compound of **MeO-PBI** ($OC_{12}H_{25}$ residues are replaced by OMe) obtained by DFT calculations (Gaussian 09) with B3-LYP as functional and def2-SVP as basis set. In the front view the *intra*molecular hydrogen-bonding is indicated by dotted red lines.

## UV/vis absorption and fluorescence spectroscopy

### Optical properties of the monomeric PBIs

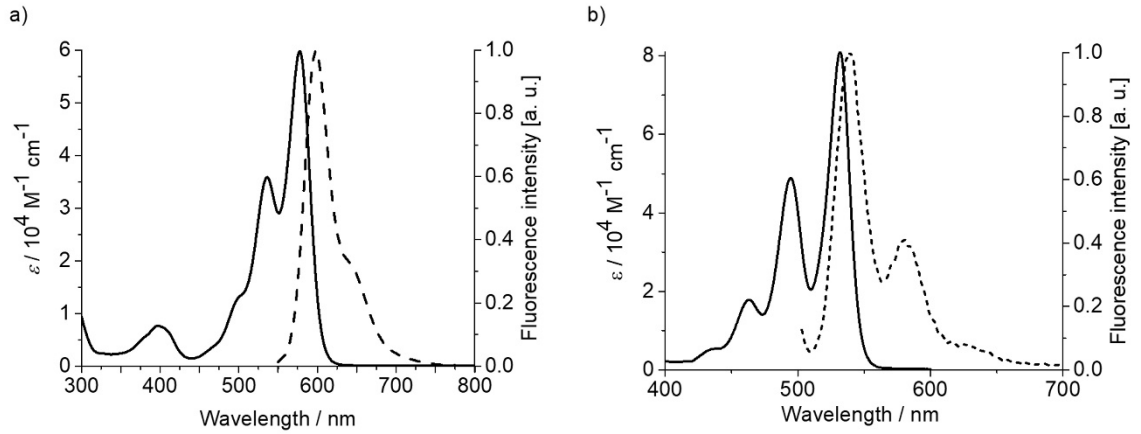


**Figure 56.** Absorption ($c_T = 20 \times 10^{-6}$ M, solid lines) and emission spectra ($c_T \approx 1 \times 10^{-6}$ M), dashed lines) of the monomeric **MeO-PBI** (a, $\lambda_{ex} = 540$ nm) and **H-PBI** (b, $\lambda_{ex} = 490$ nm) in 1,1,2,2-tetrachlorethane (TCE) at room temperature.

### Determination of the thermodynamic parameters for the aggregation of MeO-PBI

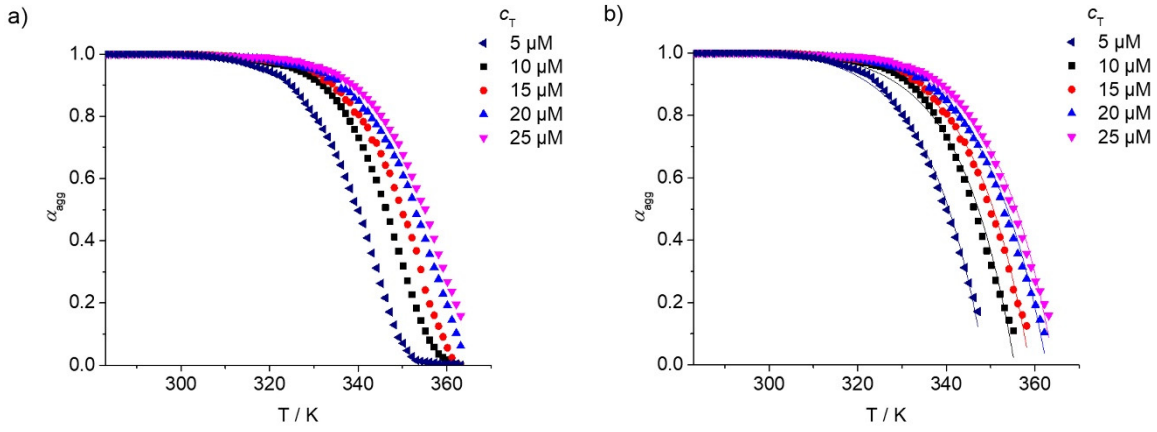


**Figure 57.** a) $\alpha_{agg}$(**MeO-PBI$_{agg\ II}$**) calculated from the apparent extinction coefficient at 560 nm and plotted against the temperature for different total concentrations ($c_T$). b) Fitting of the obtained data for the elongation process with the cooperative model proposed by Smulders et al.[27,98] for the respective concentrations (solid lines).

**Table 1.** Values of $\alpha_{sat}$, $\Delta H_e$ and $T_e$ obtained by fitting the elongation curves with the cooperative model for different concentrations.

| $c_T$ / µM | $\alpha_{sat}$ [a] | $\Delta H_e$ / kJ mol$^{-1}$ [b] | $T_e$ / K [c] |
|---|---|---|---|
| 5 | 1.020 | −84.0 | 348.7 |
| 10 | 1.022 | −86.9 | 355.4 |
| 15 | 1.014 | −88.6 | 358.8 |
| 20 | 1.011 | −84.0 | 362.6 |
| 25 | 1.012 | −88.5 | 364.3 |

a) Saturation parameter; b) elongation temperature; c) elongation enthalpy

## Van't Hoff plot analysis

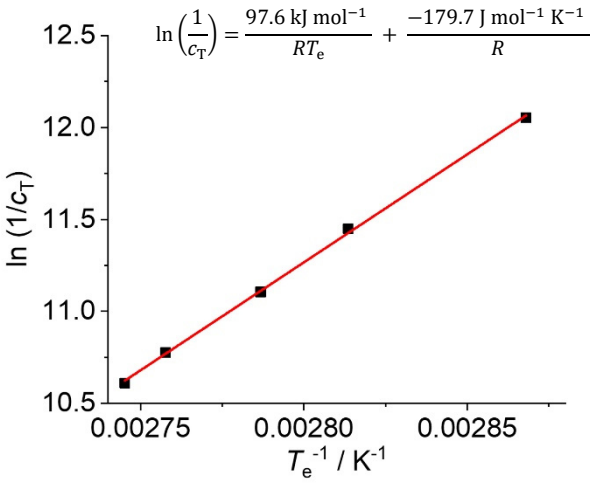


**Figure 58.** Natural logarithm of the reciprocal $c_T$ as a function of the reciprocal $T_e$ and fitting the data points with the van't Hoff equation.

**Concentration-dependent transformation of MeO-PBI$_{agg\ I}$ into MeO-PBI$_{agg\ II}$**

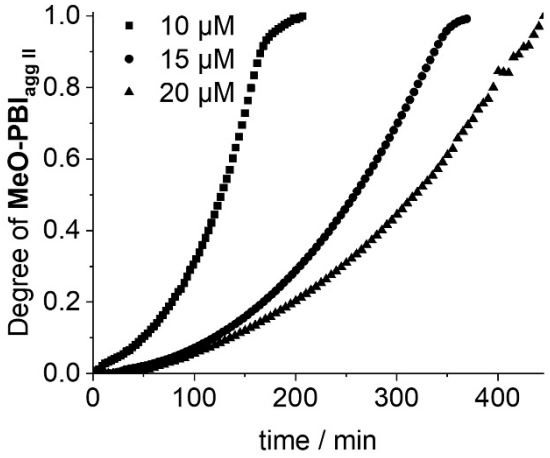


**Figure 59.** Plot of $\alpha_{agg}$(**MeO-PBI$_{agg\ II}$**) calculated from the apparent extinction coefficients at 655 nm against the time after rapid cooling from 90 to 20 °C with a rate of 10 °C/min for different total concentrations ($c_T = 10 \times 10^{-6}$ M (squares), $15 \times 10^{-6}$ M (dots) and $20 \times 10^{-6}$ M (triangles)).

**Spontaneous transformation from H- to J-aggregate at different temperatures.**

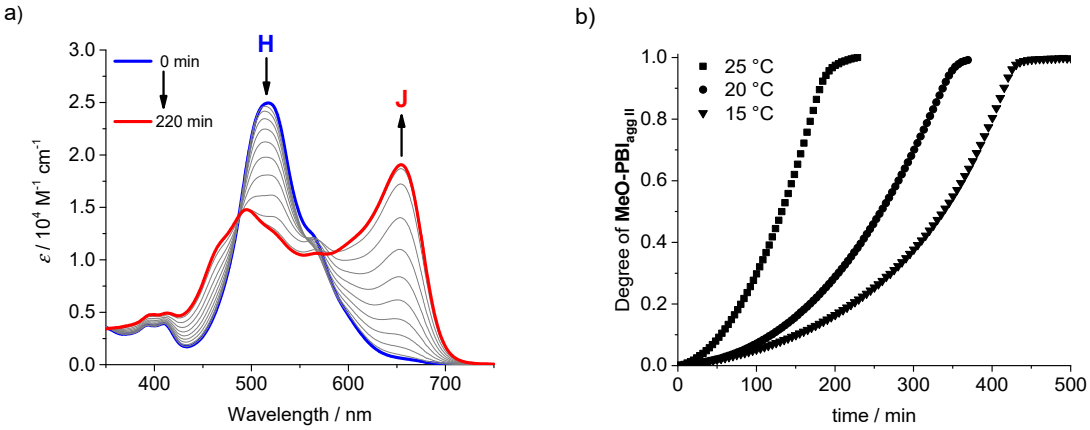


**Figure 60.** a) Time-dependent UV/vis absorption spectra of the spontaneous transformation of **MeO-PBI$_{agg\ I}$** ($c_T = 15 \times 10^{-6}$ M) into **MeO-PBI$_{agg\ II}$** at 25 °C. b) Plot of $\alpha_{agg}$(**MeO-PBI$_{agg\ II}$**) calculated from the apparent extinction coefficients at 655 nm against the time after rapid cooling (ca. 10 °C/min) to 15 °C (triangles), 20 °C (dots) and 25 °C (squares).

**Plot of the Initial slopes of the living polymerization experiment against cycle number**

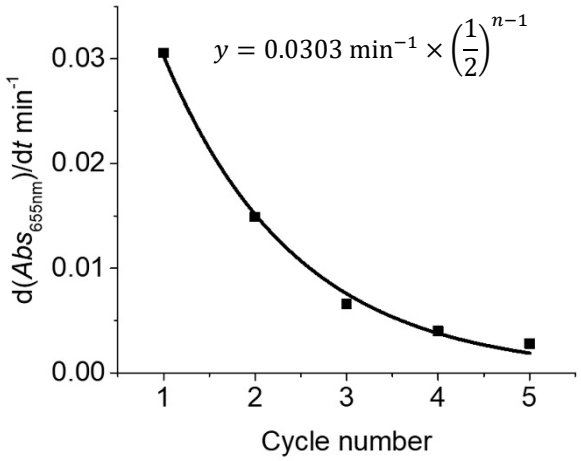


**Figure 61.** Plot of the initial slope [min$^{-1}$] obtained by a fitting of the first data points with a linear relationship against the number of cycles ($n$). The values were fitted (black line) with an exponential function to illustrate that the slope is bisected by each cycle.

**Fluorescence of the aggregate MeO-PBI$_{\mathbf{agg\ II}}$**

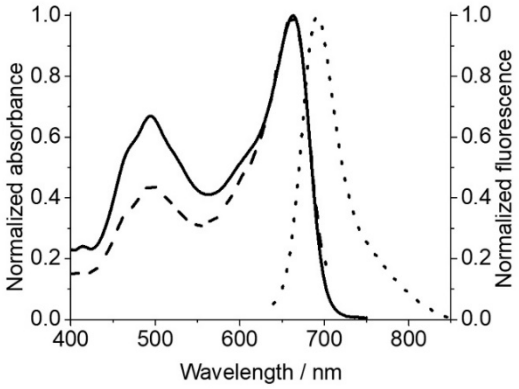


**Figure 62.** Normalized absorption (solid line), fluorescence ($\lambda_{ex}$ = 610 nm, dotted line) and excitation ($\lambda_{ex}$ = 720 nm, dashed line) spectra of the J-aggregate **MeO-PBI$_{\mathbf{agg\ II}}$** in pure MCH at 20 °C (OD < 0.05).

**FT-IR spectroscopic studies**

The influence of hydrogen bonding for the stabilization of different aggregated species was investigated by Fourier-transform infrared (FT-IR) spectroscopy. The FT-IR spectrum of **MeO-PBI** monomers in TCE at room temperature displays a N−H stretching signal at 3402 $cm^{-1}$, which is shifted to lower energy by 44 $cm^{-1}$ compared to reference benzamide **18** (Figure 63), clearly indicating the presence of *intra*molecular hydrogen bonds from amide NH to carbonyl oxygens in the monomeric state that is denoted as **MeO-PBI$_{closed}$**.[57,60] The geometry optimized structure obtained by DFT calculations reveals a distance of 2.15 Å between the amide hydrogen and the carbonyl group of the PBI core, which also confirms an *intra*molecular hydrogen bond of medium strength in the closed conformation (Figure 55).

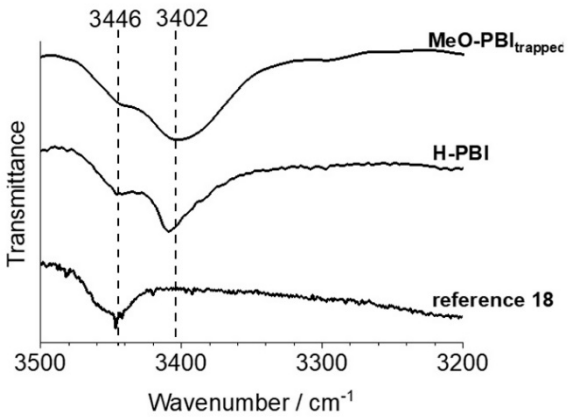


**Figure 63.** N−H stretching regions of the FT-IR spectra of the monomeric **MeO-PBI** and **H-PBI** as well as the reference benzamide **18** in TCE ($c_T = 0.5 \times 10^{-3}$ M) at room temperature.

The FT-IR spectrum of the H-aggregate **MeO-PBI$_{agg\ I}$** ($c_T = 0.2 \times 10^{-3}$ M) in toluene displays a broad signal between 3450 and 3400 $cm^{-1}$ for the N−H-stretching, indicating the presence of similar *intra*molecular hydrogen bonds in the aggregated state (Figure 64). In pure toluene the kinetically formed **MeO-PBI$_{agg\ I}$** is stable even at high concentration ($c_T = 0.2 \times 10^{-3}$ M), which is needed for the FT-IR studies. In contrast, the FT-IR spectrum of the J-aggregate **MeO-PBI$_{agg\ II}$** ($c_T = 0.5 \times 10^{-3}$ M) in MCH/Tol (2:1, v/v) shows two new N−H-stretching vibrations at 3313 and 3257 $cm^{-1}$ that correspond to the N−H stretching observed for the *inter*molecularly hydrogen-bonded amide hydrogens of previously investigated reference **H-PBI** ($\nu$(N−H) = 3271 $cm^{-1}$).[57,60,129,165]

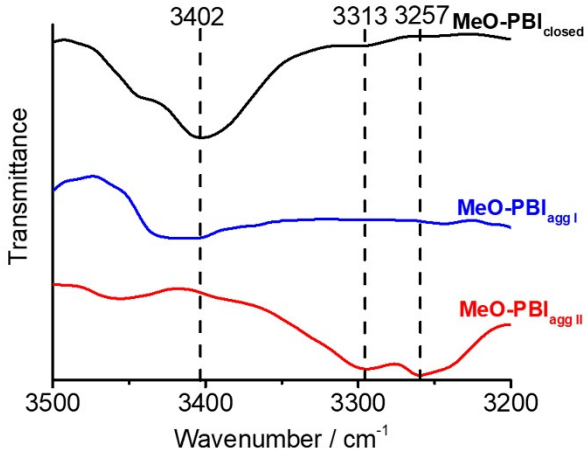


**Figure 64.** N−H stretching regions of the FT-IR spectra for the different states of **MeO-PBI**: **MeO-PBI$_{closed}$** monomer ($c_T$ = 0.5 × 10$^{-3}$ M, TCE, black line), **MeO-PBI$_{agg\ I}$** ($c_T$ = 0.2 × 10$^{-3}$ M, toluene, blue line) and **MeO-PBI$_{agg\ II}$** ($c_T$ = 0.5 × 10$^{-3}$ M, MCH/Tol (2:1, v/v), red line).

## Atomic force microscopy

### Morphology of MeO-PBI$_{agg\ I}$ spin-coated on HOPG

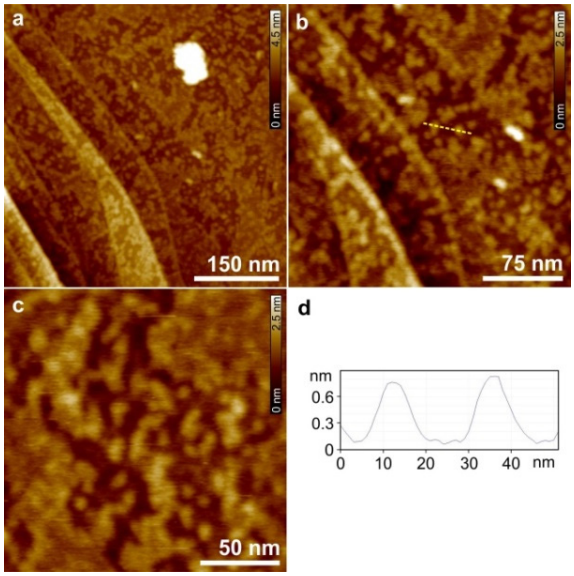


**Figure 65.** AFM height images of sample **MeO-PBI$_{agg\ I}$** prepared by spin-coating with 2000 rpm of a MCH/toluene (2:1, v/v) solution ($c_T$ = 15 µM) on HOPG. *Z* scale is 4.5 nm (a) and 2.5 nm (b,c). d) Cross-section analysis along the yellow dashed line in image (b).

### AFM studies of the seeds of MeO-PBI$_{agg\ II}$ obtained by ultrasonication

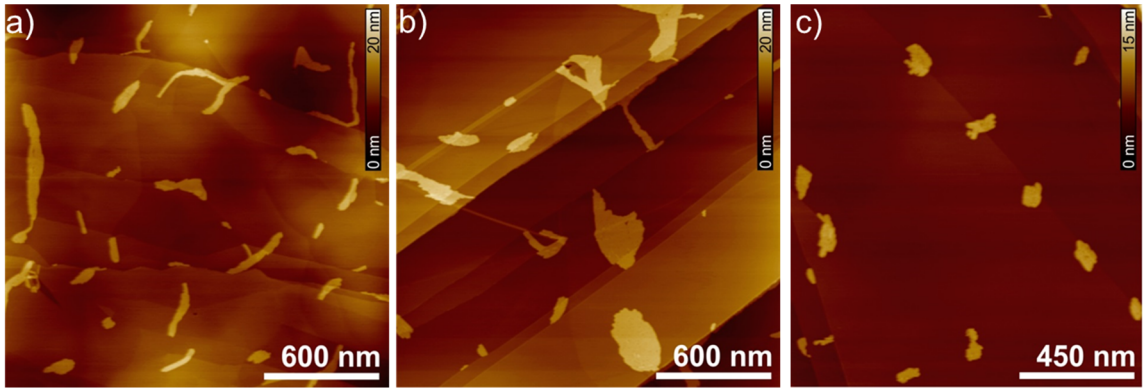


**Figure 66.** AFM height images of **MeO-PBI$_{agg\ II\text{-}seed}$** obtained after ultrasonication for 2 min (a), 5 min (b) and 10 min (c). The samples were prepared by spin-coating with 2000 rpm of the respective MCH/toluene (2:1, v/v) solution ($c_T$ = 15 µM) on HOPG. *Z* scale is 20 nm (a,b) and 15 nm (c).

The length of the seeds decreases with increasing sonication time from 55-200 nm (2 min) to 45-170 nm (5 min) and 20-80 nm. Although the seeds are agglomerating and forming insular structures on the HOPG surface, the helical structure of the individual strands is unchanged compared to that of the **MeO-PBI$_{aggII}$** polymers.

**AFM height images of the MeO-PBI$_{agg\ II}$ polymers obtained during the living polymerization experiment**

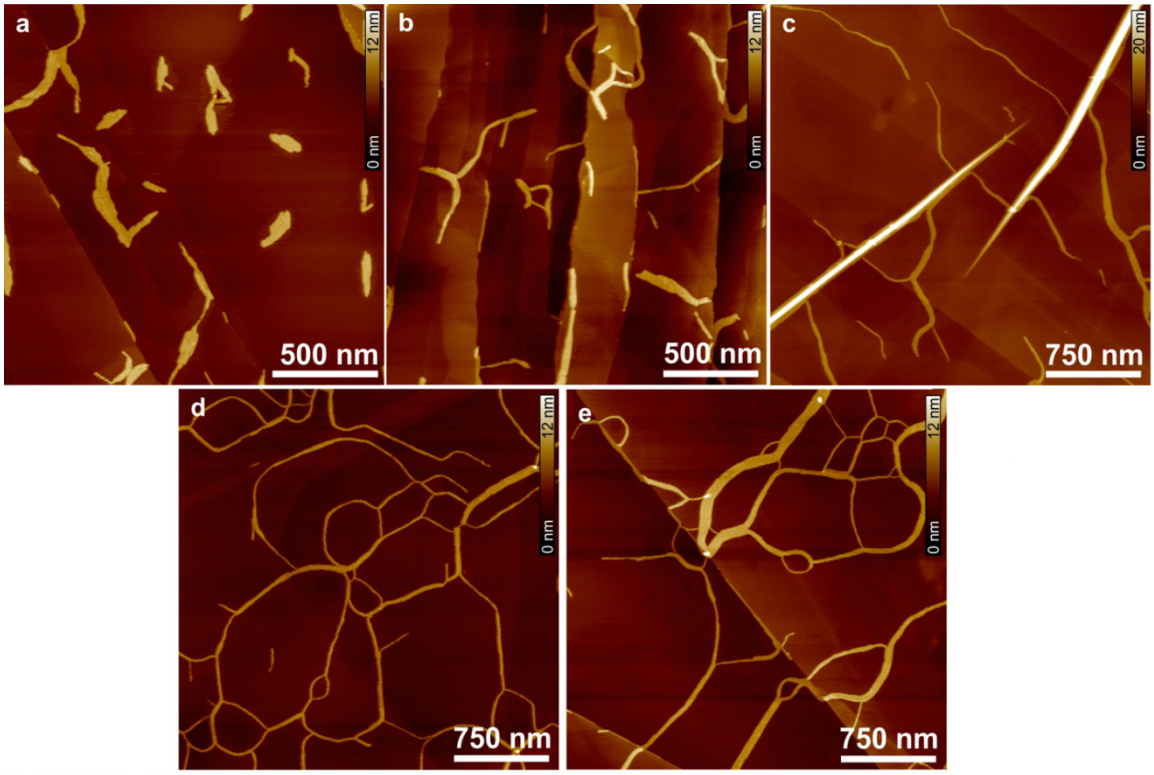


**Figure 67.** AFM height images of the polymers obtained after each cycle (1$^{st}$-5$^{th}$ cycles, a-e) in the living polymerization prepared by spin-coating with 2000 rpm of the respective solutions on HOPG. *Z* scale is 12 nm (a,b,d,e) and 20 nm (c).

**Table 2.** Characteristic values of the helical nanofibers of **MeO-PBI$_{agg\ II}$**

| | **MeO-PBI$_{agg\ II}$** |
|---|---|
| Height / nm | 4.0 |
| Width / nm | 3.9 |
| Helical pitch / nm | 5.0 |
| Molecules per turn | 14 |
| Rotation angle $\alpha$ | 26° |

## 8.2 Supporting Information for *Chapter 4*: Supramolecular Block Copolymers by Seeded Living Polymerization of Perylene Bisimides[167]

### Materials and methods

#### General

All chemicals, reagents and solvents were purchased from commercial suppliers and used, unless otherwise stated, without further purification. If needed, solvents were dried by literature known procedures. Perylene bisimide **MeO-PBI** was synthesized according to the previously reported procedure.[62]

#### NMR spectroscopy

The $^{1}$H NMR and $^{13}$C NMR spectra were recorded with a *Bruker* Avance III HD (400 MHz or 600 MHz) spectrometer and calibrated against the residual proton signal or natural abundance carbon resonance of the used deuterated solvent from tetramethylsilane as the internal standard. The chemical shifts $\delta$ are indicated in ppm and the coupling constants $J$ in Hz. The multiplicities are given at center of the respective signal as s (singlet), d (doublet), dd (doublet of doublets), t (triplet), q (quartet) and m (multiplet).

#### Mass spectrometry

The high-resolution mass spectra (HRMS) were measured by electrospray ionization (ESI) at the microTOF Focus from *Bruker* Daltonics.

#### Melting point determination

The melting points were measured at the polarization microscope BX41 of *Olympus* with the temperature controller TP94 of *Linkam Scientific* and are uncorrected.

#### UV/vis spectroscopy

The spectroscopic measurements were conducted under ambient conditions using dry solvents of spectroscopic grade. The UV/vis spectra of the samples were measured with *Jasco* V-670 and *Jasco* V-770 spectrophotometers equipped with a PAC-743R Auto Peltier 6/8-cell changer for temperature control using conventional quartz cell cuvettes (from 0.1 cm to 1 cm). The temperature-dependent absorption spectra were density corrected for the different temperatures.

**Atomic force microscopy (AFM)**

AFM measurements were performed under ambient conditions using a *Bruker* Multimode 8 SPM system operating in tapping mode in air. Silica cantilevers (OMCL-AC200TS, *Olympus*) with a resonance frequency of ~150 kHz and a spring constant of ~10 $Nm^{-1}$ were used. The samples were prepared by spin-coating the respective solutions onto silicon wafer with 1000-2000 rpm.

**DFT calculations**

DFT calculations were performed by using Gaussian09 with B3-LYP as functional and def2-SVP as basis set.

**Two-component seeded supramolecular polymerization**

The respective PBI was dissolved in a solvent mixture of MCH and Tol (2:1, v/v) and heated for ca. 15 min at 90 °C to ensure the formation of the fully monomeric state. Subsequently, 1.2 mL of the solution were placed in a cuvette and cooled down to 20 °C (for **MeO-PBI$_{trapped}$**) or to 10 °C (for **Cl-PBI$_{trapped}$** and **MeS-PBI$_{trapped}$**) by ca. 15 °C/min in the UV/vis spectrometer. The time-dependent UV/vis measurements were started at the respective temperature (20 or 10 °C). After several spectra were recorded to validate the kinetic trapping of the PBI, the seeds prepared by ultrasonication of the polymer solution for 30 min were injected just before recording the spectrum at $t$ = 12 min into the cuvette. The volume of seed solution was exactly determined by the use of *Hamilton* syringes of appropriate size to calculate seed ratio. After seed addition, the time-dependent UV/vis measurement was continued at the respective temperature. Since the addition of seed solution leads to a slight decrease of the total concentration of the respective PBIs because of the added solvent, the degree of aggregation can then be calculated by dilution correction through subtracting the absorbance caused by the polymeric seeds.

**Synthesis and characterization**

The synthesis of the new PBIs starts with isomerically pure *N*,*N'*-dicyclohexyl-1,7-dibromoperylene-3,4:9,10-tetracarboxylic acid bisimide **22**,[190] which was converted into the respective PBI precursors **23a** and **d** by a copper-mediated halogen exchange for **Cl-PBI**[195-196] or nucleophilic substitution reaction for **MeS-PBI** with NaSMe solution[197] using adapted literature procedures (Scheme 4). After saponication of the precursors **23a** and **d** with potassium hydroxide in isopropanol or *tert*-butanol according to a standard procedure for PBIs,[190] the target PBI dyes **Cl-PBI** and **MeS-PBI** were obtained by imidization of the respective bay-substituted perylene bisanhydrides **24a** and **d** with *N*-(2-aminoethyl)-3,4,5-tris(dodecyloxy)benzamide **25**.[129,165]

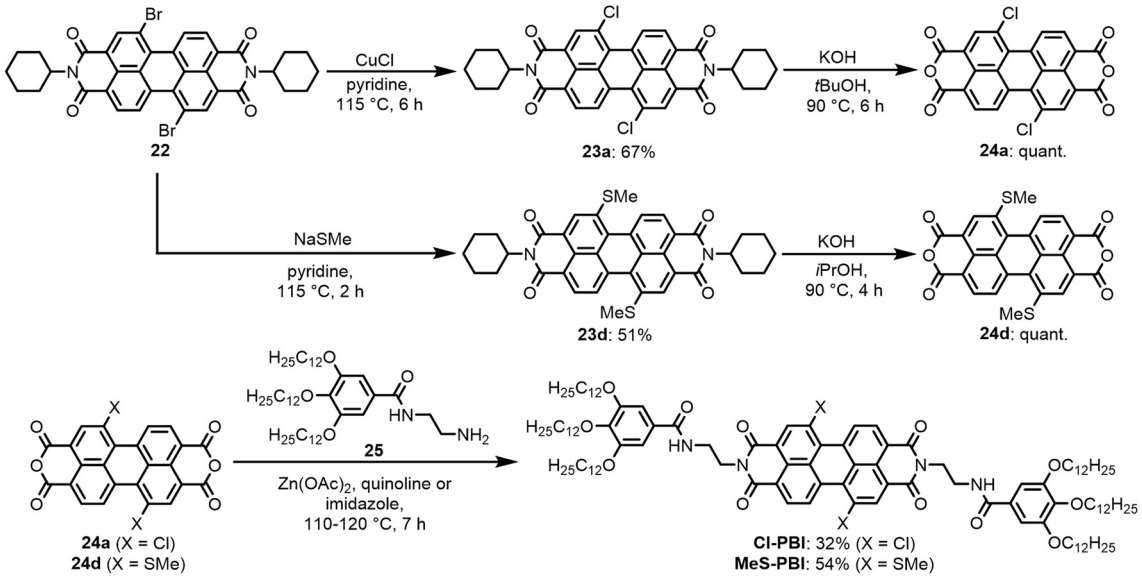


**Scheme 4.** Synthetic routes to 1,7-bay-substituted perylene bisimides **Cl-PBI** and **MeS-PBI**.

The compounds **22**[190] and **25**[129,165] were synthesized according to literature known procedures.

**_N,N'_-Dicyclohexyl-1,7-dichloroperylene-3,4:9,10-tetracarboxylic acid bisimide 23a**

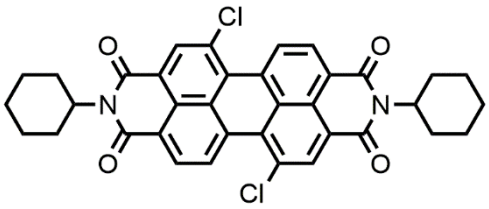

_N,N'_-Dicyclohexyl-1,7-dibromoperylene-3,4:9,10-tetracarboxylic acid bisimide **22** (262 mg, 0.368 mmol) and CuCl (492 mg, 4.97 mmol) were suspended in pyridine (15 mL) and the reaction mixture was stirred at 115 °C for 6 h under nitrogen atmosphere. The solvent was evaporated under reduced pressure and the crude product was dissolved in DCM (20 mL). The insoluble impurities were removed by filtration with Celite. The resulting crude product was purified by column chromatography on silica gel (DCM) and dried in vacuum.

**Yield**: 154 mg (247 µmol, 67%), orange solid.

**M.p.** > 350 °C.

**$^1$H NMR** (400 MHz, $CDCl_3$, 295 K): $\delta$ [ppm] = 9.45 (d, $^3J$ = 8.2 Hz, 2 H), 8.69 (s, 2 H), 8.67 (d, $^3J$ = 8.2 Hz, 2 H), 5.07-4.99 (m, 2 H), 2.60-2.50 (m, 4 H), 1.95-1.90 (m, 4 H), 1.79-1.74 (m, 6 H), 1.50-1.35 (m, 6 H).

**$^{13}$C NMR** (100 MHz, $CDCl_3$, 295 K): $\delta$ [ppm] = 163.5, 163.0, 134.8, 132.6, 132.4, 131.1, 130.3, 129.5, 129.0, 126.8, 123.8, 123.7, 54.4, 29.2, 26.6, 25.5.

**HRMS** (ESI, positive, chloroform/acetonitrile): *m/z* calculated for $C_{36}H_{28}Cl_2N_2O_4$ $[M]^+$: 622.1426, found: 622.1452.

**1,7-Dichloroperylene-3,4:9,10-tetracarboxylic acid bisanhydride 24a**

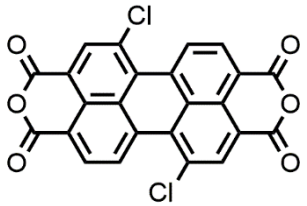

_N,N'_-Dicyclohexyl-1,7-dichloroperylene-3,4:9,10-tetracarboxylic acid bisimide **23a** (50.0 mg, 80.2 µmol) and KOH (230 mg, 4.09 mmol) were dissolved in *tert*-butanole (15 mL) and stirred at 90 °C for 6 h under nitrogen atmosphere. The reaction mixture was cooled to *rt* and 1N HCl (15 mL) was added. The suspension was stirred for 10 min at room

temperature and the precipitate was concentrated by centrifugation and collected by filtration.

**Yield**: 37.0 mg (80.2 µmol, quantitative), red solid.

The resulting crude product was dried in vacuum and used for the next reaction without further purification.

***N,N'*-(2-(3,4,5-Tris(dodecyloxy)benzamido)ethyl)-1,7-dichloroperylene-3,4:9,10-tetracarboxylic acid bisimide Cl-PBI**

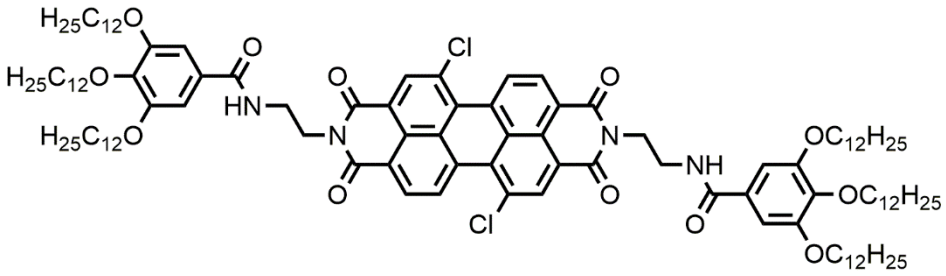


A mixture of 1,7-dichloroperylene-3,4:9,10-tetracarboxylic acid bisanhydride **24a** (37.0 mg, 80.2 µmol), *N*-(2-aminoethyl)-3,4,5-tris(dodecyloxy)-benzamide **25** (143 mg, 200 µmol), $Zn(OAc)_2$ (33.0 mg, 176 µmol) in quinoline (15 mL) was stirred at 110 °C for 7 h under nitrogen atmosphere. After cooling to *rt*, the reaction mixture was diluted with $CHCl_3$ (25 mL) and washed twice with aqueous 1N HCl (25 mL). The solvent was removed under reduced pressure and the obtained crude product was purified by column chromatography on silica gel ($CHCl_3$:MeOH 99.5 : 0.5, v/v) followed by preparative TLC ($CHCl_3$:MeOH 99.25:0.75, v/v). The resulting solid was dissolved in 2.5 mL of chloroform and then precipitated with methanol. The obtained precipitate was concentrated by centrifugation and dried in high vacuum.

**Yield**: 47.0 mg (25.3 µmol, 32%), red solid.

**M.p.** 263-266 °C.

**$^1$H NMR** (600 MHz, TCE-$d_2$, 345 K): $\delta$ [ppm] = 9.52 (d, $^3J$ = 8.2 Hz, 2 H), 8.78 (s, 2 H), 8.74 (d, $^3J$ = 8.2 Hz, 2 H), 6.97 (s, 4 H), 6.74 (t, $^3J$ = 4.9 Hz, 2 H), 4.59-4.52 (m, 4 H), 4.08-3.95 (m, 12 H), 3.91-3.86 (m, 4 H), 1.89-1.69 (m, 12 H), 1.65-1.22 (m, 108 H), 0.96-0.86 (m, 18 H).

**$^{13}$C NMR** (150 MHz, TCE-$d_2$, 345 K): $\delta$ [ppm] = 167.2, 163.3, 163.0, 153.0, 141.4, 134.7, 132.6, 132.5, 131.3, 130.3, 129.3, 128.9, 126.7, 122.8, 122.7, 105.9, 99.5, 69.4, 39.9, 39.7, 31.7, 31.7, 30.2, 29.5, 29.5, 29.5, 29.4, 29.4, 29.3, 29.3, 29.2, 29.1, 29.1, 29.0, 26.0, 25.9, 22.4, 13.9.

**HRMS** (ESI, positive, chloroform/acetonitrile): *m/z* calculated for $C_{114}H_{170}Cl_2N_4NaO_{12}$ $[M+Na]^+$: 1880.2085, found: 1880.2031

**UV/vis** ($CHCl_3$ at $10 \times 10^{-6}$ M): $\lambda_{max}$ / nm ($\varepsilon_{max}$ / L mol$^{-1}$ cm$^{-1}$) = 525 (50000).

### *N*,*N'*-Dicyclohexyl-1,7-di(methylthio)perylene-3,4:9,10-tetracarboxylic acid bisimide 23d

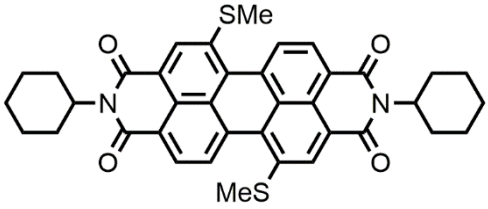


*N*,*N'*-Dicyclohexyl-1,7-dibromoperylene-3,4:9,10-tetracarboxylic acid bisimide **22** (200 mg, 281 µmol) and sodiumthiomethoxide (80.5 mg, 1.15 mmol) were suspended in pyridine (15 mL) and the reaction mixture was stirred at 115 °C for 2 h under nitrogen atmosphere. The solvent was evaporated under reduced pressure and the resulting crude product was purified by column chromatography on silica gel (DCM:cyclohexane 9:1, v/v) and dried in vacuum.

**Yield**: 92.4 mg (143 µmol, 51%), dark purple solid.

**M.p.** > 350 °C.

**$^1$H NMR** (400 MHz, $CDCl_3$, 295 K): $\delta$ [ppm] = 8.85 (d, $^3J$ = 8.1 Hz, 2 H), 8.73 (s, 2 H), 8.66 (d, $^3J$ = 8.1 Hz, 2 H), 5.10-5.02 (m, 2 H), 2.73 (s, 6 H), 2.64-2.53 (m, 4 H), 1.95-1.90 (m, 4 H), 1.81-1.71 (m, 6 H), 1.51-1.32 (m, 6 H).

**$^{13}$C NMR** (100 MHz, $CDCl_3$, 295 K): $\delta$ [ppm] = 164.1, 164.0, 139.5, 132.8, 132.1, 129.8, 129.1, 128.8, 128.5, 125.6, 122.7, 122.4, 54.2, 29.3, 26.7, 25.6, 19.0.

**HRMS** (ESI, positive, chloroform/acetonitrile): *m/z* calculated for $C_{38}H_{34}N_2O_4S_2$ $[M]^+$: 646.1954, found: 646.1949.

**1,7-Di(methylthio)perylene-3,4:9,10-tetracarboxylic acid bisanhydride 24d**

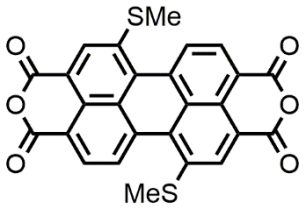


*N*,*N'*-Dicyclohexyl-1,7-di(methylthio)perylene-3,4:9,10-tetracarboxylic acid bisimide **23d** (48.4 mg, 74.8 µmol) and KOH (258 mg, 4.61 mmol) were dissolved in *iso*-propanole (20 mL) and stirred at 90 °C for 4 h under nitrogen atmosphere. The reaction mixture was cooled to *rt* and aqueous 1N HCl (25 mL) was added. The suspension was stirred for 10 min at room temperature and the precipitate was separated by centrifugation.

**Yield**: 36.2 mg (74.8 µmol, quantitative), dark purple solid.

The resulting crude product was dried in vacuum and used for the next reation without further purification.

***N*,*N'*-(2-(3,4,5-Tris(dodecyloxy)benzamido)ethyl)-1,7-di(methylthio)perylene-3,4:9,10-tetracarboxylic acid bisimide MeS-PBI**

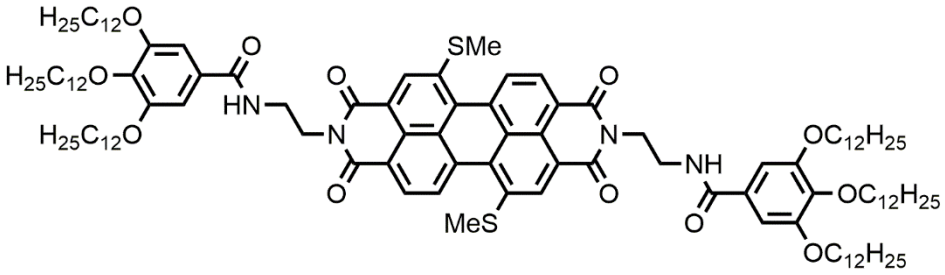


A mixture of 1,7-di(methylthio)perylene-3,4:9,10-tetracarboxylic acid bisanhydride **23d** (30.1 mg, 62.1 µmol), *N*-(2-aminoethyl)-3,4,5-tris(dodecyloxy)-benzamide **25** (102 mg, 142 µmol), $Zn(OAc)_2$ (42.3 mg, 231 µmol) in imidazole (5.00 g) was stirred at 115 °C for 7 h under nitrogen atmosphere. After cooling to room temperature, the reaction mixture was diluted with $CHCl_3$ (25 mL) and washed with aqueous 1N HCl solution (50 mL) and water (50 mL). The solvent was removed under reduced pressure and the obtained crude product was purified by column chromatography on silica gel ($CHCl_3$:MeOH 99.5:0.5, v/v) followed by preparative TLC ($CHCl_3$:MeOH 99.75:0.25, v/v). The resulting solid was dissolved in ca. 2 mL of chloroform and then precipitated with methanol (20 mL). The obtained precipitate was concentrated by centrifugation and was dried in high vacuum.

**Yield**: 62.4 mg (33.1 µmol, 54%), purple solid.

**M.p.** 287-289 °C.

**$^{1}$H NMR** (600 MHz, TCE-$d_2$, 345 K): $\delta$ [ppm] = 8.99 (d, $^{3}J$ = 8.0 Hz, 2 H), 8.81 (s, 2 H), 8.71 (d, $^{3}J$ = 8.0 Hz, 2 H), 7.00 (s, 4 H), 6.82 (t, $^{3}J$ = 4.9 Hz, 2 H), 4.61-4.55 (m, 4 H), 4.08-3.98 (m, 12 H), 3.92-3.86 (m, 4 H), 2.77 (s, 6 H), 1.89-1.73 (m, 12 H), 1.60-1.26 (m, 108 H), 0.96-0.88 (m, 18 H).

**$^{13}$C NMR** (150 MHz, TCE-$d_2$, 345 K): δ[ppm] = 167.1, 164.0, 163.8, 152.9, 141.4, 139.8, 133.1, 132.4, 130.4, 129.1, 129.0, 128.7, 128.4, 125.5, 121.7, 121.5, 106.0, 69.4, 39.8, 31.7, 31.7, 30.2, 29.5, 29.5, 29.5, 29.4, 29.4, 29.3, 29.2, 29.1, 29.1, 26.0, 25.9, 22.4, 18.8, 13.9.

**HRMS** (ESI, positive, chloroform/acetonitrile): *m/z* calculated for $C_{116}H_{176}N_4NaO_{12}S_2$ $[M+Na]^+$: 1904.2618, found: 1904.2531

**UV/vis** ($CHCl_3$ at $10 \times 10^{-6}$ M): $\lambda_{max}$ / nm ($\varepsilon_{max}$ / L mol$^{-1}$ cm$^{-1}$) = 579 (29500).

## Optical properties of the PBI monomers and aggregates

**Table 3.** Summary of the absorption properties of monomeric PBIs in $CHCl_3$ and of the equilibrated aggregates in MCH/Tol (2:1, v/v) at 23 °C obtained by UV/vis spectroscopy.

| | monomer[a] | | aggregate[b] | |
|---|---|---|---|---|
| | $\lambda_{max}$ / nm | $\varepsilon_{max}$ / M$^{-1}$ cm$^{-1}$ | $\lambda_{abs}$ / nm | $\varepsilon_{max}$ / M$^{-1}$ cm$^{-1}$ |
| **MeO-PBI** | 577 | 60000 | 655 | 20500 |
| **Cl-PBI** | 525 | 50000 | 543 | 20500 |
| **MeS-PBI** | 579 | 29500 | 624 | 15500 |

[a] Solutions in $CHCl_3$ ($c_T = 10 \times 10^{-6}$ M). [b] Solutions in MCH/Tol (2:1, v/v, $c_T = 15 \times 10^{-6}$ M).

**Thermodynamically controlled self-assembly**

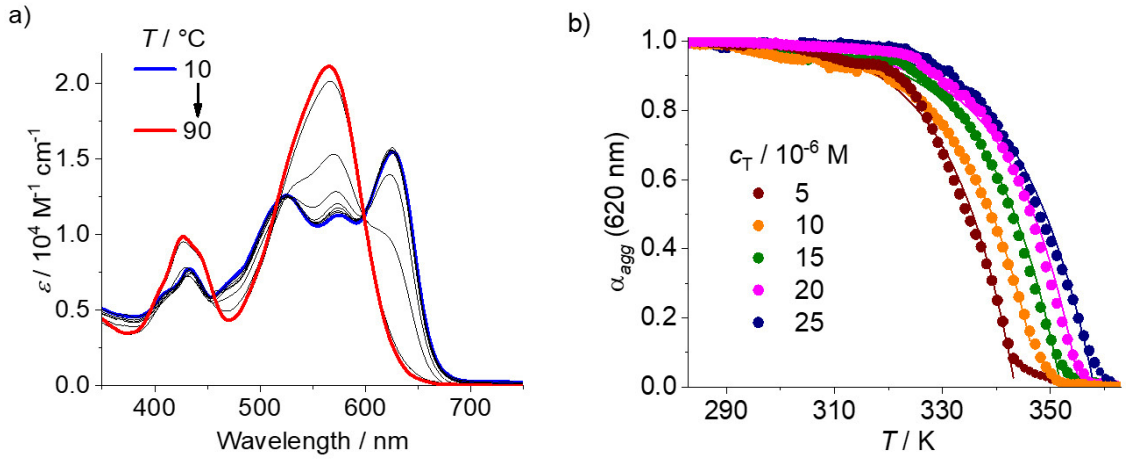


**Figure 68.** a) Temperature-dependent UV/vis spectra of **MeS-PBI** in MCH/Tol 2:1 (v/v) upon heating from 10 to 90 °C with a rate of 1 °C/min ($c_T$ = 15 × $10^{-6}$). b) Plots of the degree of aggregation, calculated from the apparent extinction coefficients, against the temperature for the disassembly processes and the respective fits of the elongation processes with the nucleation-elongation model for different total concentrations $c_T$.

**Table 4.** Thermodynamic parameters $\alpha_{sat}$, $\Delta H_e$, $T_e$ and $K_a$ obtained by fitting the temperature-dependent degree of aggregation of **Cl-PBI** in MCH/Tol 2:1 (v/v) with the cooperative model for different concentrations $c_T$.

| $c_T$ / µM | $\alpha_{sat}$ [a] | $\Delta H_e$ / kJ mol$^{-1}$ [b] | $T_e$ / K [c] | $K_a$ [d] |
|---|---|---|---|---|
| 5 | 1.0120 | −83.7 | 327.9 | 2.4 × $10^{-4}$ |
| 10 | 1.0467 | −81.6 | 330.5 | 3.6 × $10^{-4}$ |
| 15 | 1.0537 | −83.3 | 332.4 | 2.7 × $10^{-4}$ |
| 20 | 1.0383 | −83.5 | 335.2 | 5.7 × $10^{-4}$ |
| 25 | 1.0167 | −84.5 | 339.1 | 7.8 × $10^{-4}$ |

[a] Saturation parameter, [b] elongation enthalpy, [c] elongation temperature, [d] dimensionless equilibrium constant of the activation step.

**Table 5.** Thermodynamic parameters $\alpha_{sat}$, $\Delta H_e$, $T_e$ and $K_a$ obtained by fitting the temperature-dependent degree of aggregation of **MeS-PBI** in MCH/Tol 2:1 (v/v) with the cooperative model for different concentrations $c_T$.

| $c_T$ / μM | $\alpha_{sat}$ [a] | $\Delta H_e$ / kJ mol$^{-1}$ [b] | $T_e$ / K [c] | $K_a$ [d] |
|---|---|---|---|---|
| 5 | 1.01351 | −84.8 | 343.5 | $1.1 \times 10^{-3}$ |
| 10 | 0.9899 | −80.2 | 348.0 | $8.0 \times 10^{-4}$ |
| 15 | 0.9971 | −83.6 | 352.0 | $5.6 \times 10^{-4}$ |
| 20 | 0.9832 | −87.7 | 355.4 | $3.0 \times 10^{-4}$ |
| 25 | 1.0152 | −80.2 | 358.1 | $3.7 \times 10^{-4}$ |

[a] Saturation parameter, [b] elongation enthalpy, [c] elongation temperature, [d] dimensionless equilibrium constant of the activation step.

**Table 6.** Comparison of the averaged thermodynamic parameters $\Delta H_e$, $K_a$, $\langle \boldsymbol{N_N(T_e)} \rangle$ and $\Delta G^0$ obtained by fitting the UV/vis data in MCH/Tol 2:1 (v/v) of the thermodynamically controlled heating processes with nucleation-elongation model.

| | $\Delta H_e$ / kJ mol$^{-1}$ | $K_a$ | $\langle \boldsymbol{N_N(T_e)} \rangle$ | $\Delta G^0$ / kJ mol$^{-1}$ [a] |
|---|---|---|---|---|
| **MeO-PBI**[62] | −86.4 | $1.4 \times 10^{-3}$ | 9 | −44.0 |
| **Cl-PBI** | −83.3 | $4.4 \times 10^{-4}$ | 13 | −43.4 |
| **MeS-PBI** | −83.3 | $6.3 \times 10^{-4}$ | 12 | −43.7 |

[a]Values obtained by van't Hoff plot analysis.

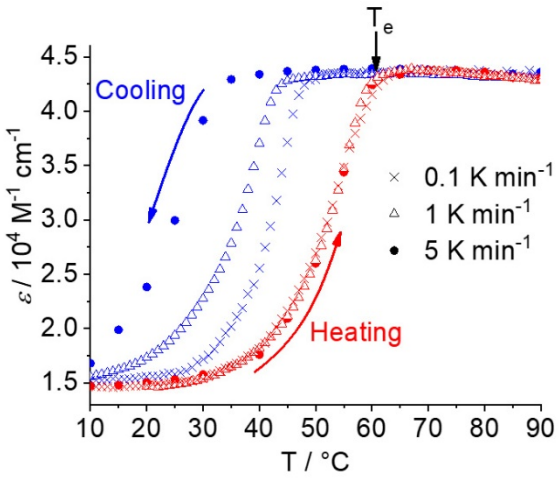


**Figure 69.** Plots of the temperature-dependent extinction coefficients at 518 nm ($\lambda_{max}$ of **Cl-PBI$_{mono}$**) of **Cl-PBI** ($c_T = 15 \times 10^{-6}$ M) in MCH/Tol 2:1 (*v*/*v*) for the aggregation (blue) and disassembly (red) processes, respectively, with different cooling/heating rates.

**Morphology of the aggregates investigated by AFM**

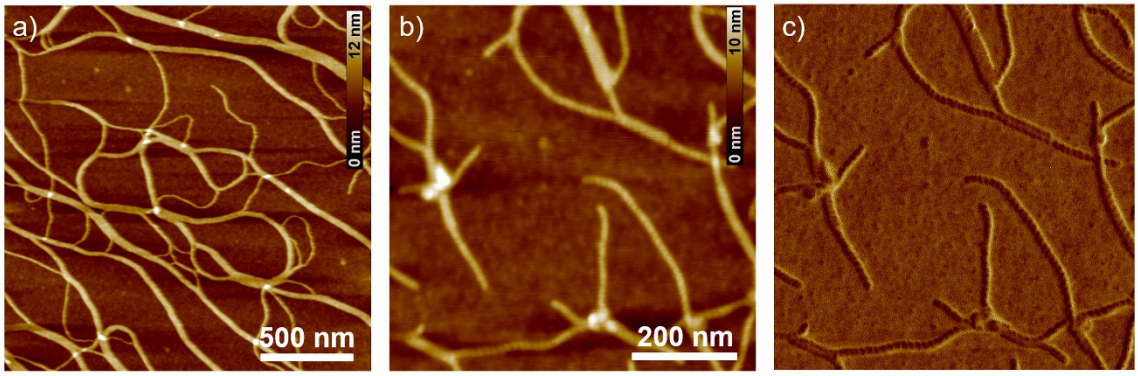


**Figure 70.** AFM height (a,b) and phase (c) images of samples prepared by spin-coating of **Cl-PBI** aggregate solutions in MCH/Tol (2:1, v/v) onto a silicon wafer. *Z* scale is 12 nm (a) and 10 nm (b).

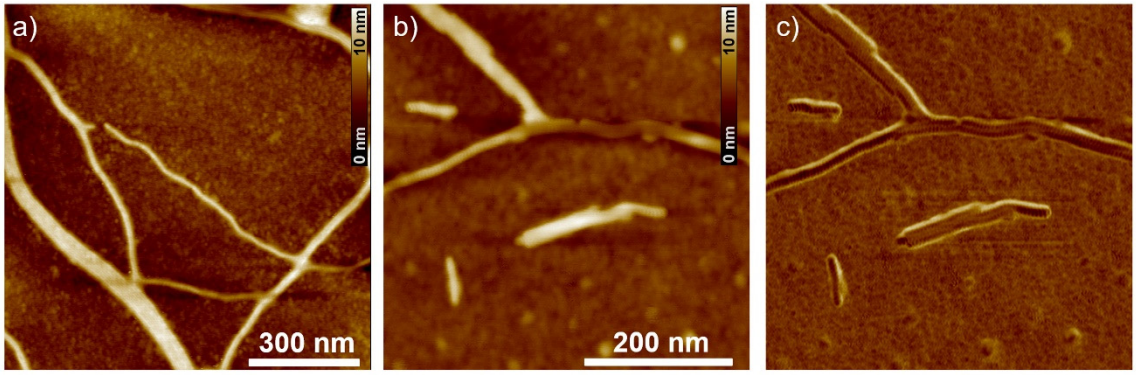


**Figure 71.** AFM height (a,b) and phase (c) images of samples prepared by spin-coating of **MeS-PBI** aggregate solutions in MCH/Tol (2:1, v/v) onto a silicon wafer. *Z* scale is 10 nm (a,b).

**Table 7.** Summary of the values obtained by atomic force microscopy.

| | Heigth / nm | Helical pitch / nm | Molecules per helical pitch [a] |
|---|---|---|---|
| **H-PBI$_{agg}$**[57] | 3.1 | 15 | 43 |
| **MeO-PBI$_{agg}$**[62] | 4.0 | 5.0 | 14 |
| **Cl-PBI$_{agg}$** | 3.6 | 10 | 29 |
| **MeS-PBI$_{agg}$** | 4.0 | 5.0 | 14 |

[a]Values are calculated for an unimolecular strand and an estimated $\pi$-$\pi$-distance of 3.5 Å.

**Formation of kinetically trapped aggregates**

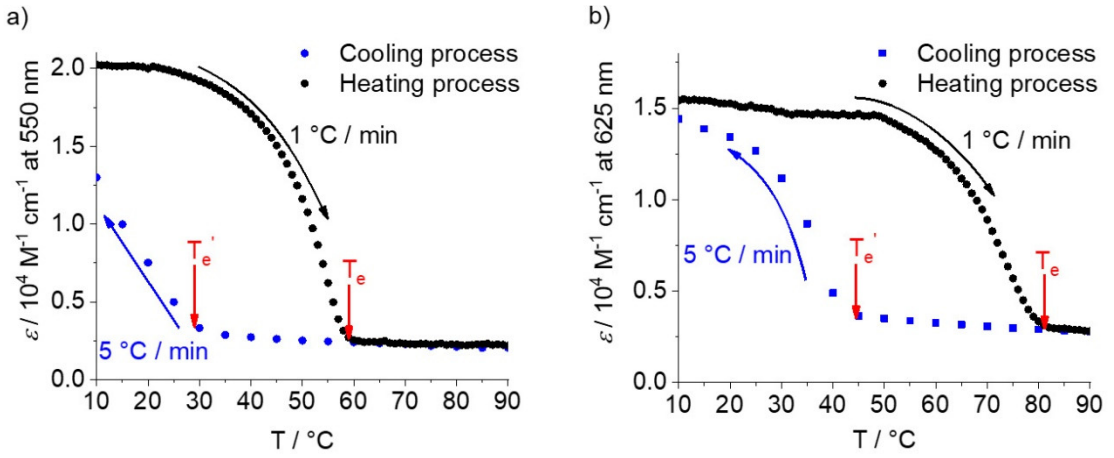


**Figure 72.** Temperature-dependent apparent extinction coefficients of **Cl-PBI** (a) and **MeS-PBI** (b) in MCH/Tol (2:1, v/v) observed in the cooling (blue) processes at a rate of 5 °C / min and heating (black) processes at a rate of 1 °C / min ($c_T$ = 15 × $10^{-6}$ M).

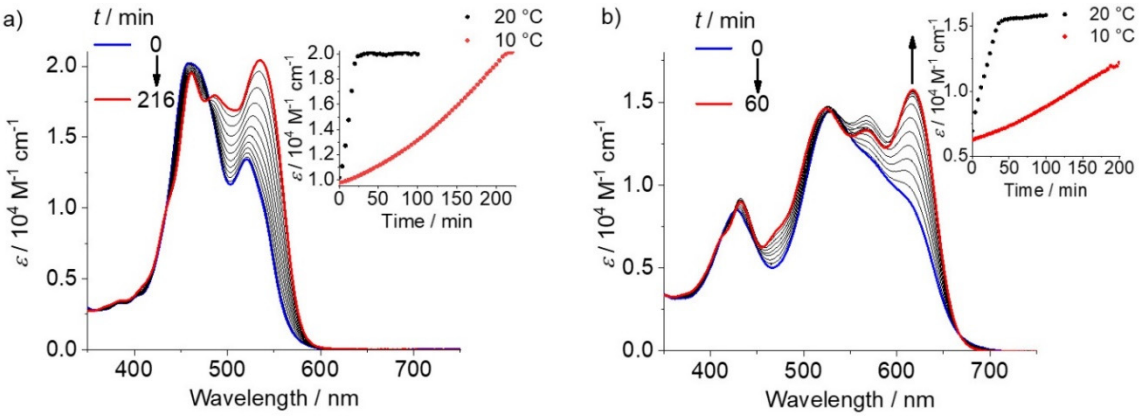


**Figure 73.** Time-dependent UV/vis spectra of **Cl-PBI** (a) and **MeS-PBI** (b) in a solvent mixture of MCH/Tol (2:1, v/v, $c_T$ = 15 × $10^{-6}$ M) after rapid cooling (15 °C/min) from 90 to 20 °C or 90 to 10 °C, respectively. The plots of the apparent extinction coefficients of **Cl-PBI** at 540 nm and **MeS-PBI** at 620 nm against the time after rapid cooling to 20 and 10 °C are shown in insets of (a) and (b), respectively.

**Self-seeded supramolecular polymerization of PBIs**

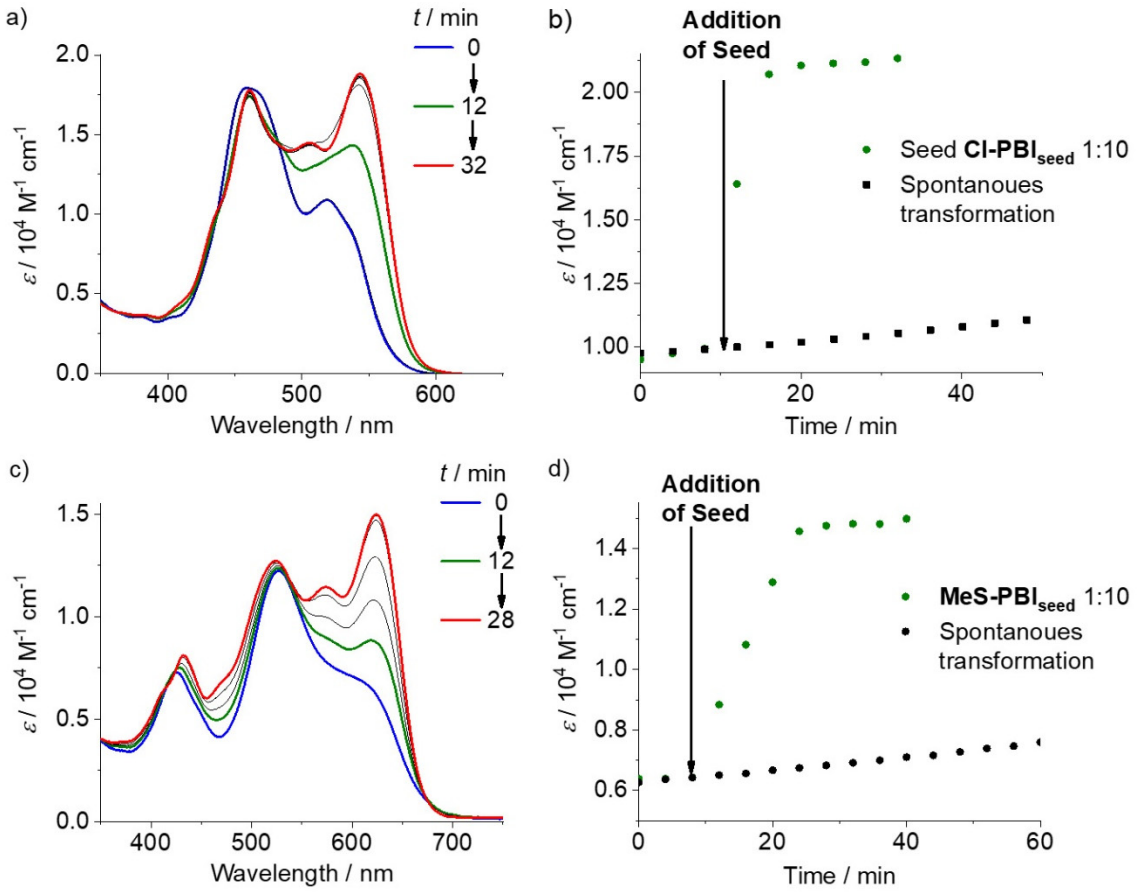


**Figure 74.** Time-dependent UV/vis spectra of the self-seeded supramolecular polymerization of **Cl-PBI$_{trapped}$** with **Cl-PBI$_{seed}$** (a) and **MeS-PBI$_{trapped}$** with **MeS-PBI$_{seed}$** (c) in a molar seed ratio of 1:10 ($c_T = 15 \times 10^{-6}$ M, MCH/Tol 2:1, v/v). Plot of the molar extinction coefficients of the respective seeded polymerization at 543 nm (b) and 620 nm (d) against the time.

## Living polymerization of MeS-PBI and Cl-PBI

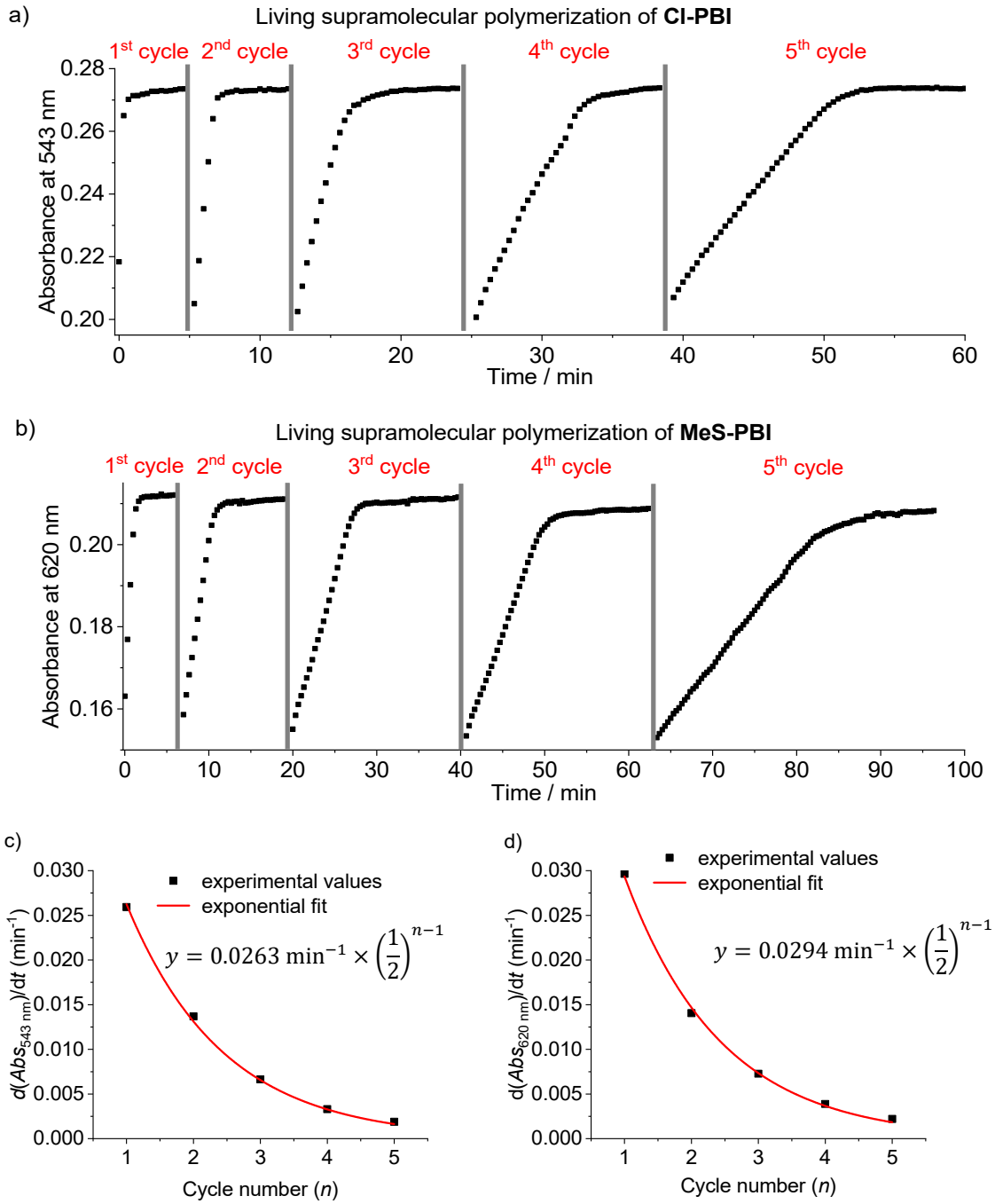


**Figure 75.** Time course of the apparent absorbance at 543 nm ($\lambda_{max}$ of **Cl-PBI$_{agg}$**) during the living polymerization of **Cl-PBI** (a) and at 620 nm ($\lambda_{max}$ of **MeS-PBI$_{agg}$**) during the living polymerization of **MeS-PBI** (b) at 10 °C. The gray areas indicate the time for opening the sample compartment to add the respective equivalent of **Cl-PBI$_{trapped}$** or **MeS-PBI$_{trapped}$**. Plot of the initial slope [min$^{-1}$] obtained by fitting of the first data points of the living polymerization of **Cl-PBI** (c) and **MeS-PBI** (d) with a linear relationship against the number of cycles ($n$). The values were fitted (red line) with an exponential function depicted as inset to illustrate that the slope is bisected by each cycle.

## Control experiment

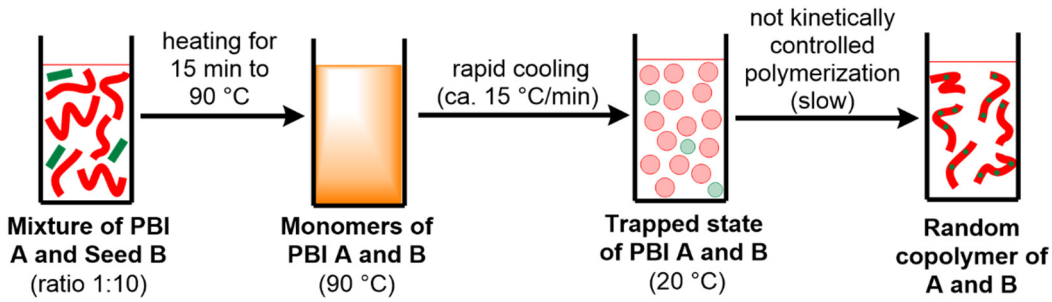


**Figure 76.** Schematic illustration of the thermodynamic control experiment of **PBI A** and **PBI B**.

## Thermodynamic stability of the A-B-A system

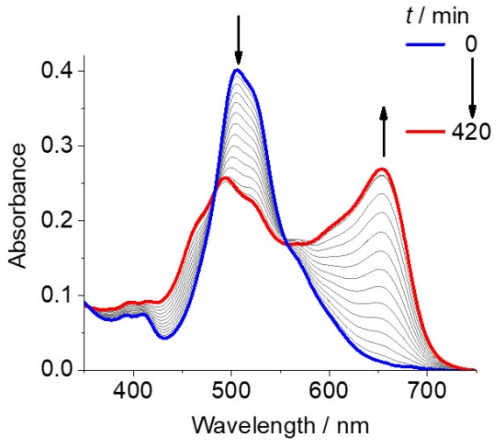


**Figure 77.** Time-dependent UV/vis spectra of the copolymerization of a mixture of **MeO-PBI$_{mono}$** and **Cl-PBI$_{mono}$** in a molecular ratio of 10:1 in MCH/Tol (2:1, v/v, $c_T$ = 15 × $10^{-6}$ M) after cooling from 90 to 20 °C.

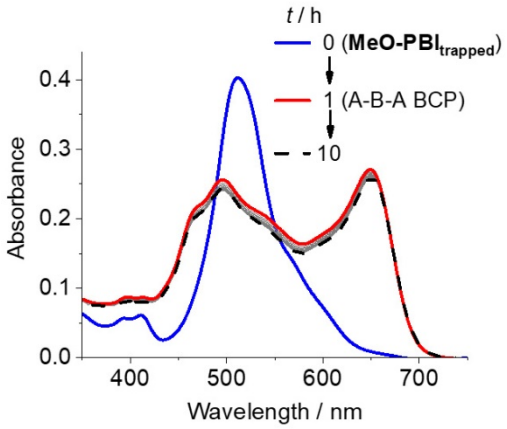


**Figure 78.** Time-dependent UV/vis spectra of the A-B-A block copolymer obtained by two-component seeded polymerization of **MeO-PBI$_{trapped}$** ($c_T$ = 15 × $10^{-6}$ M) with **Cl-PBI$_{seed}$** in MCH/Tol (2:1, v/v) with a seed ratio of 1:10 at 20 °C. The transformation of the kinetically trapped aggregate (blue line) into the block copolymer (red line) is already completed within 1 h and no further changes of the spectrum were observed until 10 h (black dotted line).

**Analysis of the UV/vis spectra of block copolymers A-B-A**

Under the assumption that the number of heterojunction points between the two components **MeO-PBI** and **Cl-PBI** in a block copolymer and thus their contribution to the overall absorption is negligibly low, the spectrum of the final block copolymer should be resembled by the calculated superposition of the spectrum of the aggregates of the individual PBIs in the respective molar ratios. Such an analysis supports the presence of blocks of the two J-aggregate species (**MeO-PBI$_{agg}$** and **Cl-PBI$_{agg}$**) because the exciton coupling between randomly aggregated **Cl-PBI** and **MeO-PBI** should provide entirely different spectra.

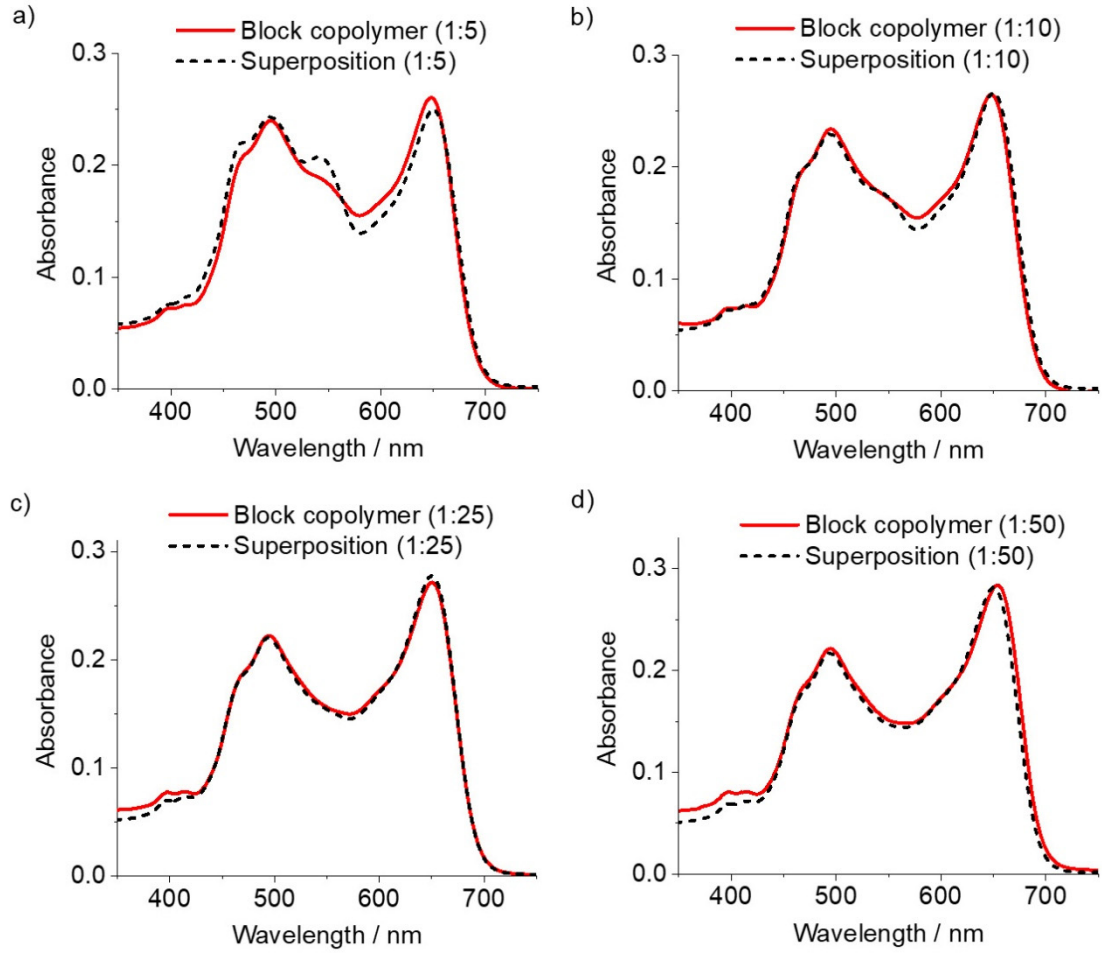


**Figure 79.** UV/vis spectrum of the block copolymer (red line) obtained after copolymerization of **Cl-PBI$_{seed}$** and **MeO-PBI$_{trapped}$** with a seed ratio of $c_T$(**Cl-PBI**) : $c_T$ (**MeO-PBI**) = 1:5 (a), 1:10 (b), 1:25 (c) and 1:50 (d) and the calculated spectrum (black dashed line) of the superposition with the respective ratio.

**Length analysis of the block copolymers of MeO-PBI$_{trapped}$ and Cl-PBI$_{seed}$**

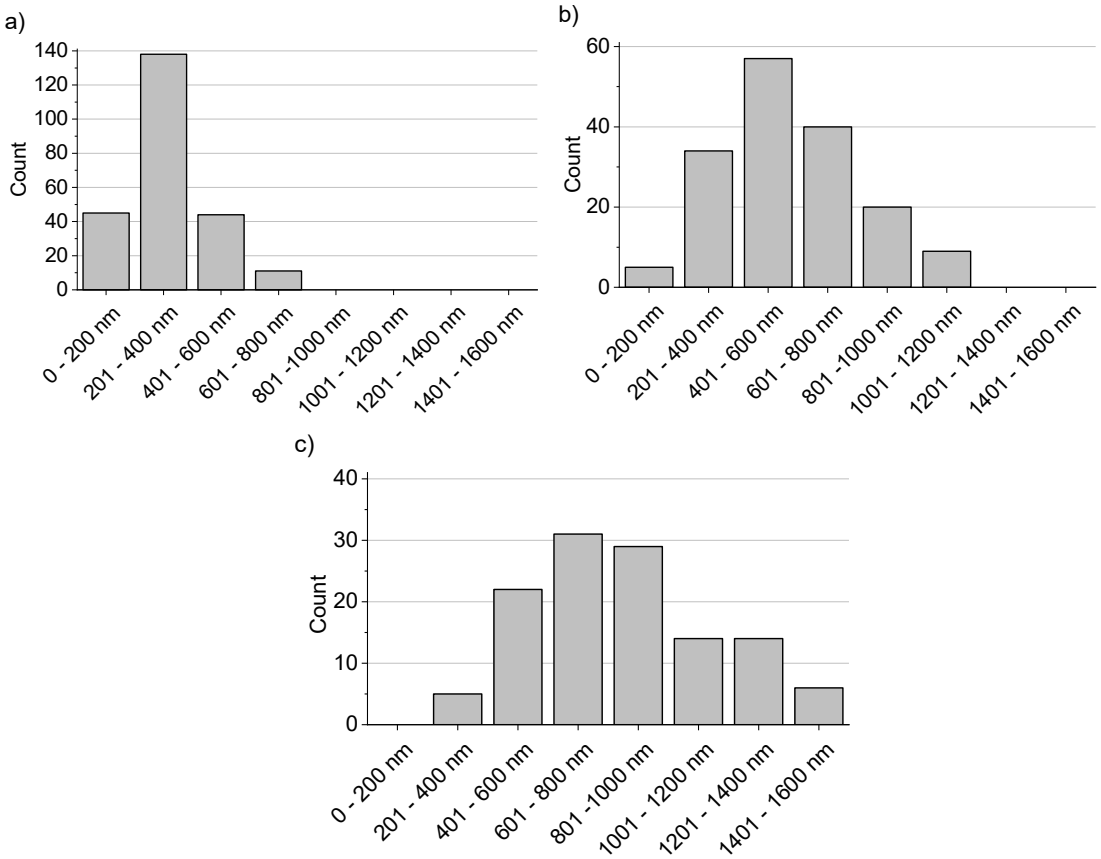


**Figure 80.** Histogram of the length distribution of block copolymers obtained by two-component seeded polymerization of **MeO-PBI$_{trapped}$** and with **Cl-PBI$_{seed}$** in different seed ratios of 1:2 (a), 1:5 (b) and 1:10 (c) obtained by analyzing the length of about 100-200 nanofibers by AFM.

**Time-dependent AFM studies of polymerization of MeO-PBI$_{trapped}$ with Cl-PBI$_{seed}$**

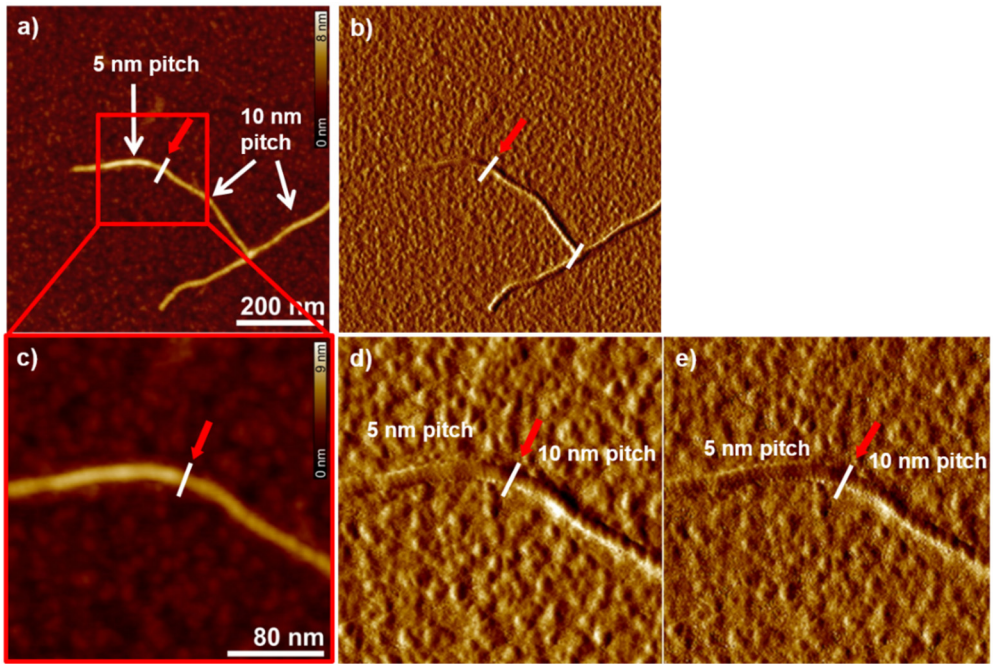


**Figure 81.** AFM height (a,c), phase (b,e) and amplitude (d) images of a sample prepared by spin-coating a solution in MCH/Tol (2:1, v/v) taken at 5 min after the addition of **Cl-PBI$_{seed}$** to **MeO-PBI$_{trapped}$** (seed ratio 1:10) onto silicon wafers. Z scale is 8 nm (a) and 9 nm (c). The red arrows indicate the position at which the helical pitch changes from 5 to 10 nm in the block copolymer.

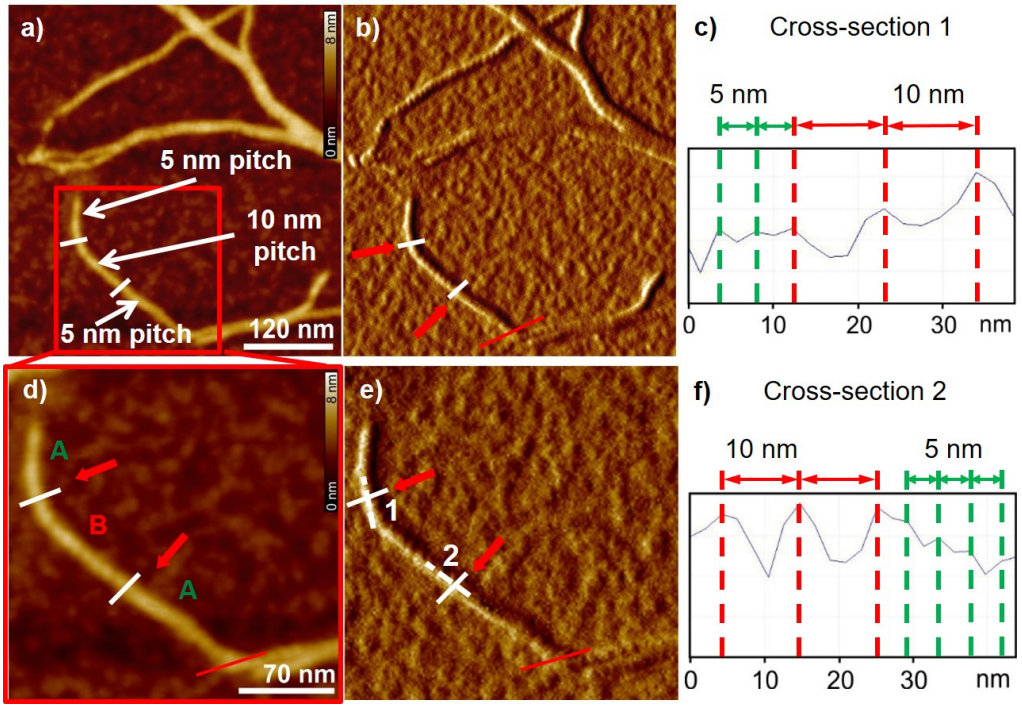


**Figure 82.** AFM height (a,d) and phase (b,e) images of a sample prepared by spin-coating a solution in MCH/Tol (2:1, v/v) taken at 10 min after addition of **Cl-PBI$_{seed}$** to **MeO-PBI$_{trapped}$** (seed ratio 1:10) onto silicon wafers. The Z scale is 8 nm (a,d). Cross-section analysis along the dashed white lines in image (e) demonstrating the change of the helical pitch from 5 to 10 nm (cross-section 1, c) and from 10 to 5 nm (cross-section 2, f). The red arrows indicate the position in the aggregate, where the helical pitch changes. The red line marks the end of the polymeric strand.

**Time-dependent UV/vis studies of polymerization of MeO-PBI$_{trapped}$ with MeS-PBI$_{seed}$**

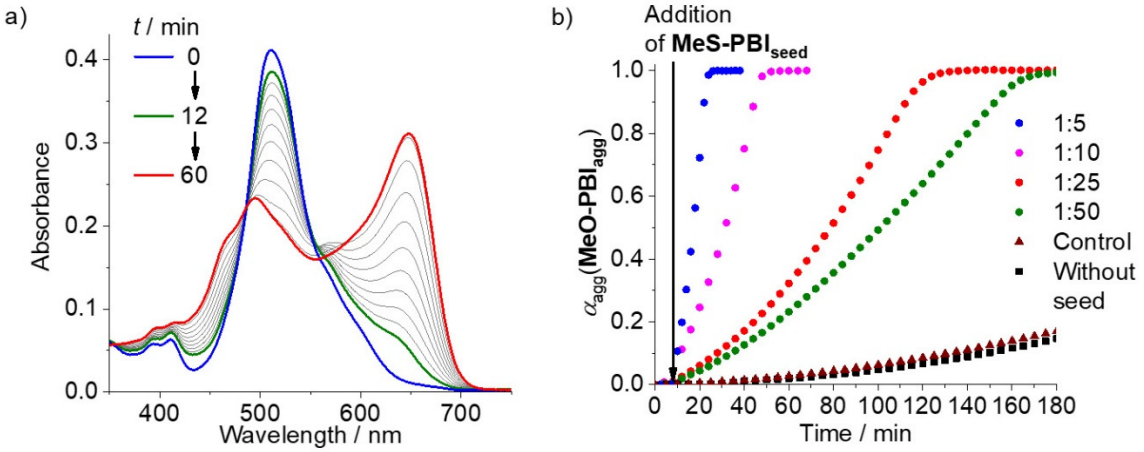


**Figure 83.** a) Time-dependent UV/vis spectra of the two-component seeded polymerization of **MeO-PBI$_{trapped}$** with **MeS-PBI$_{seed}$** (seed ratio $c_T$(**MeS-PBI$_{seed}$**) : $c_T$(**MeO-PBI$_{trapped}$**) = 1:10). b) Plots of the degree of aggregation of **MeO-PBI$_{agg}$**, calculated from the dilution corrected apparent extinction coefficient at 650 nm against the time for the two-component seeded polymerization upon addition of seed solutions of **MeS-PBI** (ratio $c_T$(**MeS-PBI$_{seed}$**) : $c_T$(**MeO-PBI$_{trapped}$** = 1:5 (blue dots), 1:10 (purple dots), 1:25 (red dots) and 1:50 (green dots)) at 20 °C. The respective thermodynamic control experiments (brown triangles) and the spontaneous polymerization of **MeO-PBI** (black squares) are shown for comparison.

**Seeded polymerization of MeO-PBI$_{trapped}$ with various seeds**

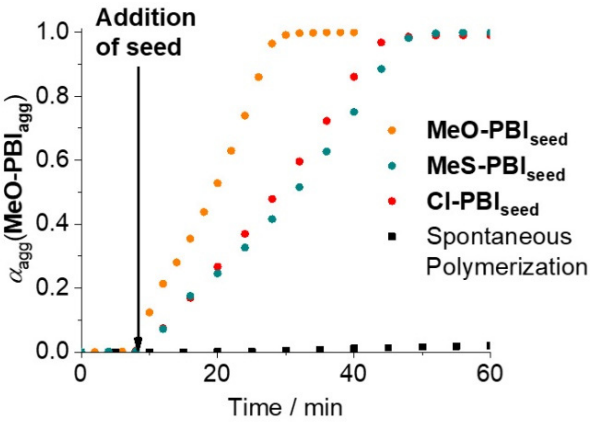


**Figure 84.** Plots of the degree of aggregation of **MeO-PBI$_{agg}$** calculated from the dilution corrected apparent extinction coefficient at 650 nm against the time upon addition of different seed solutions of **MeO-PBI**, **Cl-PBI** and **MeS-PBI** to **MeO-PBI$_{trapped}$** with a constant ratio of $c_T$(seed) : $c_T$(**MeO-PBI$_{trapped}$**) = 1:10. The spontaneous polymerization of **MeO-PBI** (black squares) is shown for comparison.

## Geometry optimized structures of the PBIs by DFT calculations

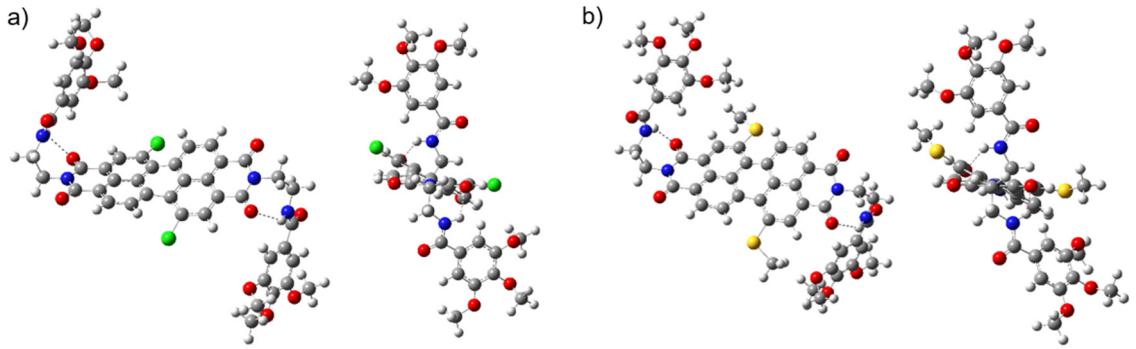


**Figure 85.** Top and front view of the energy minimized structures of the model compounds ($OC_{12}H_{25}$ residues are replaced by OMe) of **Cl-PBI** (a) and **MeS-PBI** (b) obtained by DFT calculations (Gaussian 09) with B3-LYP as functional and def2-SVP as basis set.[198-199]

**Table 8.** Summary of the calculated core twist angles $\alpha$ of the PBIs and length of the hydrogen-bonding $d$(N−H·····O=C) between the amide hydrogen of the spacer and the imide oxygen of the PBI.

| | $\alpha$ / °[a] | $d$(N−H·····O=C) / Å |
|---|---|---|
| **MeO-PBI**[62] | 11.4 | 2.1 |
| **Cl-PBI** | 20.5 | 2.3 |
| **MeS-PBI** | 20.0 | 2.1 |

[a] Dihedral angle associated with the four carbon atoms in the bay area.

## Comparison of the seeded polymerization of Cl-PBI$_{trapped}$ with various seeds

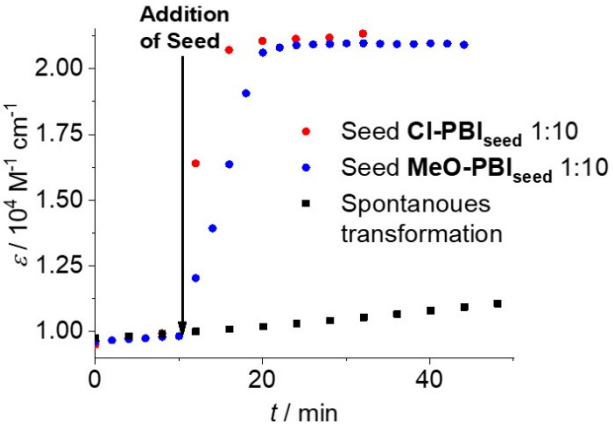


**Figure 86.** Plots of the dilution corrected apparent extinction coefficients of the seeded polymerization of **Cl-PBI** at 543 nm against the time upon addition of different seeds in a seed ratio of 1:10.

**Analysis of the spectra of the block copolymers B-A-B**

Under the assumption that the number of heterojunction points between the two components **MeO-PBI** and **Cl-PBI** in a block copolymer and thus their contribution to the overall absorption is negligibly low, the spectrum of the final block copolymer should be resembled by the calculated superposition of the spectrum of the aggregates of the individual PBIs in the respective molar ratios. Such an analysis supports the presence of blocks of the two J-aggregate species (**MeO-PBI$_{agg}$** and **Cl-PBI$_{agg}$**) because the exciton coupling between randomly aggregated **Cl-PBI** and **MeO-PBI** should provide entirely different spectra.

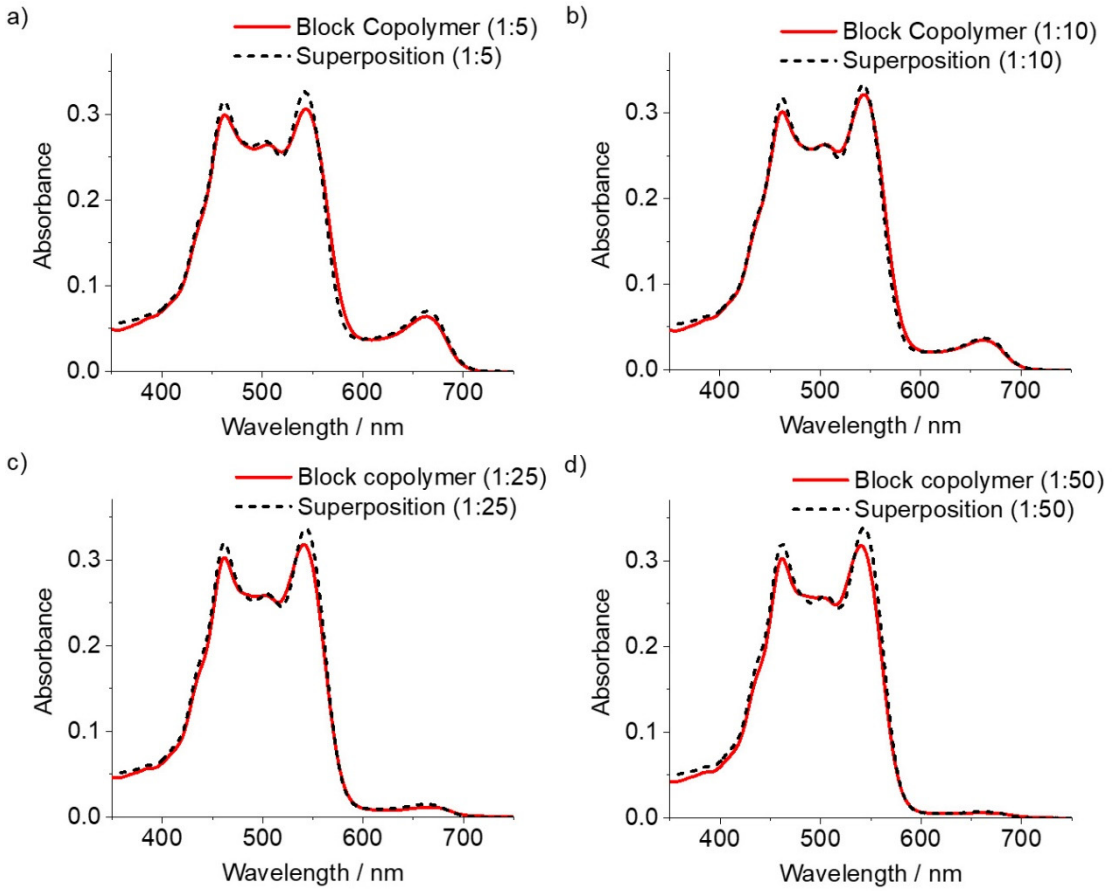


**Figure 87.** UV/vis spectrum of the block copolymer (red line) obtained after copolymerization of **MeO-PBI$_{seed}$** and **Cl-PBI$_{trapped}$** with a seed ratio of $c_T$(**MeO-PBI**) : $c_T$ (**Cl-PBI**) = 1:5 (a), 1:10 (b), 1:25 (c) and 1:50 (d) and calculated spectrum (black dashed line) of the superposition with the respective ratio.

**Thermodynamic stability of the B-A-B system**

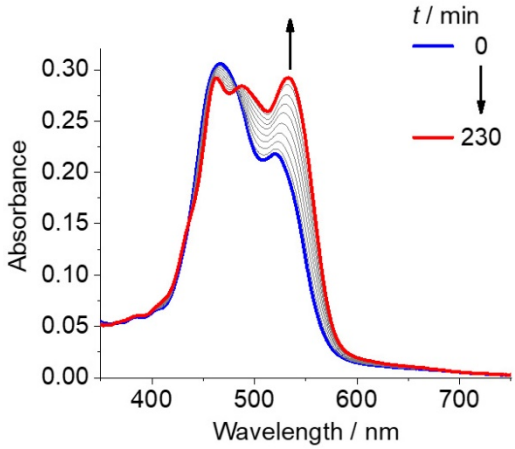


**Figure 88.** Time-dependent UV/vis spectra of the copolymerization of a mixture of **Cl-PBI$_{mono}$** and **MeO-PBI$_{mono}$** in a molecular ratio of 10:1 in MCH/Tol (2:1, v/v, $c_T$ = 15 × $10^{-6}$ M) after cooling from 90 to 10 °C.

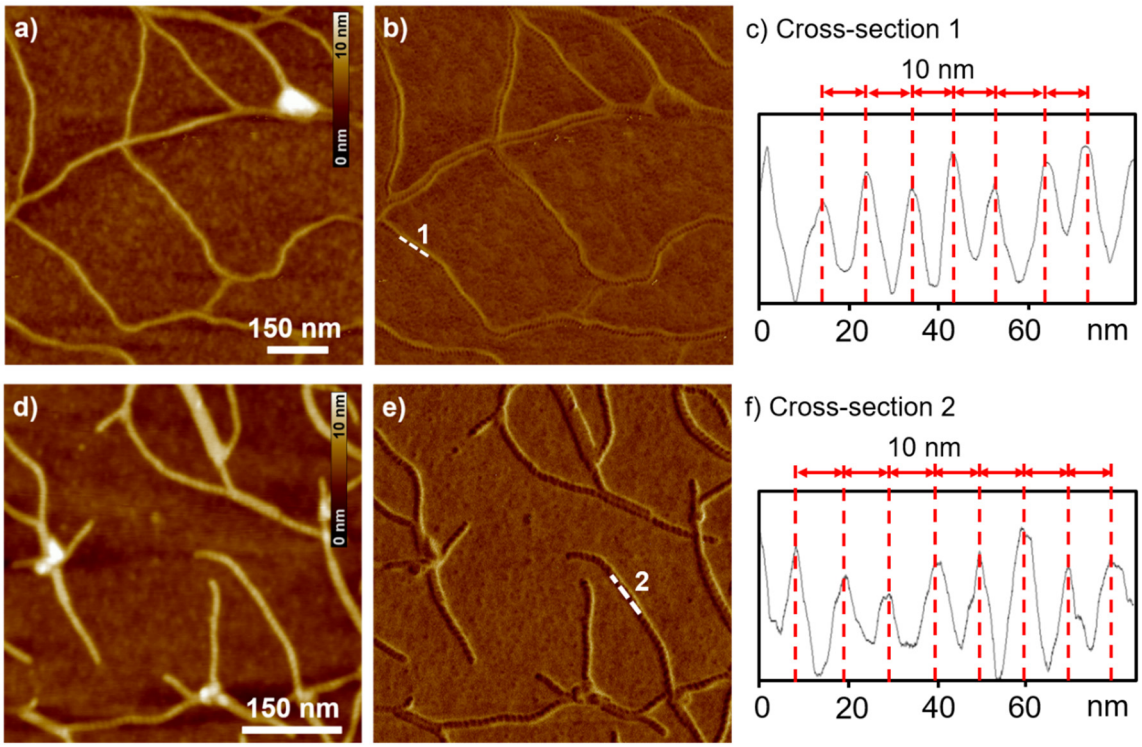


**Figure 89.** AFM height (a,d) and phase (b,e) images of a sample prepared by spin-coating the random polymers obtained by copolymerization of the monomeric mixture (a,b) of **MeO-PBI** and **Cl-PBI** (ratio 1:10) in MCH/Tol (2:1, v/v) after cooling from 90 to 10 °C (15 °C/min) or the pure **Cl-PBI** aggregate solution (d,e) onto a silicon wafer. *Z* scale is 10 nm (a,d). (c,f) Cross-section analysis along the dashed white lines in the respective phase images (b) or (e) demonstrating the helical pitch of the polymers of 10 nm.

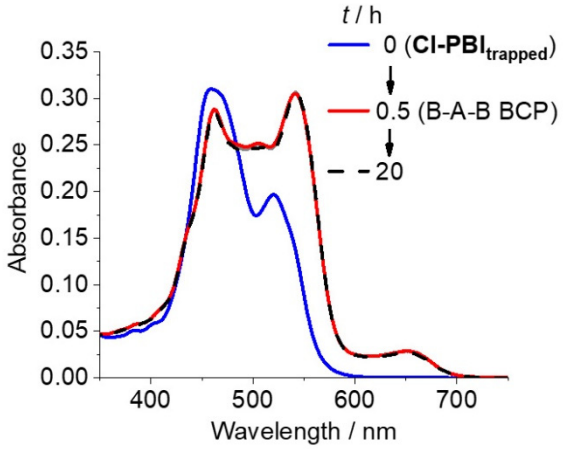


**Figure 90.** Time-dependent UV/vis spectra of the B-A-B block copolymer obtained by two-component seeded polymerization of **Cl-PBI$_{trapped}$** ($c_T$ = 15 × 10$^{-6}$ M) with **MeO-PBI$_{seed}$** in MCH/Tol (2:1, v/v) with a seed ratio of 1:10 at 10 °C. The transformation of the kinetically trapped aggregate (blue line) into the block copolymer (red line) is already completed within 30 min and no further changes of the spectrum were observed until 20 h (black dashed line).

## AFM studies of the copolymerization of Cl-PBI$_{trapped}$ with MeO-PBI$_{seed}$

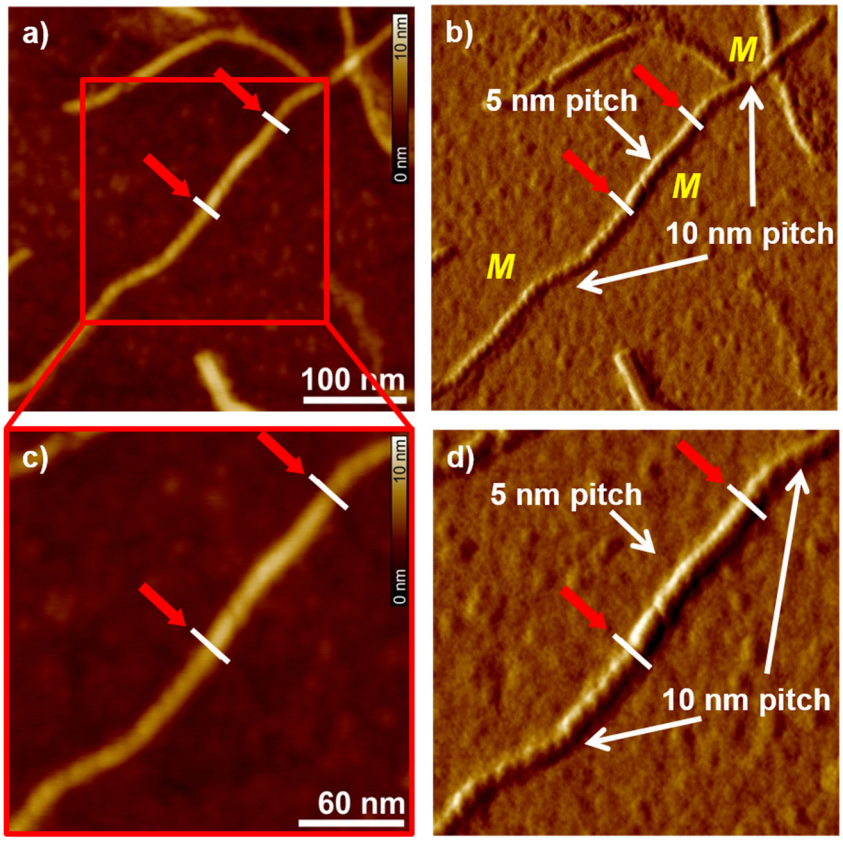


**Figure 91.** AFM height (a,c) and phase (b,d) images of a sample prepared by spin-coating a solution in MCH/Tol (2:1, v/v) taken at 4 min after addition of **MeO-PBI$_{seed}$** to **Cl-PBI$_{trapped}$** (seed ratio 1:10) onto silicon wafers. The Z scale is 10 nm (a,c). The red arrows indicate the position in the aggregate, where the helical pitch changes from 5 nm to 10 nm. In the phase image (b) the helicity (*M*) of an individual block copolymer is indicated.

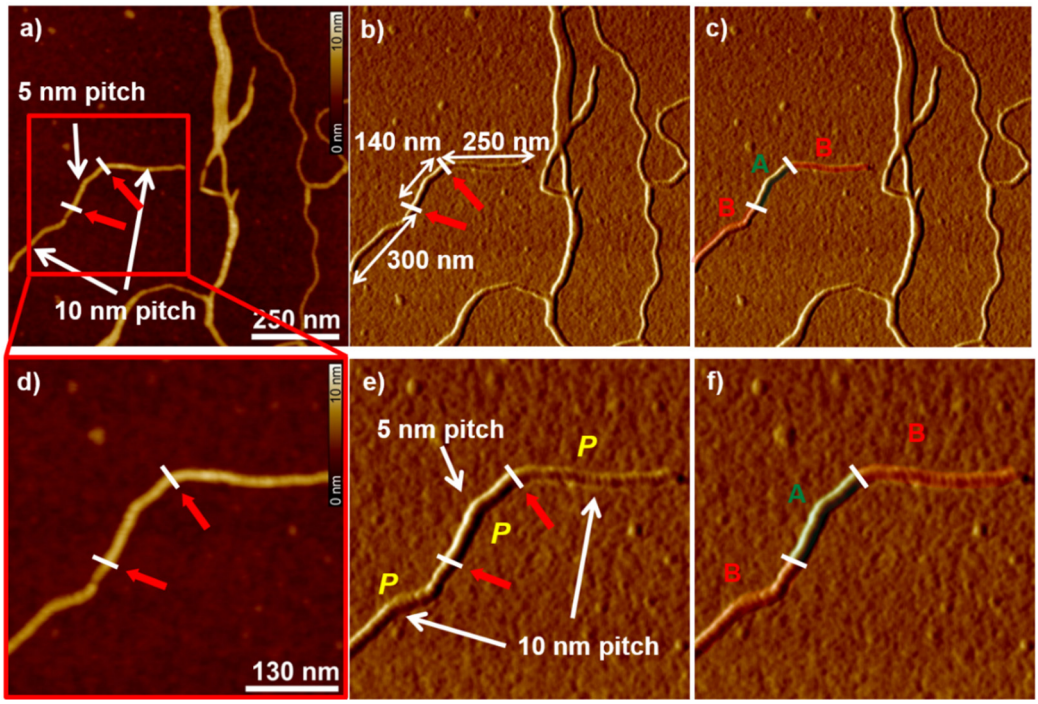


**Figure 92.** AFM height (a,d) and phase (b,c,e,f) images of a sample prepared by spin-coating a solution in MCH/Tol (2:1, v/v) taken at 8 min after addition of **MeO-PBI$_{seed}$** to **Cl-PBI$_{trapped}$** (seed ratio 1:10) onto silicon wafers. The Z scale is 10 nm (a,d). The red arrows indicate the position in the aggregate, where the helical pitch changes from 5 nm to 10 nm. In the image (c) and (f) blocks of **MeO-PBI$_{seed}$** (green) and **Cl-PBI$_{agg}$** (red) are marked in color for visualization. In the phase image (e) the helicity (*P*) of an individual block copolymer is indicated.

**Two-component seeded polymerization of MeS-PBI$_{trapped}$ with MeO-PBI$_{seed}$**

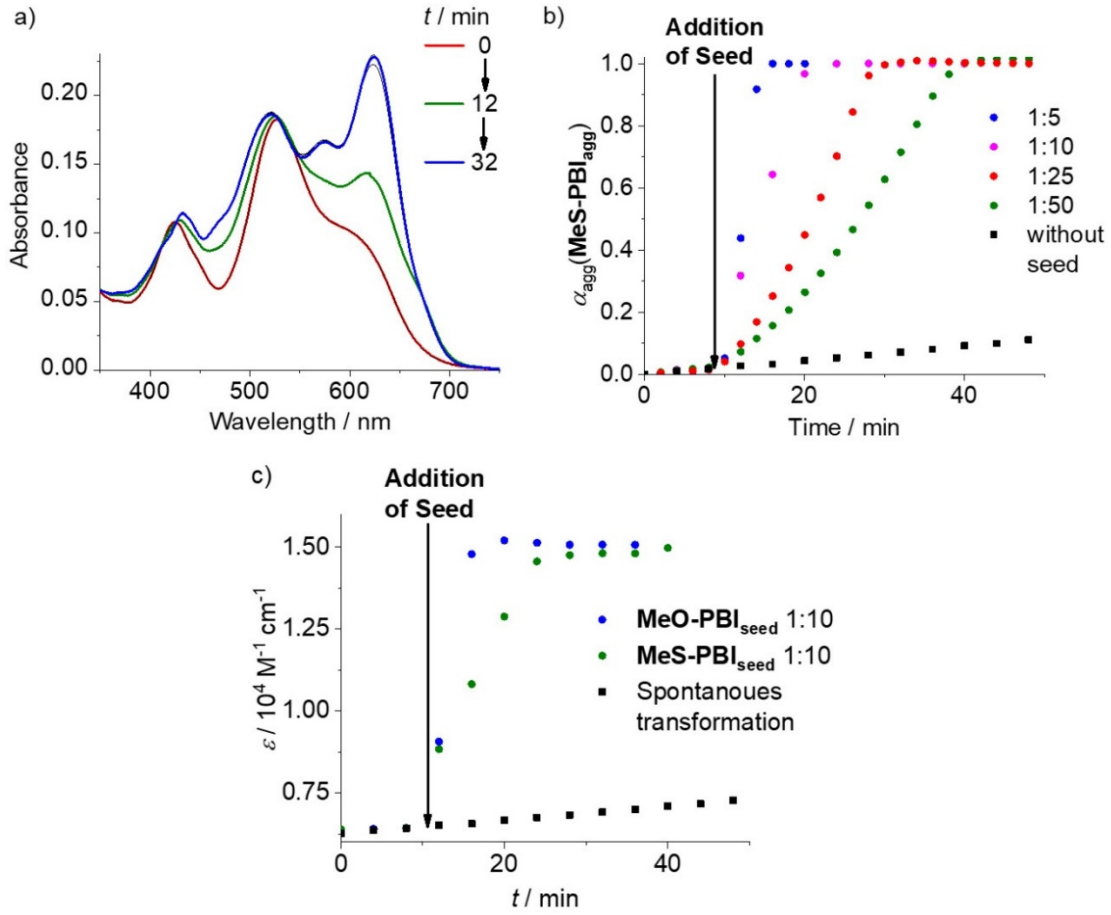


**Figure 93.** a) Time-dependent UV/vis spectra of the two-component seeded polymerization of **MeS-PBI$_{trapped}$** with **MeO-PBI$_{seed}$** in a seed ratio of 1:10 ($c_T$ = 15 × 10$^{-6}$ M, MCH/Tol 2:1, v/v) at 10 °C. b) Plots of the degree of aggregation of **MeS-PBI$_{agg}$**, calculated from the dilution corrected apparent extinction coefficient at 620 nm, against the time upon addition of **MeO-PBI$_{seed}$** (seed ratio = 1:5 (blue dots), 1:10 (purple dots), 1:25 (red dots) and 1:50 (green dots)) at 10 °C. The spontaneous polymerization of **MeS-PBI** (black squares) is shown for comparison. c) Plots of the dilution corrected apparent extinction coefficients of the seeded polymerization of **MeS-PBI$_{trapped}$** at 620 nm against the time upon addition of different seeds in a seed ratio of 1:10.

## NMR spectroscopy and high resolution mass spectrometry

### *N,N'*-Dicyclohexyl-1,7-dichloroperylene-3,4:9,10-tetracarboxylic acid bisimide 23a

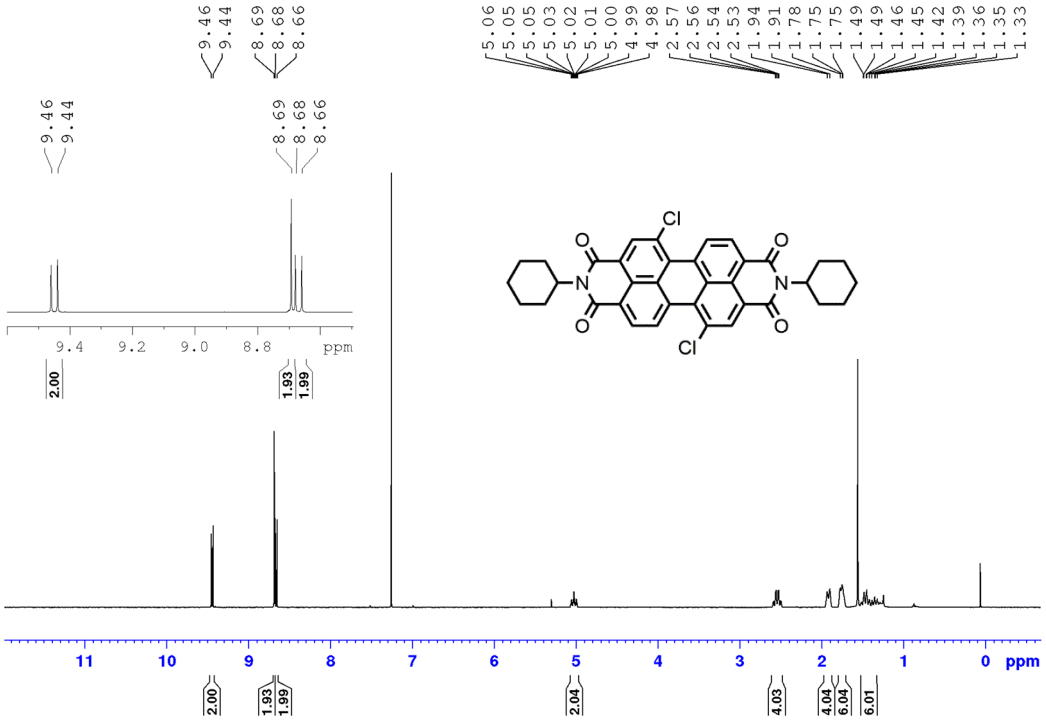


**Figure 94.** $^{1}$H NMR spectrum (400 MHz) of **23a** in $CDCl_3$ recorded at 298 K.

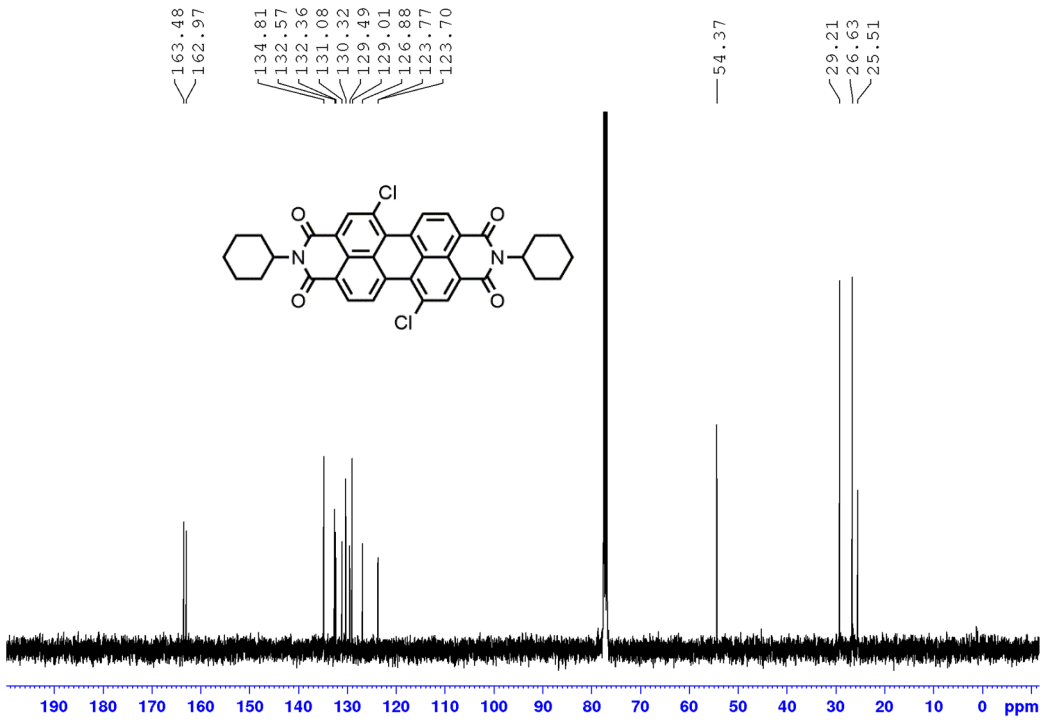


**Figure 95.** $^{13}$C NMR spectrum (100 MHz) of **23a** in $CDCl_3$ recorded at 298 K.

**_N,N'_-(2-(3,4,5-Tris(dodecyloxy)benzamido)ethyl)-1,7-dichloroperylene-3,4:9,10-tetracarboxylic acid bisimide Cl-PBI**

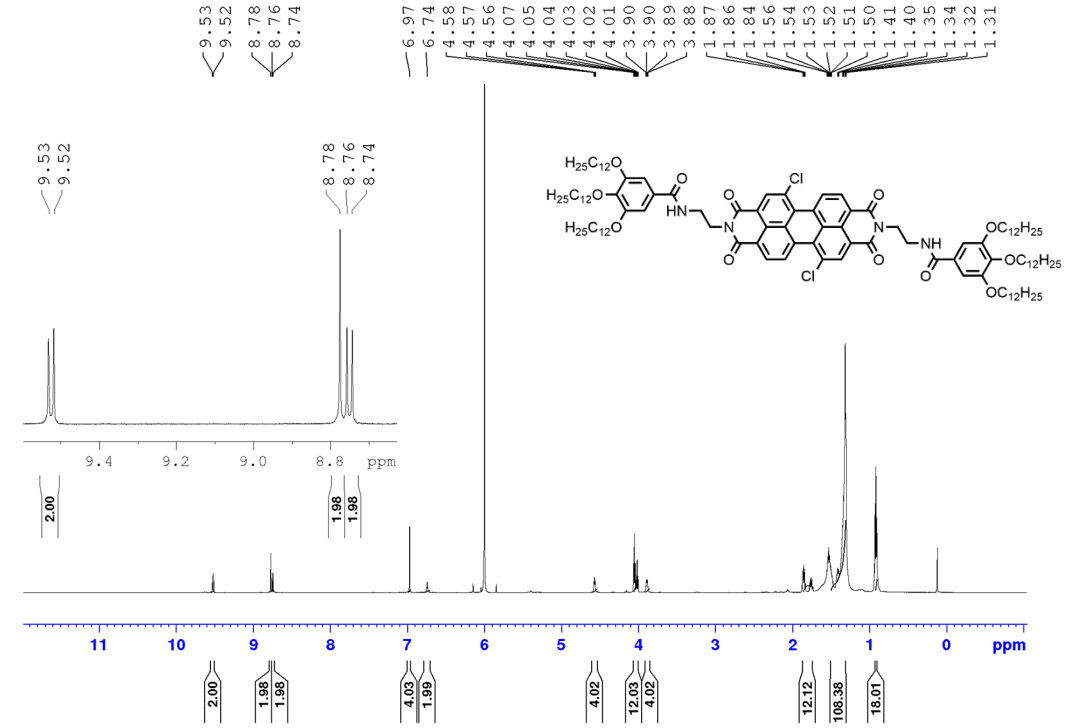


**Figure 96.** $^{1}$H NMR spectrum (600 MHz) in 1,1,2,2-tetrachloroethane-$d_2$ recorded at 345 K.

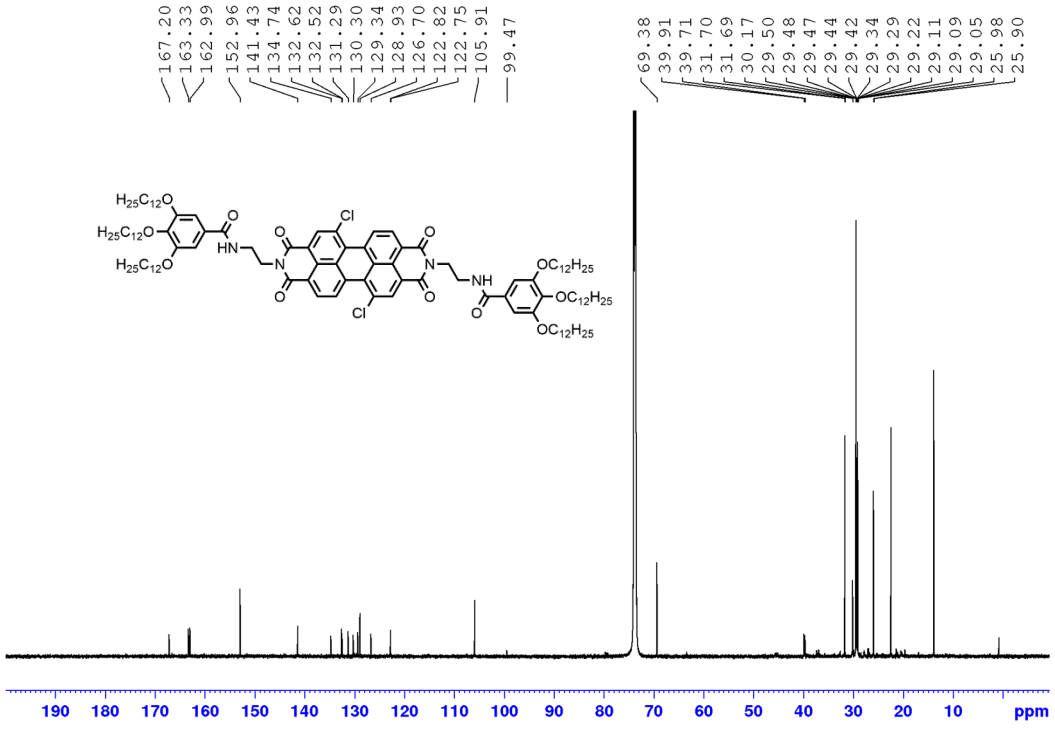


**Figure 97.** $^{13}$C NMR spectrum (150 MHz) in 1,1,2,2-tetrachloroethane-$d_2$ recorded at 345 K.

**_N,N'_-Dicyclohexyl-1,7-di(methylthio)perylene-3,4:9,10-tetracarboxylic acid bisimide 23d**

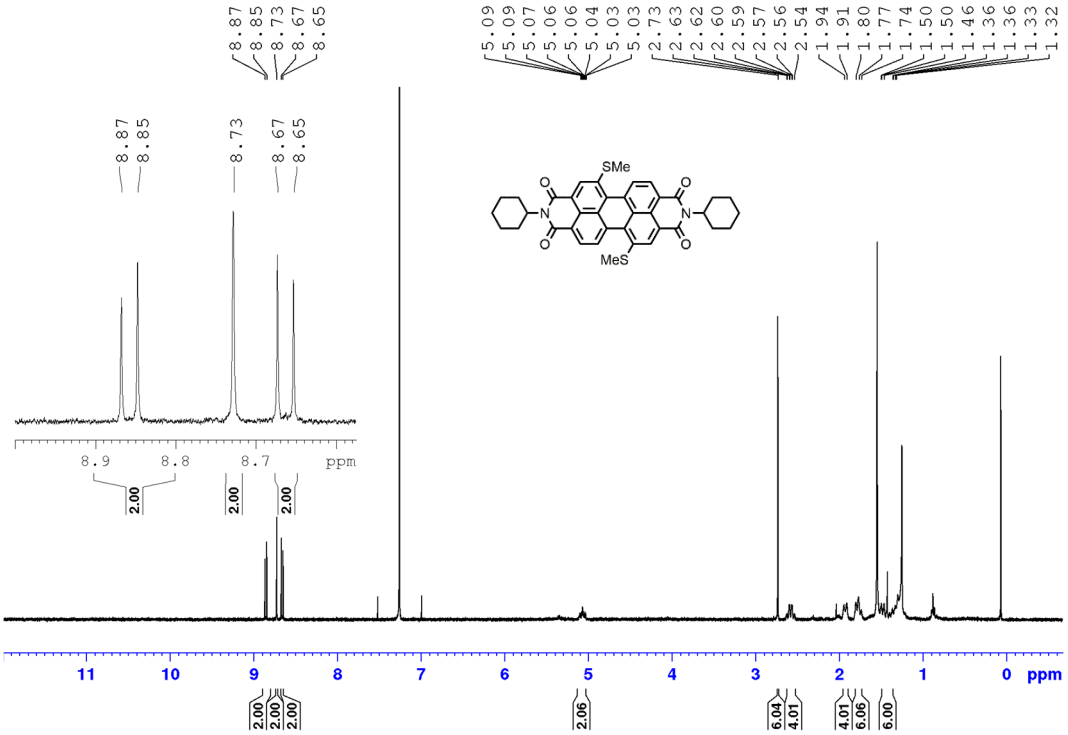


**Figure 98.** $^{1}$H NMR spectrum (400 MHz) of **23d** in $CDCl_3$ recorded at 298 K.

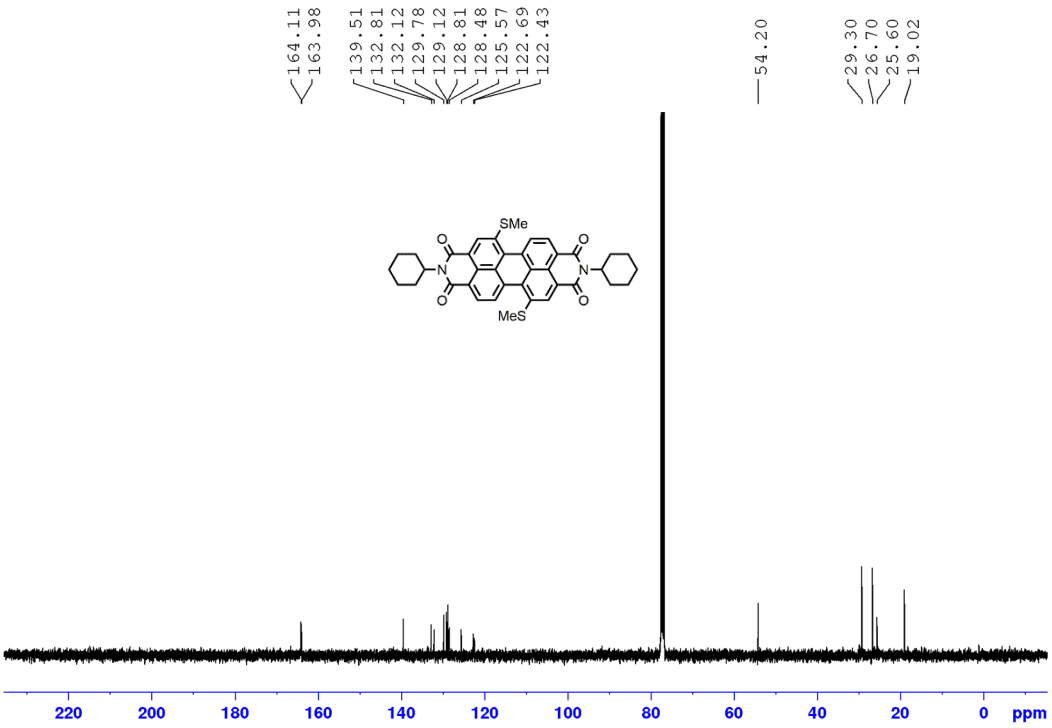


**Figure 99.** $^{13}$C NMR spectrum (100 MHz) of **23d** in $CDCl_3$ recorded at 298 K.

***N,N'*-(2-(3,4,5-Tris(dodecyloxy)benzamido)ethyl)-1,7-di(mehtylthio)perylene-3,4:9,10-tetracarboxylic acid bisimide MeS-PBI**

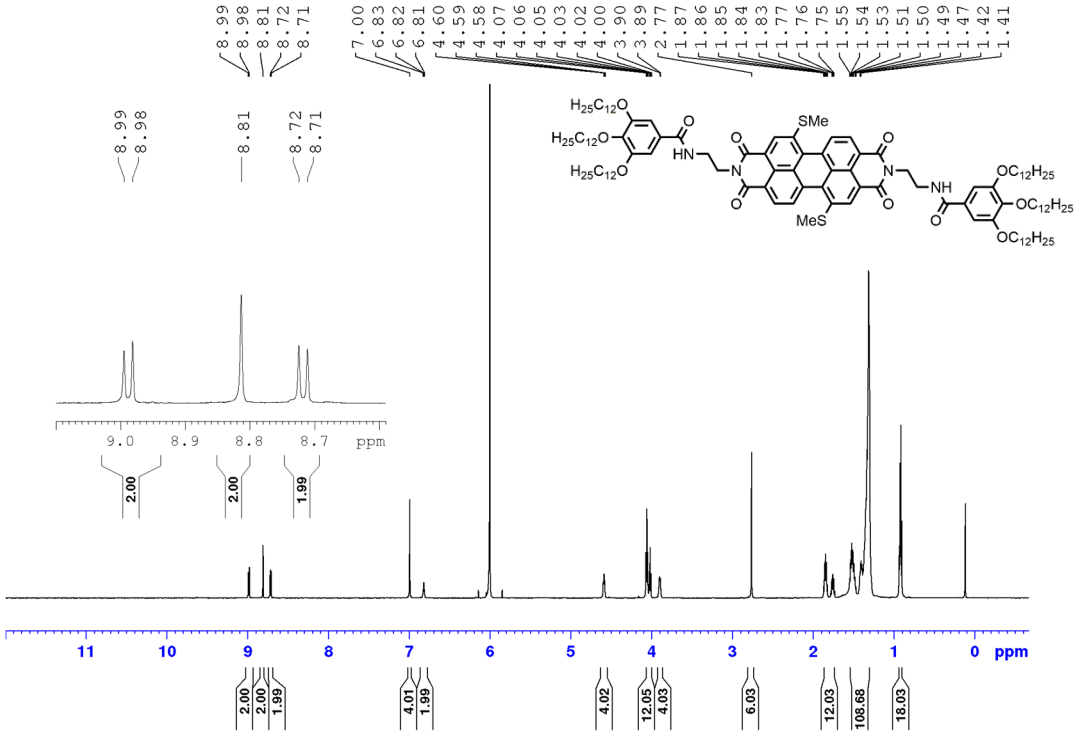


**Figure 100.** $^{1}$H NMR spectrum (600 MHz) in 1,1,2,2-tetrachloroethane-$d_2$ recorded at 345 K.

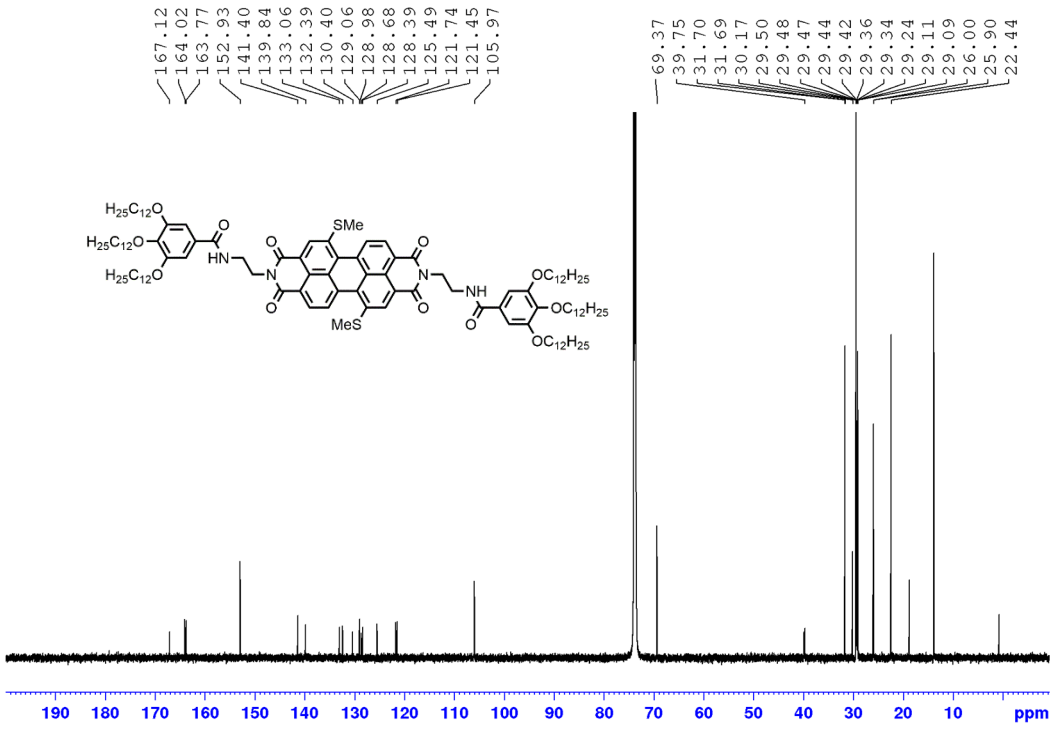


**Figure 101.** $^{13}$C NMR spectrum (150 MHz) in 1,1,2,2-tetrachloroethane-$d_2$ recorded at 345 K.

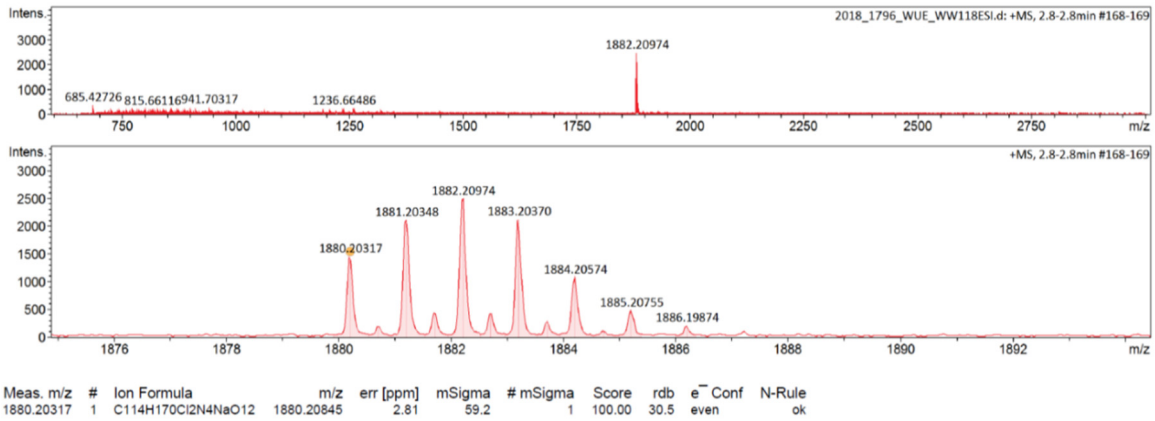


**Figure 102.** High resolution mass spectrum (ESI, positive mode, $CHCl_3/CH_3CN$ 3:1) of **Cl-PBI**.

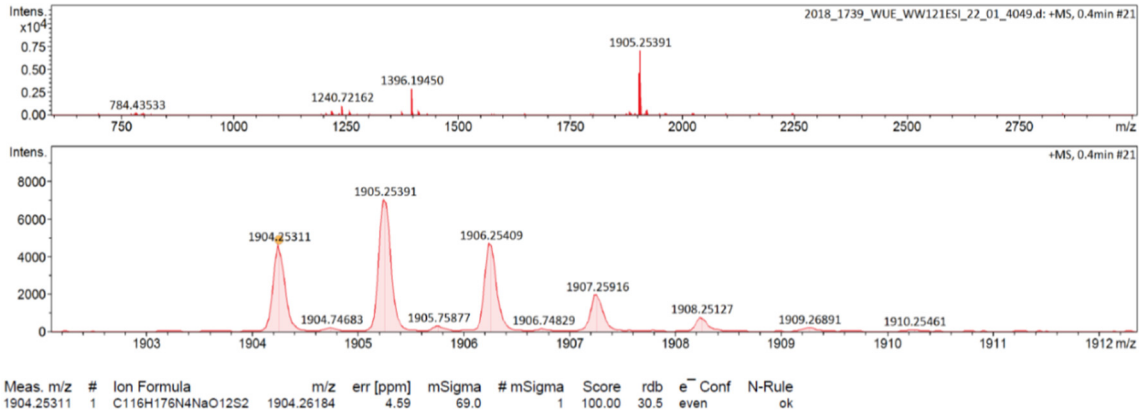


**Figure 103.** High resolution mass spectrum (ESI, positive mode, $CHCl_3/CH_3CN$ 3:1) of **MeS-PBI**.

## 8.3 Supporting Information for *Chapter 5*: Impact of Molecular Shape on Supramolecular Copolymer Synthesis in Seeded Living Polymerization of Perylene Bisimides[173]

### Materials and methods

#### General

All chemicals, reagents and solvents were purchased from commercial suppliers and used, unless otherwise stated, without further purification. If needed, solvents were dried by literature known procedures. The compounds **H-PBI**,[128] **1,7-MeO-PBI**[62] and *N*-(2-aminoethyl)-3,4,5-tris(dodecyloxy)-benzamide **25**[129,165] were synthesized according to the previously reported procedures.

#### NMR spectroscopy

The $^{1}$H NMR and $^{13}$C NMR spectra were recorded with a *Bruker* Avance III HD (400 MHz or 600 MHz) spectrometer and calibrated against the residual proton signal or natural abundance carbon resonance of the used deuterated solvent from tetramethylsilane as the internal standard. The chemical shifts $\delta$ are indicated in ppm and the coupling constants $J$ in Hz. The multiplicities are given at center of the respective signal as s (singlet), d (doublet), dd (doublet of doublets), t (triplet), q (quartet) and m (multiplet).

#### Mass spectrometry

The high-resolution mass spectra (HRMS) were measured by electrospray ionization (ESI) on a microTOF Focus instrument of *Bruker* Daltonics.

#### Melting point determination

The melting points were measured with a polarization microscope BX41 of *Olympus* with the temperature controller TP94 of *Linkam Scientific* and are uncorrected.

#### UV/vis spectroscopy

The spectroscopic measurements were conducted under ambient conditions using dry solvents of spectroscopic grade. The UV/vis spectra of the samples were measured with *Jasco* V-670 or *Jasco* V-770 spectrophotometer equipped with a PAC-743R Auto Peltier 6/8-cell changer for temperature control using conventional quartz cell cuvettes (from 0.1 cm to 1 cm). The temperature-dependent absorption spectra were density corrected for different temperatures.

**Steady state fluorescence spectroscopy**

The fluorescence spectra were recorded with an *Edinburgh Instruments* FLS 980 fluorescence spectrometer equipped with a double monochromator for emission and excitation. The spectra were corrected against photomultiplier and lamp intensity. The fluorescence quantum yields were determined by the optical dilution method (OD ≤ 0.05) as the average value of five different excitation wavelengths with Lumogen Red ($\Phi_{fl}$ = 0.96 in $CHCl_3$)[194] or Lumogen Orange ($\Phi_{fl}$ = 1.00 in $CHCl_3$)[194] as standards. The time-resolved measurements were performed with a ps laser diode (510 nm) and a TCSPS photodetector.

**Atomic force microscopy (AFM)**

AFM measurements were performed under ambient conditions using a *Bruker* Multimode 8 SPM system operating in tapping mode in air. Silica cantilevers (OMCL-AC200TS, *Olympus*) with a resonance frequency of ~150 kHz and a spring constant of ~10 $Nm^{-1}$ were used. The samples were prepared by spin-coating of respective solutions onto silicon wafers or onto highly oriented pyrolytic graphite (HOPG) substrates with 2000-3000 rpm.

**DFT calculations**

DFT calculations were performed by using Gaussian09 with B3-LYP as functional and def2-SVP as basis set.[198-199]

**Seeded supramolecular polymerization**

**1-MeO-PBI** ($c_T$ = 10 × $10^{-6}$ M) was dissolved in a solvent mixture of MCH and Tol (1:2, v/v) and heated for ca. 15 min at 90 °C to ensure the formation of the fully monomeric state. Subsequently, 3 mL of the solution were placed in a cuvette ($d$ = 1 cm) and cooled down to 30 °C by a rate of ca. 15 °C/min in the UV/vis spectrometer to obtain the kinetically trapped state **1-MeO-PBI$_{trapped}$**. After several spectra were recorded to validate the kinetic trapping of the PBI, the seeds prepared by ultrasonication of the polymer solution of **1-MeO-PBI** in MCH/Tol (1:2, v/v) for 30 min at 23 °C were injected into the cuvette just before recording the spectrum at $t$ = 10 min. The volume of seed solution was exactly determined by the use of *Hamilton* syringes of appropriate size to calculate the seed ratio. After seed addition, the time-dependent UV/vis measurement was continued at 30 °C.

**Two-component seeded supramolecular copolymerization**

The respective PBI was dissolved in pure toluene for **H-PBI**, MCH/Tol (1:2, v/v) for **1-MeO-PBI** and MCH/Tol (2:1, v/v) for **1,7-MeO-PBI** and heated for ca. 15 min at 90 °C to ensure the formation of the fully monomeric state. Subsequently, 1.2 mL of the respective solutions were placed in a cuvette and cooled down to 30 °C (for **H-PBI$_{trapped}$** and **1-MeO-PBI$_{trapped}$**) or 20 °C (for **1,7-MeO-PBI$_{trapped}$**) by a rate of ca. 15 °C/min in the UV/vis spectrometer. The time-dependent UV/vis measurements were started at the respective temperature (30 or 20 °C). After several spectra were recorded to validate the kinetic trapping of the PBI, the seeds prepared by ultrasonication of the respective polymer solution for 15 min to 30 min were injected just before recording the spectrum at $t$ = 10 min into the cuvette. The volume of seed solution was exactly determined by the use of *Hamilton* syringes of appropriate size to calculate the seed ratios. After seed addition, the time-dependent UV/vis measurement was continued at the respective temperature. Since the addition of seed solution leads to a slight decrease of the total concentration of the respective PBIs because of the added solvent, the apparent extinction coefficients and the degree of aggregation are then calculated by correction of the dilution with the solvent of the seed and by subtracting the absorbance caused by the absorption of the polymeric seeds.

**Synthesis and characterization**

The different methoxy-substituted PBI derivatives applied in this work were synthesized according to the route depicted in Scheme 5 starting from the monobromo[187,189], 1,7-dibromo[188] and 1,6,7,12-tetrabromo[186,200] perylene-3,4:9,10-tetracarboxylic acid tetrabuthylesters **19a-c** as precursors. The starting compounds **19a**[187,189] and **19b**[188] were then converted by copper-mediated nucleophilic substitution of bromine with freshly prepared sodium methanolate to the respective methoxy-substituted perylene tetracarboxylic acid methylesters **20a** and **20b**.[62,166] The analogous reaction of the 1,6,7,12-tetrabromo-substituted **19c**[186,200] afforded both 1,6,7-trimethoxy-substituted derivative **20c** and 1,6,7,12-tetramethoxy-substituted derivative **20d**.[166] The 1,6,7-trimethoxy substituted compound **20c** is formed as the main side-product of the reaction through a copper-mediated dehalogenation of one bromine substituent of the tetra bay-substituted precursor **19c**.[166] The perylene tetracarboxylic acid tetramethylesters **20c** and **20d** can be separated by column chromatography from other side-products, which are generated by incomplete methoxylation of the starting material, and were isolated in yields

of 25% (**20c**) and 20% (**20d**), respectively. The corresponding perylene bisanhydrides **21a-d** were then synthesized by deprotection of the ester function of **20a-d** with *p*-toluene sulfonic acid monohydrate in toluene. Subsequent imidization of the perylene bisanhydrides **21a-d** with *N*-(2-aminoethyl)-3,4,5-tris(dodecyloxy)benzamide **25**[129,165] in the presence of $Zn(OAc)_2$ in imidazole afforded the desired perylene bisimide derivatives **1-MeO-PBI**, **1,7-MeO-PBI**, **1,6,7-MeO-PBI** and **1,6,7,12-MeO-PBI** in 38-81% yield.

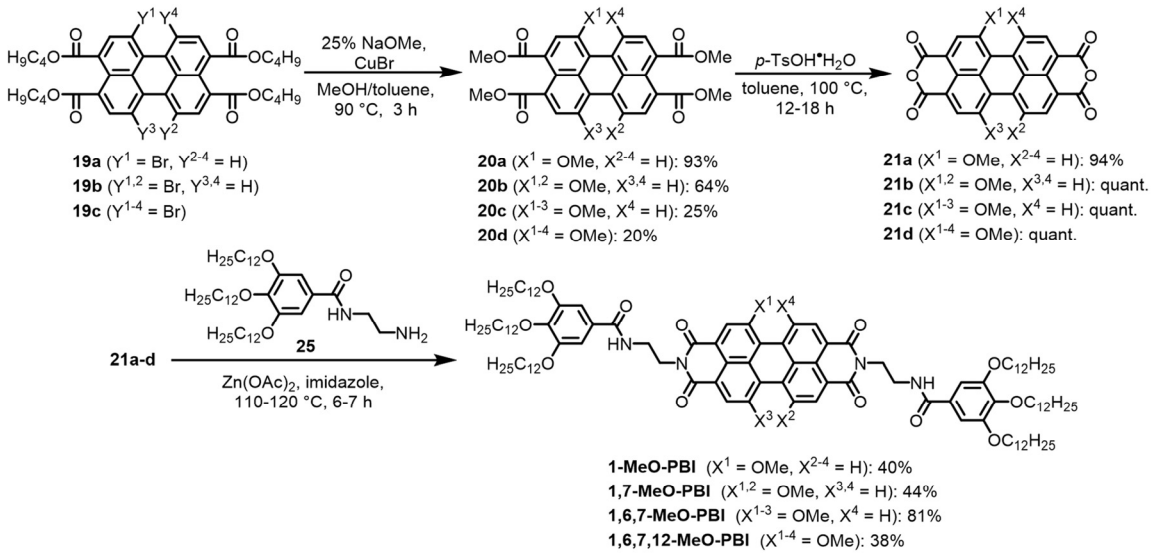


**Scheme 5.** Synthesis of 1-monomethoxy (**1-MeO-PBI**), 1,7-dimethoxy (**1,7-MeO-PBI**),[62] 1,6,7-trimethoxy (**1,6,7-MeO-PBI**) and 1,6,7,12-tetramethoxy (**1,6,7,12-MeO-PBI**) bay-substituted PBIs.

The synthetic route to the 1,7-diethoxy and 1,7-diisopropyloxy PBIs starting with regio-isomerically pure *N*,*N*′-dicyclohexyl-1,7-dibromoperylene-3,4:9,10-tetracarboxylic acid bisimide **22**[190] is displayed in Scheme 6. Perylene bisimide **22** was converted into the diethoxy-substituted **23b** and the diisopropyloxy-substituted PBI derivative **23c** by a nucleophilic substitution reaction with freshly prepared NaOEt (for **23b**) or NaO*i*Pr (for **23c**)solution employing a catalytic amount of CuBr.[166,201] Saponication of the precursors **23b** and **23c** with potassium hydroxide in isopropanol according to a standard procedure for PBIs[190] afforded the respective 1,7-bay-substituted perylene bisanhydrides **24b** and **24c**. By imidization of the later compounds with *N*-(2-aminoethyl)-3,4,5-tris(dodecyloxy)benzamide **25**[129,165] in imidazole the target PBI dyes **1,7-EtO-PBI** and **1,7-*i*PrO-PBI** were obtained in 53% and 41% yield, respectively.

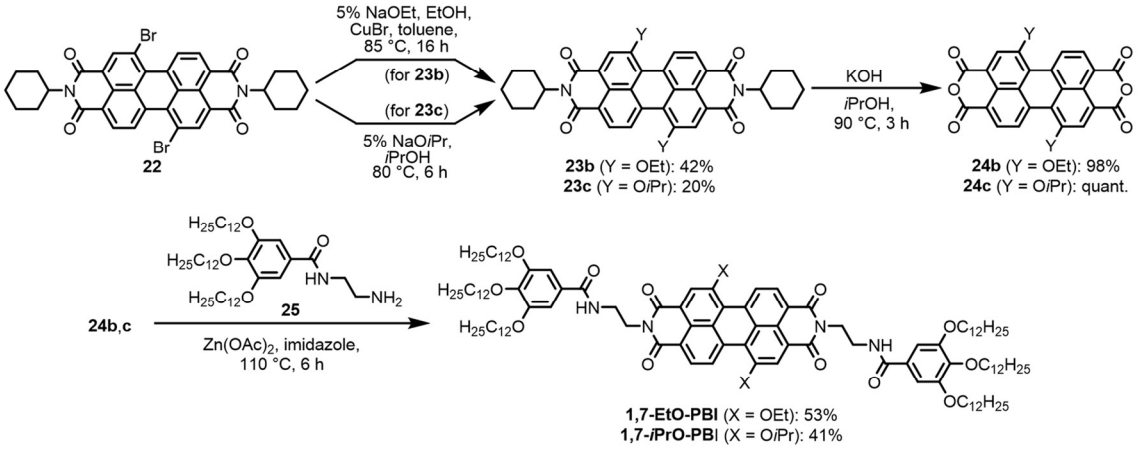


**Scheme 6.** Synthesis of 1,7-diethoxy (**1,7-EtO-PBI**) and 1,7-diisopropyloxy (**1,7-*i*PrO-PBI**) bay-substituted PBIs.

### 1-Methoxyperylene-3,4:9,10-tetracarboxylic acid tetramethylester 20a

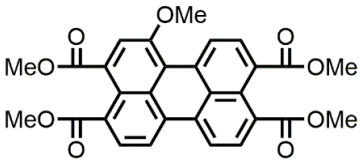

A suspension of CuBr (85.0 mg, 591 µmol) in anhydrous EtOAc (1.0 mL) was added to a freshly prepared 12% NaOMe solution in anhydrous methanol (20 mL) under nitrogen atmosphere at 60 °C. To the reaction mixture, a solution of 1-bromoperylene-3,4:9,10-tetracarboxylic acid tetrabutylester **19a** (217 mg, 296 µmol) in anhydrous toluene (3.5 mL) was added and stirred at 90 °C for 2.5 h. After cooling down to room temperature, the reaction mixture was diluted with 30 mL of DCM, quenched with water (25 mL) and the water layer was extracted twice with DCM (20 mL). The organic layer was dried over $Na_2SO_4$ and the solvent was removed under reduced pressure. The crude product was purified by column chromatography (DCM:MeOH 98:2, v/v) on silica gel.

**Yield**: 141 mg (274 µmol, 93%), dark orange solid.

**M.p.** 224-226 °C.

**$^1$H NMR** (400 MHz, $CDCl_3$): $\delta$ [ppm] = 9.14 (d, $J$ = 8.2 Hz, 1H), 8.27 (d, $J$ = 8.1 Hz, 1H), 8.24 (d, $J$ = 8.1 Hz, 1H), 8.05 (d, $J$ = 8.2 Hz, 2H), 7.97 (d, $J$ = 7.9 Hz, 1H), 7.91 (s, 1H), 4.17 (s, 3H), 3.95 (s, 6H), 3.94 (s, 3H), 3.93 (s, 3H).

**$^{13}$C NMR** (100 MHz, $CDCl_3$): $\delta$ [ppm] = 169.2, 169.1, 169.1, 168.5, 156.0, 133.5, 133.0, 132.6, 131.0, 131.0, 130.9, 130.1, 129.8, 129.6, 128.7, 128.6, 128.5, 127.1, 123.9, 122.4, 120.9, 119.3, 118.6, 56.9, 52.5, 52.4, 52.3, 52.2.

**HRMS** (ESI, positive, chloroform/acetonitrile): *m/z* calculated for $C_{29}H_{22}NaO_9$ $[M+Na]^+$: 537.1153, found 537.1156.

**1-Methoxyperylene-3,4:9,10-tetracarboxylic acid bisanhydride 21a**

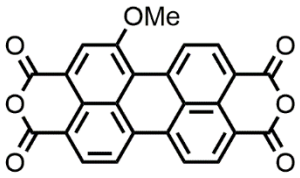


A mixture of 1-methoxyperylene-3,4:9,10-tetracarboxylic acid tetramethylester **20a** (120 mg, 233 µmol, 1.0 eq), *p*-toluenesulfonic acid monohydrate (266 mg, 1.40 mmol, 6.0 eq) and toluene (20 mL) was refluxed at 100 °C for 18 h under a nitrogen atmosphere. After removal of the solvent under reduced pressure, water was added and the mixture was sonicated at room temperature for 15 min. The precipitate was collected by centrifugation and dried in vacuum.

**Yield**: 98.4 mg (233 µmol, quantitative), dark violet solid.

**M.p.** >300 °C.

**$^1$H NMR** ($D_2SO_4$, 400 MHz): $\delta$ [ppm] = 9.83 (d, $^3J$ = 8.6 Hz, 1H, C*H*), 8.96 (d, $^3J$ = 8.4 Hz, 1H, C*H*), 8.90 (d, $^3J$ = 9.6 Hz, 1H, C*H*), 8.75 (d, $^3J$ = 7.7 Hz, 1H, C*H*), 8.62 (s, 1H, C*H*), 7.65 (d, $^3J$ = 8.3 Hz, 1H, C*H*), 7.28 (d, $^3J$ = 8.2 Hz, 1H, C*H*), 4.33 (s, 3H, OC$H_3$).

**$^{13}$C NMR** could not be measured because of the low solubility of the compound in organic solvents.

**MS** (MALDI-TOF, positive, DCTB): *m/z* calculated for $C_{25}H_{10}O_7$ $[M]^+$: 422.0427, found: 422.01.

The product was used for the next step without further purification.

***N,N'*-(2-(3,4,5-Tris(dodecyloxy)benzamido)ethyl)-1-methoxyperylene-3,4:9,10-tetracarboxylic acid bisimide 1-MeO-PBI**

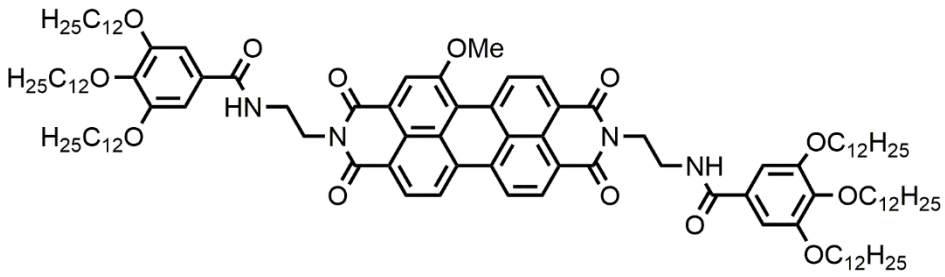


A mixture of 1-methoxyperylene-3,4:9,10-tetracarboxylic acid bisanhydride **21a** (40.0 mg, 94.7 µmol, 1.0 eq.), $Zn(OAc)_2$ (43.5 mg, 237 µmol, 2.1 eq.), *N*-(2-aminoethyl)-3,4,5-tris(dodecyloxy)-benzamide **25** (143 mg, 199 µmol, 2.5 eq.) and imidazole (4.50 g) was stirred at 110 °C for 7 h under nitrogen atmosphere. After cooling to room temperature, the reaction mixture was diluted with $CHCl_3$ (25 mL) and washed with aqueous 1N HCl solution (25 mL) and water (25 mL). The organic layer was dried over $Na_2SO_4$ and the solvent was removed under reduced pressure. The obtained crude product was purified by column chromatography on silica gel ($CHCl_3$) and preparative TLC ($CHCl_3$/MeOH 99:1, v/v). The resulting solid was dissolved in ca. 1 mL of chloroform and then precipitated with methanol. The obtained precipitate was concentrated by centrifugation and dried in high vacuum.

**Yield**: 69.2 mg (38.0 µmol, 40%), purple solid.

**M.p.** 214-217 °C.

**$^1$H NMR** (600 MHz, TCE-$d_2$, 345 K): $\delta$ [ppm] = 9.59 (d, $J$ = 8.4 Hz, 1H), 8.77-8.63 (m, 5H), 8.56 (s, 1H), 7.03 (s, 2H), 7.01 (s, 2H), 6.89-6.85 (m, 1H), 6.78-6.73 (m, 1H), 4.62-4.55 (m, 4H), 4.39 (s, 3H), 4.09-4.02 (m, 12H), 3.93-3.88 (m, 4H), 1.88-1.74 (m, 12H), 1.58-1.25 (m, 108H), 0.96-0.90 (m, 18H).

**$^{13}$C NMR** (150 MHz, TCE-$d_2$, 345 K): $\delta$ [ppm] = 167.1, 167.1, 164.2, 164.1, 164.0, 163.5, 158.5, 152.9, 152.9, 141.5, 141.3, 134.9, 134.7, 134.3, 132.1, 130.8, 129.1, 129.0, 129.0, 129.0, 128.7, 128.4, 127.0, 124.3, 123.8, 123.7, 122.6, 122.5, 122.1, 121.5, 121.3, 120.2, 118.2, 106.9, 99.5, 79.7, 79.5, 79.4, 69.4, 69.3, 59.4, 56.9, 40.0, 39.8, 39.7, 39.6, 38.0, 31.7, 31.7, 31.1, 30.2, 29.5, 29.5, 29.5, 29.5, 29.4, 29.4, 29.3, 29.3, 29.2, 29.2, 29.1, 29.1, 26.0, 26.0, 25.9, 22.4, 22.4, 13.9.

**HRMS** (ESI, positive, chloroform/acetonitrile): *m/z* calculated for $C_{115}H_{175}N_4O_{13}$ $[M+H]^+$: 1820.3150, found 1820.3085.

**UV/Vis** ($CHCl_3$ at $10 \times 10^{-6}$ M): $\lambda_{max}$ / nm ($\varepsilon_{max}$ / L mol$^{-1}$ cm$^{-1}$) = 558 (63000).

**Fluorescence** ($CHCl_3$, $\lambda_{ex}$ = 500 nm): $\lambda_{max}$ / nm = 575, $\Phi_{fl}$ = 0.21.

**1,6,7-Trimethoxyperylene-3,4:9,10-tetracarboxylic acid tetramethylester 20c / 1,6,7,12-tetramethoxyperylene-3,4:9,10-tetracarboxylic acid tetramethylester 20d [166]**

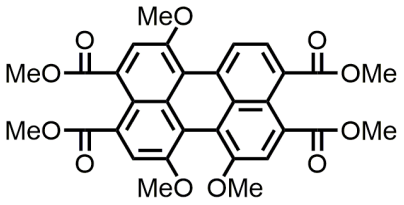


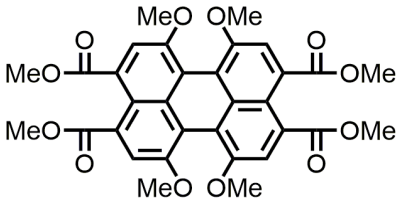


A suspension of CuBr (360 mg, 2.51 mmol, 2.4 eq.) in anhydrous EtOAc (1.0 mL) was added to a freshly prepared 25% NaOMe solution in methanol (25 mL) under nitrogen atmosphere. A solution of 1,6,7,12-tetrabromoperylene-3,4:9,10-tetracarboxylic acid tetrabuthylester **19c** (1.0 g, 1.03 mmol, 1.0 eq.) in anhydrous toluene (4 mL) was then added and the reaction mixture was stirred at 90 °C for 3 h. After being cooled to room temperature, the reaction mixture was quenched with water (50 mL) and the product was extracted with DCM (3 × 50 mL). The organic layer was dried over $MgSO_4$ and the solvent was evaporated. The crude product was purified by column chromatography (*n*-pentane:acetone 7:3) on silica gel to give and as red orange solids.

**Yield 20c**: 148 mg (0.258 mmol, 25%), red orange solid

**Yield 20d**:123 mg (0.203 mmol, 20%), red orange solid.

**$^1$H NMR** of **20c** (400 MHz, $CDCl_3$): $\delta$ [ppm] = 8.83 (d, $^3J$ = 8.1 Hz, 1 H), 7.99 (d, $^3J$ = 8.1 Hz, 1 H), 7.91 (s, 1 H), 7.83 (s, 1 H), 7.79 (s, 1 H), 4.12 (s, 3 H), 4.10-4.05 (m, 6 H), 4.00-3.85 (m, 12 H).

**$^1$H NMR** of **20d** (400 MHz, $CDCl_3$): $\delta$ [ppm] = 7.81 (s, 4 H), 4.06 (s, 12 H), 3.93 (s, 12 H).

The data are in accordance with literature.[166]

**1,6,7-Trimethoxyperylene-3,4:9,10-tetracarboxylic acid bisanhydride 21c**

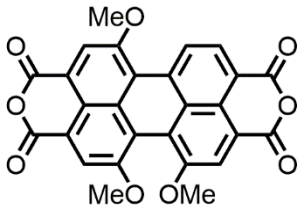


A mixture of 1,6,7-trimethoxyperylene-3,4:9,10-tetracarboxylic acid tetramethylester **20c** (40.0 mg, 74.5 µmol, 1 eq), *p*-toluenesulfonic acid monohydrate (88.9 mg, 467 µmol, 6.0 eq) and toluene (10 mL) was refluxed at 100 °C for 18 h under a nitrogen atmosphere. After evaporation of the solvent, water (25 mL) was added and the mixture was sonicated at room temperature for 15 min. The precipitate was collected by centrifugation and dried in vacuum.

**Yield**: 36.0 mg (74.5 µmol, quantitative), dark violet solid.

**M.p.** >300 °C.

The product was used for the next step without further purification.

***N,N'*-(2-(3,4,5-Tris(dodecyloxy)benzamido)ethyl)-1,6,7-trimethoxyperylene-3,4:9,10-tetracarboxylic acid bisimide 1,6,7-MeO-PBI**

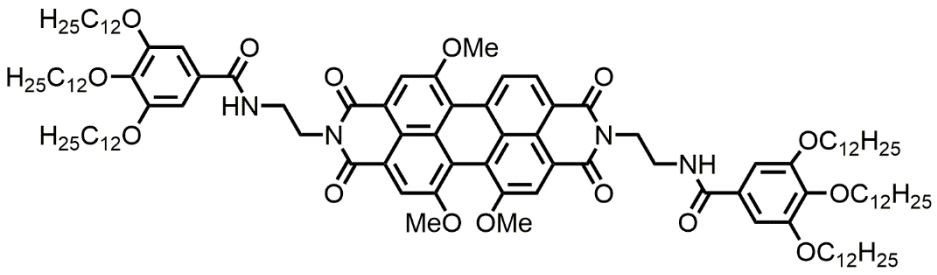


A mixture of 1,6,7-trimethoxyperylene-3,4:9,10-tetracarboxylic acid bisanhydride (26.0 mg, 53.9 µmol, 1.0 eq.) **20c**, $Zn(OAc)_2$ (28.5 mg, 0.155 mmol, 2.9 eq), *N*-(2-aminoethyl)-3,4,5-tris(dodecyloxy)-benzamide **25** (104 mg, 0.145 mmol, 2.7 eq.) and imidazole (2.35 g) was stirred at 110 °C for 6 h under nitrogen atmosphere. After being cooled to room temperature, the reaction mixture was diluted with $CHCl_3$ (25 mL) and washed with aqueous 1N HCl solution (30 mL) and water (30 mL). The organic layer was dried over $Na_2SO_4$ and the solvent was removed under reduced pressure. The obtained crude product was purified by column chromatography on silica gel ($CHCl_3$:MeOH 99:1,

v/v) and preparative TLC ($CHCl_3$:MeOH 99.5:0.5, v/v). The resulting solid was dissolved in ca. 1 mL of chloroform and then precipitated with methanol. The precipitate was concentrated by centrifugation and dried in high vacuum.

**Yield**: 82.6 mg (43.9 μmol, 81%), dark violet solid.

**M.p.** 271-273 °C.

**$^1$H NMR** (400 MHz, $CDCl_3$): $\delta$ [ppm] = 9.13 (d, $J$ = 8.2 Hz, 1H), 8.45 (d, $J$ = 8.2 Hz, 1H), 8.36 (s, 1H), 8.27 (s, 1H), 8.25 (s, 1H), 7.19-7.13 (m, 1H), 7.07-7.02 (m, 1H), 7.01 (s, 2H), 6.99 (s, 2H), 4.62-4.53 (m, 4H), 4.21 (s, 3H), 4.17 (s, 3H), 4.16 (s, 3H), 4.04-3.94 (m, 12H), 3.92-3.85 (m, 4H), 1.83-1.69 (m, 12H), 1.50-1.17 (m, 108H), 0.90-0.81 (m, 18H).

**$^{13}$C NMR** ($CDCl_3$, 100 MHz): $\delta$ [ppm] = 165.0, 164.6, 164.3, 157.8, 157.3, 156.3, 153.1, 153.1, 141.0, 140.8, 133.4, 131.2, 130.0, 129.4, 127.6, 123.3, 122.8, 122.1, 121.9, 120.7, 120.6, 120.3, 119.7, 118.7, 115.2, 105.7, 105.7, 73.6, 69.3, 69.2, 56.9, 56.7, 56.7, 32.1, 32.1, 20.5, 29.9, 29.9, 29.8, 29.8, 29.7, 29.6, 29.5, 26.3, 26.2, 22.8, 22.8, 14.3.

**HRMS** (ESI, positive, chloroform/acetonitrile): *m/z* calculated for $C_{117}H_{178}N_4O_{15}Na$ $[M+Na]^+$: 1902.3181, found 1902.3163.

**UV/Vis** ($CHCl_3$ at 10 × $10^{-6}$ M): $\lambda_{max}$ / nm ($\varepsilon_{max}$ / L $mol^{-1}$ $cm^{-1}$) = 600 (51000).

**Fluorescence** ($CHCl_3$, $\lambda_{ex}$ = 530 nm): $\lambda_{max}$ / nm = 633, $\Phi_{fl}$ = 0.79.

**1,6,7,12-Tetramethoxyperylene-3,4:9,10-tetracarboxylic acid bisanhydride 21d**[166]

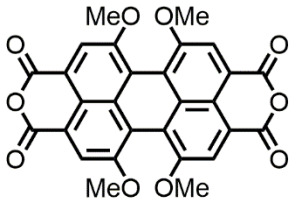


A suspension of 1,6,7,12-tetramethoxyperylene-3,4:9,10-tetracarboxylic acid tetramethylester **20d** (71.0 mg, 0.117 mmol) and *p*-toluenesulfonic acid mono hydrate (125 mg, 0.664 mmol) in toluene (10 mL) was refluxed under argon atmosphere at 100 °C for 14 h. After cooling down to *rt*, the solvent was evaporated, water (50 mL) was added to the residue and sonicated for 5 min. The precipitate was filtered and washed several times with water and dried in vacuum.

**Yield**: 60.0 mg (0.117 mmol, quantitative), dark violet solid.

**M.p.** >300 °C.

**$^1$H NMR** (400 MHz, $CDCl_3$): $\delta$ [ppm] = 8.32 (s, 4H), 4.24 (s, 12H).

The data are in good accordance with literature.[166]

***N*,*N*′-(2-(3,4,5-Tris(dodecyloxy)benzamido)ethyl)-1,6,7,12-tetramethoxyperylene-3,4:9,10-tetracarboxylic acid bisimide 1,6,7,12-MeO-PBI**

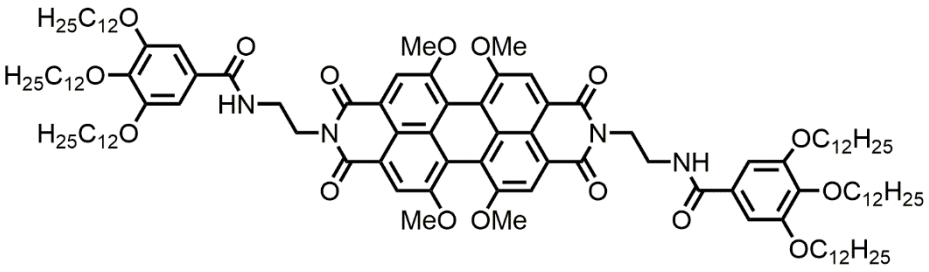


A mixture of 1,6,7,12-tetramethoxyperylene-3,4:9,10-tetracarboxylic acid bisanhydride **21d** (26.7 mg, 52.1 µmol, 1.0 eq.), $Zn(OAc)_2$ (33 mg, 0.180 mmol, 3.0 eq), *N*-(2-aminoethyl)-3,4,5-tris(dodecyloxy)-benzamide **25** (119 mg, 0.166 mmol, 2.8 eq.) and imidazole (3.03 g) was stirred at 110 °C for 7 h under nitrogen atmosphere. After cooling down to room temperature, the reaction mixture was diluted with $CHCl_3$ (25 mL) and washed with aqueous 1N HCl solution and water. The organic layer was dried over $Na_2SO_4$ and the solvent was removed under reduced pressure. The obtained crude product was purified by column chromatography on silica gel ($CHCl_3$:acetone 98:2, v/v). The resulting solid was dissolved in ca. 1 mL of chloroform and then precipitated with methanol. The precipitate was concentrated by centrifugation and dried in high vacuum.

**Yield**: 37.5 mg (19.7 µmol, 38%), dark violet solid.

**M.p.** 211-213 °C.

**$^1$H NMR** (400 MHz, $CDCl_3$): $\delta$ [ppm] = 8.31 (s, 4H), 7.03-6.99 (m, 2H), 6.98 (s, 4H), 4.60-4.56 (m, 4H), 4.20 (s, 12H), 4.04-3.94 (m, 12H), 3.91-3.87 (m, 4H), 1.81-1.69 (m, 12H), 1.49-1.18 (m, 108H), 0.89-0.82 (m, 18H).

**$^{13}$C NMR** (100 MHz, $CDCl_3$): $\delta$ [ppm] = 167.5, 164.9, 157.0, 153.1, 141.0, 129.4, 121.8, 119.5, 114.9, 105.6, 73.6, 69.3, 56.8, 32.1, 32.1, 30.5, 29.9, 29.8, 29.8, 29.7, 29.6, 29.5, 29.5, 26.3, 26.2, 22.8, 14.3.

**HRMS** (ESI, positive, chloroform/acetonitrile): *m/z* calculated for $C_{118}H_{181}N_4O_{16}$ $[M+H]^+$: 1910.3467, found 1910.3465.

**UV/Vis** ($CHCl_3$ at $20 \times 10^{-6}$ M): $\lambda_{max}$ / nm ($\varepsilon_{max}$ / L $mol^{-1}$ $cm^{-1}$) = 616 (46500).

**Fluorescence** ($CHCl_3$, $\lambda_{ex}$ = 480 nm): $\lambda_{max}$ / nm = 647, $\Phi_{fl}$ = 0.85.

***N,N'*-Dicyclohexyl-1,7-diethoxyperylene-3,4:9,10-tetracarcoxylic acid bisimide 23b**[201]

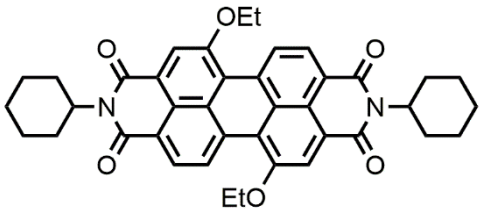


To a freshly prepared 5% NaOEt solution in ethanol (50 mL), CuBr (100 mg, 0.697 mmol, 1.0 eq.) and *N,N'*-dicyclohexyl-1,7-dibromo-perylene-3,4:9,10-tetracarboxylic acid bisimide **22** (500 mg, 0.703 mmol, 1.0 eq.) were added. The mixture was stirred under nitrogen atmosphere at 85 °C for 16 h. After being cooled down to room temperature, the reaction mixture was quenched with water and the product was extracted with dichloromethane (2 × 100 mL). The organic phase was dried over $Na_2SO_4$ and the solvent was removed under vacuum. The crude product was purified by flash column chromatography (DCM:cyclohexane 1:1 → 8:2) on silica gel.

**Yield:** 190 mg (296 µmol, 42%), dark purple solid.

**M.p.** > 300 °C.

**$^1$H NMR** (400 MHz, $CDCl_3$): $\delta$ [ppm] = 9.66 (d, $^3J$ = 8.4 Hz, 2H), 8.57 (d, $^3J$ = 8.4 Hz, 2H), 8.48 (s, 2H), 5.10-5.02 (m, 2H), 4.57 (q, $^3J$ = 6.9 Hz, 4H), 2.65-2.51 (m, 4H), 1.97-1.88 (m, 4H), 1.84- 1.76 (m, 4H), 1.72 (t, $^3J$ = 6.9 Hz, 6H), 1.53-1.45 (m, 8H).

$^1$H NMR data are in accordance with literature.[201]

**1,7-Diethoxyperylene-3,4:9,10-tetracarboxylic acid bisanhydride 24b**

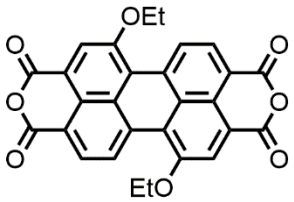


*N*,*N'*-Dicyclohexyl-1,7-diethoxyperylene-3,4:9,10-tetracarboxylic acid bisimide **23b** (105 mg, 163 µmol) and KOH (740 mg, 13.2 mmol) were dissolved in isopropanole (30 mL) and stirred at 90 °C for 3 h under nitrogen atmosphere. The dark purple suspension was cooled to room temperature and poured into acetic acid (20 mL). The suspension was stirred for 20 min at room temperature and the precipitate was collected by filtration and dried in vacuum.

**Yield**: 56.0 mg (117 µmol, 72%), dark purple solid.

**M.p.** >300 °C.

The resulting crude product was used for the next reaction without further purification.

***N*,*N'*-(2-(3,4,5-Tris(dodecyloxy)benzamido)ethyl)-1,7-diethoxyperylene-3,4:9,10-tetracarboxylic acid bisimide 1,7-EtO-PBI**

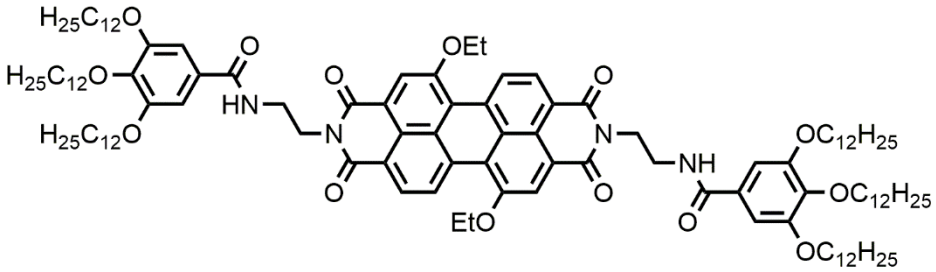


A mixture of 1,7-diethoxyperylene-3,4:9,10-tetracarboxylic acid bisanhydride **24b** (27.4 mg, 57.0 µmol, 1.0 eq.), *N*-(2-aminoethyl)-3,4,5-tris(dodecyloxy)benzamide **25** (90.1 mg, 126 µmol, 2.2 eq.) and $Zn(OAc)_2$ (31.4 mg, 171 µmol, 3.0 eq.) in imidazole (3.41 g) was stirred at 110 °C for 6 h under nitrogen atmosphere. After being cooled down to *rt*, the reaction mixture was diluted with $CHCl_3$ (50 mL) and washed with aqueous 1N HCl (50 mL) solution and water (50 mL). The organic layer was dried over $Na_2SO_4$ and the solvent was removed under reduced pressure. The obtained crude product was purified by column chromatography on silica gel ($CHCl_3$) followed by preparative TLC ($CHCl_3$:MeOH 99.5:0.5). The resulting solid was dissolved in ca. 1 mL of chloroform and then precipitated

with methanol. The obtained precipitate was concentrated by centrifugation and dried in high vacuum.

**Yield**: 56.3 mg (29.9 μmol, 53%), purple solid.

**M.p.** 237-239 °C.

**$^1$H NMR** (600 MHz, TCE-$d_2$, 345 K): $\delta$ [ppm] = 9.72 (d, $^3J$ = 8.4 Hz, 2H), 8.64 (d, $^3J$ = 8.4 Hz, 2H), 8.54 (s, 2H), 7.02 (s, 4H), 6.85 (t, $^3J$ = 4.9 Hz, 2H), 4.65-4.56 (m, 8H), 4.09-4.00 (m, 12H), 3.93- 3.88 (m, 4H), 1.90-1.72 (m, 18H), 1.60-1.28 (m, 108H), 0.97-0.90 (m, 18H).

**$^{13}$C NMR** (150 MHz, TCE-$d_2$, 345 K: $\delta$ [ppm] = 167.7, 164.2, 163.8, 156.8, 152.9, 141.6, 134.1, 129.3, 129.2, 129.1, 128.6, 123.7, 123.1, 122.1, 121.1, 118.3, 106.3, 99.5, 79.7, 79.5, 79.4, 69.5, 66.4, 39.9, 39,7, 31.7, 31.6, 30.2, 29.5, 29.4, 29.4, 29.4, 29,4 29.3, 29.2, 29.1, 29.0, 26.0, 25.9, 22.4, 22.4, 14.8, 13.8.

**HRMS** (ESI, positive, chloroform/acetonitrile): *m/z* calculated for $C_{118}H_{180}N_4NaO_{14}$ $[M+Na]^+$: 1900.3393, found: 1900.3388.

**UV/Vis** ($CHCl_3$ at 10 × $10^{-6}$ M): $\lambda_{max}$ / nm ($\varepsilon_{max}$ / L $mol^{-1}$ $cm^{-1}$) = 577 (60000).

**Fluorescence** ($CHCl_3$, $\lambda_{ex}$ = 530 nm): $\lambda_{max}$ / nm = 598, $\Phi_{fl}$ = 0.77.

### *N*,*N*'-Dicyclohexyl-1,7-diisopropyloxyperylene-3,4:9,10-tetracarcoxylic acid bisimide 23c

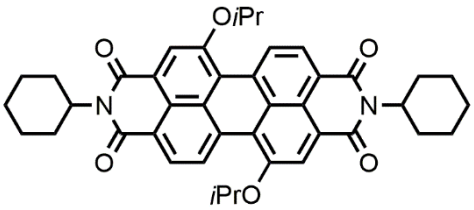


To a freshly prepared 5% NaO*i*Pr solution in dry isopropanole (25 mL), *N*,*N*'-dicyclohexyl-1,7-dibromo-perylene-3,4:9,10-tetracarboxylic acid bisimide **22** (200 mg, 0.281 mmol) was added. The mixture was stirred under nitrogen atmosphere at 80 °C for 6 h. After being cooled to *rt*, the reaction mixture was quenched with water (30 mL) and the product was extracted with dichloromethane (2 × 30 mL). The organic phase was dried over $Na_2SO_4$ and the solvent was removed under vacuum. The crude product was purified by flash column chromatography (dichloromethane:cyclohexane 8:2 → 9:1) on silica gel. Beside

the target compound, 31.0 mg (43.5 µmol) of pure starting material **5** (*N*,*N'*-dicyclohexyl-1,7-dibromo-perylene-3,4:9,10-tetracarboxylic acid bisimide) could be reisolated by this column chromatography.

**Yield:** 31.5 mg (47.0 µmol, 20%), dark purple solid.

**M.p.** > 350 °C.

**$^1$H NMR** (400 MHz, $CDCl_3$, 295K): $\delta$ [ppm] = 9.60 (d, $^3J$ = 8.4 Hz, 2H), 8.52 (d, $^3J$ = 8.4 Hz, 2H), 8.41 (s, 2H), 5.12-5.0 (m, 4H), 2.65-2.51 (m, 4H), 1.95-1.90 (m, 4H), 1.83-1.70 (m, 6H), 1.58 (s, 6H), 1.57 (s, 6H), 1.55-1.30 (m, 6H).

**$^{13}$C NMR** (100 MHz, $CDCl_3$, 295K): $\delta$ [ppm] = 164.3, 164.1, 155.8, 133.9, 129.5, 129.0, 128.7, 123.9, 123.7, 122.4, 121.9, 119.3, 73.5, 54.1, 29.8, 29.3, 26.7, 25.6, 22.6.

**HRMS** (ESI, positive, chloroform/acetonitrile): *m/z* calculated for $C_{42}H_{42}N_2O_6$ $[M]^+$: 670.3043, found: 670.3046.

**1,7-Diisopropyloxyperylene-3,4:9,10-tetracarboxylic acid bisanhydride 24c**

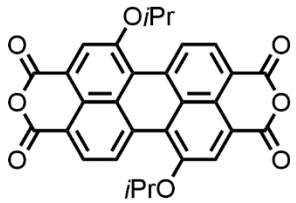


*N*,*N'*-Dicyclohexyl-1,7-diisopropyloxyperylene-3,4:9,10-tetracarboxylic acid bisimide **23c** (15.4 mg, 23.4 µmol) and KOH (110 mg, 1.96 mmol) were dissolved in isopropanole (5 mL) and stirred at 90 °C for 4 h under nitrogen atmosphere. The dark purple suspension was cooled to room temperature and aqueous 1N HCl solution (5 mL) was added. The suspension was stirred for 10 min at room temperature and the obtained precipitate was concentrated by centrifugation and dried in vacuum.

**Yield**: 11.9 mg (23.4 µmol, quantitative), dark purple solid.

**M.p.** >300 °C.

The resulting crude product was used for further reaction without purification.

**_N_,_N_′-(2-(3,4,5-Tris(dodecyloxy)benzamido)ethyl)-1,7-diisopropylperylene-3,4:9,10-tetracarboxylic acid bisimide 1,7-*i*PrO-PBI**

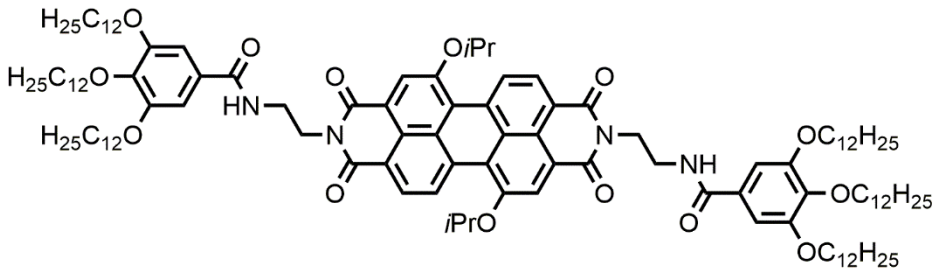


A mixture of 1,7-diisopropylperylene-3,4:9,10-tetracarboxylic acid bisanhydride **24c** (11.9 mg, 23.4 µmol), *N*-(2-aminoethyl)-3,4,5-tris(dodecyloxy)-benzamide **25** (36.9 mg, 51.5 µmol), $Zn(OAc)_2$ (12.9 mg, 70.2 µmol) and 3 g of imidazole was stirred at 110 °C for 6 h under nitrogen atmosphere. During cooling to room temperature, the reaction mixture was diluted with chloroform (15 mL) and washed with aqueous 1N HCl solution (15 mL) and water (15 mL). The solvent was removed under reduced pressure and the obtained crude product was purified by column chromatography on silica gel ($CHCl_3$:MeOH 99.25:0.75). The resulting solid was dissolved in ca. 2.5 mL of chloroform and then precipitated with methanol. The obtained precipitate was concentrated by centrifugation and dried in high vacuum.

**Yield**: 18.3 mg (9.60 µmol, 41%), dark purple solid.

**M.p.** 213-215 °C.

**$^1$H NMR** (600 MHz, TCE-$d_2$, 345 K): $\delta$[ppm] = 9.75 (d, $^3J$ = 8.4 Hz, 2H), 8.63 (d, $^3J$ = 8.4 Hz, 2H), 8.54 (s, 2H), 7.01 (s, 4H), 6.89 (t, $^3J$ = 4.9 Hz, 2H), 5.19-5.10 (m, 2H), 4.61-4.56 (m, 4H), 4.09-3.99 (m, 12H), 3.92-3.86 (m, 4H), 1.90-1.74 (m, 12H), 1.64 (s, 6H), 1.63 (s, 6H), 1.58-1.25 (m, 108H), 0.99-0.88 (m, 18H).

**$^{13}$C NMR** (150 MHz, TCE-$d_2$, 345 K): $\delta$ [ppm] = 167.0, 164.4, 163.9, 155.8, 152.9, 141.4, 134.2, 129.5, 129.1, 129.0, 128.6, 123.6, 123.0, 122.8, 121.0, 120.2, 119.7, 106.0, 99.5, 79.7, 79.5, 79.4, 69.4, 40.0, 39.7, 31.7, 31.7, 30.2, 29.6, 29.5, 29.5, 29.5, 29.4, 29.4, 29.4, 29.3, 29.3, 29.2, 29.1, 29.1, 29.0, 28.9, 27.1, 26.0, 25.9, 22.4, 22.4, 22.3, 13.9.

**HRMS** (ESI, positive, chloroform/acetonitrile): *m/z* calculated for $C_{120}H_{185}N_4O_{14}$ $[M+H]^+$: 1906.3882, found:1906.3850.

**UV/Vis** ($CHCl_3$ at $10 \times 10^{-6}$ M): $\lambda_{max}$ / nm ($\varepsilon_{max}$ / L mol$^{-1}$ cm$^{-1}$) = 575 (53000).

**Fluorescence** ($CHCl_3$, $\lambda_{ex}$ = 530 nm): $\lambda_{max}$ / nm = 605, $\Phi_{fl}$ = 0.78.

## Optical properties of the monomeric PBIs

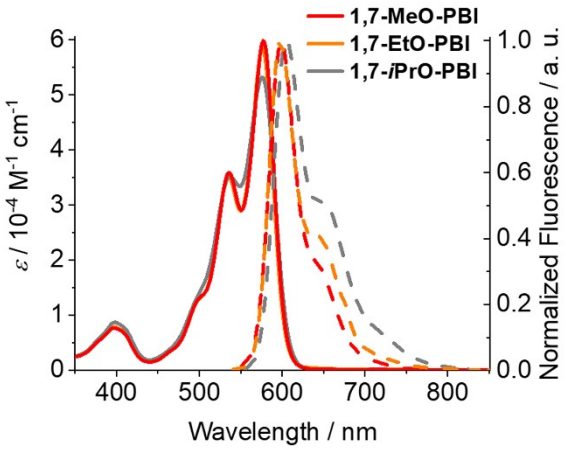


**Figure 104.** UV/vis absorption ($c_T$ = 10 × 10$^{-6}$ M, solid lines) and fluorescence spectra (OD ≤ 0.05, dashed lines, $\lambda_{ex}$ = 530 nm) of monomeric **1,7-MeO-PBI**, **1,7-EtO-PBI** and **1,7-*i*PrO-PBI** in $CHCl_3$ at 23 °C.

**Table 9.** Summary of the UV/vis absorption and emission properties of the monomeric PBIs in $CHCl_3$ ($c_T$ = 10 × 10$^{-6}$ M for UV/vis and $c_T$ ≈ 1 × 10$^{-6}$ M for fluorescence measurements) at 23 °C.

| | $\lambda_{max}$ / nm | $\varepsilon_{max}$ / M$^{-1}$ cm$^{-1}$ | $\lambda_{em}$ / nm[a] | $\Phi_{fl}$ / % | Lifetime / ns (amplitude) |
|---|---|---|---|---|---|
| **1-MeO-PBI$_{mono}$** | 558 | 63000 | 575 | 21 | $\tau_1$ = 1.47 (100%) |
| **1,7-MeO-PBI$_{mono}$** | 577 | 60000 | 598 | 68 | $\tau_1$ = 3.84 (100%) |
| **1,6,7-MeO-PBI$_{mono}$** | 600 | 51000 | 633 | 79 | $\tau_1$ = 5.87 (100%) |
| **1,6,7,12-MeO-PBI$_{mono}$** | 616 | 46500 | 647 | 85 | $\tau_1$ = 6.41 (100%) |
| **1,7-EtO-PBI$_{mono}$** | 577 | 58500 | 598 | 77 | $\tau_1$ = 4.19 (100%) |
| **1,7-*i*PrO-PBI$_{mono}$** | 575 | 53000 | 605 | 78 | $\tau_1$ = 4.77 (100%) |

[a] Excitation wavelengths ($\lambda_{ex}$): **1-MeO-PBI** (500 nm), **1,7-MeO-PBI** (540 nm), 1,7-**EtO-PBI** (530 nm), **1,7-*i*PrO-PBI** (530 nm), **1,6,7-MeO-PBI** (550 nm) and **1,6,7,12-MeO-PBI** (570 nm).

**FT-IR spectra of the monomeric PBIs**

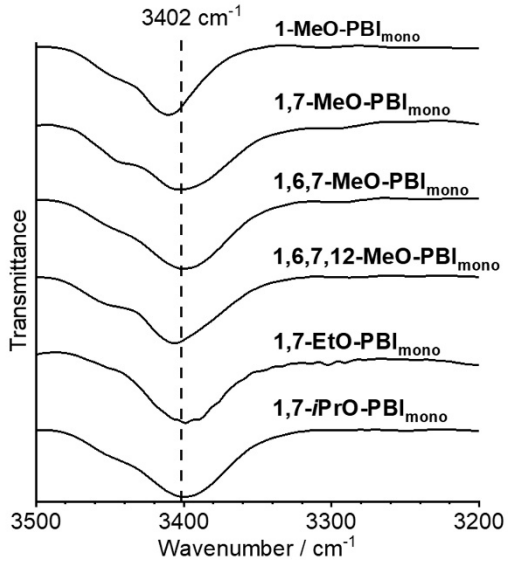


| | $\nu$(N−H) / cm$^{-1}$ |
|---|---|
| **H-PBI**[57] | 3409 |
| **1-MeO-PBI** | 3409 |
| **1,7-MeO-PBI**[62] | 3402 |
| **1,6,7-MeO-PBI** | 3400 |
| **1,6,7,12-MeO-PBI** | 3406 |
| **1,7-EtO-PBI** | 3400 |
| **1,7-*i*PrO-PBI** | 3400 |

**Figure 105.** N−H stretching regions of the FT-IR spectra of monomeric **1-MeO-PBI**, **1,7-MeO-PBI**, **1,6,7-MeO-PBI**, **1,6,7,12-MeO-PBI**, **1,7-EtO-PBI** and **1,7-*i*PrO-PBI** in $CHCl_3$ ($c_T = 0.5 \times 10^{-3}$ M) at 23 °C and comparison of the N−H stretching frequencies.

**Geometry-optimized structures by DFT calculations**

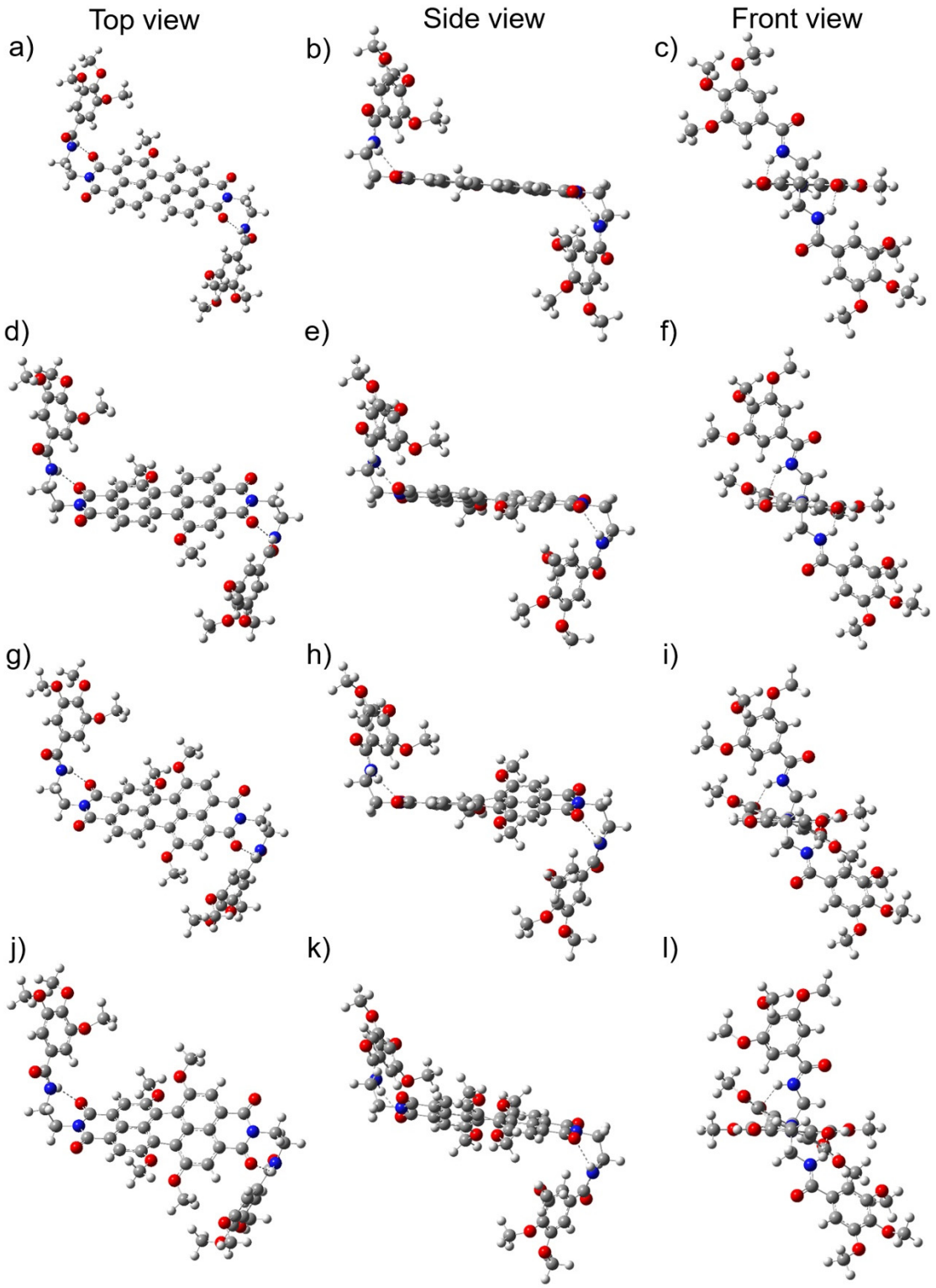


**Figure 106.** Respective top, side and front view of the energy minimized structures of model compounds ($OC_{12}H_{25}$ residues are replaced by OMe) of **1-MeO-PBI** (a-c), **1,7-MeO-PBI** (d-f), **1,6,7-MeO-PBI** (g-i) and **1,6,7,12-MeO-PBI** (j-l) obtained by DFT calculations (Gaussian 09) with B3-LYP as functional and def2-SVP as basis set.[198-199]

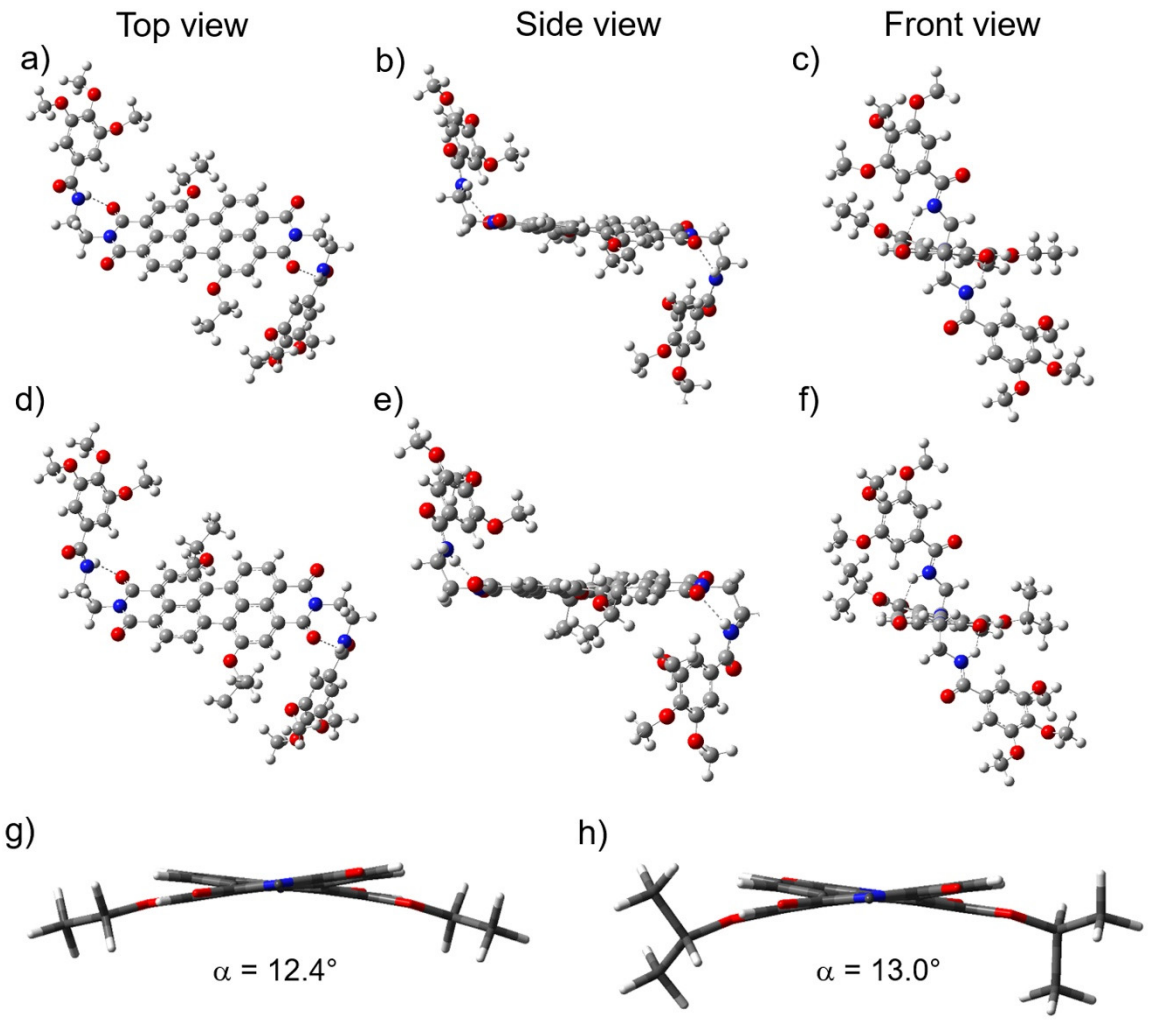


**Figure 107.** Respective top, side and front view of the energy minimized structures of model compounds ($OC_{12}H_{25}$ residues are replaced by OMe) of **1,7-EtO-PBI** (a-c), **1,7-*i*PrO-PBI** (d-f) obtained by DFT calculations (Gaussian 09) with B3-LYP as functional and def2-SVP as basis set.[198-199] Molecular structure (view along the *N*–*N* axis) of **1,7-EtO-PBI** (g) and **1,7-*i*PrO-PBI** (h). In (g) and (h) the imide substituents are omitted for better visualization of the twist angles of the PBI cores.

**Table 10.** Summary of the calculated core twist angles $\alpha$ of the PBIs and length of the hydrogen-bonding $d$(N−H·····O=C) between the amide hydrogen of the spacer and the carbonyl group of the PBI.

| | $\alpha$ / °[a] | $d$(N−H·····O=C) / Å |
|---|---|---|
| **1-MeO-PBI** | 0, 0.7 | 2.2, 2.2 |
| **1,7-MeO-PBI**[62] | 11.4 | 2.1 |
| **1,6,7-MeO-PBI** | 15.0, 29.9 | 2.1, 2.2 |
| **1,6,7,12-MeO-PBI** | 30.5 | 2.1 |
| **1,7-EtO-PBI** | 12.4 | 2.1 |
| **1,7-*i*PrO-PBI** | 13.0 | 2.1 |

[a] Dihedral angle associated with the four carbon atoms in the bay area.

## Optical properties of the thermodynamically favored aggregates

**Table 11.** Summary of the UV/vis absorption properties of the thermodynamically favored aggregates in MCH/Tol (2:1, v/v) of **1-MeO-PBI** ($c_T$ = 20 × $10^{-6}$ M), **1,7-MeO-PBI** ($c_T$ = 20 × $10^{-6}$ M), **1,6,7-MeO-PBI** ($c_T$ = 20 × $10^{-6}$ M), **1,6,7,12-MeO-PBI** ($c_T$ = 200 × $10^{-6}$ M), **1,7-EtO-PBI** ($c_T$ = 20 × $10^{-6}$ M) and **1,7-*i*PrO-PBI** ($c_T$ = 30 × $10^{-6}$ M) at 23 °C.

| | $\lambda_{abs}$ / nm | $\varepsilon_{max}$ / $M^{-1}$ $cm^{-1}$ |
|---|---|---|
| **1-MeO-PBI$_{agg}$** | 507 | 24500 |
| **1,7-MeO-PBI$_{agg}$** | 657 | 21500 |
| **1,6,7-MeO-PBI$_{agg}$** | 531 | 24500 |
| **1,6,7,12-MeO-PBI$_{agg}$** | 547 | 22000 |
| **1,7-EtO-PBI$_{agg}$** | 657 | 16500 |
| **1,7-*i*PrO-PBI$_{agg}$** | 640 | 17000 |

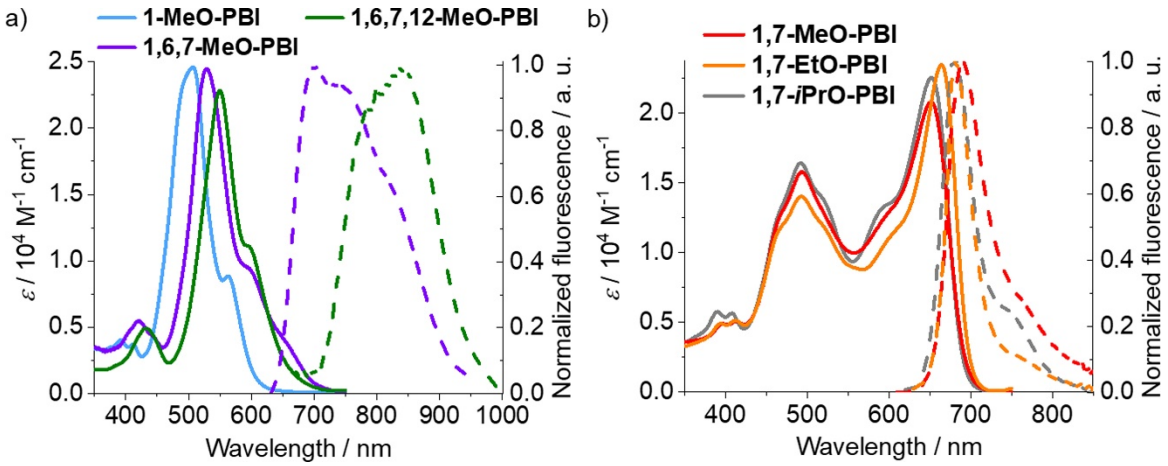


**Figure 108.** UV/vis absorption ($c_T$ = 20 × $10^{-6}$ M, respective solid lines) and emission spectra (OD ≤ 0.05, respective dashed lines) of the thermodynamically favored aggregates in MCH at 23 °C of (a) **1-MeO-PBI** (light blue), **1,6,7-MeO-PBI** (purple) and **1,6,7,12-MeO-PBI** (green) and (b) **1,7-MeO-PBI** (red), **1,7-EtO-PBI** (orange) and **1,7-*i*PrO-PBI** (gray). $\lambda_{ex}$ = 600 nm (**1,7-MeO-PBI$_{agg}$**, **1,7-EtO-PBI$_{agg}$**), 580 nm (**1,7-*i*PrO-PBI$_{agg}$**), 530 nm (**1,6,7-MeO-PBI$_{agg}$**) and 520 nm (**1,6,7,12-MeO-PBI$_{agg}$**).

Note that the fluorescence properties (Figure 108, Table 12) of the thermodynamically favored aggregates were determined in pure MCH instead of MCH/Tol (2:1) to facilitate measurements under higher dilution (OD ≤ 0.05).

**Table 12**. Summary of the UV/vis absorption and emission properties of the thermodynamically favored aggregates of the PBI dyes in pure MCH.

| | $\lambda_{abs}$ / nm | $\varepsilon_{max}$ / $M^{-1}$ $cm^{-1}$ | $\lambda_{em}$ / nm[a] | $\Phi_{fl}$ / % | Lifetime / ns (amplitude) |
|---|---|---|---|---|---|
| **1-MeO-PBI$_{agg}$** | 507 | 24500 | No emission | | |
| **1,7-MeO-PBI$_{agg}$** | 651 | 21500 | 692 | 14 | $\tau_1$ = 1.90 (35%)<br>$\tau_2$ = 3.73 (65%) |
| **1,6,7-MeO-PBI$_{agg}$** | 529 | 24500 | 699 | 2.0 | $\tau_1$ = 3.37 (36%)<br>$\tau_2$ = 7.38 (64%) |
| **1,6,7,12-MeO-PBI$_{agg}$** | 550 | 23000 | 833 | < 1 | n. d. |
| **1,7-EtO-PBI$_{agg}$** | 664 | 23500 | 683 | 21 | $\tau_1$ = 1.79 (37%)<br>$\tau_2$ = 4.04 (63%) |
| **1,7-*i*PrO-PBI$_{agg}$** | 652 | 22500 | 681 | 22 | $\tau_1$ = 3.09 (28%)<br>$\tau_2$ = 6.25 (72%) |

[a] Excitation wavelengths ($\lambda_{ex}$): **1,7-MeO-PBI$_{agg}$** (600 nm), **1,7-EtO-PBI$_{agg}$** (600 nm) and **1,7-*i*PrO-PBI$_{agg}$** (580 nm), **1,6,7-MeO-PBI$_{agg}$** (530 nm), **1,6,7,12-MeO-PBI$_{agg}$** (520 nm).

**Thermodynamically controlled self-assembly**

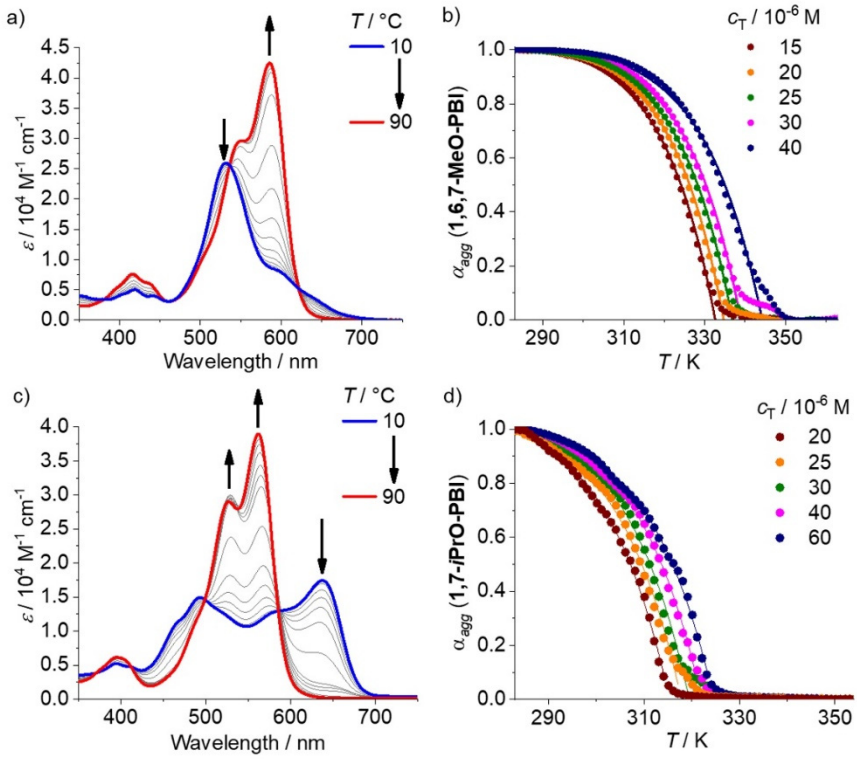


**Figure 109.** Temperature-dependent UV/vis spectra of (a) **1,6,7-MeO-PBI** ($c_T = 20 \times 10^{-6}$ M) and (c) **1,7-*i*PrO-PBI** ($c_T = 30 \times 10^{-6}$ M) in MCH/Tol 2:1 (v/v) upon heating from 10 to 90 °C with 1 °C/min. Plots of the degree of aggregation ($\alpha_{agg}$), calculated from the apparent extinction coefficients at 585 nm or 561 nm ($\lambda_{max}$ of the monomers), respectively, against the temperature for the thermodynamically controlled disassembly processes and the respective fits of the elongation processes with the nucleation-elongation model for (b) **1,6,7-MeO-PBI** and (d) **1,7-*i*PrO-PBI** at different total concentrations $c_T$.

**Table 13.** Thermodynamic parameters $\alpha_{sat}$, $\Delta H_e$, $T_e$ and $K_a$ obtained by fitting of the temperature-dependent degree of aggregation of **1-MeO-PBI** with the cooperative model for different concentrations $c_T$.

| $c_T$ / µM | $\alpha_{sat}$ [a] | $\Delta H_e$ / kJ mol$^{-1}$ [b] | $T_e$ / K [c] | $K_a$ [d] |
|---|---|---|---|---|
| 5 | 1.0239 | −96.6 | 338.1 | $3.9 \times 10^{-3}$ |
| 10 | 1.0215 | −93.2 | 343.9 | $2.5 \times 10^{-3}$ |
| 15 | 1.0158 | −94.5 | 346.8 | $2.7 \times 10^{-3}$ |
| 20 | 1.0133 | −92.4 | 349.4 | $1.6 \times 10^{-3}$ |
| 25 | 1.0421 | −95.3 | 352.5 | $2.8 \times 10^{-3}$ |

[a] Saturation parameter; [b] elongation enthalpy; [c] elongation temperature; [d] dimensionless equilibrium constant of the activation step.

Averaged values: $\Delta H_e = -94.4$ kJ mol$^{-1}$; $K_a = 2.7 \times 10^{-3}$.

**Table 14.** Thermodynamic parameters $\alpha_{sat}$, $\Delta H_e$, $T_e$ and $K_a$ obtained by fitting of the temperature-dependent degree of aggregation of **1,6,7-MeO-PBI** with the cooperative model for different concentrations $c_T$.

| $c_T$ / μM | $\alpha_{sat}$ [a] | $\Delta H_e$ / kJ mol$^{-1}$ [b] | $T_e$ / K [c] | $K_a$ [d] |
|---|---|---|---|---|
| 15 | 1.0407 | −71.1 | 332.6 | $6.9 \times 10^{-4}$ |
| 20 | 1.0329 | −73.1 | 334.7 | $8.2 \times 10^{-4}$ |
| 25 | 1.0306 | −72.9 | 336.9 | $7.7 \times 10^{-4}$ |
| 30 | 1.0300 | −73.5 | 338.9 | $3.7 \times 10^{-4}$ |
| 40 | 1.0319 | −70.7 | 344.2 | $6.3 \times 10^{-4}$ |

[a] Saturation parameter; [b] elongation enthalpy; [c] elongation temperature, [d] dimensionless equilibrium constant of the activation step.

Averaged values: $\Delta H_e = -72.3$ kJ mol$^{-1}$; $K_a = 6.6 \times 10^{-4}$.

**Table 15.** Thermodynamic parameters $\alpha_{sat}$, $\Delta H_e$, $T_e$ and $K_a$ obtained by fitting of the temperature-dependent degree of aggregation of **1,7-EtO-PBI** with the cooperative model for different concentrations $c_T$.

| $c_T$ / μM | $\alpha_{sat}$ [a] | $\Delta H_e$ / kJ mol$^{-1}$ [b] | $T_e$ / K [c] | $K_a$ [d] |
|---|---|---|---|---|
| 15 | 1.0201 | −79.2 | 330.5 | $2.1 \times 10^{-4}$ |
| 20 | 1.0039 | −75.8 | 335.3 | $3.4 \times 10^{-4}$ |
| 25 | 1.0213 | −77.3 | 337.6 | $9.1 \times 10^{-4}$ |
| 40 | 0.9937 | −80.6 | 338.5 | $2.4 \times 10^{-4}$ |
| 60 | 0.9914 | −78.3 | 341.4 | $2.1 \times 10^{-4}$ |

[a] Saturation parameter; [b] elongation enthalpy; [c] elongation temperature, [d] dimensionless equilibrium constant of the activation step.

Average values: $\Delta H_e = -78.2$ kJ mol$^{-1}$; $K_a = 3.8 \times 10^{-4}$

**Table 16.** Thermodynamic parameters $\alpha_{sat}$, $\Delta H_e$, $T_e$ and $K_a$ obtained by fitting of the temperature-dependent degree of aggregation of **1,7-*i*PrO-PBI** with the cooperative model for different concentrations $c_T$.

| $c_T$ / µM | $\alpha_{sat}$ [a] | $\Delta H_e$ / kJ mol$^{-1}$ [b] | $T_e$ / K [c] | $K_a$ [d] |
|---|---|---|---|---|
| 20 | 1.0956 | −61.6 | 315.4 | $2.1 \times 10^{-4}$ |
| 25 | 1.0746 | −63.3 | 317.9 | $1.4 \times 10^{-4}$ |
| 30 | 1.0779 | −64.6 | 319.5 | $1.5 \times 10^{-4}$ |
| 40 | 1.0676 | −65.2 | 322.1 | $4.4 \times 10^{-4}$ |
| 60 | 1.0547 | −65.2 | 324.6 | $2.8 \times 10^{-4}$ |

[a] Saturation parameter; [b] elongation enthalpy; [c] elongation temperature, [d] dimensionless equilibrium constant of the activation step.

Average values: $\Delta H_e = -64.0$ kJ mol$^{-1}$; $K_a = 2.4 \times 10^{-4}$

**Table 17.** Thermodynamic parameters $\Delta H$, $T_m$, $K_{iso}$ and $\Delta G^0$ obtained by fitting of the temperature-dependent degree of aggregation of **1,6,7,12-MeO-PBI** with the isodesmic model for different concentrations $c_T$.

| $c_T$ / µM | $\Delta H$ / kJ mol$^{-1}$ [a] | $T_m$ / K [b] | $K_{iso}$ / M$^{-1}$ [c] | $\Delta G^0$ / kJ mol$^{-1}$ [d] |
|---|---|---|---|---|
| 100 | −105.4 | 309.6 | 37000 | −26.1 |
| 200 | −103.5 | 315.9 | 32000 | −25.7 |
| 300 | −101.0 | 321.1 | 37000 | −26.1 |
| 400 | −104.1 | 325.7 | 42000 | −26.4 |
| 500 | −102.4 | 329.5 | 49000 | −26.8 |

[a] Molar enthalpy; [b] melting temperature; [c] equilibrium constant (values determined at 298.15 K); [d] standard Gibbs free energy.

Averaged values: $\Delta H = -103.3$ kJ mol$^{-1}$; $\Delta G^0 = -26.2$ kJ mol$^{-1}$.

**Van't Hoff plot analysis**

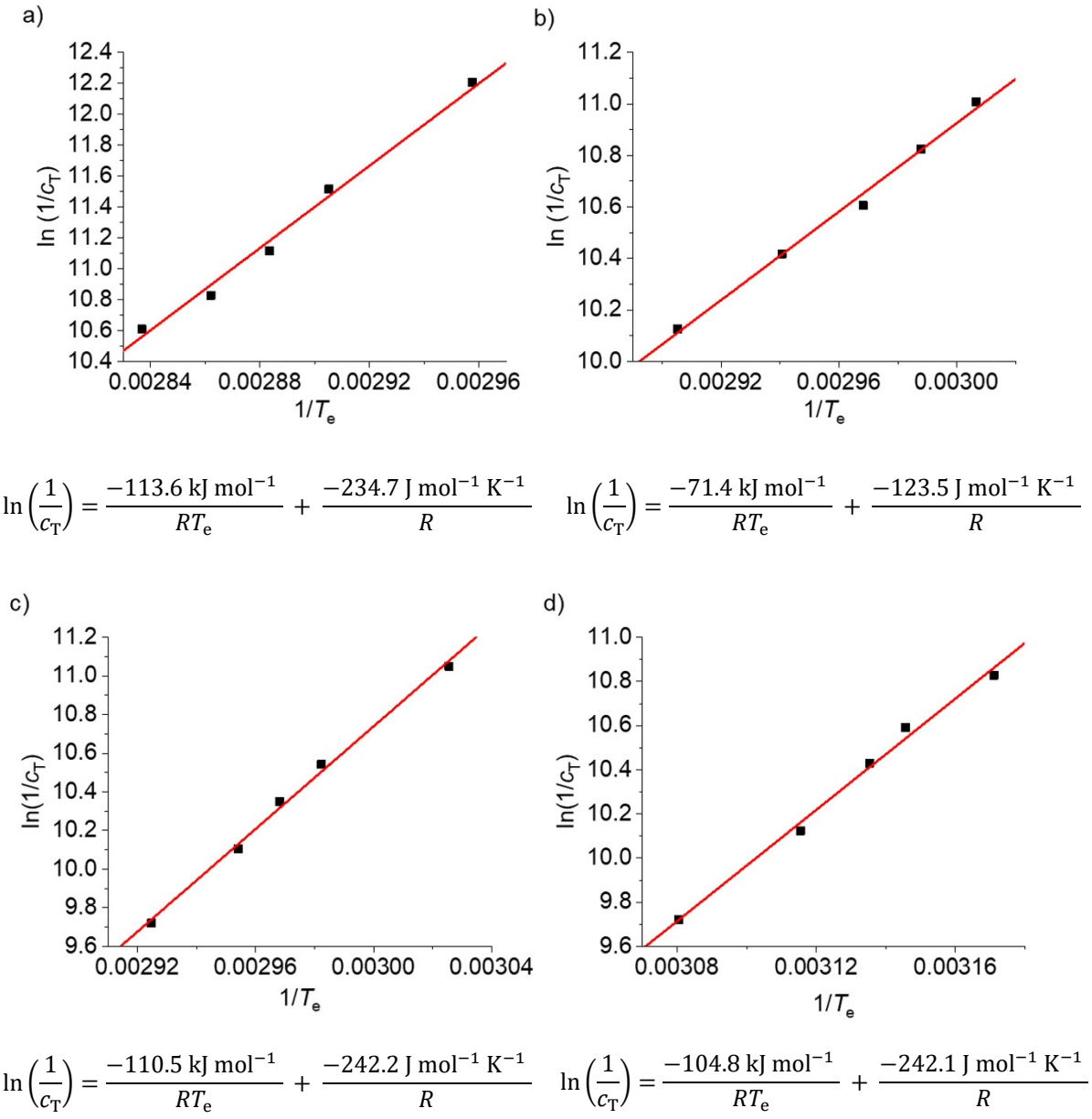


**Figure 110.** Natural logarithm of the reciprocal total concentration $c_T$ as a function of the reciprocal elongation temperatures $T_e$ and fitting of the data points with the van't Hoff equations depicted below the respective graph for (a) **1-MeO-PBI**, (b) 1**,6,7-MeO-PBI**, (c) 1**,7-EtO-PBI** and (d) **1,7-*i*PrO-PBI**.

**1-MeO-PBI**: $\Delta H^0 = -113.6$ kJ mol$^{-1}$, $\Delta S^0 = -234.7$ J mol$^{-1}$ K$^{-1}$, $\Delta G^0 = -44.8$ kJ mol$^{-1}$.

**1,6,7-MeO-PBI**: $\Delta H^0 = -71.4$ kJ mol$^{-1}$, $\Delta S^0 = -123.5$ J mol$^{-1}$ K$^{-1}$, $\Delta G^0 = -35.2$ kJ mol$^{-1}$.

**1,7-EtO-PBI**: $\Delta H^0 = -110.5$ kJ mol$^{-1}$, $\Delta S^0 = -242.2$ J mol$^{-1}$ K$^{-1}$, $\Delta G^0 = -39.5$ kJ mol$^{-1}$.

**1,7-*i*PrO-PBI**: $\Delta H^0 = -104.8$ kJ mol$^{-1}$, $\Delta S^0 = -242.1$ J mol$^{-1}$ K$^{-1}$, $\Delta G^0 = -33.8$ kJ mol$^{-1}$.

## Comparison of the thermodynamic parameters

**Table 18.** Comparison of the thermodynamic parameters $\Delta H_e$, $K_a$ and $\langle \mathbf{N_N}(\mathbf{T_e}) \rangle$ obtained by fitting the UV/vis data of thermodynamically controlled heating processes with nucleation-elongation model.

| | $\Delta H_e$ / kJ mol$^{-1}$ | $K_a$ | $\langle N_N(T_e) \rangle$ | $\Delta G^0$ / kJ mol$^{-1}$ |
|---|---|---|---|---|
| **H-PBI**[57] | −108.1 | $3.2 \times 10^{-3}$ | 15 | −47.2[a] |
| **1-MeO-PBI** | −94.4 | $2.7 \times 10^{-3}$ | 7 | −44.8[a] |
| **1,7-MeO-PBI**[62] | −86.4 | $1.4 \times 10^{-3}$ | 9 | −44.0[a] |
| **1,6,7-MeO-PBI** | −72.2 | $6.6 \times 10^{-4}$ | 11 | −35.2[a] |
| **1,6,7,12-MeO-PBI** | isodesmic aggregation | | | −26.2[b] |
| **1,7-EtO-PBI** | −78.2 | $3.8 \times 10^{-4}$ | 14 | −39.5[a] |
| **1,7-*i*PrO-PBI** | −64.0 | $2.4 \times 10^{-4}$ | 16 | −33.8[a] |

[a] Values obtained from van't Hoff plot. [b] Value determined by fitting with isodesmic model.

**Morphology of the aggregates studied by AFM**

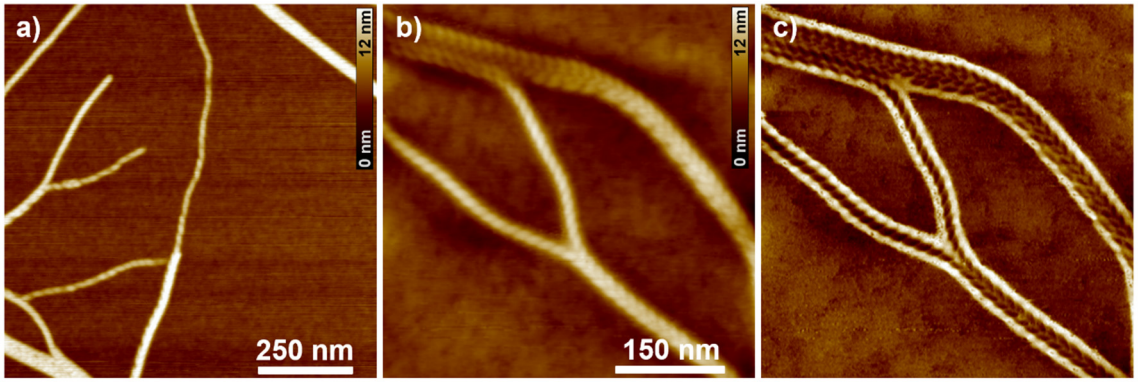


**Figure 111.** AFM height (a,b) and phase (c) images of samples prepared by spin-coating of **1-MeO-PBI** aggregate solution in MCH/Tol (2:1, v/v) onto a silicon wafer. *Z* scale is 12 nm (a,b).

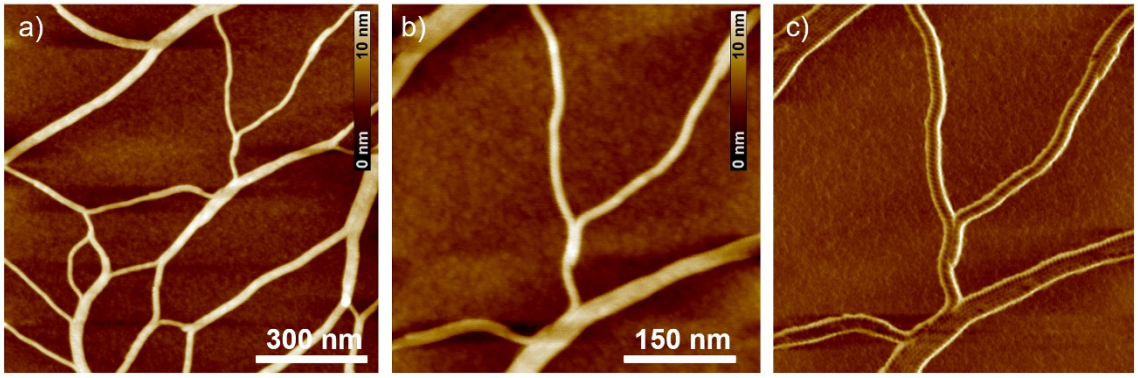


**Figure 112.** AFM height (a,b) and phase (c) images of samples prepared by spin-coating of **1,6,7-MeO-PBI** aggregate solution in MCH/Tol (2:1, v/v) onto a silicon wafer. *Z* scale is 10 nm (a,b).

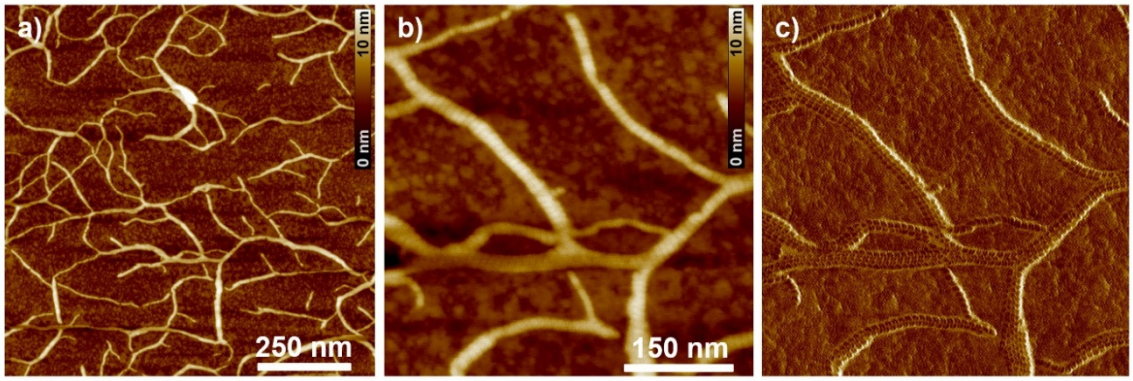


**Figure 113.** AFM height (a,b) and phase (c) images of samples prepared by spin-coating of **1,6,7,12-MeO-PBI** aggregate solution in MCH/Tol (2:1, v/v) onto a silicon wafer. *Z* scale is 10 nm (a,b).

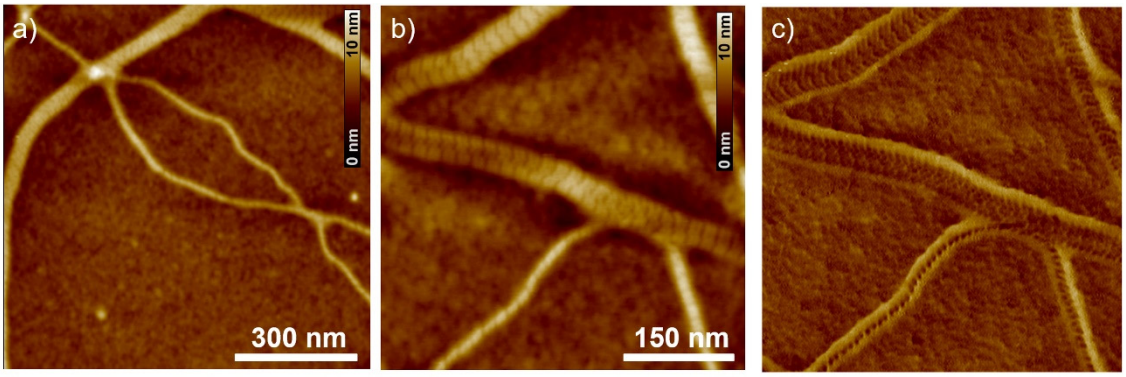


**Figure 114.** AFM height (a,b) and phase (c) images of samples prepared by spin-coating of **1,7-EtO-PBI** aggregate solution in MCH/Tol (2:1, v/v) onto a silicon wafer. *Z* scale is 10 nm (a,b).

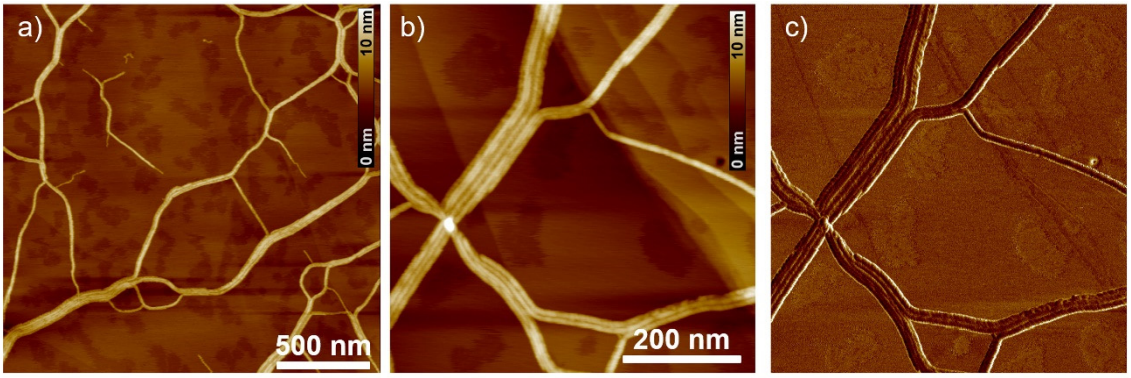


**Figure 115.** AFM height (a,b) and phase (c) images of samples prepared by spin-coating of **1,7-*i*PrO-PBI** aggregate solution in MCH/Tol (2:1, v/v) onto a silicon wafer. *Z* scale is 10 nm (a,b).

**Table 19.** Summary of the values obtained by atomic force microscopy (AFM).

| | **Heigth / nm** | **Helical pitch / nm** | **Molecules per turn[a]** |
|---|---|---|---|
| **H-PBI$_{agg}$**[57] | 4.0 | 15 | 43 |
| **1-MeO-PBI$_{agg}$** | 4.4 | 14 | 40 |
| **1,7-MeO-PBI$_{agg}$**[62] | 4.0 | 5.0 | 14 |
| **1,6,7-MeO-PBI$_{agg}$** | 4.2 | 5.3 | 15 |
| **1,6,7,12-MeO-PBI$_{agg}$** | 3.8 | 8.9 | 25 |
| **1,7-EtO-PBI$_{agg}$** | 4.2 | 7.1 | 20 |
| **1,7-*i*PrO-PBI$_{agg}$** | 3.8 | 7.6 | 22 |

[a] Values are calculated for an estimated $\pi$-$\pi$-distance of 3.5 Å.

**Kinetically controlled aggregation**

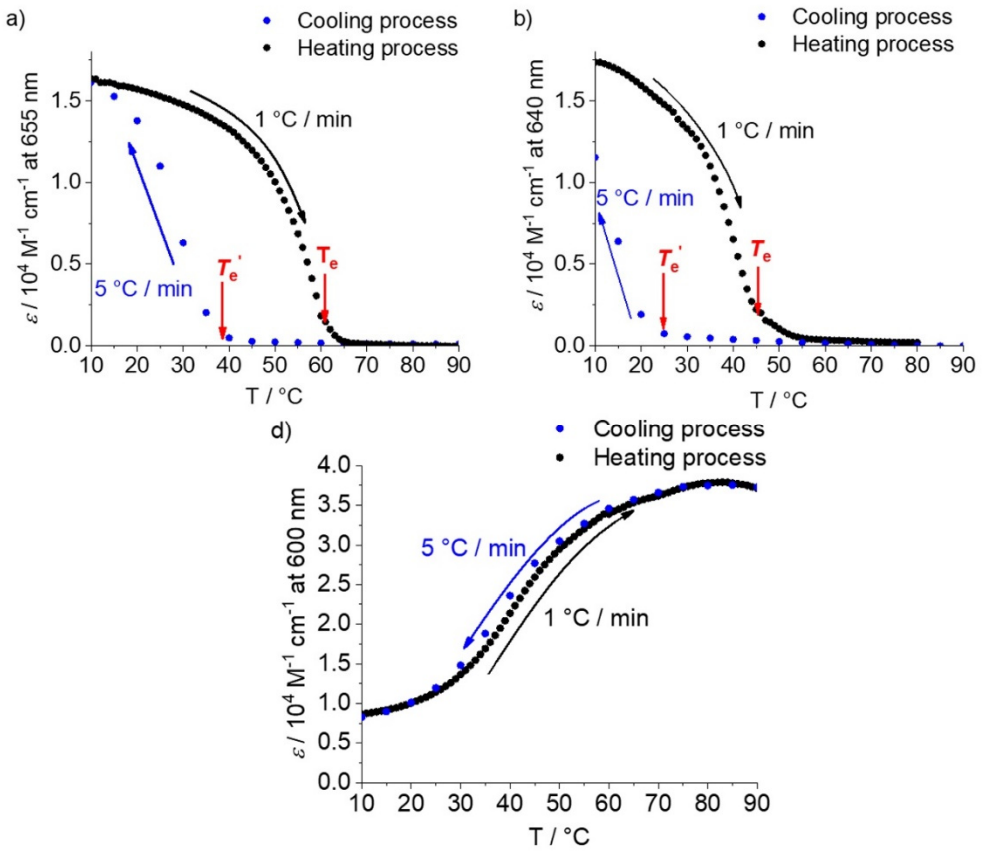


**Figure 116.** Temperature-dependent apparent extinction coefficients of (a) **1,7-EtO-PBI** at 655 nm, (b) **1,7-*i*PrO-PBI** at 640 nm and (c) **1,6,7,12-MeO-PBI** at 600 nm in MCH/Tol (2:1, v/v) observed in the respective cooling (blue) processes at a rate of 5 °C/min and respective heating (black) processes at a rate of 1 °C/min (**1,7-EtO-PBI**: $c_T$ = 20 × $10^{-6}$ M, **1,7-*i*PrO-PBI**: $c_T$ = 30 × $10^{-6}$ M and **1,6,7,12-MeO-PBI**: $c_T$ = 200 × $10^{-6}$ M).

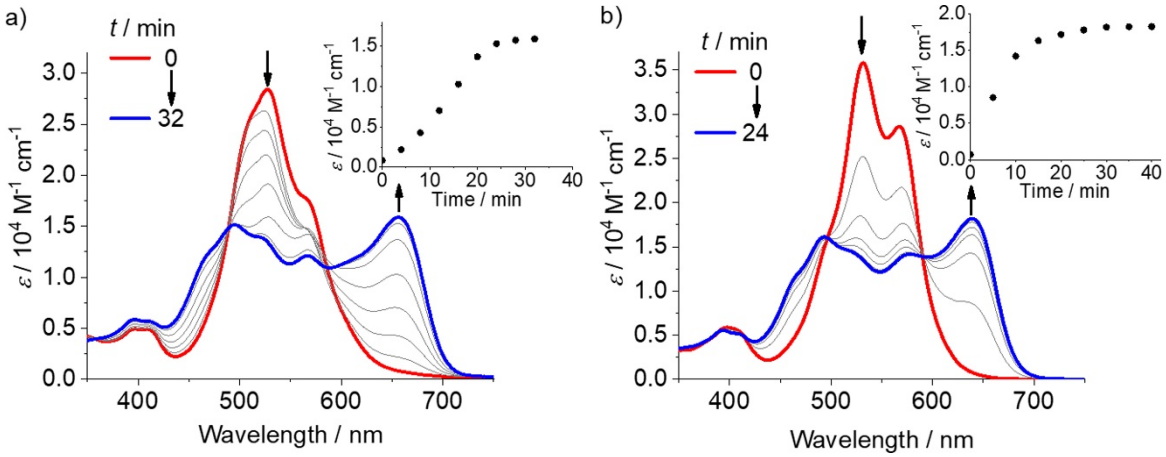


**Figure 117.** Time-dependent UV/vis spectra of (a) **1,7-EtO-PBI** ($c_T$ = 15 × $10^{-6}$ M) and (b) **1,7-*i*PrO-PBI** ($c_T$ = 40 × $10^{-6}$ M) in a solvent mixture of MCH/Tol (2:1, v/v) after rapid cooling (15 °C/min) from 90 to 20 °C (time interval between individual spectra: 4 min). Inset: Plot of the apparent extinction coefficients of (a) **1,7-EtO-PBI** at 655 nm and (b) **1,7-*i*PrO-PBI** at 640 nm, respectively, against the time after cooling from 90 to 20 °C.

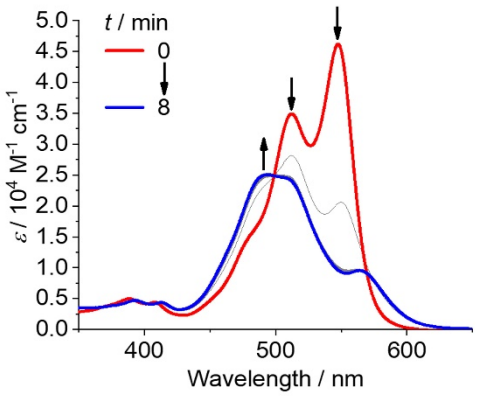


**Figure 118.** Time-dependent UV/vis spectra of **1-MeO-PBI** ($c_T$ = 10 × $10^{-6}$ M) in MCH/Tol (2:1, v/v) after rapid cooling from 90 to 30 °C (time interval between individual spectra: 2 min).

## Stability of the kinetically trapped monomer

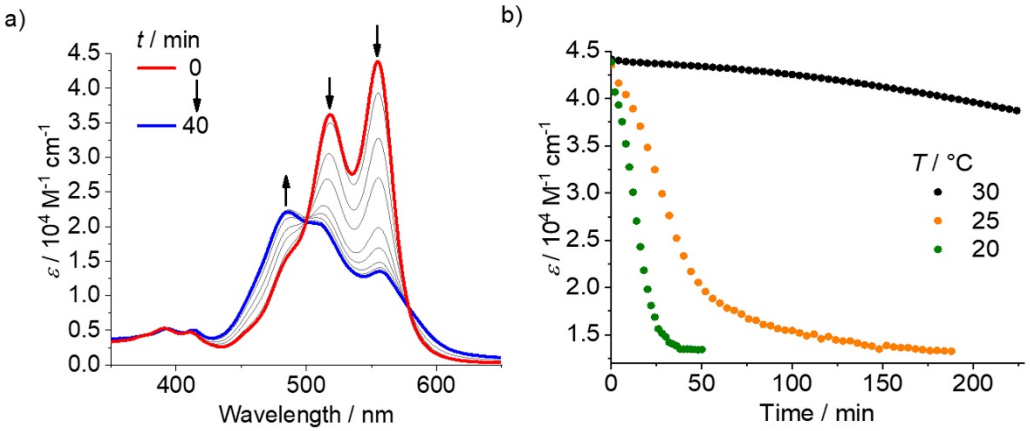


**Figure 119.** a) Time-dependent UV/vis absorption spectra of **1-MeO-PBI** in MCH/Tol (1:2, v/v, $c_T$ = 10 × $10^{-6}$ M) after rapid cooling from 90 to 20 °C (time interval between individual spectra: 4 min). b) Plots of the apparent extinction coefficients of **1-MeO-PBI** at 555 nm against the time after rapid cooling to 30, 25 and 20 °C.

**Two-component seeded polymerization**

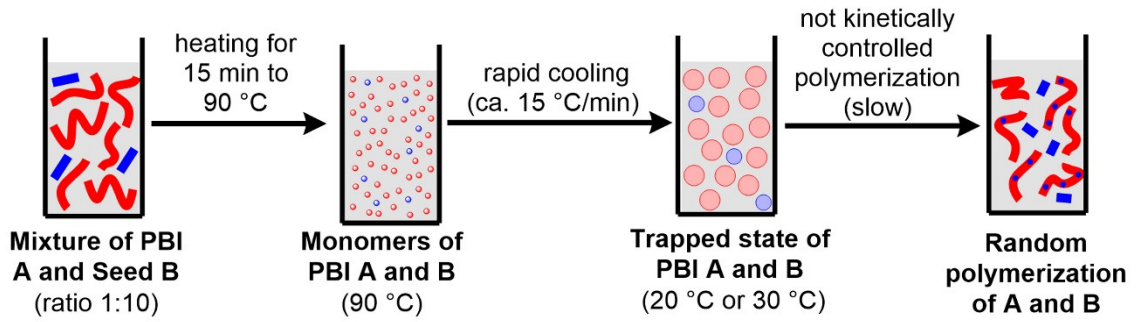


**Figure 120.** Schematic illustration of the thermodynamic control experiment of **PBI A** and **PBI B**.

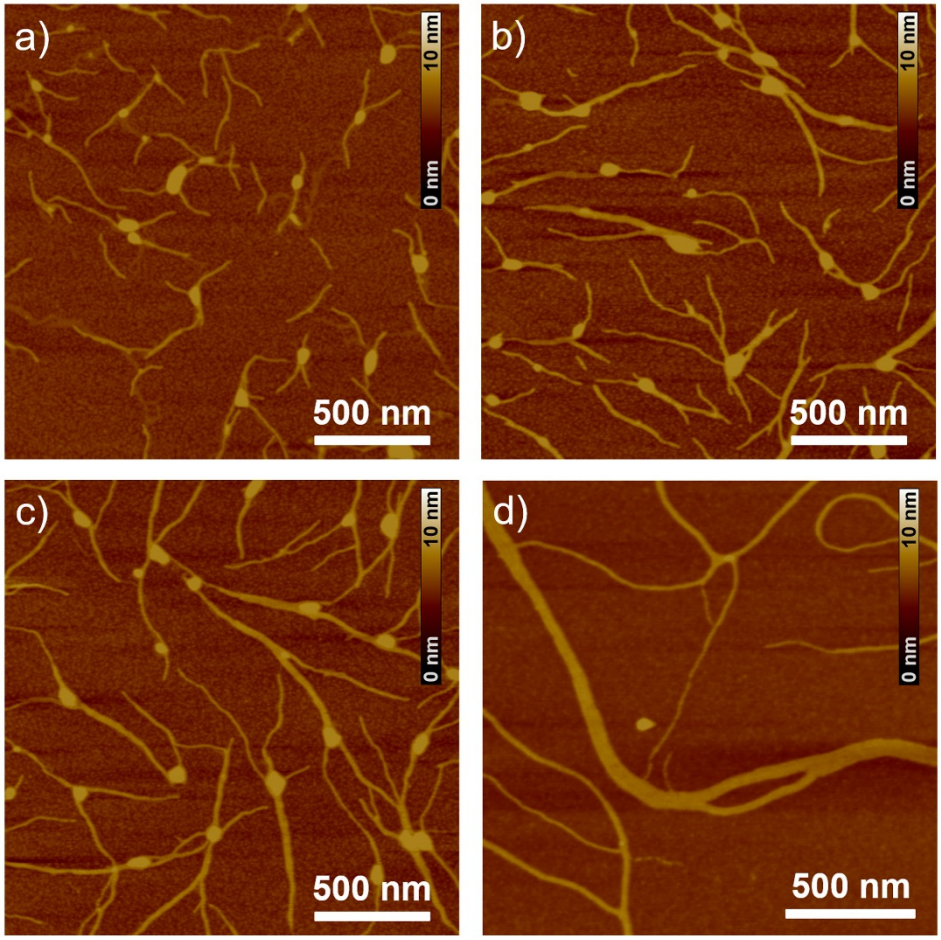


**Figure 121.** AFM height images of samples prepared by spin-coating of the respective solutions onto silicon wafers taken at (a) 5, (b) 10, (c) 20 and (d) 30 min after addition of **1,7-EtO-PBI$_{seed}$** with a seed ratio of 1:10 to the kinetically trapped **1,7-MeO-PBI$_{trapped}$** ($c_T$ = 15 × $10^{-6}$ M) in MCH/Tol (1:2, v/v) at 20 °C. The *Z* scale is 10 nm (a,b,c,d).

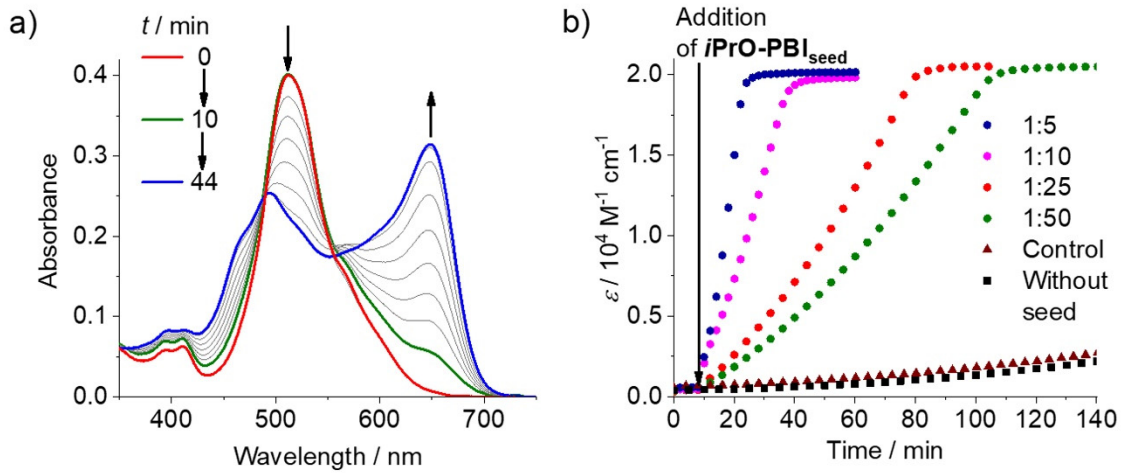


**Figure 122.** a) Time-dependent UV/vis spectra of the two-component seeded copolymerization of **1,7-MeO-PBI$_{trapped}$** ($c_T$ = 15 × 10$^{-6}$ M) with **1,7-*i*PrO-PBI$_{seed}$** [seed ratio $c_T$(**1,7-*i*PrO-PBI$_{seed}$**) : $c_T$(**1,7-MeO-PBI$_{trapped}$**) = 1:10 in MCH/Tol 2:1 (v/v)] at 20 °C. b) Plots of the apparent extinction coefficients at 650 nm of 1,7-MeO-PBI$_{agg}$ against time upon addition of seed solution of **1,7-*i*PrO-PBI$_{seed}$** in ratios of $c_T$(**1,7-iPrO-PBI$_{seed}$**) : $c_T$(**1,7-MeO-PBI$_{trapped}$**) = 1:5 (blue dots), 1:10 (purple dots), 1:25 (red dots) and 1:50 (green dots). The control experiment of a 1:10 mixture of **1,7-*i*PrO-PBI** and **1,7-MeO-PBI** (brown triangles) and spontaneous polymerization of unimolecular **1,7-MeO-PBI** (black squares) are shown for comparison.

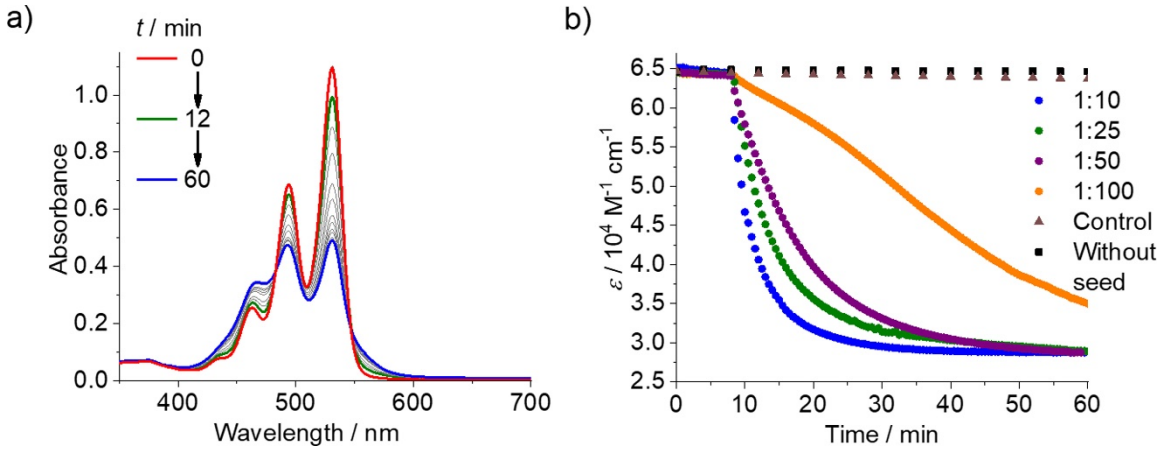


**Figure 123.** a) Time-dependent UV/vis spectra of the two-component seeded copolymerization of **H-PBI$_{trapped}$** ($c_T$ = 20 × 10$^{-6}$ M) with **1-MeO-PBI$_{seed}$** (seed ratio $c_T$(**1-MeO-PBI$_{seed}$**) : $c_T$(**H-PBI$_{trapped}$**) = 1:50 in toluene at 30 °C. b) Plots of the apparent extinction coefficients at 530 nm ($\varepsilon$) of **H-PBI$_{agg}$** against time upon addition of seed solution of **1-MeO-PBI** in ratios of $c_T$(**1-MeO-PBI$_{seed}$**) : $c_T$(**H-PBI$_{trapped}$**) = 1:10 (blue dots), 1:25 (green dots), 1:50 (purple dots) and 1:100 (orange dots). The control experiment of a 1:10 mixture of **1-MeO-PBI** and **H-PBI** (brown triangles) and spontaneous polymerization of unimolecular **H-PBI** (black squares) are shown for comparison.

## NMR Spectra

### 1-Methoxyperylene-3,4:9,10-tetracarboxylic acid tetramethylester 20a

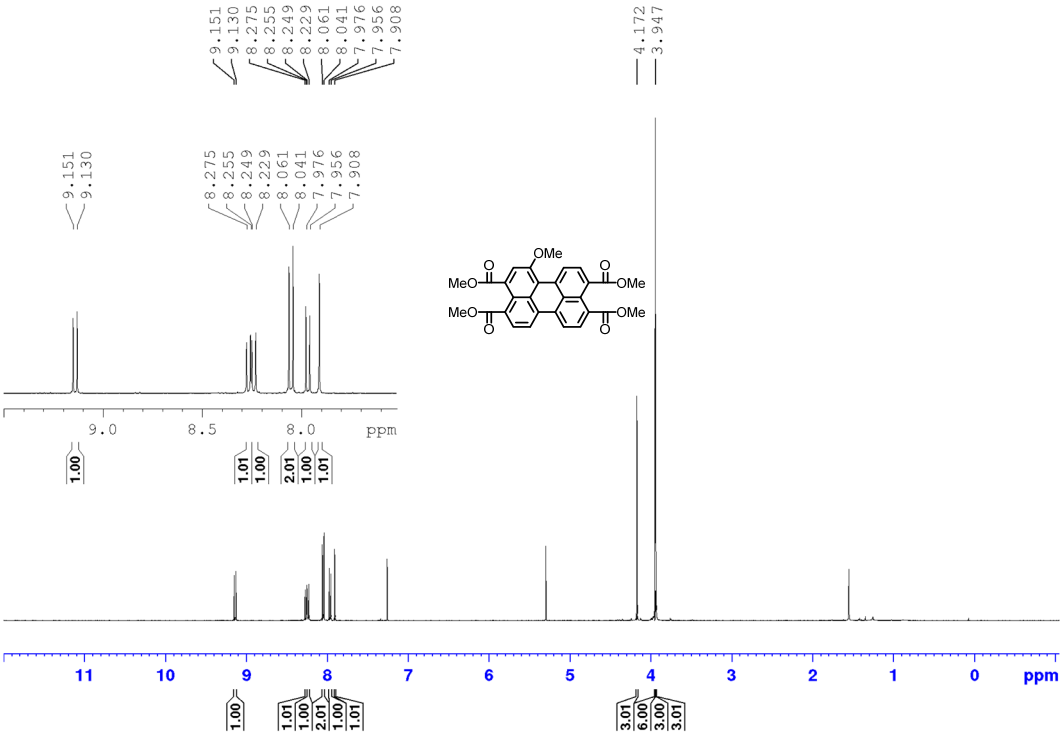


**Figure 124.** $^{1}$H NMR spectrum (400 MHz) of **20a** in $CDCl_3$ recorded at 298 K.

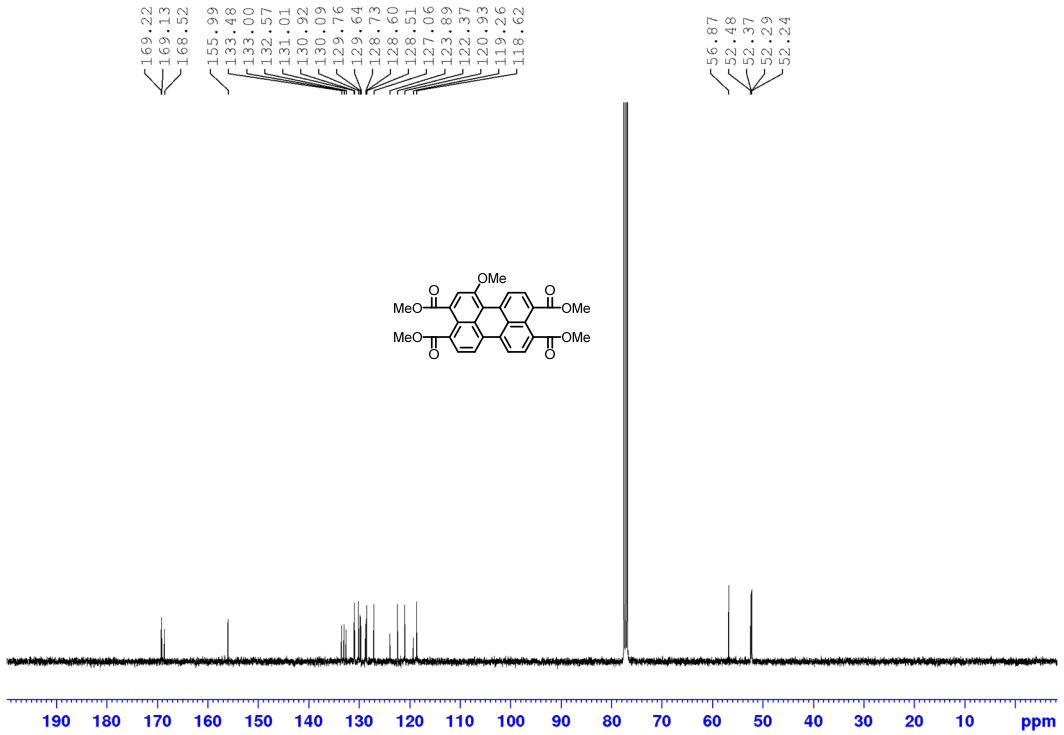


**Figure 125.** $^{13}$C NMR spectrum (100 MHz) of **20a** in $CDCl_3$ recorded at 298 K.

**_N,N'_-(2-(3,4,5-Tris(dodecyloxy)benzamido)ethyl)-1-methoxyperylene-3,4:9,10-tetracarboxylic acid bisimide 1-MeO-PBI**

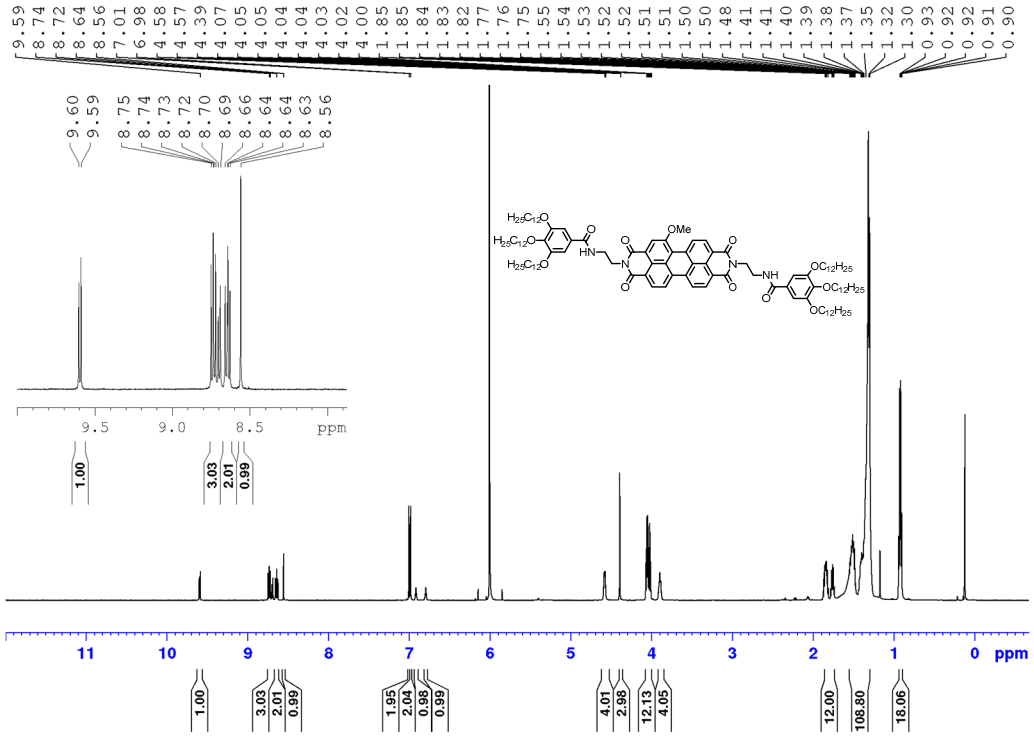

**Figure 126.** $^{1}$H NMR spectrum (600 MHz) of **1-MeO-PBI** in 1,1,2,2-tetrachloroethane-$d_2$ recorded at 345 K.

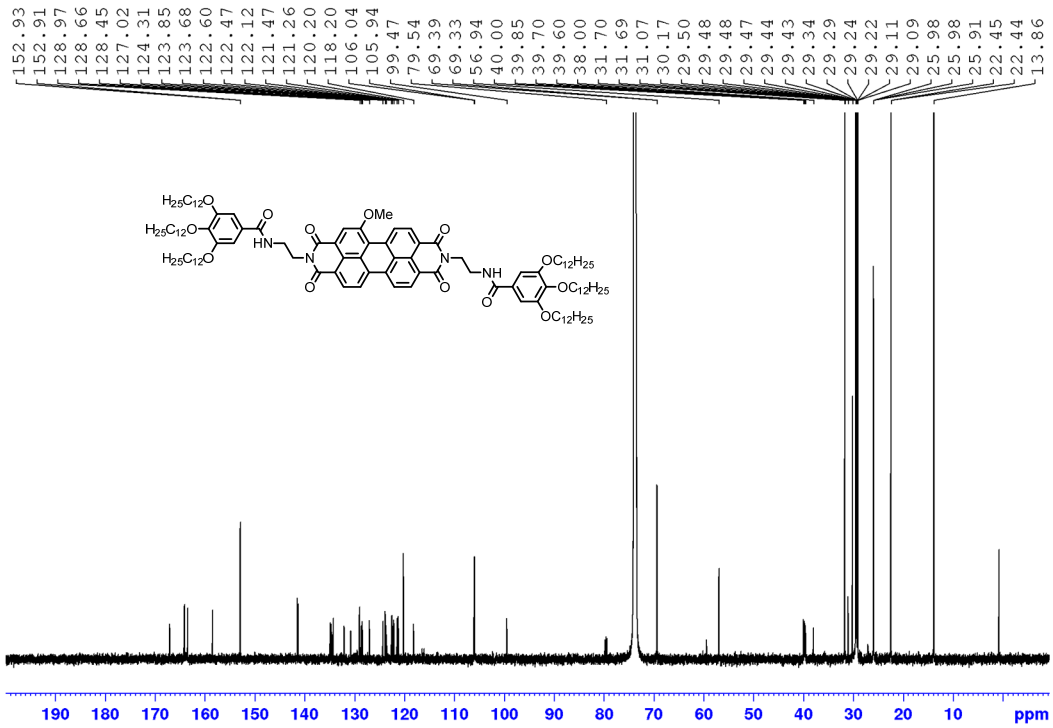

**Figure 127.** $^{13}$C NMR spectrum (150 MHz) of **1-MeO-PBI** in 1,1,2,2-tetrachloroethane-$d_2$ recorded at 345 K.

**_N,N'_-(2-(3,4,5-Tris(dodecyloxy)benzamido)ethyl)-1,6,7-tri(methoxy)-perylene-3,4:9,10-tetracarboxylic acid bisimide 1,6,7-MeO-PBI**

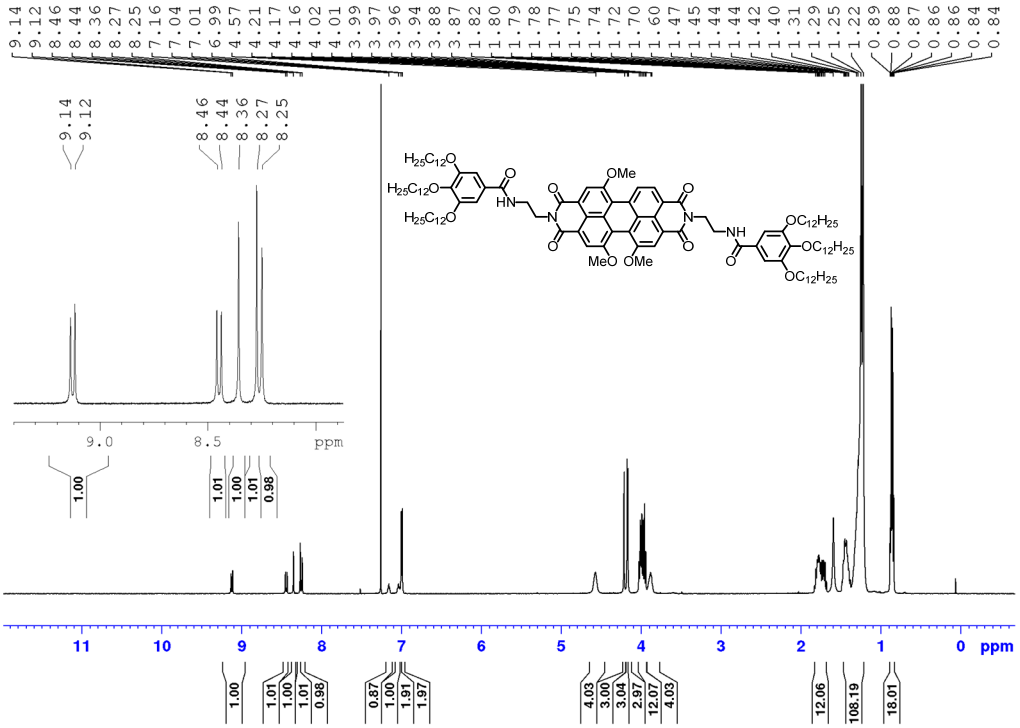


**Figure 128.** $^{1}$H NMR spectrum (400 MHz) of **1,6,7-MeO-PBI** in $CDCl_3$ recorded at 298 K.

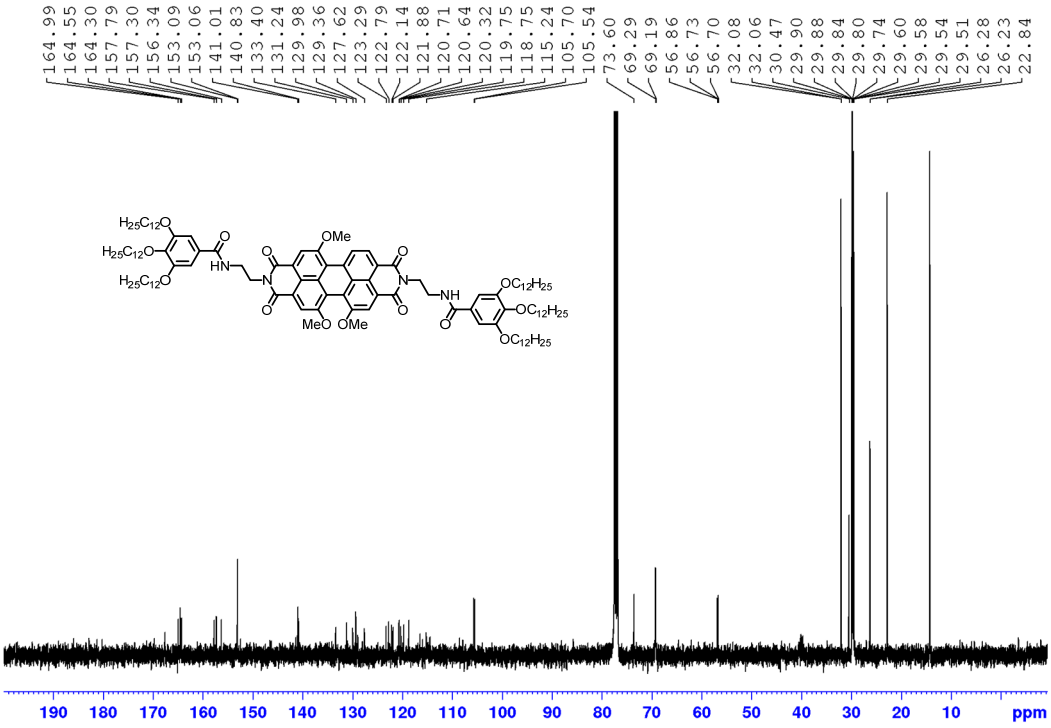


**Figure 129.** $^{13}$C NMR spectrum (100 MHz) of **1,6,7-MeO-PBI** in $CDCl_3$ recorded at 298 K.

***N,N'*-(2-(3,4,5-Tris(dodecyloxy)benzamido)ethyl)-1,6,7,12-tetramethoxyperylene-3,4:9,10-tetracarboxylic acid bisimide 1,6,7,12-MeO-PBI**

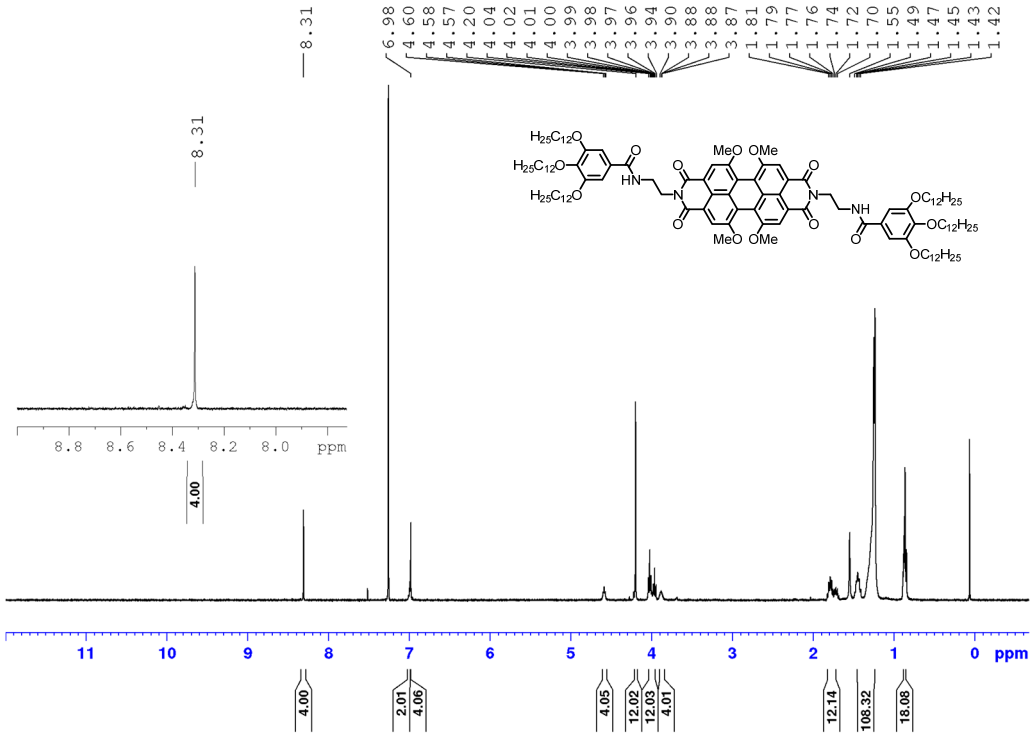


**Figure 130.** $^{1}$H NMR spectrum (400 MHz) of **1,6,7,12-MeO-PBI** in $CDCl_3$ recorded at 298 K.

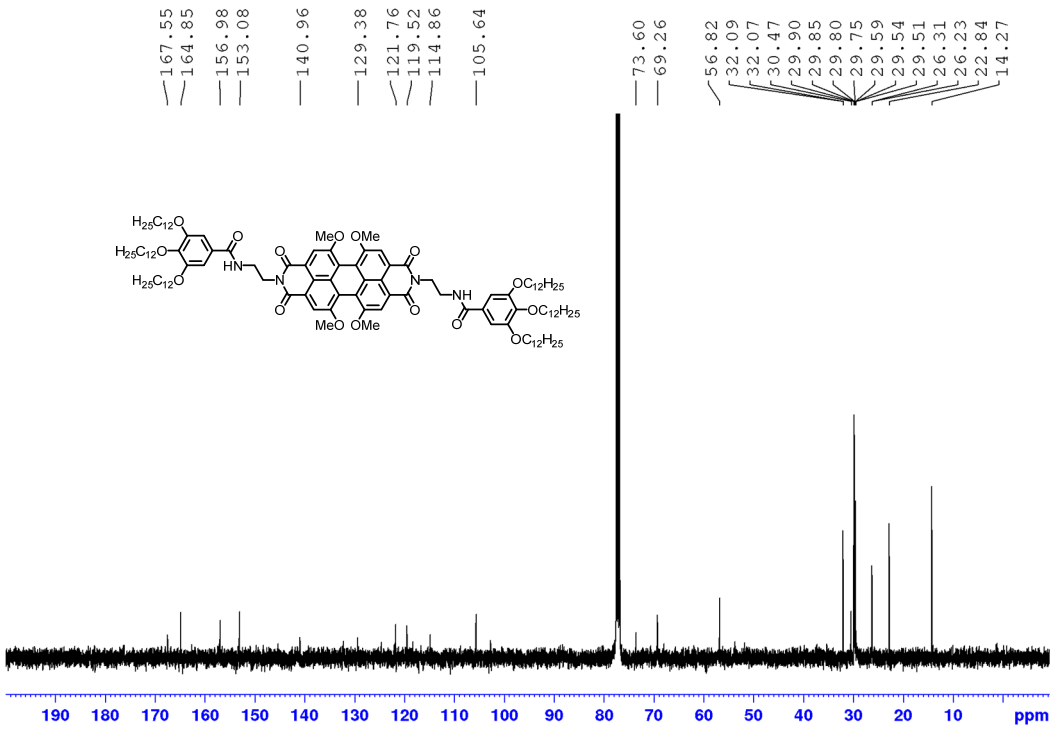


**Figure 131.** $^{13}$C NMR spectrum (100 MHz) of **1,6,7,12-MeO-PBI** in $CDCl_3$ recorded at 298 K.

**_N,N'_-(2-(3,4,5-Tris(dodecyloxy)benzamido)ethyl)-1,7-diethoxyperylene-3,4:9,10-tetracarboxylic acid bisimide 1,7-EtO-PBI**

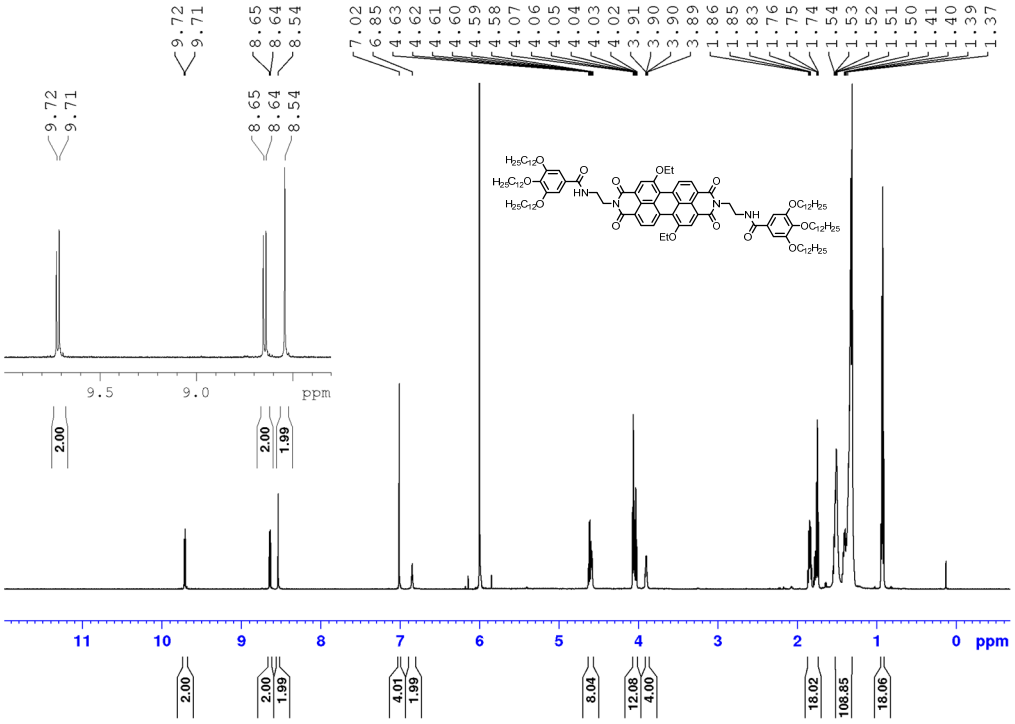


**Figure 132.** $^{1}$H NMR spectrum (600 MHz) of **1,7-EtO-PBI** in 1,1,2,2-tetrachloroethane-$d_2$ recorded at 345 K.

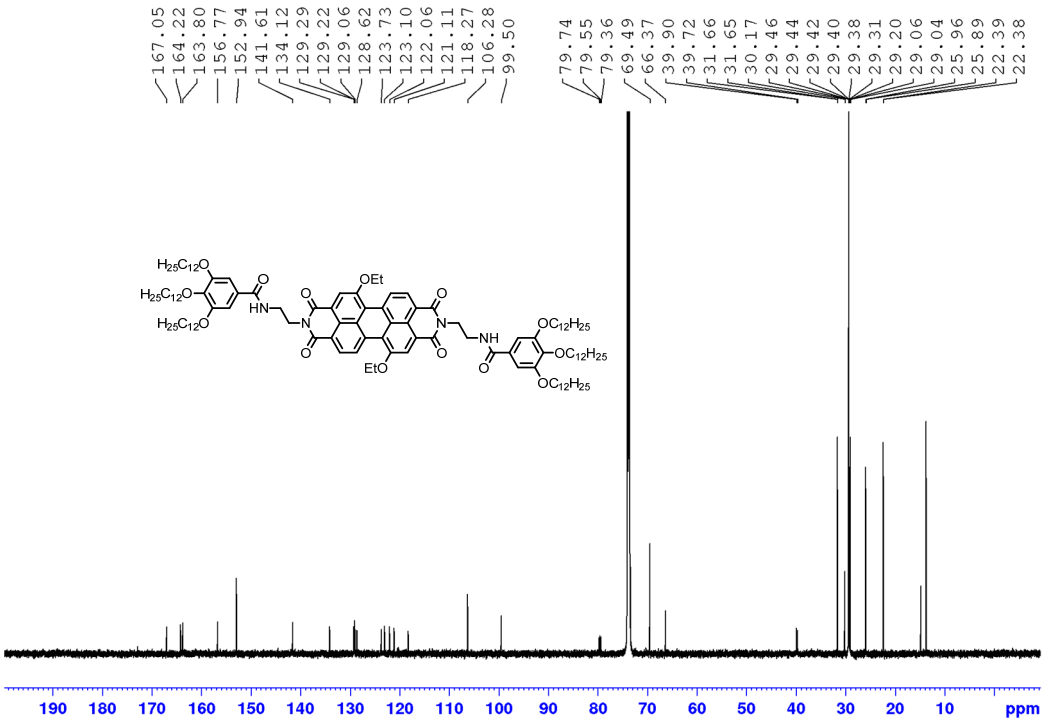


**Figure 133.** $^{13}$C NMR spectrum (150 MHz) of **1,7-EtO-PBI** in 1,1,2,2-tetrachloroethane-$d_2$ recorded at 345 K.

**_N,N'_-Dicyclohexyl-1,7-diisopropyloxyperylene-3,4:9,10-tetracarcoxylic acid bisimide 23c**

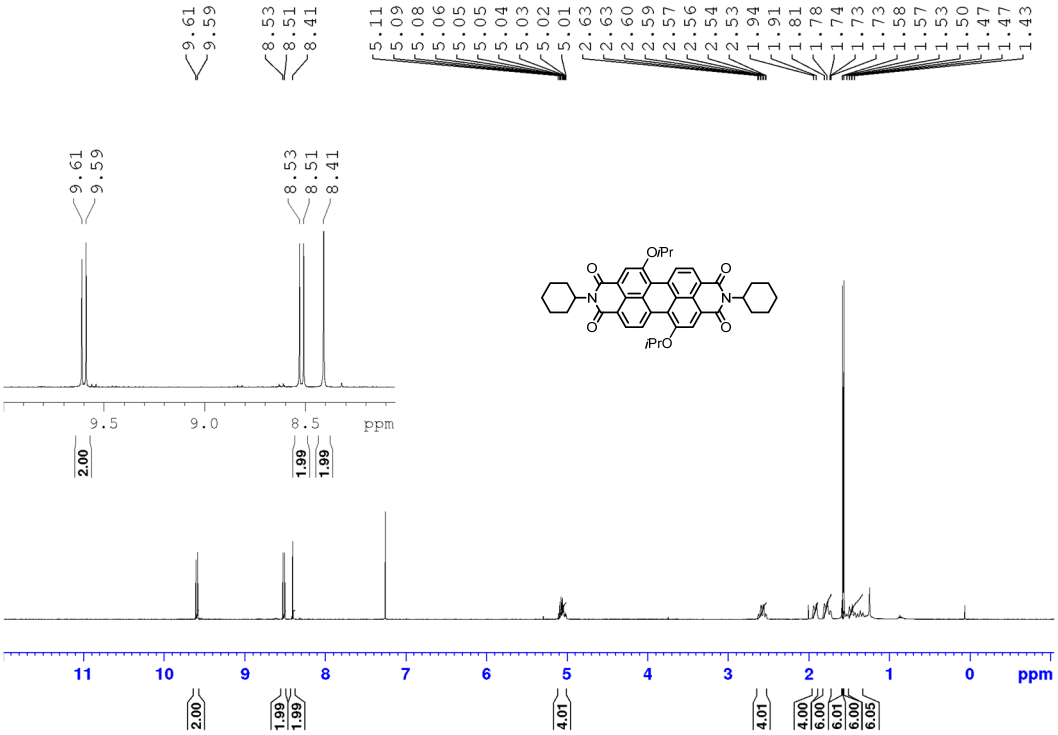


**Figure 134.** $^{1}$H NMR spectrum (400 MHz) of **23c** in $CDCl_3$ recorded at 298 K.

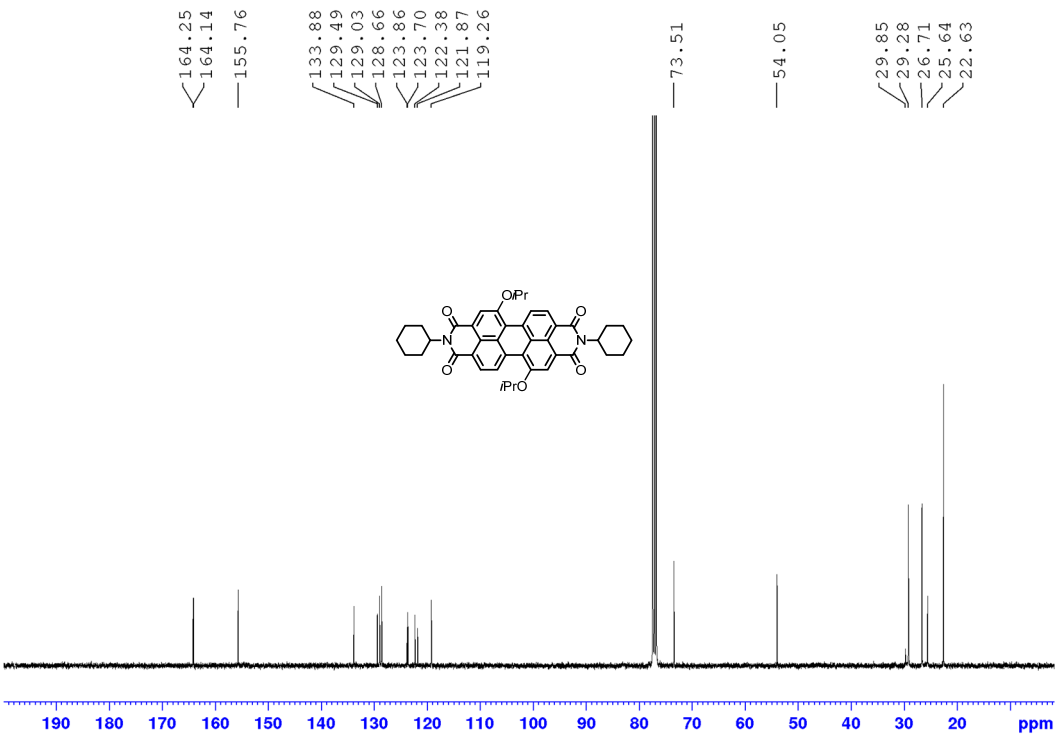


**Figure 135.** $^{13}$C NMR spectrum (100 MHz) of **23c** in $CDCl_3$ recorded at 298 K.

**_N,N'_-(2-(3,4,5-tris(dodecyloxy)benzamido)ethyl)-1,7-diisopropylperylene-3,4:9,10-tetracarboxylic acid bisimide 1,7-_i_PrO-PBI**

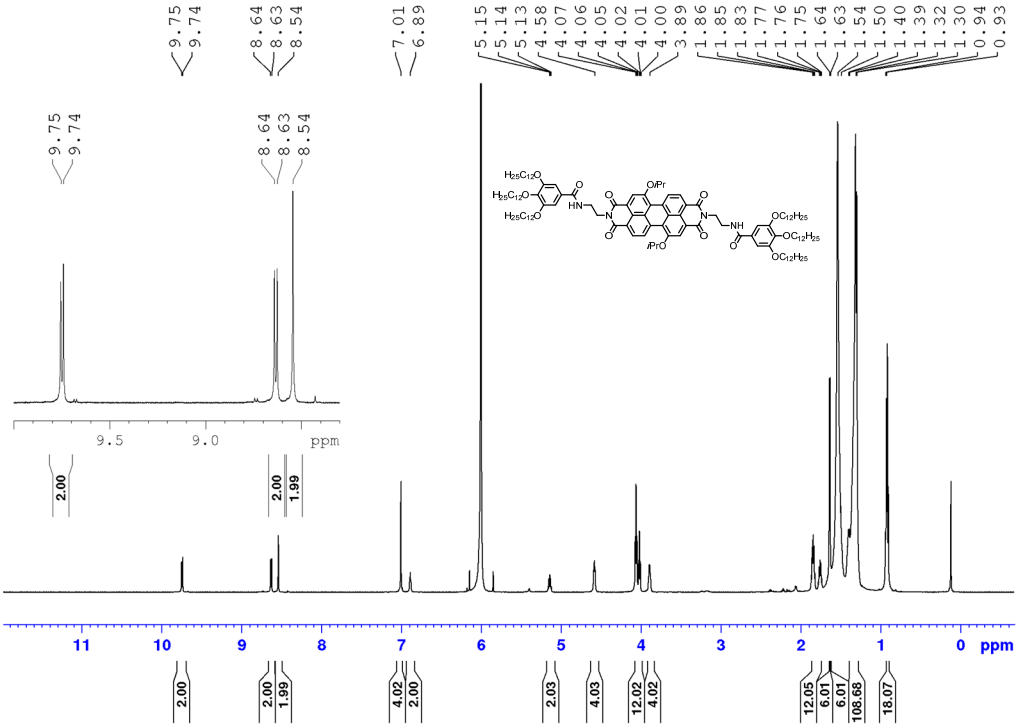


**Figure 136.** $^{1}$H NMR spectrum (600 MHz) of **1,7-*i*PrO-PBI** in 1,1,2,2-tetrachloroethane-$d_2$ recorded at 345 K.

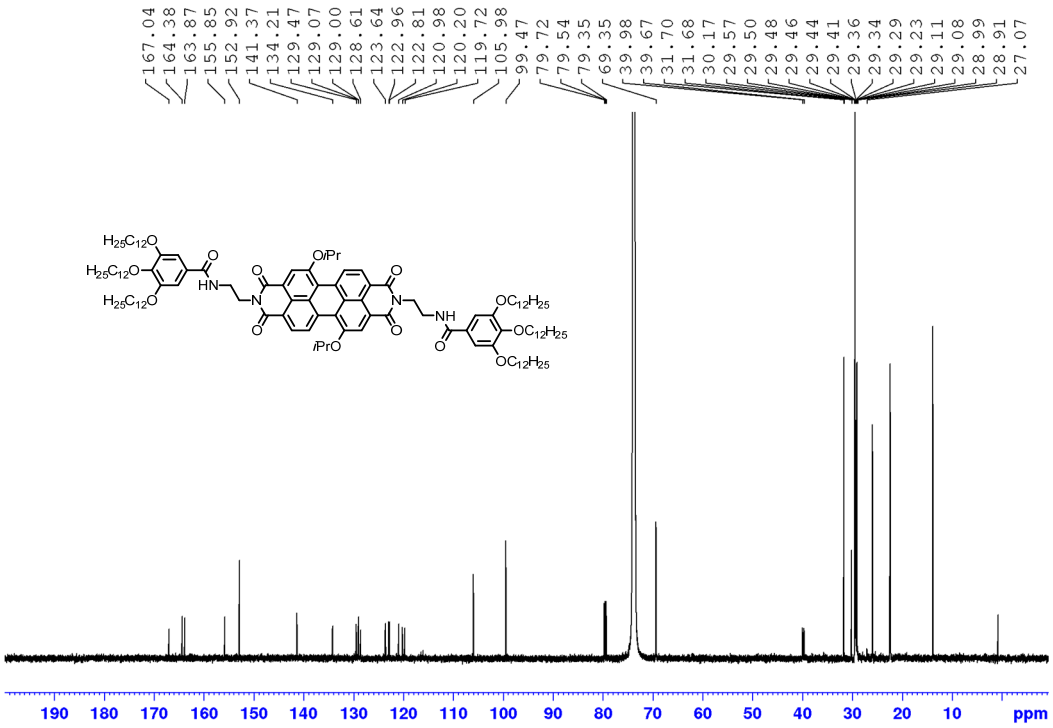


**Figure 137.** $^{13}$C NMR spectrum (150 MHz) of **1,7-*i*PrO-PBI** in 1,1,2,2-tetrachloroethane-$d_2$ recorded at 345 K.

## High resolution mass spectrometry

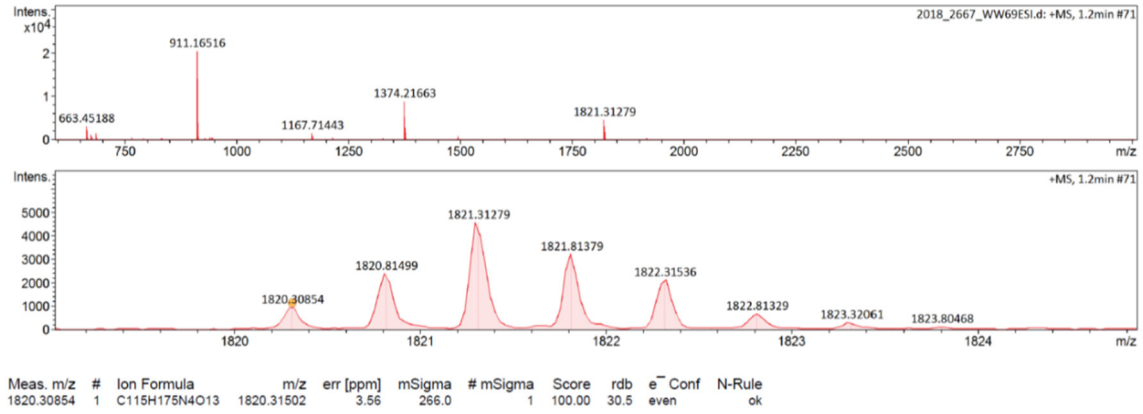


**Figure 138.** High resolution mass spectrum (ESI, positive mode, $CHCl_3/CH_3CN$) of **1-MeO-PBI**.

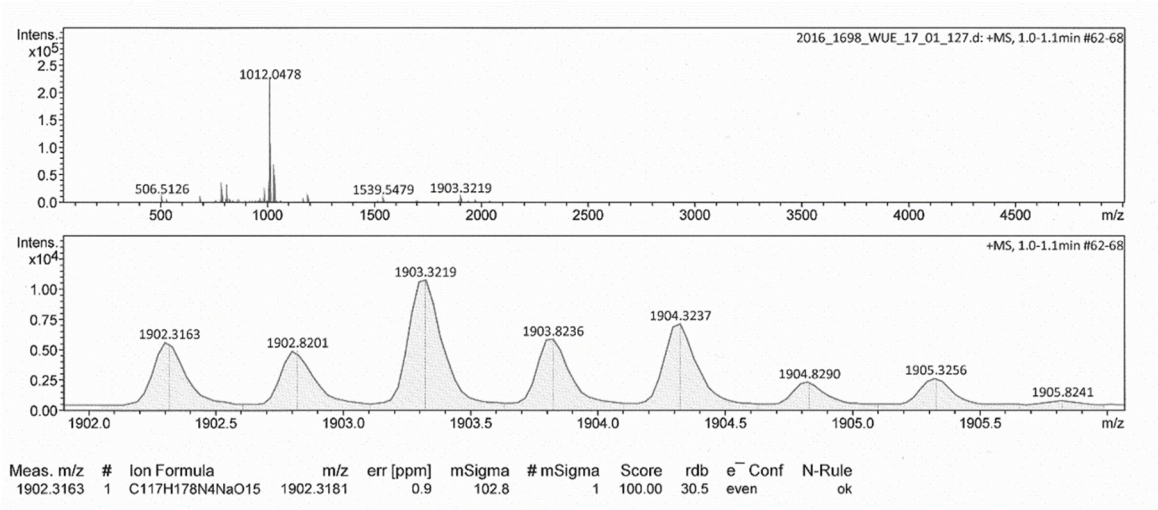


**Figure 139.** High resolution mass spectrum (ESI, positive mode, $CHCl_3/CH_3CN$) of **1,6,7-MeO-PBI.**

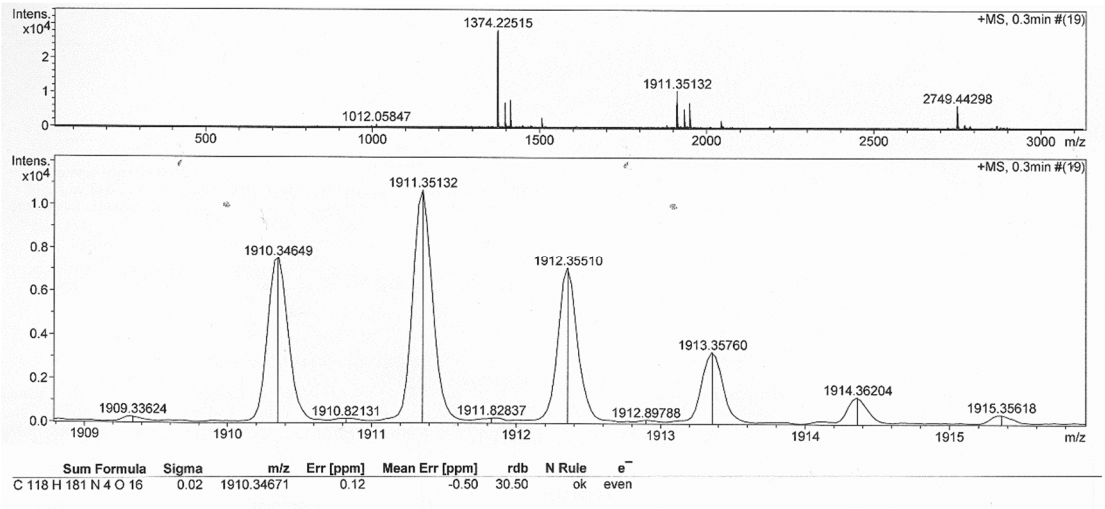


**Figure 140.** High resolution mass spectrum (ESI, positive mode, $CHCl_3/CH_3CN$) of **1,6,7,12-MeO-PBI.**

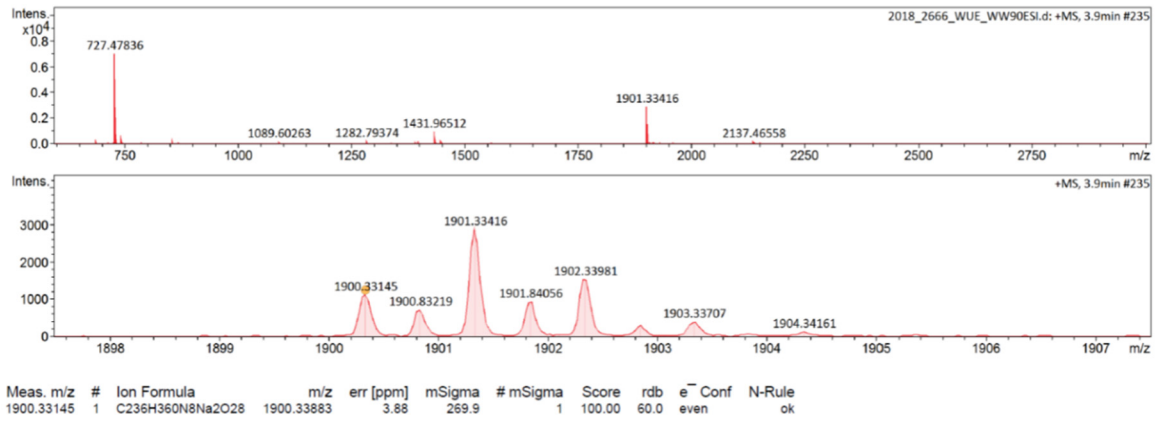


**Figure 141.** High resolution mass spectrum (ESI, positive mode, $CHCl_3/CH_3CN$) of **1,7-EtO-PBI**.

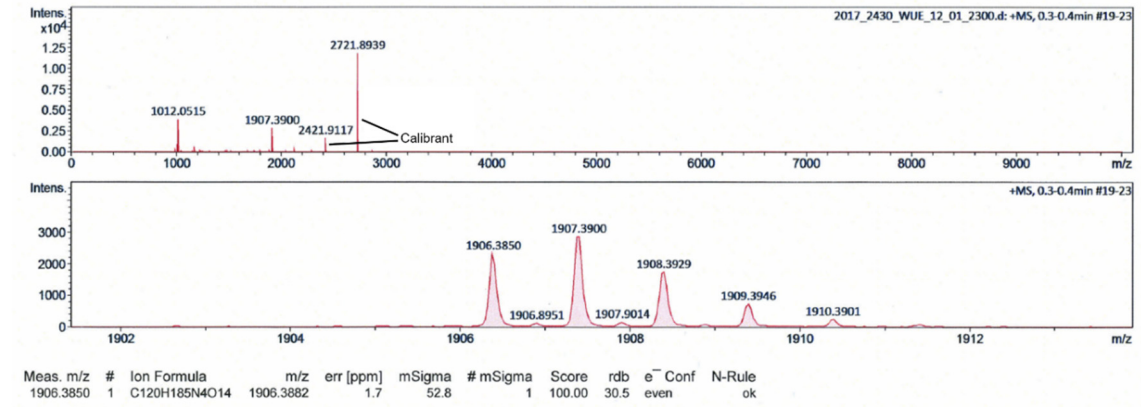


**Figure 142.** High resolution mass spectrum (ESI, positive mode, $CHCl_3/CH_3CN$) of **1,7-*i*PrO-PBI**.

# Bibliography


[1] M. Szwarc, *Nature* **1956**, *178*, 1168-1169.

[2] O. W. Webster, *Science* **1991**, *251*, 887-893.

[3] R. B. Grubbs, R. H. Grubbs, *Macromolecules* **2017**, *50*, 6979-6997.

[4] H.-C. Kim, S.-M. Park, W. D. Hinsberg, *Chem. Rev.* **2010**, *110*, 146-177.

[5] F. H. Schacher, P. A. Rupar, I. Manners, *Angew. Chem. Int. Ed.* **2012**, *51*, 7898-7921.

[6] Y. Mai, A. Eisenberg, *Chem. Soc. Rev.* **2012**, *41*, 5969-5985.

[7] M. Elsabahy, G. S. Heo, S.-M. Lim, G. Sun, K. L. Wooley, *Chem. Rev.* **2015**, *115*, 10967-11011.

[8] J. Jennings, G. He, S. M. Howdle, P. B. Zetterlund, *Chem. Soc. Rev.* **2016**, *45*, 5055-5084.

[9] H. Feng, X. Lu, W. Wang, N.-G. Kang, J. W. Mays, *Polymers* **2017**, *9*, 494.

[10] R. P. Sijbesma, F. H. Beijer, L. Brunsveld, B. J. B. Folmer, J. H. K. K. Hirschberg, R. F. M. Lange, J. K. L. Lowe, E. W. Meijer, *Science* **1997**, *278*, 1601-1604.

[11] L. Brunsveld, B. J. B. Folmer, E. W. Meijer, R. P. Sijbesma, *Chem. Rev.* **2001**, *101*, 4071-4097.

[12] A. Ciferri, *Supramolecular Polymers*, 2nd ed., CRC Press, Boca Raton, **2005**.

[13] T. F. A. De Greef, M. M. J. Smulders, M. Wolffs, A. P. H. J. Schenning, R. P. Sijbesma, E. W. Meijer, *Chem. Rev.* **2009**, *109*, 5687-5754.

[14] T. Aida, E. W. Meijer, S. I. Stupp, *Science* **2012**, *335*, 813-817.

[15] L. Yang, X. Tan, Z. Wang, X. Zhang, *Chem. Rev.* **2015**, *115*, 7196-7239.

[16] M. J. Webber, E. A. Appel, E. W. Meijer, R. Langer, *Nat. Mater.* **2015**, *15*, 13-26.

[17] E. Krieg, M. M. C. Bastings, P. Besenius, B. Rybtchinski, *Chem. Rev.* **2016**, *116*, 2414-2477.

[18] B. M. Rosen, C. J. Wilson, D. A. Wilson, M. Peterca, M. R. Imam, V. Percec, *Chem. Rev.* **2009**, *109*, 6275-6540.

[19] S. K. Yang, A. V. Ambade, M. Weck, *Chem. Soc. Rev.* **2011**, *40*, 129-137.

[20] A. Sorrenti, J. Leira-Iglesias, A. J. Markvoort, T. F. A. de Greef, T. M. Hermans, *Chem. Soc. Rev.* **2017**, *46*, 5476-5490.

[21] X. Yan, F. Wang, B. Zheng, F. Huang, *Chem. Soc. Rev.* **2012**, *41*, 6042-6065.

[22] D. Zhao, J. S. Moore, *Org. Biomol. Chem.* **2003**, *1*, 3471-3491.

[23] Z. Chen, A. Lohr, C. R. Saha-Möller, F. Würthner, *Chem. Soc. Rev.* **2009**, *38*, 564-584.

[24] C. Rest, R. Kandanelli, G. Fernandez, *Chem. Soc. Rev.* **2015**, *44*, 2543-2572.

[25] A. J. Markvoort, H. M. M. ten Eikelder, P. A. J. Hilbers, T. F. A. de Greef, E. W. Meijer, *Nat. Commun.* **2011**, *2*, 509.

[26] H.-J. Sun, S. Zhang, V. Percec, *Chem. Soc. Rev.* **2015**, *44*, 3900-3923.

[27] M. M. J. Smulders, M. M. L. Nieuwenhuizen, T. F. A. de Greef, P. van der Schoot, A. P. H. J. Schenning, E. W. Meijer, *Chem. Eur. J.* **2010**, *16*, 362-367.

[28] A. Lohr, M. Lysetska, F. Würthner, *Angew. Chem. Int. Ed.* **2005**, *44*, 5071-5074.

[29] Y. Tidhar, H. Weissman, S. G. Wolf, A. Gulino, B. Rybtchinski, *Chem. Eur. J.* **2011**, *17*, 6068-6075.

[30] P. A. Korevaar, S. J. George, A. J. Markvoort, M. M. J. Smulders, P. A. J. Hilbers, A. P. H. J. Schenning, T. F. A. De Greef, E. W. Meijer, *Nature* **2012**, *481*, 492-496.

[31] J. Baram, H. Weissman, B. Rybtchinski, *J. Phys. Chem. B* **2014**, *118*, 12068-12073.

[32] S. Ogi, T. Fukui, M. L. Jue, M. Takeuchi, K. Sugiyasu, *Angew. Chem. Int. Ed.* **2014**, *53*, 14363-14367.

[33] E. Mattia, S. Otto, *Nat. Nanotechnol.* **2015**, *10*, 111-119.

[34] H. Frisch, E.-C. Fritz, F. Stricker, L. Schmüser, D. Spitzer, T. Weidner, B. J. Ravoo, P. Besenius, *Angew. Chem. Int. Ed.* **2016**, *55*, 7242-7246.

[35] A. Aliprandi, M. Mauro, L. De Cola, *Nat. Chem.* **2016**, *8*, 10-15.

[36] A. J. Markvoort, H. M. M. t. Eikelder, P. A. J. Hilbers, T. F. A. de Greef, *ACS Cent. Sci.* **2016**, *2*, 232-241.

[37] J. Leira-Iglesias, A. Sorrenti, A. Sato, P. A. Dunne, T. M. Hermans, *Chem. Commun.* **2016**, *52*, 9009-9012.

[38] H. Chen, Z. Huang, H. Wu, J.-F. Xu, X. Zhang, *Angew. Chem. Int. Ed.* **2017**, *56*, 16575-16578.

[39] K. Venkata Rao, D. Miyajima, A. Nihonyanagi, T. Aida, *Nat. Chem.* **2017**, *9*, 1133-1139.

[40] Z. Chen, Y. Liu, W. Wagner, V. Stepanenko, X. Ren, S. Ogi, F. Würthner, *Angew. Chem. Int. Ed.* **2017**, *56*, 5729-5733.

[41] K. Zhang, M. C.-L. Yeung, S. Y.-L. Leung, V. W.-W. Yam, *J. Am. Chem. Soc.* **2018**, *140*, 9594-9605.

[42] D. S. Pal, H. Kar, S. Ghosh, *Chem. Commun.* **2018**, *54*, 928-931.

[43] P. A. Korevaar, T. F. A. de Greef, E. W. Meijer, *Chem. Mater.* **2014**, *26*, 576-586.

[44] D. van der Zwaag, P. A. Pieters, P. A. Korevaar, A. J. Markvoort, A. J. H. Spiering, T. F. A. de Greef, E. W. Meijer, *J. Am. Chem. Soc.* **2015**, *137*, 12677-12688.

[45] X. Wang, G. Guerin, H. Wang, Y. Wang, I. Manners, M. A. Winnik, *Science* **2007**, *317*, 644-647.

[46] J. Gilroy, T. Gädt, G. Whittell, L. Chabanne, J. Mitchels, R. Richardson, M. Winnik, I. Manners, *Nat. Chem.* **2010**, *2*, 566-570.

[47] S. K. Patra, R. Ahmed, G. R. Whittell, D. J. Lunn, E. L. Dunphy, M. A. Winnik, I. Manners, *J. Am. Chem. Soc.* **2011**, *133*, 8842-8845.

[48] P. A. Rupar, L. Chabanne, M. A. Winnik, I. Manners, *Science* **2012**, *337*, 559-562.

[49] H. Qiu, G. Russo, P. A. Rupar, L. Chabanne, M. A. Winnik, I. Manners, *Angew. Chem. Int. Ed.* **2012**, *51*, 11882-11885.

[50] H. Qiu, Z. M. Hudson, M. A. Winnik, I. Manners, *Science* **2015**, *347*, 1329-1332.

[51] M. E. Robinson, A. Nazemi, D. J. Lunn, D. W. Hayward, C. E. Boott, M.-S. Hsiao, R. L. Harniman, S. A. Davis, G. R. Whittell, R. M. Richardson, L. De Cola, I. Manners, *ACS Nano* **2017**, *11*, 9162-9175.

[52] A. Nazemi, X. He, L. R. MacFarlane, R. L. Harniman, M.-S. Hsiao, M. A. Winnik, C. F. J. Faul, I. Manners, *J. Am. Chem. Soc.* **2017**, *139*, 4409-4417.

[53] S. Ogi, K. Sugiyasu, S. Manna, S. Samitsu, M. Takeuchi, *Nat. Chem.* **2014**, *6*, 188-195.

[54] F. Würthner, *Nat. Chem.* **2014**, *6*, 171-173.

[55] R. D. Mukhopadhyay, A. Ajayaghosh, *Science* **2015**, *349*, 241-242.

[56] D. Van der Zwaag, T. F. A. de Greef, E. W. Meijer, *Angew. Chem. Int. Ed.* **2015**, *54*, 8334-8336.

[57] S. Ogi, V. Stepanenko, K. Sugiyasu, M. Takeuchi, F. Würthner, *J. Am. Chem. Soc.* **2015**, *137*, 3300-3307.

[58] J. Kang, D. Miyajima, T. Mori, Y. Inoue, Y. Itoh, T. Aida, *Science* **2015**, *347*, 646-651.

[59] M. Endo, T. Fukui, S. H. Jung, S. Yagai, M. Takeuchi, K. Sugiyasu, *J. Am. Chem. Soc.* **2016**, *138*, 14347-14353.

[60] S. Ogi, V. Stepanenko, J. Thein, F. Würthner, *J. Am. Chem. Soc.* **2016**, *138*, 670-678.

[61] X. Ma, Y. Zhang, Y. Zhang, Y. Liu, Y. Che, J. Zhao, *Angew. Chem. Int. Ed.* **2016**, 9539–9543.

[62] W. Wagner, M. Wehner, V. Stepanenko, S. Ogi, F. Würthner, *Angew. Chem. Int. Ed.* **2017**, *56*, 16008-16012.

[63] T. Fukui, S. Kawai, S. Fujinuma, Y. Matsushita, T. Yasuda, T. Sakurai, S. Seki, M. Takeuchi, K. Sugiyasu, *Nat. Chem.* **2017**, *9*, 493-499.

[64] S. Ogi, K. Matsumoto, S. Yamaguchi, *Angew. Chem. Int. Ed.* **2018**, *57*, 2339-2343.

[65] J. S. Valera, R. Gómez, L. Sánchez, *Small* **2018**, *14*, 1702437.

[66] E. E. Greciano, B. Matarranz, L. Sánchez, *Angew. Chem. Int. Ed.* **2018**, *57*, 4697-4701.

[67] G. Ghosh, S. Ghosh, *Chem. Commun.* **2018**, *54*, 5720-5723.

[68] A. Jain, S. Dhiman, A. Dhayani, P. K. Vemula, S. J. George, *Nat. Commun.* **2019**, *10*, 450.

[69] J. Matern, Y. Dorca, L. Sánchez, G. Fernandez, *Angew. Chem. Int. Ed.* **2019**, *58*, 10.1002/anie.201905724.

[70] S. H. Jung, D. Bochicchio, G. M. Pavan, M. Takeuchi, K. Sugiyasu, *J. Am. Chem. Soc.* **2018**, *140*, 10570-10577.

[71] C. Jarrett-Wilkins, X. He, H. E. Symons, R. L. Harniman, C. F. J. Faul, I. Manners, *Chem. Eur. J.* **2018**, *24*, 15556-15565.

[72] B. Adelizzi, N. J. Van Zee, L. N. J. de Windt, A. R. A. Palmans, E. W. Meijer, *J. Am. Chem. Soc.* **2019**, *141*, 6110-6121.

[73] Z. M. Hudson, C. E. Boott, M. E. Robinson, P. A. Rupar, M. A. Winnik, I. Manners, *Nat. Chem.* **2014**, *6*, 893-898.

[74] X.-H. Jin, M. B. Price, J. R. Finnegan, C. E. Boott, J. M. Richter, A. Rao, S. M. Menke, R. H. Friend, G. R. Whittell, I. Manners, *Science* **2018**, *360*, 897-900.

[75] W. Zhang, W. Jin, T. Fukushima, A. Saeki, S. Seki, T. Aida, *Science* **2011**, *334*, 340-343.

[76] A. Pal, M. Malakoutikhah, G. Leonetti, M. Tezcan, M. Colomb-Delsuc, V. D. Nguyen, J. van der Gucht, S. Otto, *Angew. Chem. Int. Ed.* **2015**, *54*, 7852-7856.

[77] B. Adelizzi, A. Aloi, A. J. Markvoort, H. M. M. Ten Eikelder, I. K. Voets, A. R. A. Palmans, E. W. Meijer, *J. Am. Chem. Soc.* **2018**, *140*, 7168-7175.

[78] F. Würthner, C. R. Saha-Möller, B. Fimmel, S. Ogi, P. Leowanawat, D. Schmidt, *Chem. Rev.* **2016**, *116*, 962-1052.

[79] A. Nowak-Król, F. Würthner, *Org. Chem. Front.* **2019**, *6*, 1272-1318.

[80] F. Würthner, *Chem. Commun.* **2004**, *14*, 1564-1579.

[81] C. Huang, S. Barlow, S. R. Marder, *J. Org. Chem.* **2011**, *76*, 2386-2407.

[82] H. Langhals, *Heterocycles* **1995**, *40*, 477-500.

[83] X. Zhan, A. Facchetti, S. Barlow, T. J. Marks, M. A. Ratner, M. R. Wasielewski, S. R. Marder, *Adv. Mater.* **2011**, *23*, 268-284.

[84] Z. Liu, G. Zhang, Z. Cai, X. Chen, H. Luo, Y. Li, J. Wang, D. Zhang, *Adv. Mater.* **2014**, *26*, 6965-6977.

[85] Y. Zhong, M. T. Trinh, R. Chen, G. E. Purdum, P. P. Khlyabich, M. Sezen, S. Oh, H. Zhu, B. Fowler, B. Zhang, W. Wang, C.-Y. Nam, M. Y. Sfeir, C. T. Black, M. L. Steigerwald, Y.-L. Loo, F. Ng, X. Y. Zhu, C. Nuckolls, *Nat. Commun.* **2015**, *6*, 8242.

[86] D. Meng, D. Sun, C. Zhong, T. Liu, B. Fan, L. Huo, Y. Li, W. Jiang, H. Choi, T. Kim, J. Y. Kim, Y. Sun, Z. Wang, A. J. Heeger, *J. Am. Chem. Soc.* **2016**, *138*, 375-380.

[87] C. Fouquey, J.-M. Lehn, A.-M. Levelut, *Adv. Mater.* **1990**, *2*, 254-257.

[88] T. F. A. de Greef, E. W. Meijer, *Aust. J. Chem.* **2010**, *63*, 596-598.

[89] O. J. G. M. Goor, S. I. S. Hendrikse, P. Y. W. Dankers, E. W. Meijer, *Chem. Soc. Rev.* **2017**, *46*, 6621-6637.

[90] A. W. Bosman, R. P. Sijbesma, E. W. Meijer, *Mater. Today* **2004**, *7*, 34-39.

[91] Y. Yamamoto, T. Fukushima, Y. Suna, N. Ishii, A. Saeki, S. Seki, S. Tagawa, M. Taniguchi, T. Kawai, T. Aida, *Science* **2006**, *314*, 1761-1764.

[92] J. D. Hartgerink, E. Beniash, S. I. Stupp, *Science* **2001**, *294*, 1684-1688.

[93] Z. Chen, A. Lohr, C. R. Saha-Moller, F. Würthner, *Chem. Soc. Rev.* **2009**, *38*, 564-584.

[94] F. Würthner, S. Yao, T. Debaerdemaeker, R. Wortmann, *J. Am. Chem. Soc.* **2002**, *124*, 9431-9447.

[95] R. Wortmann, U. Rösch, M. Redi-Abshiro, F. Würthner, *Angew. Chem. Int. Ed.* **2003**, *42*, 2080-2083.

[96] J. Seibt, A. Lohr, F. Würthner, V. Engel, *Phys. Chem. Chem. Phys.* **2007**, *9*, 6214-6218.

[97] R. B. Martin, *Chem. Rev.* **1996**, *96*, 3043-3064.

[98] G. Fernández, M. Stolte, V. Stepanenko, F. Würthner, *Chem. Eur. J.* **2013**, *19*, 206-217.

[99] R. F. Goldstein, L. Stryer, *Biophys. J.* **1986**, *50*, 583-599.

[100] J. Gershberg, F. Fennel, T. H. Rehm, S. Lochbrunner, F. Würthner, *Chem. Sci.* **2016**, *7*, 1729-1737.

[101] P. Jonkheijm, P. van der Schoot, A. P. H. J. Schenning, E. W. Meijer, *Science* **2006**, *313*, 80-83.

[102] M. M. J. Smulders, A. P. H. J. Schenning, E. W. Meijer, *J. Am. Chem. Soc.* **2008**, *130*, 606-611.

[103] T. Heek, C. Fasting, C. Rest, X. Zhang, F. Würthner, R. Haag, *Chem. Commun.* **2010**, *46*, 1884-1886.

[104] F. Würthner, *Acc. Chem. Res.* **2016**, *49*, 868-876.

[105] Y. Liu, Y. Zhang, F. Fennel, W. Wagner, F. Würthner, Y. Chen, Z. Chen, *Chem. Eur. J.* **2018**, *24*, 16388-16394.

[106] F. Fennel, S. Wolter, Z. Xie, P. A. Plötz, O. Kühn, F. Würthner, S. Lochbrunner, *J. Am. Chem. Soc.* **2013**, *135*, 18722-18725.

[107] M. Wehner, F. Würthner, *Nat. Rev. Chem.* **2019**, *accepted article*.

[108] S. Dhiman, A. Sarkar, S. J. George, *RSC Adv.* **2018**, *8*, 18913-18925.

[109] S. A. P. van Rossum, M. Tena-Solsona, J. H. van Esch, R. Eelkema, J. Boekhoven, *Chem. Soc. Rev.* **2017**, *46*, 5519-5535.

[110] R. F. Ludlow, S. Otto, *Chem. Soc. Rev.* **2008**, *37*, 101-108.

[111] J. Boekhoven, W. E. Hendriksen, G. J. M. Koper, R. Eelkema, J. H. van Esch, *Science* **2015**, *349*, 1075-1079.

[112] J. Leira-Iglesias, A. Tassoni, T. Adachi, M. Stich, T. M. Hermans, *Nat. Nanotechnol.* **2018**, *13*, 1021-1027.

[113] E. T. Powers, D. L. Powers, *Biophys. J.* **2006**, *91*, 122-132.

[114] E. T. Powers, D. L. Powers, *Biophys. J.* **2008**, *94*, 379-391.

[115] A. T. Haedler, S. C. J. Meskers, R. H. Zha, M. Kivala, H.-W. Schmidt, E. W. Meijer, *J. Am. Chem. Soc.* **2016**, *138*, 10539-10545.

[116] M. F. J. Mabesoone, A. J. Markvoort, M. Banno, T. Yamaguchi, F. Helmich, Y. Naito, E. Yashima, A. R. A. Palmans, E. W. Meijer, *J. Am. Chem. Soc.* **2018**, *140*, 7810-7819.

[117] N. Komiya, T. Muraoka, M. Iida, M. Miyanaga, K. Takahashi, T. Naota, *J. Am. Chem. Soc.* **2011**, *133*, 16054-16061.

[118] S. Yagai, S. Okamura, Y. Nakano, M. Yamauchi, K. Kishikawa, T. Karatsu, A. Kitamura, A. Ueno, D. Kuzuhara, H. Yamada, T. Seki, H. Ito, *Nat. Commun.* **2014**, *5*, 4013.

[119] P. A. Korevaar, C. Schaefer, T. F. A. de Greef, E. W. Meijer, *J. Am. Chem. Soc.* **2012**, *134*, 13482-13491.

[120] P. A. Korevaar, C. J. Newcomb, E. W. Meijer, S. I. Stupp, *J. Am. Chem. Soc.* **2014**, *136*, 8540-8543.

[121] A. Lohr, F. Würthner, *Isr. J. Chem.* **2011**, *51*, 1052-1066.

[122] A. P. H. J. Schenning, P. Jonkheijm, E. Peeters, E. W. Meijer, *J. Am. Chem. Soc.* **2001**, *123*, 409-416.

[123] N. J. Van Zee, B. Adelizzi, M. F. J. Mabesoone, X. Meng, A. Aloi, R. H. Zha, M. Lutz, I. A. W. Filot, A. R. A. Palmans, E. W. Meijer, *Nature* **2018**, *558*, 100-103.

[124] M. Wehner, M. I. S. Röhr, M. Bühler, V. Stepanenko, W. Wagner, F. Würthner, *J. Am. Chem. Soc.* **2019**, *141*, 6092-6107.

[125] A. R. A. Palmans, J. A. J. M. Vekemans, E. E. Havinga, E. W. Meijer, *Angew. Chem. Int. Ed.* **1997**, *36*, 2648-2651.

[126] A. Lohr, F. Würthner, *Chem. Commun.* **2008**, 2227-2229.

[127] T. E. Kaiser, V. Stepanenko, F. Würthner, *J. Am. Chem. Soc.* **2009**, *131*, 6719-6732.

[128] X.-Q. Li, V. Stepanenko, Z. Chen, P. Prins, L. D. A. Siebbeles, F. Würthner, *Chem. Commun.* **2006**, *37*, 3871-3873.

[129] V. Stepanenko, X.-Q. Li, J. Gershberg, F. Würthner, *Chem. Eur. J.* **2013**, *19*, 4176-4183.

[130] T. Fukui, N. Sasaki, M. Takeuchi, K. Sugiyasu, *Chem. Sci.* **2019**, *10*, 6770-6776.

[131] A. R. A. Palmans, E. W. Meijer, *Angew. Chem. Int. Ed.* **2007**, *46*, 8948-8968.

[132] A. Ajayaghosh, R. Varghese, S. J. George, C. Vijayakumar, *Angew. Chem. Int. Ed.* **2006**, *45*, 1141-1144.

[133] T. Kim, T. Mori, T. Aida, D. Miyajima, *Chem. Sci.* **2016**, *7*, 6689-6694.

[134] J. van Gestel, A. R. A. Palmans, B. Titulaer, J. A. J. M. Vekemans, E. W. Meijer, *J. Am. Chem. Soc.* **2005**, *127*, 5490-5494.

[135] W. Jin, T. Fukushima, M. Niki, A. Kosaka, N. Ishii, T. Aida, *Proc. Nat. Acad. Sci. USA* **2005**, *102*, 10801-10806.

[136] A. Lohr, F. Würthner, *Angew. Chem. Int. Ed.* **2008**, *47*, 1232-1236.

[137] P. J. M. Stals, J. C. Everts, R. de Bruijn, I. A. W. Filot, M. M. J. Smulders, R. Martín-Rapún, E. A. Pidko, T. F. A. de Greef, A. R. A. Palmans, E. W. Meijer, *Chem. Eur. J.* **2010**, *16*, 810-821.

[138] M. M. J. Smulders, P. J. M. Stals, T. Mes, T. F. E. Paffen, A. P. H. J. Schenning, A. R. A. Palmans, E. W. Meijer, *J. Am. Chem. Soc.* **2010**, *132*, 620-626.

[139] F. Helmich, M. M. J. Smulders, C. C. Lee, A. P. H. J. Schenning, E. W. Meijer, *J. Am. Chem. Soc.* **2011**, *133*, 12238-12246.

[140] B. N. S. Thota, X. Lou, D. Bochicchio, T. F. E. Paffen, R. P. M. Lafleur, J. L. J. van Dongen, S. Ehrmann, R. Haag, G. M. Pavan, A. R. A. Palmans, E. W. Meijer, *Angew. Chem. Int. Ed.* **2018**, *57*, 6843-6847.

[141] M. K. Müller, L. Brunsveld, *Angew. Chem. Int. Ed.* **2009**, *48*, 2921-2924.

[142] K. Petkau-Milroy, M. H. Sonntag, A. H. A. M. van Onzen, L. Brunsveld, *J. Am. Chem. Soc.* **2012**, *134*, 8086-8089.

[143] J.-M. Lehn, *Angew. Chem. Int. Ed.* **1990**, *29*, 1304-1319.

[144] S. Sivakova, S. J. Rowan, *Chem. Soc. Rev.* **2005**, *34*, 9-21.

[145] S.-G. Chen, Y. Yu, X. Zhao, Y. Ma, X.-K. Jiang, Z.-T. Li, *J. Am. Chem. Soc.* **2011**, *133*, 11124-11127.

[146] K. Jalani, M. Kumar, S. J. George, *Chem. Commun.* **2013**, *49*, 5174-5176.

[147] A. Das, S. Ghosh, *Angew. Chem. Int. Ed.* **2014**, *53*, 2038-2054.

[148] H. Frisch, J. P. Unsleber, D. Lüdeker, M. Peterlechner, G. Brunklaus, M. Waller, P. Besenius, *Angew. Chem. Int. Ed.* **2013**, *52*, 10097-10101.

[149] P. Besenius, *J. Polym. Sci. Pol. Chem.* **2017**, *55*, 34-78.

[150] H. Frisch, Y. Nie, S. Raunser, P. Besenius, *Chem. Eur. J.* **2015**, *21*, 3304-3309.

[151] T. Hirao, H. Kudo, T. Amimoto, T. Haino, *Nat. Commun.* **2017**, *8*, 634.

[152] S. Yagai, S. Hamamura, H. Wang, V. Stepanenko, T. Seki, K. Unoike, Y. Kikkawa, T. Karatsu, A. Kitamura, F. Würthner, *Org. Biomol. Chem.* **2009**, *7*, 3926-3929.

[153] D. Görl, X. Zhang, V. Stepanenko, F. Würthner, *Nat. Commun.* **2015**, *6*, 7009.

[154] Z. M. Hudson, D. J. Lunn, M. A. Winnik, I. Manners, *Nat. Commun.* **2014**, *5*, 3372.

[155] J. Xu, H. Zhou, Q. Yu, I. Manners, M. A. Winnik, *J. Am. Chem. Soc.* **2018**, *140*, 2619-2628.

[156] J. R. Finnegan, D. J. Lunn, O. E. C. Gould, Z. M. Hudson, G. R. Whittell, M. A. Winnik, I. Manners, *J. Am. Chem. Soc.* **2014**, *136*, 13835-13844.

[157] X. Li, Y. Gao, C. E. Boott, M. A. Winnik, I. Manners, *Nat. Commun.* **2015**, *6*, 8127.

[158] X. Li, Y. Gao, C. E. Boott, D. W. Hayward, R. Harniman, G. R. Whittell, R. M. Richardson, M. A. Winnik, I. Manners, *J. Am. Chem. Soc.* **2016**, *138*, 4087-4095.

[159] S. Shin, F. Menk, Y. Kim, J. Lim, K. Char, R. Zentel, T.-L. Choi, *J. Am. Chem. Soc.* **2018**, *140*, 6088-6094.

[160] W. Zhang, W. Jin, T. Fukushima, T. Mori, T. Aida, *J. Am. Chem. Soc.* **2015**, *137*, 13792-13795.

[161] G. Odian, *Principles of Polymerization*, 4th ed., WILEY-VCH Verlag GmbH, Hoboken, NJ, **2004**.

[162] J. M. G. Cowie, V. Arrighi, *Polymerization: Chemistry and Physics of Modern Materials*, Taylor & Francis Inc, CRC Press, Boca Raton, **2007**.

[163] M. E. Robinson, D. J. Lunn, A. Nazemi, G. R. Whittell, L. De Cola, I. Manners, *Chem. Commun.* **2015**, *51*, 15921-15924.

[164] F. Würthner, T. E. Kaiser, C. R. Saha-Möller, *Angew. Chem. Int. Ed.* **2011**, *50*, 3376-3410.

[165] S. Ghosh, X.-Q. Li, V. Stepanenko, F. Würthner, *Chem. Eur. J.* **2008**, *14*, 11343-11357.

[166] P. Leowanawat, A. Nowak-Krol, F. Würthner, *Org. Chem. Front.* **2016**, *3*, 537-544.

[167] W. Wagner, M. Wehner, V. Stepanenko, F. Würthner, *J. Am. Chem. Soc.* **2019**, *141*, 12044-12054.

[168] R. K. Castellano, D. M. Rudkevich, J. Rebek, *Proc. Nat. Acad. Sci. USA* **1997**, *94*, 7132-7137.

[169] C. Kulkarni, S. Balasubramanian, S. J. George, *Chem. Phys. Chem.* **2013**, *14*, 661-673.

[170] K. Cai, J. Xie, D. Zhang, W. Shi, Q. Yan, D. Zhao, *J. Am. Chem. Soc.* **2018**, *140*, 5764-5773.

[171] B. Kemper, L. Zengerling, D. Spitzer, R. Otter, T. Bauer, P. Besenius, *J. Am. Chem. Soc.* **2018**, *140*, 534-537.

[172] K. Zhang, M. C.-L. Yeung, S. Y.-L. Leung, V. W.-W. Yam, *Proc. Nat. Acad. Sci. USA* **2017**, *114*, 11844-11849.

[173] W. Wagner, M. Wehner, V. Stepanenko, F. Würthner, *CCS Chem.* **2019**, *1*, *accepted article*.

[174] R. Dobrawa, F. Würthner, *J. Polym. Sci. A* **2005**, *43*, 4981-4995.

[175] J.-F. Lutz, J.-M. Lehn, E. W. Meijer, K. Matyjaszewski, *Nat. Rev. Mater.* **2016**, *1*, 16024.

[176] J. Shi, H. Jia, H. Chen, X. Wang, J.-F. Xu, W. Ren, J. Zhao, X. Zhou, Y. Dong, D. Liu, *CCS Chem.* **2019**, *1*, 296-303.

[177] Z. Yin, G. Song, Y. Jiao, P. Zheng, J.-F. Xu, X. Zhang, *CCS Chem.* **2019**, *1*, 335-342.

[178] S. Chen, P. Slattum, C. Wang, L. Zang, *Chem. Rev.* **2015**, *115*, 11967-11998.

[179] P. Osswald, F. Würthner, *J. Am. Chem. Soc.* **2007**, *129*, 14319-14326.

[180] F. Würthner, *Pure Appl. Chem.* **2006**, *78*, 2349.

[181] P. Osswald, F. Würthner, *Chem. Eur. J.* **2007**, *13*, 7395-7409.

[182] M. R. Wasielewski, *Acc. Chem. Res.* **2009**, *42*, 1910-1921.

[183] Z. Chen, U. Baumeister, C. Tschierske, F. Würthner, *Chem. Eur. J.* **2007**, *13*, 450-465.

[184] X.-Q. Li, X. Zhang, S. Ghosh, F. Würthner, *Chem. Eur. J.* **2008**, *14*, 8074-8078.

[185] B. E. Partridge, P. Leowanawat, E. Aqad, M. R. Imam, H.-J. Sun, M. Peterca, P. A. Heiney, R. Graf, H. W. Spiess, X. Zeng, G. Ungar, V. Percec, *J. Am. Chem. Soc.* **2015**, *137*, 5210-5224.

[186] M. Queste, C. Cadiou, B. Pagoaga, L. Giraudet, N. Hoffmann, *New J. Chem.* **2010**, *34*, 2537-2545.

[187] Y. Li, C. Wang, C. Li, S. Di Motta, F. Negri, Z. Wang, *Org. Lett.* **2012**, *14*, 5278-5281.

[188] S. Sengupta, R. K. Dubey, R. W. M. Hoek, S. P. P. van Eeden, D. D. Gunbaş, F. C. Grozema, E. J. R. Sudhölter, W. F. Jager, *J. Org. Chem.* **2014**, *79*, 6655-6662.

[189] M. Takahashi, K. Asaba, T. T. Lua, T. Inuzuka, N. Uemura, M. Sakamoto, T. Sengoku, H. Yoda, *J. Org. Chem.* **2018**, *83*, 624-631.

[190] F. Würthner, V. Stepanenko, Z. Chen, C. R. Saha-Möller, N. Kocher, D. Stalke, *J. Org. Chem.* **2004**, *69*, 7933-7939.

[191] E. H. A. Beckers, S. C. J. Meskers, A. P. H. J. Schenning, Z. Chen, F. Würthner, P. Marsal, D. Beljonne, J. Cornil, R. A. J. Janssen, *J. Am. Chem. Soc.* **2006**, *128*, 649-657.

[192] R. F. Fink, J. Seibt, V. Engel, M. Renz, M. Kaupp, S. Lochbrunner, H.-M. Zhao, J. Pfister, F. Würthner, B. Engels, *J. Am. Chem. Soc.* **2008**, *130*, 12858-12859.

[193] M. M. Safont-Sempere, G. Fernández, F. Würthner, *Chem. Rev.* **2011**, *111*, 5784-5814.

[194] A. M. Brouwer, *Pure Appl. Chem.* **2011**, *83*, 2213-2228.

[195] R. G. R. Bacon, H. A. O. Hill, *J. Chem. Soc.* **1964**, 1097-1107.

[196] T. D. Sheppard, *Org. Biomol. Chem.* **2009**, *7*, 1043-1052.

[197] L. M. A. Perdigao, A. Saywell, G. N. Fontes, P. A. Staniec, G. Goretzki, A. G. Phillips, N. R. Champness, P. H. Beton, *Chem. Eur. J.* **2008**, *14*, 7600-7607.

[198] A. D. Becke, *J. Chem. Phys.* **1993**, *98*, 5648-5652.

[199] F. Weigend, R. Ahlrichs, *Phys. Chem. Chem. Phys.* **2005**, *7*, 3297-3305.

[200] K. Kodama, A. Kobayashi, T. Hirose, *Tetrahedron Lett.* **2013**, *54*, 5514-5517.

[201] D. A. Doval, A. Fin, M. Takahashi-Umebayashi, H. Riezman, A. Roux, N. Sakai, S. Matile, *Org. Biomol. Chem.* **2012**, *10*, 6087-6093.

# Individual Contribution

The coauthors of the manuscripts included in this cumulative thesis are informed and agree with the reprint and the respective individual contributions as stated below.

**Living Supramolecular Polymerization of a Perylene Bisimide Dye into Fluorescent J-aggregates**

W. Wagner, M. Wehner, V. Stepanenko, S. Ogi, F. Würthner, *Angew. Chem. Int. Ed.* **2017**, *56*, 16008-16012.

| Author | W.W. | M.W. | V.S. | S.O. | F.W. |
|---|---|---|---|---|---|
| Design of research | 30% | 10% | - | 30% | 30% |
| Synthesis and characterization | 100% | - | - | - | - |
| UV/vis spectroscopy | 100% | - | - | - | - |
| Fluorescence spectroscopy | 100% | - | - | - | - |
| FT-IR spectroscopy | 80% | - | - | 20% | - |
| Atomic force microscopy | 10% | - | 90% | - | - |
| Publication writing | 50% | 10% | - | 20% | 20% |
| Publication correction | - | - | - | 40% | 60% |
| Publication coordination | 20% | - | - | 20% | 60% |

**Supramolecular Block Copolymers by Seeded Living Polymerization of Perylene Bisimides**

W. Wagner, M. Wehner, V. Stepanenko, F. Würthner, *J. Am. Chem. Soc.*. **2019**, *141*, 12044-12054.

| Author | W.W. | M.W. | V.S. | F.W. |
|---|---|---|---|---|
| Design of research | 50% | - | - | 50% |
| Synthesis and characterization | 100% | - | - | - |
| UV/vis spectroscopy | 100% | - | - | - |
| Studies on (co-)polymerization | 100% | - | - | - |
| Atomic force microscopy | 30% | - | 70% | - |
| Publication writing | 70% | 20% | - | 10% |
| Publication correction | - | - | 10% | 90% |
| Publication coordination | 50% | - | - | 50% |

**Impact of Molecular Shape on Supramolecular Copolymer Synthesis in Seeded Living Polymerization of Perylene Bisimides**

W. Wagner, M. Wehner, V. Stepanenko, F. Würthner, *CCS Chem.* **2019**, *1*, *accepted article (September 2019)*.

| Author | W.W. | M.W. | V.S. | F.W. |
|---|---|---|---|---|
| Design of research | 60% | - | - | 40% |
| Synthesis and characterization | 100% | - | - | - |
| UV/vis spectroscopy | 100% | - | - | - |
| Fluorescence spectroscopy | 100% | - | - | - |
| Studies on (co-)polymerization | 100% | - | - | - |
| FT-IR spectroscopy | 100% | - | - | - |
| Atomic force microscopy | 50% | - | 50% | - |
| Publication writing | 70% | 20% | - | 10% |
| Publication correction | - | - | 10% | 90% |
| Publication coordination | 50% | - | - | 50% |

# Acknowledgement/Danksagung

Mein besonderer Dank gilt meinem Doktorvater Prof. Dr. Frank Würthner für das Überlassen eines sehr interessanten Forschungsthemas, sowie für die zahlreichen wissenschaftlichen Diskussionen und hilfreichen Ratschläge. Des Weiteren bedanke ich mich bei Ihm für die hervorragenden Arbeitsbedingungen, die mir während der Promotion zur Verfügung standen, und für die wissenschaftlichen Freiheiten zur Entwicklung des Forschungsprojekts.

Mein weiterer Dank gilt Prof. Dr. Frank Würthner, Dr. Chantu Saha-Möller, Dr. Bartolome Soberats Reus, Dr. Matthias Stolte und Dr. Soichiro Ogi für die Betreuung im Rahmen der „Subgroups“ und die damit verbundenen anregenden fachlichen Diskussionen. Im Speziellen bedanke ich mich sehr bei Dr. Chantu Saha-Möller für die große Unterstützung beim Verfassen und Überarbeiten von Manuskripten. Außerdem möchte ich mich bei Dr. Soichiro Ogi für seine kompetente Einführung in das Thema der lebenden und Saat-induzierten supramolekularen Polymerisation bedanken, was den Grundstein für meine weiteren Arbeiten gelegt hat.

Ebenfalls bedanke ich mich bei Dr. Vladimir Stepanenko für die Durchführung von zahlreichen AFM Studien und die Hilfe bei der Interpretation der erhaltenen Daten. Insbesondere möchte ich mich für seinen intensiven Einsatz bei den langwierigen Experimenten zur Identifizierung der einzelnen Blöcke der supramolekularen Blockcopolymere bedanken.

Bei Dr. David Bialas und Pradeep Peethambaran Nair Syamala möchte ich mich für die Hilfe bei den DFT-Rechnungen bedanken. Ebenfalls bedanke ich mich bei Dr. Matthias Grüne, Patricia Altenberger und Marvin Grüne für die Durchführung von zahlreichen temperaturabhängigen NMR Experimenten, sowie Hilfe bei deren Auswertung. Bei Dr. Michael Büchner und Juliane Adelmann bedanke ich mich für die Aufnahmen und Analyse der Massenspektren.

Ich bedanke mich des Weiteren bei Christiana Toussaint und Eleonore Klaus für die Hilfe bei organisatorischen Angelegenheiten und die Vorbereitung von Dienstreisen zu nationalen und internationalen Konferenzen.

Mein Dank gilt außerdem Tim Schlossarek, Manuel Weh und Marius Wehner für das Korrekturlesen der Doktorarbeit.

Ein sehr großer Dank gilt meinem Laborpartner Marius Wehner für die intensive wissenschaftliche Zusammenarbeit, die tolle Arbeitsatmosphäre und den Spaß, der den Laboralltag bereichert hat.

Außerdem möchte ich mich bei Markus Hecht, Christina Kaufmann, Tim Schlossarek, Johannes Thein, Manuel Weh und Marius Wehner für die unterhaltsame Atmosphäre im Labor bedanken. Ich hoffe, die eingeführten „Schlager-Freitage“ werden sich weiterhin etablieren. Für die Unterstützung bei der Synthesearbeit bedanke ich mich bei meinen Praktikanten Tim Schlossarek, Nils Schopper, Malte Jürgensen und Tabea Gerlach sowie bei der Auszubildenden Ann-Kathrin Lenz.

Ein ganz besonderer Dank gilt zudem allen Mitgliedern des AK Würthner und des AK Beuerle für die hilfsbereite und freundschaftliche Arbeitsatmosphäre sowie für die legendären Abende und unvergesslichen Erlebnisse unter anderem bei den durchgeführten „Stammtischen“. Es war mir eine große Ehre, für die in der Arbeitsgruppe verbrachte Zeit, euer „Captain“ gewesen zu sein.

Zuletzt möchte ich mich bei meiner (Schwieger-)Familie und meinen Freunden für die immerwährende Unterstützung und ihr Verständnis während der ganzen Promotionszeit bedanken. Mein herzlichster Dank gilt hier meiner Frau Julia, die mir bedingungslos zur Seite steht und immer ein zuverlässiger Rückhalt war.

# List of Publications

*Near-IR Absorbing J-aggregate of an Amphiphilic $BF_2$-azadipyrromethene Dye by Kinetic Cooperative Self-assembly*
Z. Chen, Y. Liu, W. Wagner, V. Stepanenko, X. Ren, S. Ogi, F. Würthner, *Angew. Chem. Int. Ed.* **2017**, *56*, 5729-5733.

*Living Supramolecular Polymerization of a Perylene Bisimide Dye into Fluorescent J-aggregates*
W. Wagner, M. Wehner, V. Stepanenko, S. Ogi, F. Würthner, *Angew. Chem. Int. Ed.* **2017**, *56*, 16008-16012.

*Coupled Cooperative Supramolecular Polymerization: A New Model Applied to the Competing Aggregation Pathways of an Amphiphilic Aza-BODIPY Dye into Spherical and Rod-like Aggregates*
Y. Liu, Y. Zhang, F. Fennel, W. Wagner, F. Würthner, Y. Chen, Z. Chen, *Chem. Eur. J.* **2018**, *24*, 16388-16394.

*Supramolecular Polymorphism in One-dimensional Self-assembly by Kinetic Pathway Control*
M. Wehner, M. I. S. Röhr, M. Bühler, V. Stepanenko, W. Wagner, F. Würthner, *J. Am. Chem. Soc.* **2019**, *141*, 6092-6107.

*Supramolecular Block Copolymers by Seeded Living Polymerization of Perylene Bisimides*
W. Wagner, M. Wehner, V. Stepanenko, F. Würthner, *J. Am. Chem. Soc.* **2019**, *141*, 12044-12054.

*Impact of Molecular Shape on Supramolecular Copolymer Synthesis in Seeded Living Polymerization of Perylene Bisimides*
W. Wagner, M. Wehner, V. Stepanenko, F. Würthner, *CCS Chem.* **2019**, *1*, *accepted article (September 2019)*.